Synthetic Simulation and Modeling of Image Intensified CCDs (IICCD)

Emmett J. Ientilucci

A.A.S. Monroe Community College (1989)
B.S. Rochester Institute of Technology (1996)

A thesis submitted in partial fulfillment of the
requirements for the degree of Master of Science
in the Center for Imaging Science in the College of Science
Rochester Institute of Technology

March 31, 2000

Signature of Author____

Emmett J. Ientilucci

Accepted by____

Coordinator, M.S. Degree Program Date

THESIS RELEASE PERMISSION
ROCHESTER INSTITUTE OF TECHNOLOGY
COLLEGE OF SCIENCE

Synthetic Simulation and Modeling of Image Intensified CCD's (IICCD)

Signature of Author____

Emmett J. Ientilucci

Date____

CHESTER F. CARLSON
CENTER FOR IMAGING SCIENCE
COLLEGE OF SCIENCE
ROCHESTER INSTITUTE OF TECHNOLOGY
ROCHESTER, NEW YORK

CERTIFICATE OF APPROVAL

M.S. DEGREE THESIS

The M.S. Degree of Emmett J. Ientilucci
has been examined and approved by the thesis committee
as satisfactory for the thesis requirement for the
Master of Science degree in Imaging Science

Dr. John R. Schott, Thesis Advisor

Mr. Rolando V. Raqueño

Dr. Jeff B. Pelz

Date

Abstract

Image intensifying cameras have been found to be extremely useful in low-light-level (LLL) scenarios including military night-vision and civilian rescue operations. These sensors utilize the available visible region photons and an amplification process to produce high-contrast imagery. Today's image intensifiers are usually attached to a CCD and incorporate a microchannel plate (MCP) for amplification purposes. These devices are commonly referred to as image intensified CCDs (IICCD).

To date, there has not been much work in the area of still-frame, low-light-level simulations with radiometric accuracy in mind. Most work has been geared toward real-time simulations where the emphasis is on situational awareness. This research proposes that a high fidelity simulation environment capable of producing radiometrically correct multi-band imagery for low-light-level conditions can be an extremely useful tool for sensor design engineers and image analysts. The Digital Imaging and Remote Sensing (DIRS) laboratory's Image Generation (DIRSIG) model has evolved to respond to such modeling requirements.

The presented work demonstrates a low-light-level simulation environment (DIRSIG) which incorporates man-made secondary sources and exoatmospheric sources such as the moon and starlight. Similarly, a user-defined IICCD camera model has been developed that takes into account parameters such as MTF and noise.

Acknowledgments

I would personally like to acknowledge all those who helped in the development and completion of this research. First off, I would like to thank all the participants who helped in the ground truth collection: Rolando Raqueño, Bryce Nordgren, my nephew Justin Ientilucci, and Mary Ellen Miller. Thanks for staying on the roof with me till 3am. Also Andy Silano and Jeff Pelz for the use of their secondary sources. Garrett Johnson for his help with the spectral radiometer and outdoor spectral data collections. I would also like to thank all those at RIT’s physical plant for turning off the lights on one side of campus and letting my have access to their blueprints of various buildings and surrounding pieces of real estate. Jason Gibson for the use of the radiometer and indoor data collections. My girlfriend Lori for supporting me and putting up with all those endless nights of not being able to go out. Finally, thanks to Scott Brown, Lee Sanders, and Erich Hernandez-Baquero for all their helpful insights and problem solving skills.

Dedication

LOVE LIVES ON

Those we love remain with us for love itself lives on,

And cherished memories never fade

Because a loved one's gone…

Those we love can never be more than a thought apart

For as long as there is memory, they'll live on in the heart.

This work is dedicated to my sister who I know would have been extremely proud to see me finish this body of work.

Table of Contents

List of Figures

List of Tables

Chapter 1

1. Introduction

1.1 Overview

Image intensifier tubes, sometimes called IITs, are relatively new cameras designed to be used in low-light-level conditions. Their basic function is to amplify the image of a scene. This is done by amplifying existing photons present in the scene of interest. These cameras are sometimes in the form of night vision goggles and are frequently used by the Navy and Coast Guard to find shipwreck victims at sea. Other applications include astronomy, mine detection, and X-ray imaging.

Today's IITs are usually attached to a charge coupled device (CCD) and incorporate a microchannel plate (MCP) for amplification purposes. Low-light-level (LLL) cameras in this configuration are often called *image intensified charge coupled devices* (IICCDs). These devices operate in the panchromatic (PAN) / visible (VIS) region of the electromagnetic (EM) spectrum with near infrared (NIR) sensitivity. Today's IICCD cameras are used for unmanned, remote, and covert surveillance. The size, low power requirements, and ruggedness of the units makes them also suitable for airborne, shipboard, and vehicle mounting systems. Furthermore, these devices can be found in weapon or field observation systems, lab instrumentation, microscopes, telescopes or low light optical systems. A shoreline under a cloudy, moonlit night or an unlit estate would be examples of applications where the intensified camera would be well suited. Not mentioned in the above description of IICCDs is their small intrascene dynamic range and their inherent "blooming" problems. The latter occurs when the camera reaches saturation due to an excessive number of photons in the original scene being amplified. For example, this phenomenon could be in the form of a bright street lamp or headlights from an automobile.

So far we have described a novel low-light-level sensor system that amplifies photons to a level that a human observer can readily analyze while mentioning some inherent device problems. It is clear that there are many applications for such a device, some areas having greater success than others. These successes rely on parameters like high camera gain, low noise, adequate light levels, minimal blurring, optimum viewing conditions, etc. These parameters fall in the category of optimal sensor design. But at what cost? Typical LLL sensor systems can cost anywhere from $10,000 to $30,000. One might ask, where does the design engineer cut corners on design parameters? Obviously, this is application specific. Another area of concern is that once the system is designed, how will it perform in the field and what kind of results might it yield? Lastly, what image scenarios might be best suited for the particular design of interest? The common answer to all these questions lies in the field of simulation.

Thus far, there has not been much work in the area of still-frame, low-light-level simulations with radiometric accuracy in mind. Most work has been geared toward real time simulations where the emphasis is on situational awareness and perceived realism. This research proposes that a high fidelity simulation environment is capable of producing radiometrically correct multi-band imagery for low-light-level conditions. This can be an extremely useful tool for solving the many questions posed earlier. The Digital Imaging and Remote Sensing (DIRS) laboratory's Image Generation (DIRSIG) model has evolved to respond to such modeling requirements.

Within the imaging community, simulations take on the form of image modeling. This area has gained significant popularity over the past several years. The main reason for this is the increase in computational power. As a result, the understanding of the phenomenology needed to generate the synthetic images has improved. However, it has not outpaced the rate of growth in CPU speed. The availability in computational power has lead to the development of artificial images that can be used in computer animation, flight simulation, and computer-aided design and manufacturing.

The remote sensing community can also reap the benefits of synthetic image generation (SIG) modeling. Here SIG can be used as a tool to train image analysts on the appearance of a target under different meteorological conditions, times of day, and look angles, for example. In addition, SIG can be used to help designers evaluate various sensor systems before actual hardware is fabricated. Synthetic images can also help determine the optimum acquisition parameters for a real imaging system by predicting the time at which the greatest contrast or resolution will be obtained for the desired targets. Furthermore, SIG can be useful in mission rehearsal planning, as an exploitation aid, and help in the analysis and development of algorithms. The end result is a large savings in research and development cost as well as increased performance and operational capabilities.

Originally DIRSIG was designed as a longwave infrared (LWIR) sensor model aimed at simple target-to-background calculations for IR signature studies. It evolved to a full 3-D thermal IR image generation model with an imbedded thermal model for target and background temperature estimation. In the 1980's, solar reflection terms were added and the model's spectral range was extended from the long wave infrared (LWIR) down into the visible [1]. Today DIRSIG incorporates transmissive objects, plume modeling, and the results from this research, low-light-level sensor capability, which includes lunar and secondary man-made sources. The incorporation of a LLL sensor model further enhances DIRSIG's capabilities. All the above mentioned uses can now be applied to simulating a LLL sensor system. Another example of this enhanced capability could be in the form of exploiting potential VIS/IR fusion algorithms through synthetic simulation.

The utility of these synthetic images is diminished if the output does not closely imitate the real world. As a result, the output from SIG must be evaluated and assessed according to criteria such as spectral and radiometric accuracy, geometric fidelity, robustness of application, and speed of image generation [2]. These parameters, however, will vary depending on the use of the SIG imagery. In this research we will concern ourselves with preserving radiometric and geometric fidelity as well as replicating common artifacts from intensifying sensors such as quantum noise, electronic noise, and MTF effects.

The motivation for this research is to generate a baseline tool in a synthetic image generated (SIG) environment for future analysis of IICCD designs, applications, and algorithms. The first step towards this goal is to fully understand the technology and workings behind image intensified sensor systems. This will provide a knowledge base for the creation of a new LLL sensor model in the SIG environment. From this we can characterize the image intensifier and validate an improved (radiometrically correct) sensor model, exploiting potential advantages and pitfalls.

1.2 Objectives (Statement of Work)

The objectives of this research are listed:

a) A literature review of related areas will be conducted. These areas include: image intensifier types, designs, performance, characterization, including noise and MTF effects, and low-light-level simulation work.
b) Implement lunar and secondary sources, including starlight, into DIRSIG.
c) Evaluate and characterize the IICCD in terms of its MTF and noise.
d) Implement new LLL sensor model in DIRSIG and render some existing scenes.
e) Collection: Truth imagery will be acquired with the IICCD sensor system. The scene content will represent the various dynamics of the image intensifier, including calibrated gray panels and resolution targets. The scenes will be classified into two subsets, one with secondary sources and one set without. The illumination conditions will vary within each subset. One case will contain the moon at some illumination percentage while the other will have the moon absent from the night sky (new moon case).
f) Generate the CAD equivalent of the truth scenes in DIRSIG. This includes drawing objects such as humans, vehicles, light poles, grass, parking lots, etc.
g) Render CAD images with LLL artifacts and perform a comparison and analysis.

Chapter 2

2. Background

2.1 Intensifiers

Sometimes it is useful to start out, appropriately enough, with a formal definition of the topic at hand. According to Webster's Dictionary, the definition of intensify is "to increase in density and contrast, to make more acute: sharpen." [3] Image intensifiers, or image converters, do just what the former statement suggests. Their basic function is to amplify the image of a scene. Image intensifiers, sometimes called image tubes, make up a small percentage of the more generalized photoelectronic technologies, as seen in Figure 2-1. At the center of this chart lies the photocathode, the prime detector, which is responsible for converting incident photons to photoelectrons. These photoelectrons can then be processed in a variety of ways to produce useful output imagery.

While the displayed image must be in the visible range, the input image may be formed in any spectral band from the ultraviolet to the far infrared. This is why they are sometimes called "image converters". In general, image intensifiers are among the simplest and first-developed electronic imaging devices [4-5].

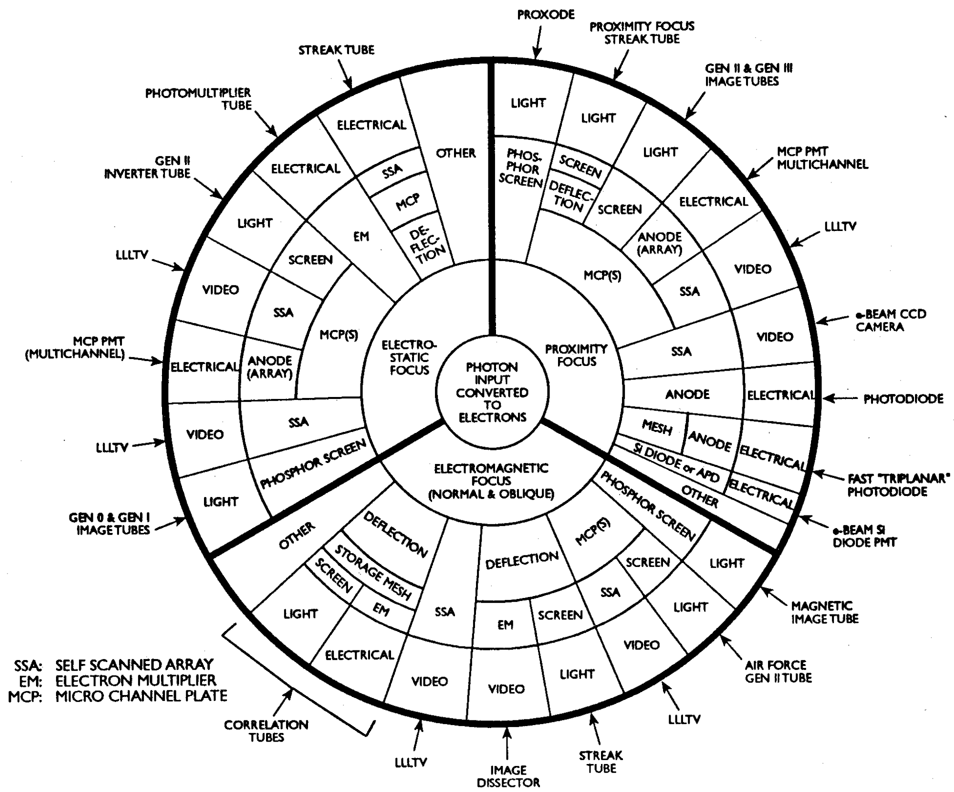

Figure 2-1 Diagram showing the broad range of photoelectronic technologies [6].

The discovery and explanation of the photoelectric effect dates back to the turn of the century. Albert Einstein explained the effect in 1905, for which he was awarded the Nobel Prize. However, practical electronic imaging devices based on the photoelectric effect did not start appearing on the market until the late 1950s and early 1960s. This was the result of extensive experimentation in the 1930s. Since then, image intensifiers have evolved into mature and highly capable devices [7]. Today's image intensifiers are much more sensitive and robust than those of the late 50s. These devices have numerous applications and are used in a variety of situations ranging from night-time surveillance to X-ray imaging (section 2.2).

2.1.1 Basic Image Intensifier Operation

The soul purpose of an image intensifier is to amplify the image of a scene. This is usually done by amplifying available photons contained in and around the scene of interest. For the most part, image intensifiers contain a photocathode surface which is irradiated by available photons found in the scene as seen in Figure 2-2. This may be done through the use of a front-end optical system. The photocathode absorbs incident light and converts it to photoelectrons, forming a low-energy input photoelectron image. This photoelectron image is then accelerated by several kilovolts due to a potential difference between the photocathode and a phosphor screen located at the rear of the intensifier. The (focused) accelerated photoelectrons then impact the fluorescent screen consisting of P20 or RCA-10-52 designate phosphor, which displays the output image [8]. Since a phosphor screen can emit several hundred photons when impacted by a photoelectron having 10 to 20 keV energy, an overall net gain in the number of photons can result (see Figure 2-3). This is the basis for image intensification. The intensifier, however, is not limited to incident radiation in the visible part of the EM spectrum. For example, the photocathode can be made sensitive to X-rays, ultraviolet (UV), or infrared (IR) radiation (section 2.1.4.4). In this context, the intensifier performs a means of image conversion.

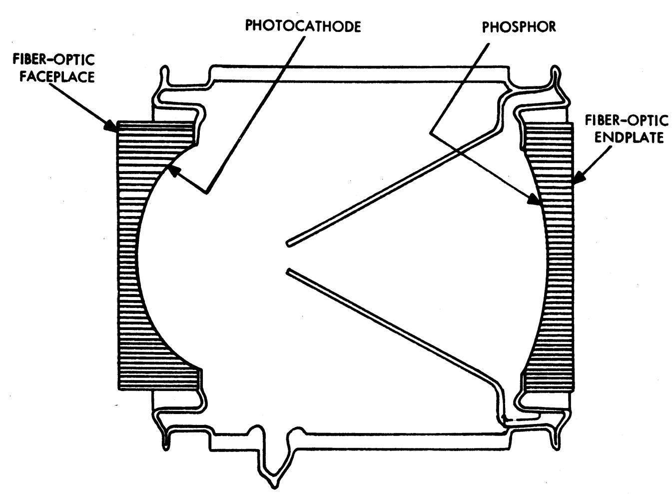

Figure 2-2 Schematic of a simple first-generation electrostatically focused intensifier [9].

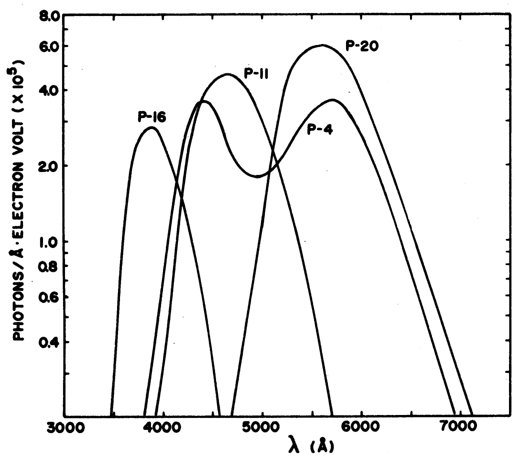

Figure 2-3 Light intensity output (photons/Å) of commonly used phosphor screens versus wavelength, per electron volt of energy deposited by bombarding electrons. (Courtesy of ITT Electron Tube Division).

2.1.2 Image Intensifier Focusing Techniques

A key element in the amplification process lies in the image intensifier's ability to maintain resolution and geometric fidelity in the output image with respect to the input image or image incident on the photocathode. This is largely due to the spreading of the photoelectrons from the photocathode. To minimize blur on the phosphor, intensifiers use three basic focusing schemes. These are proximity, electrostatic, and magnetic focusing.

2.1.2.1 Proximity Focused

Of the three techniques, proximity focusing is the simplest (see Figure 2-4). This can be misleading, however, since no actual focusing of the photoelectrons takes place. The objective here is to simply minimize the spreading of the photoelectrons by placing the photocathode and phosphor screen in close proximity to one another. Although the photoelectrons are accelerated by the potential difference in the direction perpendicular to the plane of the electrodes, spreading of photoelectrons emitted from a point on the photocathode occurs because they are released from the photocathode with nonzero velocities (due to the difference between the energy threshold of photoelectric emission and the actual energy of the absorbed photon) and in random directions [9]. Therefore the initial emission velocity will contain an axial component as well as a transverse component, which characterizes lateral movement. Though the electric field between the photocathode and phosphor directly affects the axial component, it has no affect on the transverse vector. The fact that the potential between the electrodes has no affect on the transverse component leads to divergence of the photoelectron trajectories and image blurring. This is directly due to the divergence of the photoelectron trajectories from the photocathode.

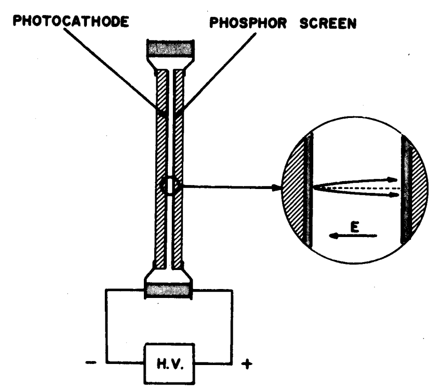

Figure 2-4 Example of proximity focusing technique used in an image intensifier [9].

The spread of a point image is proportional to the maximum initial transverse or radial velocity v_r and the time of flight t from cathode to anode [9]. Only the time of flight variable t can be modified. The time can be minimized by decreasing the photocathode-anode dimension L and by increasing the acceleration potential V_L (see Figure 2-5).

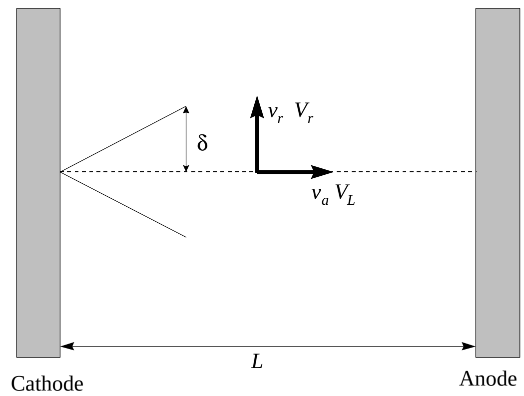

Figure 2-5 Modeling the spread of a point image in an proximity focused image intensifier where v_r and v_a are the radial and axial velocities, respectively.

The lateral displacement δ of a photoelectron is given by

$$d = v_r t = \left(\frac{2eV_r}{m}\right)^{1/2} 2L\left(\frac{2eV_r}{m}\right)^{-1/2} = 2L\left(\frac{V_r}{V_L}\right)^{1/2} \qquad (2.1)$$

and the maximum diameter of a point image is therefore $D_{max} = 2\delta$ [9]. Realistically, however, there is a limit to what the minimum spacing L and the maximum potential V_L can be. If the cathode and anode are too close, one runs the risk of high-voltage breakdown between the electrodes. Typically, the electric field $E = V_L / L$ should not exceed 5 kV/mm [9]. Furthermore, the resolution increases as $1/V_L$. That is to say, as the acceleration voltage V_L increases (in the optimal scenario) the resolution at the phosphor will degrade. However, V_L is also a function of the cathode-anode spacing L. Hence, the acceleration voltage is reduced with closer spacings.

Proximity-focused image intensifiers have relatively low spatial resolutions. Some literature states that typical resolutions are on the order of 15 - 20 lp/mm [9]. The trade-off here, due to physical construction, is in their size. Because of their simplicity and compactness, they can easily be made in very large diameter formats which can, in some cases, compensate for low spatial resolution. In some applications they are also unaffected by external magnetic fields.

2.1.2.2 Electrostatically Focused

Electrostatic focusing uses electric fields to actively focus photoelectrons in transit from the photocathode to the phosphor screen (see Figure 2-6). A useful analogy here is the observation that a particle in a potential field will follow laws similar to those followed by light rays in a medium of varying refractive index. The velocity of an electron at a given point in space is proportional to the “index of refraction” in this analogy. Furthermore, equipotential surfaces are analogous to lens surfaces in traditional optics.

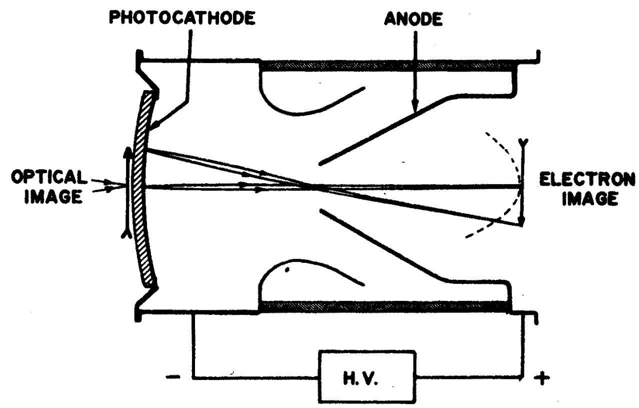

Figure 2-6 Example of electrostatic focusing technique used in an image intensifier [9].

An electrostatically focused intensifier differs from a proximity focused one in that the former has a conical accelerating electrode with an aperture to accelerate and focus the photoelectrons. They also differ in that the photocathode and phosphor screens are curved toward each other. With electrostatic focusing the resolution is almost double that of a proximity focused intensifier. Though the resolution is better at the center of the field, compared to proximity focusing, it tends to decrease at the edges.

Electrostatically focused intensifiers can also achieve demagnification ratios of less than one. The ratio here being image size on the photocathode compared to the image size on the phosphor. Demagnification of the photocathode image of 2:1 to 10:1 is often used, especially in applications involving large-area, low-resolution images (such as in many medical or industrial X-ray applications) [9]. Naturally the demagnification process will yield a brighter image on the phosphor due to the concentration of photoelectrons. This will also mean that a given image resolution on the phosphor corresponds to a lower resolution as measured at the photocathode surface.

2.1.2.3 Magnetically Focused

In a magnetic focused image intensifier electric as well as magnetic fields are used to accelerate and focus photoelectrons (see Figure 2-7). Here the photocathode and phosphor are parallel to one another. The magnetic field corrects for the spreading of photoelectrons by confining the radial components of velocities to circles centered on magnetic field lines. The focusing condition requires that the photoelectrons complete at least one loop of the magnetic field line circle, in the radial direction, in the time it take the photoelectron to reach the phosphor. This condition can be shown to be satisfied when the distance *L*, magnetic field *B*, and accelerating potential *V* are related by

$$L = \frac{p}{B}\left(\frac{2mV}{e}\right)^{1/2} \tag{2.2}$$

for single-loop focusing [9]. This focusing technique can produce resolutions that are much greater than those achieved with electrostatically focused intensifiers (>100 lp/mm). However, the main drawback is the need for large focusing magnets or solenoid coils.

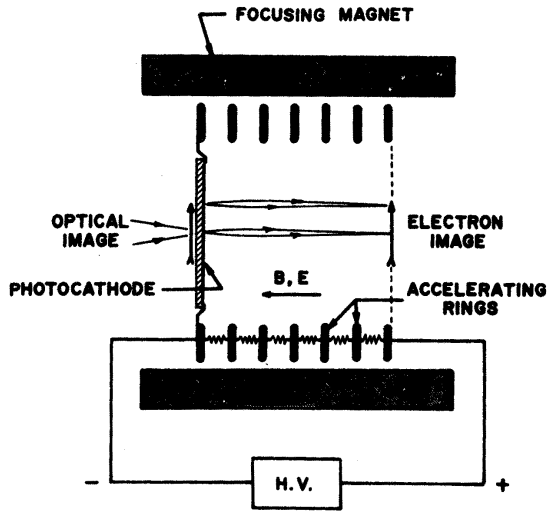

Figure 2-7 Example of magnetic focusing technique used in an image intensifier [9].

2.1.3 Microchannel Plate Technology (MCP)

A key device found in many of today's intensifiers is the microchannel plate (MCP). Microchannel plates have the same characteristics as photomultiplier tubes (PMT) in that they are both devices used to amplify photoelectrons. The difference between the two lies in their constructions. A typical PMT, as seen in Figure 2-8, makes use of several discrete dynodes, each held at a fixed potential relative to the photocathode. The electrical potential gets increasingly larger through the dynode string where it reaches its maximum at the anode. The photoelectrons, from photoemission, collide with the first dynode, exhibit secondary emission, and are accelerated to the second dynode where secondary emission occurs again. This chain of events continues until the photoelectrons reach the anode thus producing an overall gain in photocurrent.

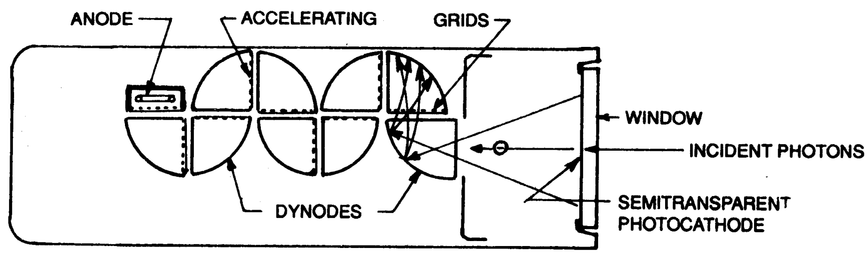

Figure 2-8 Typical operation of a photomultiplier tube (PMT) [9].

Devices called channel multipliers [10] perform a similar operation to that of PMTs (see Figure 2-9). The dynode string in the PMT is replaced by a single, continuous tube of semiconducting glass whose inside surface is specially processed to have a high secondary emission coefficient. When incident radiation (e.g., photons or charged particles) impinges on the input side of the channel multiplier with sufficient energy to overcome the work function, secondary emission occurs. These secondary electrons are accelerated down the channel and multiplied along the continuous dynode in an electron avalanche. This process continues until a charge cloud, initiated by a single event, exits the channel as shown in Figure 2-10. The channel multiplier has the advantage, over the PMT, of being much simpler and more compact. However, they are limited to operation at lower light levels than can be handled by photomultipliers because of current limitations in the walls of the channel multiplier.

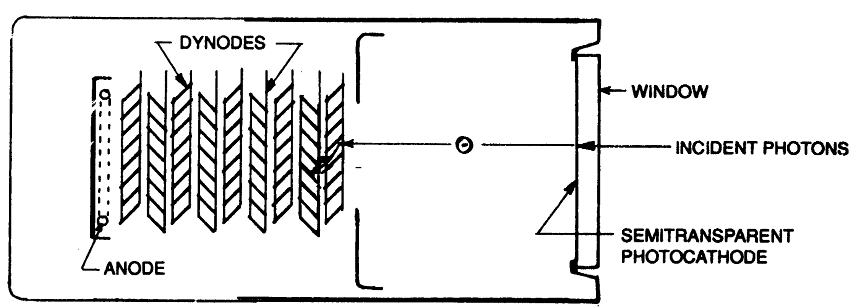

Figure 2-9 Typical operation of a channel multiplier [9].

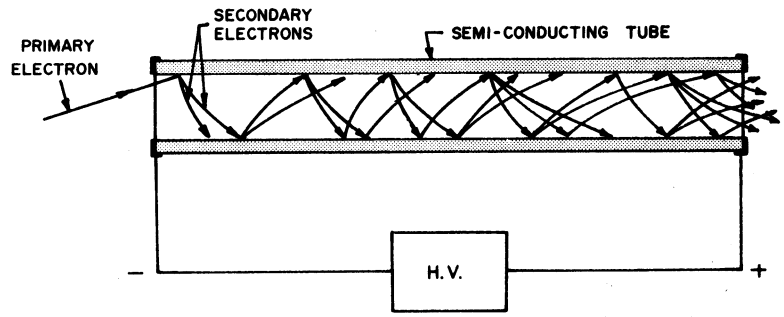

Figure 2-10 Principle operation of a continuous channel electron multiplier [9].

2.1.3.1 Ion Feedback

Ion feedback is a phenomenon that occurs when a straight-channel electron multiplier, like the one in Figure 2-10, is operated at gains above 10^4. The problem is caused by positive ions feeding back through the channel. These ions are created at the end of the channel multiplier where the voltage potential is considerably high. When a photoelectron impinges on the wall of the multiplier at this location, positive ions are created. These ions are then, in turn, attracted to the front end (lower potential) of the multiplier (i.e., they are traveling in the opposite direction to that of the photoelectrons). If the ions strike the lower-potential front end, secondary electrons will be released along with the ones created by the photoelectrons. The end result is that there will be false counts or noise emanating from the output of the channel.

To help eliminate this problem, channel multipliers are usually constructed with a curved shape, as shown in Figure 2-11. This curved shape prevents the heavy positive ions from traveling up the channel while still allowing the lighter photoelectrons to travel down the channel. Curved channel multipliers can be used at gains as high as 10^7 without significant ion-feedback problems [9].

A natural progression would be to utilize the single channel multiplier in a two-dimensional configuration [11]. This can be done by placing holes in a large plate of semiconducting glass, hence the name microchannel plate (MCP). Figure 2-12 and Figure 2-13 shows an example of a straight-channeled MCP. The plate consists of millions of independent microscopic channel electron multipliers all fused together in a rigid, wafer-like array which is sensitive to electrons, ions, accelerated neutrals, UV photons and soft X-rays [12]. These MCPs can be made into a variety of shapes and sizes (see Figure 2-14). The plates can be 18 mm, 25 mm, or 40 mm in diameter, depending on the intensifier type. These devices have ultrahigh temporal resolution and spatial resolution limited by channel spacing (typically 8 μm-diameter channels on 10 μm centers). Significantly improved spatial resolution is expected to result from micro-fabrication of microchannel arrays with channel spacings less than 5 microns [12]. This small, compact size makes microchannel plates ideal for imaging and non-imaging applications.

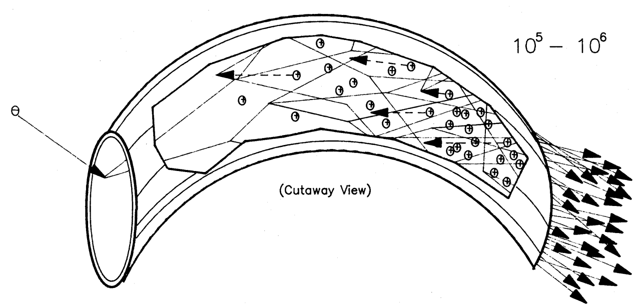

Figure 2-11 Curved channel electron multiplier inhibits ion feedback [12].

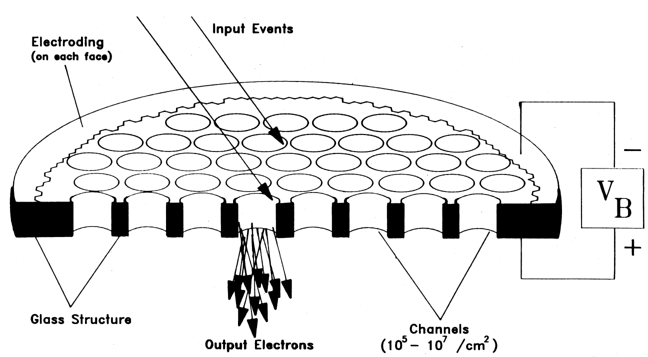

Figure 2-12 An example of a two-dimensional microchannel plate [12] where the input event can be either a photon or photoelectron.

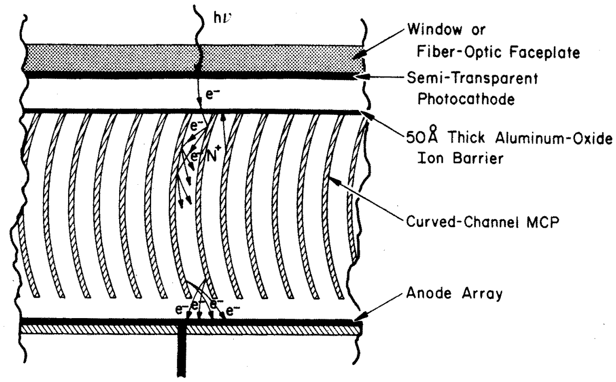

Figure 2-13 Cross section of a typical curved microchannel plate [27].

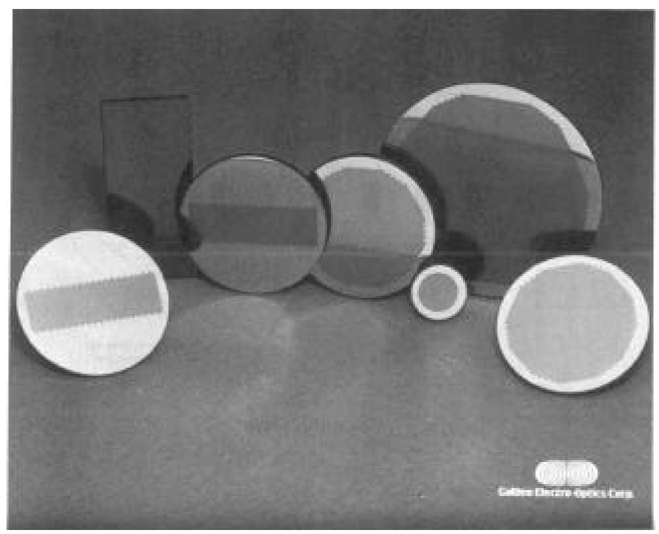

Figure 2-14 Some examples of various formats and sizes of microchannel plates [12].

2.1.3.2 Stacking Microchannel Plates

It is much more difficult to manufacture a *curved* microchannel plate than it is to generate a *curved* channel electron multiplier. However, attempts at curved MCPs have been performed with moderate results with gains as high as 10^6 [13-14]. A technique used to get around this mechanical problem is to stack two or more straight-channeled MCPs in series with one another, as can be seen in Figure 2-15. Each straight-channeled MCP has a gain less than 10^4 but when stacked together, the overall gain is increased significantly. To inhibit the ion feedback problem the channels are tilted with respect to one another. This combination simulates a curved channel MCP and reduces overall ion feedback. A *chevron configuration* is when two MCPs are stacked in series. Similarly, a *Z configuration* is when three MCPs are stacked together (see Figure 2-16). Figure 2-15 shows the various gains that can be achieved using different MCP configurations. A straight channel MCP can yield a gain of around 10^4 while a curved MCP has a higher gain of about 10^6. By stacking single MCPs together gains on the order of 10^6 to 10^8 can be achieved [15].

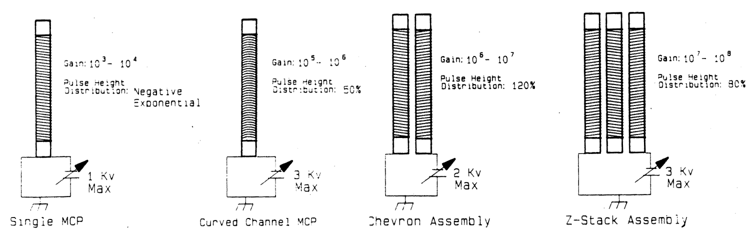

Figure 2-15 Examples of increased gain due to MCP stacking. The use of two MCPs in cascade can produce a gain of 10^6 - 10^7, while the addition of a third plate will provide a gain of 10^7 - 10^8 [12].

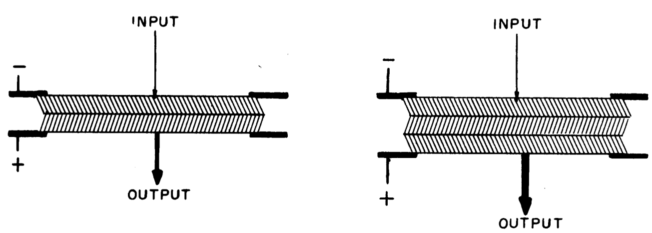

Figure 2-16 Use of two microchannel plates, stacked in series ("chevron" configuration) or three stacked together ("Z" configuration) to obtain higher electron multiplication gain than possible with a single, straight-channel plate [9].

2.1.4 Image Intensifier Types

Early image intensifiers were not suited for practical applications because of poor resolution, speed of response, power gain, and operating life [7]. Furthermore, they were much too heavy and very bulky at best. Advances came only after extensive research on improved photocathodes, high-resolution phosphor screens, high-resolution fiber-optic and microchannel plates, and suitable power supplies, gating networks, and glass optics for input and output [7].

The first image intensifier used in active night-vision applications was an infrared light image converter designated now as the Generation Zero device (see Figure 2-17) [8]. For passive night vision, astronomy, aerial and high-speed photography and X-ray image intensification, the *electromagnetically focused* (section 2.1.2.3) image intensifier tube was developed. This intensifier, for all practical purposes, is now called the Generation ½ device. The Generation ½ intensifier had a high light level resolution of up to 45 lp/mm and a luminous gain of about a half million [8].

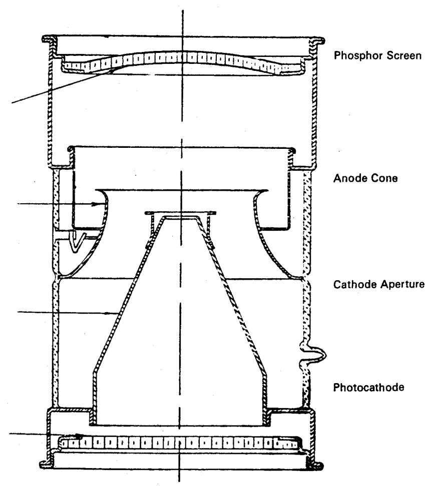

Figure 2-17 Example of a Generation zero image intensifier [16].

The Generation I intensifier, as seen in Figure 2-18, was produced for the military out of the need for small, light-weight, brightness-scaleable passive night vision telescopes. Unlike its predecessors, the Generation I intensifier was *electrostatically focused* (section 2.1.2.2). These devices had resolutions on the order of 25 to 36 lp/mm [8] and typical gains of 20 - 100 provided by a 5-15 thousand volt differential [17]. The photocathode of a generation I intensifier is typically multialkali (section 2.1.4.4) resulting in a 400 - 900 nm spectral response [17]. By the early 1960s, all three of the above mentioned intensifiers had been placed into full-scale production. Further improvements on intensifier technology gave way to the Generation II electrostatic image inverter tube (see Figure 2-19). This device, produced in the late 1960s and early 1970s, was a passive night-vision intensifier that utilized a multialkali photocathode for sensing the input image and a microchannel plate for internal photocurrent multiplication. It was originally developed for telescopic applications. Today the Generation II comes in a variety of flavors depending on the photocathode sensitivity.

By the late 1970s and early 1980s, the Generation III image intensifier had been developed, as can be seen in Figure 2-20. This intensifier was very similar in design to the Generation II. The only difference between the Generation II and the Generation III is that the latter has a highly sensitive GaAs/GaAlAs photocathode and utilizes an ion-barrier-coated microchannel plate. This new material shifts the spectral response to the near infrared.

The original Generation II intensifiers were limited to UV and RED responses of 200nm to 800nm and 400nm to 900nm, respectively. Similarly, the Generation III was limited to a spectral response of 600nm to 900nm. Today many improvements have been made to the Generation III intensifiers with moderate changes for the Gen. II intensifiers. The Gen. III has evolved from the Gen. III RED to the Gen. III extended blue, Gen. III green, and the Gen. III near IR [18].

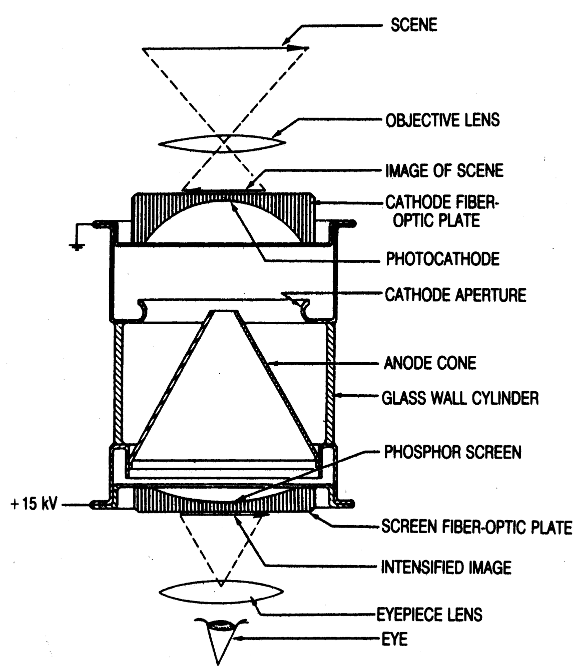

Figure 2-18 Example of a Generation I electrostatically focused image intensifier tube. The central field and the anode aperture lens form an inverted image of the cathode on the screen sphere [16].

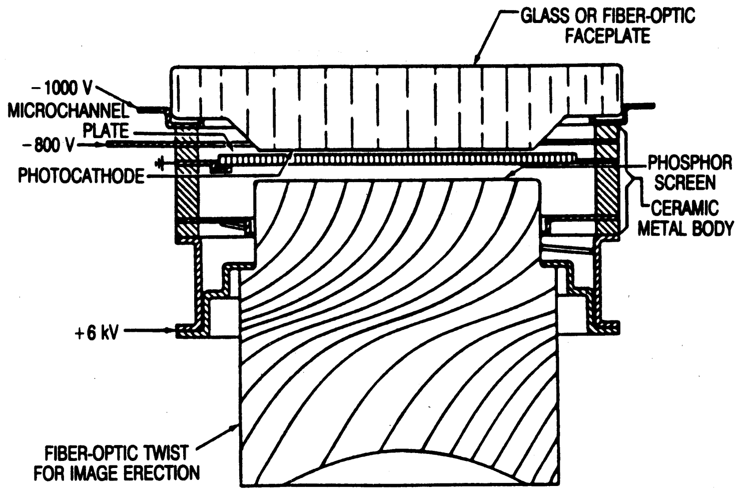

Figure 2-19 Example of a Generation II image intensifier tube. The photocathode and the output of the microchannel plate are proximity focused on the microchannel plate input and output phosphor screen respectively [16].

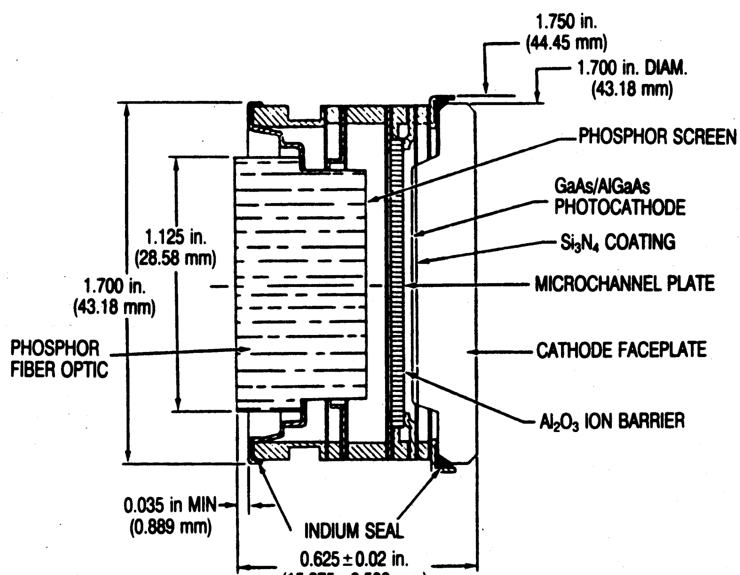

Figure 2-20 Example of a 25 mm, proximity focused, Generation III image intensifier tube [16].

Intensifiers, in general, can be classified into three main categories: 1) photon-counting devices; 2) solid state detectors (i.e., CCDs); and 3) image intensified CCDs, which are a combination of the two former technologies. A typical "Generation x" intensifier is usually classified as operating under one of these technologies.

2.1.4.1 Photon Counting Devices (MCP, no CCD)

Photon-counting imaging devices are cameras which make use of the photoelectric effect in such a way that they can detect individual photons. These devices are based on the direct detection and processing of the amplified photoelectron events which exit the back surface of an MCP or stack of MCPs. These include various schemes for determining the spatial location (x, y coordinates) of the individual events. Several types of photon-counters are currently being used for low-light imaging, including precision analog photon address (PAPA) detectors, resistive anode devices, wedge-and-strip detectors, and multianode microchannel array (MAMA) detectors [19]. These all use a microchannel plate (MCP) or MCP stack for signal amplification. The photocathodes in these devices can be made of a number of different materials depending on what wavelengths response is desired.

Photon-counting devices have traditionally been used at low light levels, where CCDs cannot be used because of read noise. Because the same photocathode materials are available for all of these cameras, they all have about the same limiting quantum efficiency. What really distinguishes one photon-counting camera from another is the way that the output of the MCP is read out. This process affects not only the overall efficiency of the device, but also its linearity and timing resolution.

Precision Analog Photon Address (PAPA) Detectors

Figure 2-21 shows the basic operation of a precision analog photon address (PAPA) detector. These detectors were developed by Papaliolios and Mertz [20] and their collaborators. Here, the charge cloud exiting the MCP stack strikes a phosphor screen and produces a spot of light. An image of the phosphor screen is sent via optics to 19 phototubes, 18 of which have their active area covered by one of nine different gray-scale masks. The 19th phototube has no mask and acts as an event strobe, simply registering a pulse if the spot on the phosphor is detected. Nine of the phototubes are used to obtain positional information in one direction, and the other nine obtain the positional information in the orthogonal direction. The same gray scale is therefore used on two phototubes, but the orientation of one is perpendicular to the other. If the phosphor hit is in a region not covered by the mask, the event is detected by the phototube. If the phosphor hit is registered in an area covered by the mask, no event is recorded. By taking the information from each phototube and making a conversion from gray scale to binary address, events can be recorded as a list of photon addresses and arrival times. The advantage of gray-scale encoding instead of binary mask encoding is that events on a white-black boundary of a mask suffer at most a 1-bit error rather than multiple bit errors in the positional address, as is the case with binary masks.

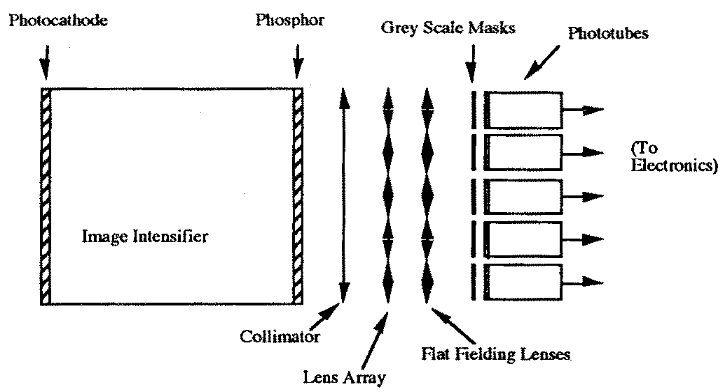

Figure 2-21 Example of precision analog photon address (PAPA) detector [19].

Resistive Anode Detectors

The resistive anode microchannel plate device was originally developed in the 1970s by Lampton and Paresce [21] and Parkes *et al.* [22]. These techniques have been implemented as both one and two-dimensional devices [23-24]. In the one-dimensional configuration (see Figure 2-22), a continuous strip of semiconducting material is placed beneath the MCP to collect the charge clouds from events. Amplifiers are attached to two ends of the strip for a one-dimensional readout. The position x along the strip (length L) is determined from the ratio of the charge pulse amplitudes input to the two amplifiers, proportional to $x/(L - x)$. Advantages of the resistive strip readout technique are simplicity and need for fewer amplifiers. However, the spatial resolution and maximum count rate are less than for some other approaches. The resolution is limited by thermal noise in the resistive strip, although it can be improved by using higher MCP gain. In the two-dimensional configuration (Figure 2-23), a sheet replaces the strip beneath the MCP. Here, amplifiers are attached to four ends of the sheet for a two-dimensional readout. A measure of position is then obtained by using the one-dimensional technique applied in both dimensions.

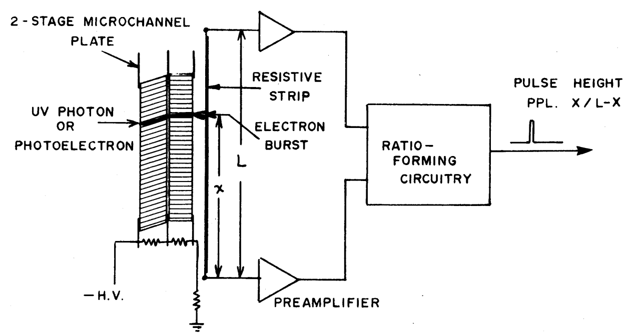

Figure 2-22 One-dimensional version of a resistive-anode readout microchannel plate detector. The location of a photoevent is determined from the ratio of signal amplitudes output by each end of the anode [9].

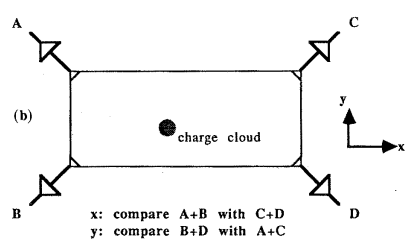

Figure 2-23 Two-dimensional configuration for a resistive anode detector [19].

This system does have limitations, however. The spatial resolution is critically dependent on the gain of the MCP, and for the best spatial resolution, the resistive-anode encoder requires gains in excess of 10^7 electrons pulse^{-1} dictating the use of “chevron” or “Z-plate” MCPs in which the charge is spread over a number of channels in the second and third MCPs in the stack. A resolution of 50 μm requires a stack of five MCPs to produce a gain on the order of 3×10^7 electrons pulse^{-1} [31].

Wedge-and-Strip Detectors

A simple conductive multianode array, which eliminates some of the limitations of the resistive anode, is the wedge-and-strip. This was originally developed by Martin *et al*. [26] at the University of California, Berkely, and later evaluated by Seigmund [27]. A schematic of a typical array configuration is shown in Figure 2-24. In this array, charge is collected on a number of discrete conduction electrodes; but positional information is determined by the ratio of the charge collected on the different electrodes. In the array shown in Figure 2-24, the coordinates of the event in the horizontal (X) axis are determined by the ratio of the charge collected on electrodes C and D, and in the vertical (Y) axis by the ratio of the charged collected on the electrodes A and B. A disadvantage of the wedge-and-strip array as compared with the resistive-anode array is that the anode must be placed about 1 cm behind the output face of the MCP in order to allow the emerging charge cloud to spread over more than one repetition period of the pattern. This requires careful magnetic shielding of the detector since a magnetic field of 1 gauss can deflect the image by about 100 microns [28].

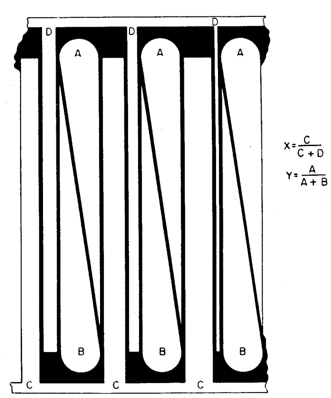

Figure 2-24 A portion of a wedge-and-strip array devised by H. O. Anger (1966). Black regions are insulators and white areas are conductors. Anodes A and B are used to determine the vertical (Y) location of the event and anodes C and D are used to determine the horizontal (X) location of the event [26].

Multianode Microchannel Array (MAMA) Detectors

MAMA detectors were originally developed by Timothy and Bybee in the late 1970s, and current versions of the detector were described more recently by Timothy *et al.* [29]. This technique is illustrated in Figure 2-25. Although a crossed grid of discrete electrodes is used, the technique allows an array of a ´ b pixels in one dimension to be read out using $a + b$ readout amplifiers, where a = coarse-encoding electrodes and b = fine-encoding electrodes, as shown in Figure 2-26 for a one-dimensional array. A photoevent is sensed simultaneously on at least one fine and one coarse electrode; the coarse electrodes remove the ambiguity which results from using a fine electrode to sense positions at different segments of the array. A two-dimensional image of $(a \times b)^2$ pixels can be read out using $2(a + b)$ electrodes. MAMAs with up to 1024 x 1024 pixels are currently in use [7]. The MAMA typically uses a curved-channel MCP with a gain of 10^5 to 10^6, with the anode layer in close proximity (about 50 mm) to the back surface of the MCP to minimize spreading of the charge cloud before it is detected [9].

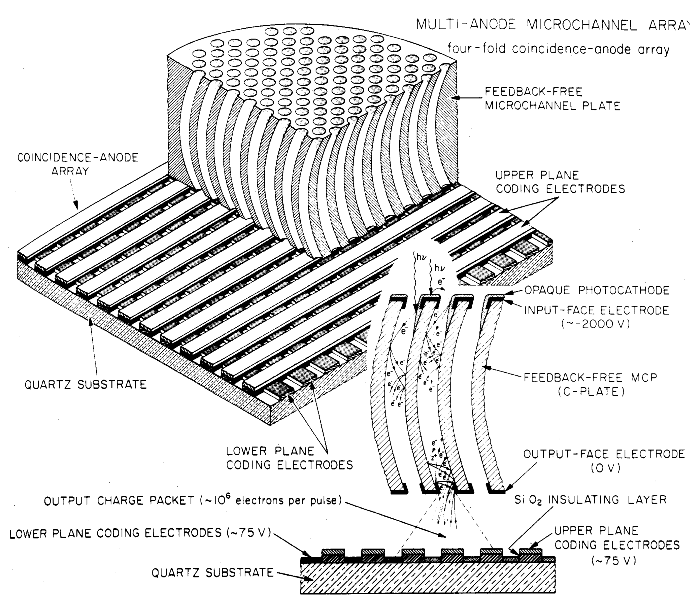

Figure 2-25 Diagram of a Multi-Anode Microchannel Array (MAMA) detector [30].

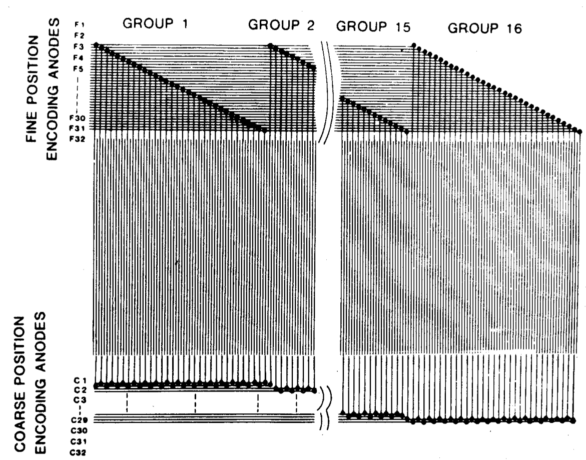

Figure 2-26 Illustration of a one-dimensional array of coarse and fine encoding anodes, which can localize photoevents in *a* ´ *b* positions with only *a* + *b* amplifiers [31].

2.1.4.2 Image Intensified CCD (MCP and CCD)

Intensifiers that are used in industrial and scientific applications are usually coupled to CCDs. These systems are called, appropriately enough, Image Intensified CCDs (IICCD) or just Intensified CCDs (ICCD). Some of the highest performance cameras utilize a Generation III imager intensifier tube optically coupled to a standard CCD chip. Figure 2-27 shows a simple representation of the ICCD process. Basically, these devices have an image intensifier (a microchannel plate or microchannel plate stack with a phosphor screen on the outside), which is then optically coupled to a CCD array. The image is therefore imaged onto the photocathode, and an intensified copy then is produced on the phosphor, which the CCD records. These detectors are similar to the photon counting cameras in that the quantum efficiency is limited by the photocathode material. The CCD is sometimes read out in what is known as "frame transfer mode," where only half of the CCD pixels are used for imaging and the other half store the previous frame while it is being read out. In this way, the system can read out frames typically at a video rate (~30 frames /s), and can be directly stored on videotape.

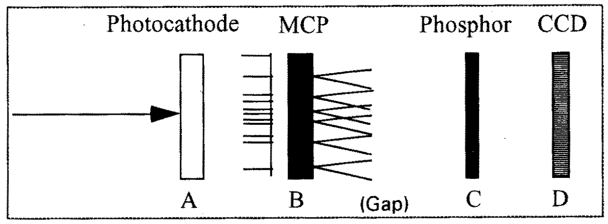

Figure 2-27 Basic schematic of the intensified CCD process [32].

One feature of ICCDs is that CCD read noise is not generally a problem, because the image recorded is already intensified to a level to make read noise insignificant [19]. In contrast with some of the more exotic photoelectric devices discussed in sections 2.1.4.1 and 2.1.4.3, these systems are relatively inexpensive. The ideal photon-counting device gives a δ function response to a detected photon event, in both space and time. With ICCDs, individual photons are not recorded as δ functions, but are the images of phosphor flashes, which can spread over several pixels and may last more than one frame, depending on the phosphor decay time [19].

2.1.4.3 Solid State Detectors (CCD, no MCP)

Many of the low-light-level real-time video imaging problems impose stringent requirements on the performance characteristics of the detectors used. Such stringent requirements are on sensitivity and spatial resolution, for example. The routine approach of optically coupling a Generation I, II, or III image intensifier with a readout CCD can provide either high light gain (for the Generation II or III image intensifiers) and moderate spatial resolution, or poor light gain (for the Generation I image intensifiers) with high spatial resolution [33-34]. Furthermore, additional lag in traditional systems can be attributed to the use of phosphor screens.

Some of these limitations can be circumvented by using electron-sensitive CCDs capable of detecting photoelectrons directly. This new class of video-rate imagers is based on back-illuminated and thinned CCDs. These promise to replace conventional image intensifiers for most military, industrial, and scientific applications. Thinned, back-illuminated CCDs (BCCD) and electron-bombarded CCDs (EBCCD) offer low light level performance superior to conventional image intensifier coupled CCD (ICCD) approaches [35]. Other work in this new field, including detector performance, can be found in the literature [36-39].

Back-illuminated CCD (BCCD)

Thinned, back-illuminated CCDs overcome the performance limits of conventional front-illuminated CCDs by illuminating and collecting charge through the back surface (see Figure 2-28). When the CCD is mounted face down on a substrate and the bulk silicon is removed, only a thin layer of silicon containing the circuit's device structures remains. Without having to pass through the polysilicon gate electrodes, the photons from the image enter the CCD back surface unobstructed. By illuminating the CCD through the back surface in this manner, quantum efficiencies greater than 90 percent can be achieved [35]. This device is also capable of imaging radiation found in the ultraviolet and X-ray energy regions of the EM spectrum. Furthermore, in a front illuminated CCD almost all the UV energy is absorbed whereas in the BCCD a quantum efficiency of about 50% can be achieved at 200 nm [35].

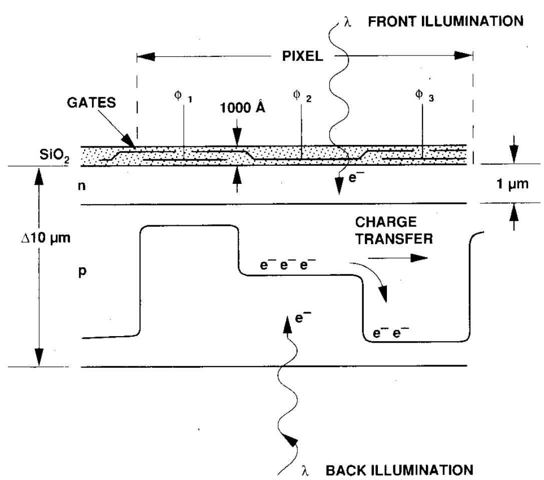

Figure 2-28 A cross section comparing front-illuminated and back-thinned CCD operation. Front-illuminated devices are supported by a thick substrate and have substantially higher yields, but much lower short wavelength quantum efficiencies. Back-illuminated devices must have the silicon substrate removed and the rear surface treated to accumulate any trap states. These devices are more difficult to fabricate, but have a greatly enhanced UV and X-ray quantum efficiency and are able to efficiently detect energetic electrons [38].

Electron Bombarded CCD (EBCCD)

William's *et al*, [35] state that the EBCCD imager eliminates the complicated image transfer chain associated with conventional ICCDs by integrating the CCD directly into the vacuum of the image tube. The back-illuminated CCD forms the anode of the EBCCD sensor, eliminating the need for a microchannel plate, phosphor screen, and a fiber optic coupler. The photoelectrons emitted from the EBCCD photocathode are proximity focused (section 2.1.2.1) directly onto the electron sensitive CCD. Entering the back surface of the thinned CCD, the silicon dissipates the incident photoelectron energy as electron-hole pairs, and electron bombarded semiconductor (EBS) gain occurs. The EBS process is significantly lower in noise than the electron gain obtained using a microchannel plate. It is ideal in the sense that it can provide nearly noiseless gain in excess of 3,000 [35], more than sufficient to overcome the system's noise sources. Electron bombarded CCDs can provide other benefits such as higher dynamic range, a larger signal to noise ratio, and greater spatial resolution. All this is not without a price, and currently, several difficulties relating to manufacturing technology have prevented image intensifiers using EBCCDs as readout structures from becoming the standard device, as opposed to the novel item they are currently relegated to.

2.1.4.4 Photocathode Considerations

The spectral response of an image intensifier is primarily dependent upon the materials used in the photocathode. For example, a Generation II intensifier utilizes a bi-alkali or multi-alkali photocathode while a Generation III intensifier uses a gallium arsenide (GaAs) photocathode. The photocathode can be doped in various combinations for determination of sensitivity at various wavelengths of light. Figure 2-29 shows some spectral sensitivities and quantum efficiencies of various photoemmiters, some of which are used in today's image intensifiers. Recently, Generation II and III intensifiers use the improved photocathode designs shown in Figure 2-30.

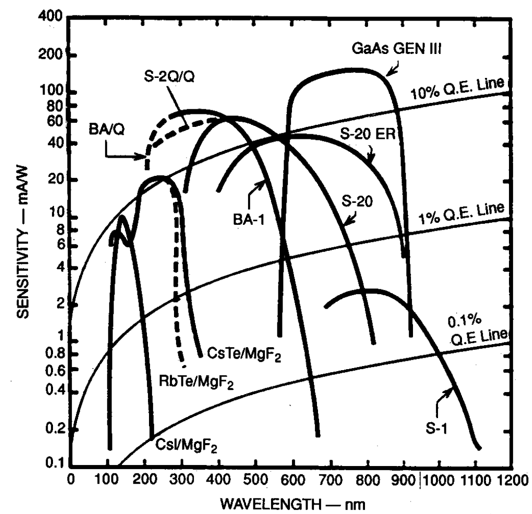

Figure 2-29 Spectral sensitivity versus wavelength for various photoemitters [9].

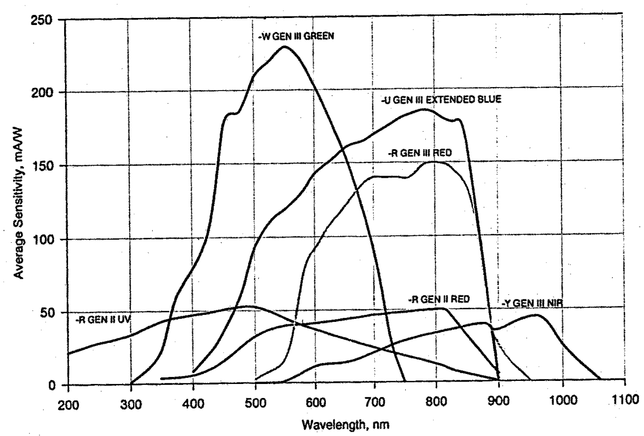

Figure 2-30 Photocathode spectral responses (sensitivity) for various Generation II and III intensifiers [18].

The various materials also effect the quantum efficiency (QE) of the photocathode. Strurz [18] expresses this metric in the following relationship,

$$QE = \frac{(123.950) \times \text{ Radiant Sensitivity (mA / W)}}{l} \tag{2.3}$$

where wavelength (λ) is in nanometers. The other form of this expression which relates quantum efficiency and responsivity is

$$QE(l) = \frac{b(l)\,hc}{e\;l} \tag{2.4}$$

where:

$b(l)$ = responsivity [A/W]
h = 6.6 E^{-34} [Js]
c = 3 E^{8} [m/s]
e = e- charge = 1.6 E^{-19} [coulomb]

Figure 2-31 shows the quantum efficiencies for the various photocathodes in Figure 2-30. These quantum efficiency values were derived from equation 2.3. Figure 2-32 compares some of the more traditional photocathodes in terms of quantum efficiency. This includes the GaAs, bi-alkali, and (S-20) multi-alkali photocathodes.

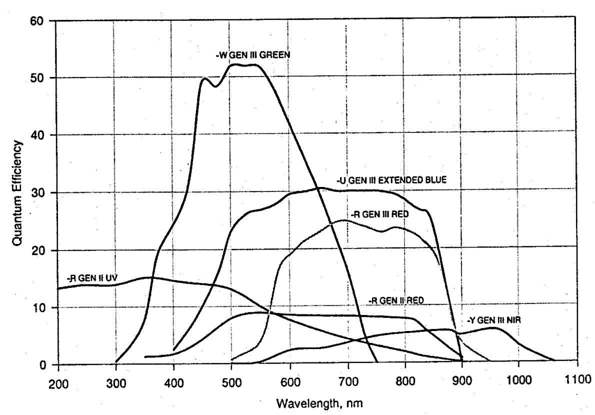

Figure 2-31 Image Intensifier photocathode quantum efficiencies for various Generation II and III intensifiers [18].

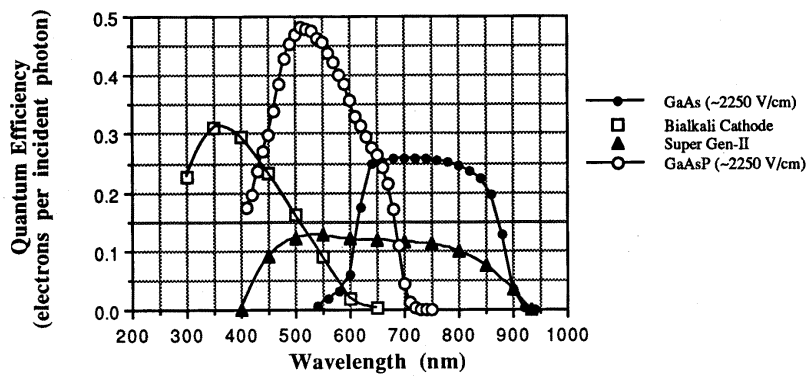

Figure 2-32 A comparison of photocathodes. The GaAs referred to is the standard night vision variety. Super Generation II photocathode refers to a standard multialkali (S-20) with extended response in the IR [40].

2.2 Applications and State of the Technology

There are many different types of image intensifiers on the market today, as pointed out in section 2.1.4. The choice of intensifier is usually based on the type of application for which it will be used. These intensifiers all have advantages and disadvantages which must be considered when finding an appropriate match for the intended application. Furthermore, an additional match can be made based on the wavelength of incident light. This entails picking an appropriate photocathode that is sensitive to the wavelengths of interest.

Since the pre-WWII years, many new applications for image intensifiers have been found. Most of these intensifiers, however, have been confined to tactical night vision applications such as surveillance, mine detection, and search and rescue operations. The emphasis here is on improving the red sensitivity and spatial resolution of image tubes to obtain a better match to the night sky radiation and a larger target range. On the surveillance front, for example, image intensifier tubes have been integrated into a helmet system for use in the TIGER [41], which is a second generation anti-tank helicopter built by the French and German ministries. Other applications include laser-induced fluorescence, and non-destructive testing.

Though the military applications of intensifiers seems to dominate, there has been an ever-growing integration of these devices into the scientific community for use as a research tool. For example, in the medical field an X-ray image intensifier is used to enhance weak X-ray images.

They can be a useful aide in such devices as the ophthalmoscope [42], which allows for an oriented examination of the fundus. These X-ray image intensifiers are used in many other research and application fields as well [43] including investigation of illegal electronic circuits and forged IC chips.

Recently, the ability to shutter the electrons emitted from the photocathode before they form an image has enabled researchers to image phenomena in the hundreds of picosecond time scale [44]. This adds a whole new dimension to the current state of the technology. Other trends include the integration of color image intensification utilizing spectral gate and color assignment [45]. This research suggests one will realize larger information quantity then with conventional image intensification techniques.

2.3 Image Modeling

We now discuss the arena of image modeling and why it is important in this research. There are a variety of reasons why image modeling can prove to be beneficial in almost any field. An obvious one is that a product designer, for example, can optimize and test a product prior to manufacturing it, thus realizing potential cost savings. In the remote sensing community, an example of such a product might be an orbiting satellite. Satellites are very expensive to manufacture and put in orbit. Therefore modeling its performance prior to launch can be extremely beneficial. There are others in the remote sensing community that are interested in image modeling as well. These include sensor designers, systems operators, algorithm developers, image analysts, and systems engineers, who are interested in using the synthetic imager generation (SIG) approach to study the image chain.

2.3.1 Governing Radiance Equation, Energy Paths and the Big Equation

When dealing with the generation of synthetic imagery, it is very useful to try and understand all the ways in which electromagnetic radiation can reach the sensor. This first entails understanding the underlying physics and interactions in the capture of a real image. In describing these energy paths we will follow the convention used by Schott [46]. Some of the most significant solar energy paths are illustrated in Figure 2-33. Here we have four types of solar photon energy paths. Type A photons are those that are directly reflected from the target and attenuated by the atmosphere and clouds while type G are solar photons reflected from the background onto the target. Type B photons are scattered by the atmosphere onto the target. Finally, type C photons are those that are scattered by the atmosphere back toward the detector. The later are sometimes referred to as *upwelled radiance*.

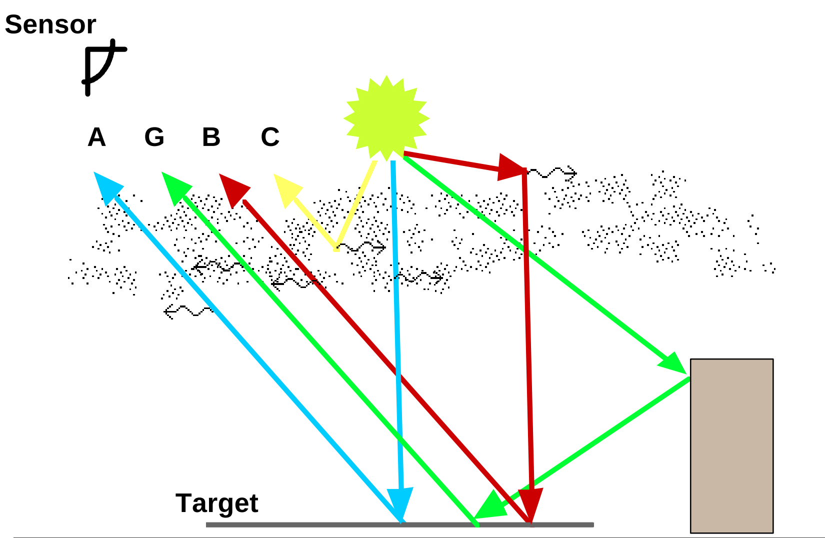

Figure 2-33 Solar energy paths.

We can describe the photons discussed so far in the following relationship and resulting equation where the definitions of each term can be found on page 37.

$$L_{solar(l)} = A_{photons} + B_{photons} + G_{photons} + C_{photons}$$

$$L_{sl} = E'_{sl} \cos s' \frac{r(l)}{p} t_1(l) t_2(l) + FE_{dl} \frac{r(l)}{p} t_2(l) + (1-F) L_{blavg} r(l) t_2(l) + L_{ul} \qquad (2.5)$$

We also have contributions from objects with temperatures above absolute zero. These are the self-emitted photons which become important around the 10μm region of the EM spectrum. The photons most often of interest are caused by radiation due to the temperature of the target itself, however, other contributions must also be taken into consideration. These are illustrated in Figure 2-34. Type D photons come from the target itself while type H emanate from background objects. Type E photons are reflected from the target via the atmosphere while type F photons come from the radiating atmosphere itself.

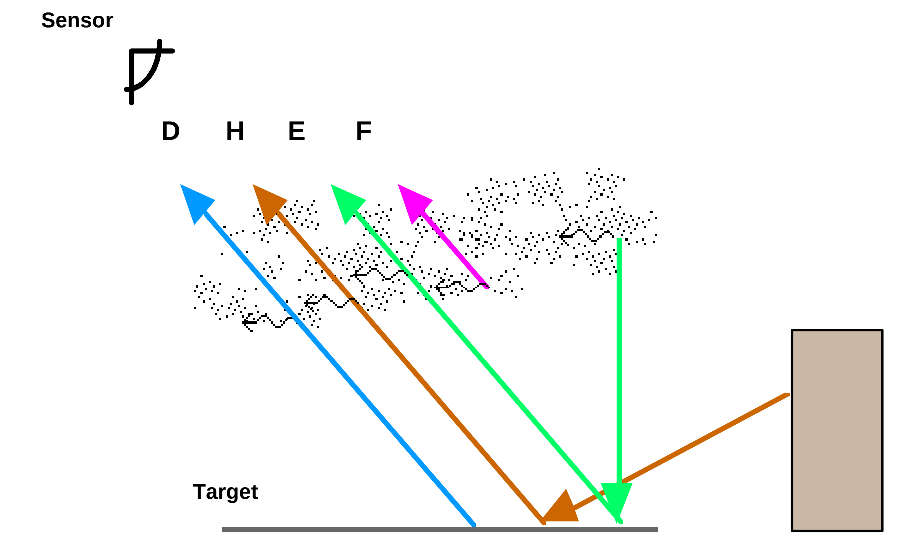

Figure 2-34 Self-emitted thermal energy paths.

We can also generate a relationship and equation to describe these contributions;

$$L_{self-emitted} = D_{photons} + E_{photons} + H_{photons} + F_{photons}$$

$$L_{self-emitted} = e(l)L_{Tl}\, t_2(l) + F \cdot \frac{r(l)}{p} E_{del}\, t_2(l) + (1-F)r \cdot L_{bel}\, t_2(l) + L_{uel} \quad (2.6)$$

Finally, we combine both sources of radiation reaching the sensor. This results in the, so-called, big equation, which is the overall governing equation for the radiance reaching the sensor.

$$L_l = \left\{ E'_{sl} \cos s' t_1(l) \frac{r(l)}{p} + e(l) L_{Tl} + F\left[E_{dsl} + E_{del}\right] \frac{r(l)}{p} + (1-F)\left[L_{bsl} + L_{bel}\right] r(l) \right\} t_2(l)$$

$$+ L_{usl} + L_{uel} \tag{2.7}$$

where:

E_s'	-Exoatmospheric irradiance
s'	-The angle from the target normal to the sun
t_1	-Transmission of the atmosphere from the sun to the target
t_2	-Transmission of the atmosphere from the target to the sensor
r	-Target reflectance (diffuse)
e	-Target emissivity
L_{Tl}	-Self-emitted radiance from target with temperature, T
F	-Shape factor (amount of sky hemisphere that the target can see)
E_{dsl}	-Solar downwelled irradiance
E_{del}	-Self-emitted downwelled irradiance from the sky
L_{bsl}	-Background radiance from scattering
L_{bel}	-Background radiance from self-emission
L_{usl}	-Upwelled radiance due to scattering of the atmosphere
L_{uel}	-Upwelled radiance due to self-emission of the atmosphere

The source types that are lacking in DIRSIG are those shown in Figure 2-35. Here we have light due to the stars and sky, moon, and man-made or secondary sources. The inclusion of these sources is one of the primary contributions of this research.

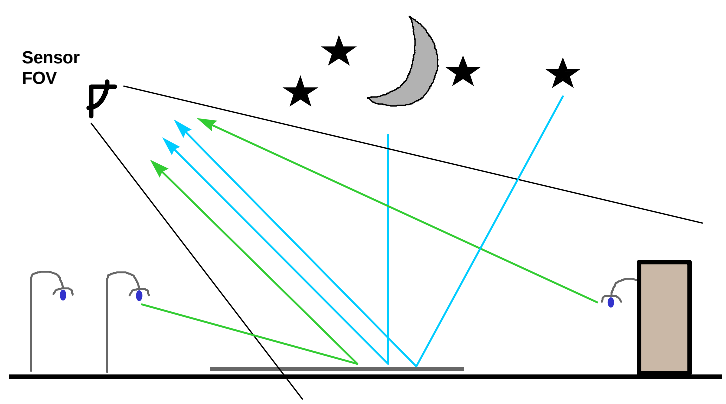

Figure 2-35 Man-made, sky, and lunar source contributions to the SIG model.

2.3.2 RIT's Synthetic Image Generation Model (DIRSIG)

Scene modeling and fusion algorithm evaluation will be performed with the aide of a Synthetic Image Generation (SIG) model. The Digital Imaging and Remote Sensing (DIRS) laboratory's Synthetic Image Generation (DIRSIG) model takes into account much of the radiometry associated with real world scenes. DIRSIG is a first principles based multi-spectral synthetic image generation model capable of producing an arbitrary number of bands in the 0.28 to 20 μm region. This model features a rigorous radiometric prediction of target signatures that utilizes surface BRDF to predict surface leaving radiance based on the incident radiance from the hemisphere above the target [47] and spectrally applied surface textures [48]. MODTRAN [54] is utilized to compute path dependent transmission, scattering, emission and downwelling radiances. Additional reflective region components include natural illumination sources such as the sun. The outcome of this research will incorporate other sources such as the moon and secondary man-made sources such as lights. In the thermal region, temperature predictions are produced by THERM, a passive slab thermal model that incorporates thermodynamic attributed, 48-hours of weather, pixel-by-pixel sun-shadow history and sky exposure factors [49].

DIRSIG can produce simulated imagery from both framing array sensors and scanning focal planes (line-scanners, push-broom scanners, etc.) at a user defined spatial resolution. The output image can be either integrated radiances from multispectral systems (discrete bands) and hyper-spectral imaging spectrometers (continuous adjacent bands), or spectral radiances at a user defined spectral resolution (possible for post-simulation application of a suite of sensor responses).

When generating an image, DIRSIG requires many input parameters all of which are handled by various submodels. These submodels interact with one another to produce a final radiance image. A brief explanation of these submodels, as found in reference [50], is given below.

Geometry Submodel

The scene geometry submodel is a multi-dimensional geometric data base of the scene to be simulated. This geometric data base structure provides the three-dimensional orientation of entities within the scene and the links to specific attributes, including material properties, optical characteristics, and physical parameters inherent to each entity. These quantities are used as partial inputs to drive the various submodels subsequently invoked during a simulation.

Ray-Tracer Submodel

The ray-tracer submodel is the module that integrates the individual submodels to synthesize an overall imaging system. The primary task of the ray-tracer submodel is to simulate an image produced by a given sensor viewing the 3-D geometric scene submodel. As the name implies, the submodel ray-traces all the ray-paths of photons through an optical system which is assumed to be of the pin-hole camera configuration. Computer graphics ray-tracing differs in that it extends these calculation beyond the modeled optical system to encompass the modeled scene being imaged. This process determines the itinerary and scene interaction of each photon reaching the sensor. This information enables the proper radiance incident on each picture element to be calculated based on energy losses due to material absorption, atmospheric attenuation, and energy redistribution due to reflection and self-emission. This accounting process on the resultant energy reaching the sensor should emulate the image produced by a real sensor, given the proper spectral characteristics and accurate submodels.

Thermal Submodel

The fundamental purpose of the thermal submodel is to calculate the time-dependent temperatures of objects within the scene as influenced by their environment. This is handled by THERM [49], which is a linear differential temperature generation model written by the DCS Corporation. Temperatures are calculated separately for each facet as a function of time based on first-principles models which determine the rate of heat transfer corresponding to a specific temperature difference between and object and its environment. Each facet is assumed to be thermally independent of the others and exhibit an isothermal surface behavior. THERM predicts an object's thermal signature based on solar parameters, meteorological conditions, and material properties.

Radiometry Submodel

Once the geometric characteristics for each facet comprising the scene have been described by the scene geometry and ray tracer submodels and the temperature for these facets determined by the thermal submodel, radiance leaving these facets and arriving at the front end of the sensor needs to be determined. In order to accomplish this, a modeled characterization of the intervening atmosphere needs to be established which includes the following: transmission between each element in the scene and both the sensor and source, the upwelling path radiance in the sensor target path, and the downwelled sky radiance from each point on a hemisphere above the scene. The exoatmospheric source radiance as well as the facet self-emitted radiance also need to be determined. MODTRAN was chosen for this purpose because of its wide acceptance and availability throughout the remote sensing community (see section 2.3.3). This model can be executed to produce exoatmospheric solar irradiance, transmission from space to the target, transmission from the target to the sensing platform, path radiance from atmospheric self-emission as well as scattered sunlight and target self-emission.

Sensor Submodel

The gross geometry surrounding the creation of a synthetic image involves positioning a sensor at a particular location in the world. In the DIRSIG model the sensor's ground coordinates and flying altitude are specified relative to an origin placed at the center of the simulated scene. Also specified is the sensor field-of-view in the x- and y-directions as well as the number of pixels desired from the system. This submodel converts the radiance values from the radiometry submodel to digital count values, employing the spectral response of the sensor in the calculations. The spectral response of the sensor describes the normalized responsivity of the sensor at different wavelengths.

The usefulness of these synthetic images is negated if the output does not closely imitate the real world [51]. As a result, the output from SIG must be evaluated and assessed according to criteria such as spectral and radiometric accuracy, geometric fidelity, robustness of application, and speed of image generation. The relative importance of these parameters, however, will vary depending on the use of the SIG imagery. In this research we will concern ourselves with preserving radiometric and geometric fidelity as well as replicating common artifacts from intensifying sensors such as shot noise, electronic noise, and MTF effects.

As mentioned in the introduction, most of the people that perform LLL sensor modeling do so in a real-time simulation environment [52-53]. This treatment tends to emphasize situational awareness with applications to mission rehearsal or planning. It seems that there has been no attempt to generate radiometrically-correct synthetic radiance field images with the inclusion of LLL effects. This research will introduce such a model environment.

2.3.3 MODTRAN

MODTRAN [54] is a moderate resolution atmospheric propagation modeling program. It can provide an abundance of information about the atmosphere when given the appropriate input parameters. For example, it can provide information such as transmission, solar and lunar effects including scattering, concentrations of various compounds, temperatures and pressures as a function of altitude, absorption information, atmospheric radiance, path scattered radiance, ground reflected radiance, and total radiance all as a function of wavelength. MODTRAN is currently supported by the Airforce Geophysics Laboratory (AFGL).

For this research, MODTRAN's output information will be used as input to the synthetic image generator (DIRSIG). In order to model a scene correctly, DIRSIG needs solar and/or lunar atmospheric information. Previously, MODTRAN was only used to generate atmospheric information with the sun as the extraterrestrial source. For this research, however, the principle investigator will exploit MODTRAN's capabilities regarding lunar sources. To date, MODTRAN provides lunar atmospheric information given azimuth angle, zenith angle, and phase angle of the moon. The position and phase angle of the moon will be generated by code extracted from an ephemeris program which is supported by the National Optical Astronomy Observatories (NOAO). The latest version of MODTRAN, however, does not have starlight capability. This information is researched by the principle investigator. Relevant values will be incorporated into DIRSIG and taken into account for conditions when the moon is below the horizon.

Chapter 3

3. Experimental Approach

The main objective of this research is to characterize the image intensifier and validate an improved (radiometrically correct) sensor model exploiting potential advantages and pitfalls. The first step in the above statement, characterization of the intensifier, is undoubtedly the most important. This is because a majority of the sensor parameters analyzed will serve as a basis for our synthetic sensor model.

3.1 Image Acquisition

Real imagery should be obtained before any synthetic scenes are to be constructed, because it is somewhat easier to generate a synthetic scene based on a real image than it is to compose a real-life scene based on a previously built synthetic scene. It should be noted, however, that there are a few pre-fabricated synthetic scenes (of RIT parking lots) already in existence. Conceivably, real imagery could be acquired based on these scenes. This approach would be dependent upon whether or not the truth equivalent of the synthetic scenes met the criteria for image acquisition. Instead, the principle investigator collected ground truth over the course of two evenings. The content of the imagery collected represented the various dynamics of the intensifier. In order to do this, multiple scenes were imaged, each varying in illumination condition and content. All scenes had calibrated gray panels and resolution targets in them. Close ups of the panels and resolution targets were imaged for later analysis.

3.1.1 Scenes Imaged

Scene One. This scene was imaged under starlight conditions only. A key factor in this image was the lack of secondary sources and reasonable visibility. The goal was to capture imagery on a cloud-free evening with a new moon present in the absence of light sources such as street, automobile, building, or city lights. **Scene Two**. This was the same as scene one (cloud-free with new moon) except for the presence of secondary sources. Here the secondary sources, as mentioned above, were an off-axis light source and a hand-made street lamp. These secondary sources aided in the analysis of the IICCD blooming phenomenon. **Scene Three**. The ideal scene here was to image the described objects above on a clear night with the moon at some illumination percentage excluding secondary sources. **Scene Four**. This was the same as scene three except for the inclusion of secondary sources.

The summary of the proposed scenes is stated in Table 3-1. Common to all these cases is the assumption that the night sky was relatively free from cloud cover. However, this was not the case at the time of acquisition. In the event of this scenario, data was collected with the intent of including these effects, such as cloud cover and varying phase, in the simulated imagery. The location for the collection was at the North Range Laboratory which is located on the roof of the Center for Imaging Science building on the RIT campus.

Table 3-1 Summary of imaged low-light acquisition conditions.

	New Moon (starlight)	Moon present	Secondary Sources
Scene 1	x		
Scene 2	x		x
Scene 3		x	
Scene 4		x	x

3.1.2 Use of the Ephemeris Utility

Not mentioned in the above section is the fact that the moon is not always present in the night sky. Not only does one have to consider weather conditions at the time of acquisition, but more importantly, whether or not the moon is above the horizon. This became a critical issue because of time constraints on acquisition. To circumvent this, a program called “ephem” (provided by the National Optical Astronomy Observatories (NOAO) was used to predict the moon’s position in the sky for a given time and day of year. Ephem is an interactive astronomical program that displays ephemerides for all the planets. It is based on standards set forth by NOAO. Information displayed about each object includes:

- Right ascension and declination precessed to any epoch
- Local azimuth and altitude
- Heliocentric coordinates
- Distance from sun and earth
- Solar elongation
- Angular size
- Visual magnitude
- Illumination percentage
- Local rise
- Transit and set times
- Length of time up
- Constellation
- Angular separations between all combinations of objects

Observing circumstances information include:

- Universal coordinated time (UTC) and local date and time
- Local sidereal time
- Times of astronomical twilight
- Length of day and night
- Local temperature, and pressure
- Height above sea level for the refraction model

The use of this program was invaluable in predicting which days were better candidates than others for image capture. Of course, it does not predict weather conditions so this will always be a factor to consider at the time of acquisition. Since ephem can predict ephemerides for all the planets with the utmost accuracy, it was also integrated into DIRSIG. Currently sun location, for example, comes form LOWTRAN and THERM. With the incorporation of ephem, DIRSIG can obtain ephemerides information from a single location with high precision.

3.2 Image Intensified CCD Characterization

Characterization of the IICCD is important for synthetic modeling purposes. Some of the parameters are used to create a "new" low-light-level sensor in the synthetic image generation (SIG) environment. Some work has already been published on modeling and performance characteristics of various imaging tubes [55-61]. Published work ranges from resolution testing on gated intensifiers [62] to improved photocathode designs [63-64]. The intensified sensor that was modeled here is of the IICCD flavor; specifically, it is a Generation III intensifier with a GaAs photocathode. Key effects to be considered in the evaluation of an image intensified CCD can include, but are not limited to, light quantum parameters such as luminance gain, automatic brightness control specification, photocathode sensitivity (luminous sensitivity and radiant sensitivities), signal-to-noise ratio (S/N), and modulation transfer function (MTF). Geometric parameters include resolution (center and peripheral, high and low light level, high and low contrast), magnification, (non) linearities, and blooming effects. In this research we concerned ourselves with parameters such as gain, signal to noise ratio, shot noise, pre-amplifier noise, blooming, and MTF.

3.3 Image Modeling in DIRSIG

Once adequate characterization of the IICCD was complete, synthetic image modeling was performed. The synthetic modeling for this research had two steps; 1) generate a valid low-light-level sensor model in DIRSIG, including lunar and secondary sources, and 2) create and capture synthetic and truth imagery for comparison purposes.

3.3.1 IICCD Sensor Modeling

Currently DIRSIG does not have LLL sensor capability. As of this writing, it is only capable of modeling thermal and daylight-visible imagery. Validation of DIRSIG's current modeling capability has been performed by White, Kraska, and Kuo [65-67]. In the scope of this research the principle investigator generated the appropriate parameters that adequately characterized the low-light-level sensor. The sensor type in this case was an image intensified CCD (IICCD), Generation III device with a GaAs photocathode. The testing of the new LLL sensor model involved synthetic scenes generated from this research. These scenes contained all the attributes to fully validate the sensor including secondary sources and artifacts that lead to poor resolution and SNR. An overview of how this was put together can be seen in Figure 3-1.

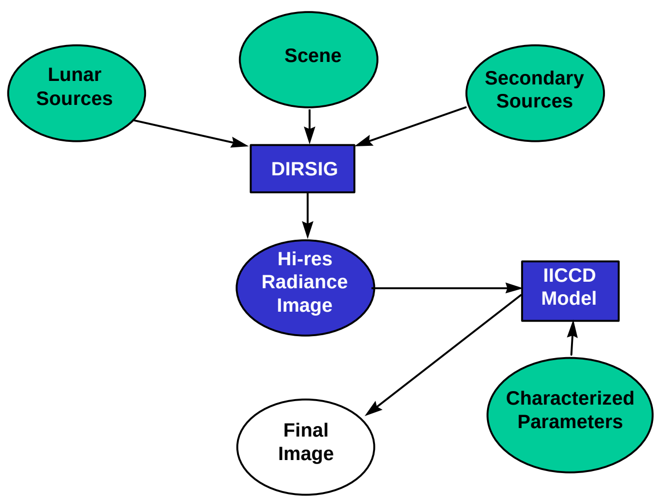

Figure 3-1 Steps to implement low-light-level sensor model.

3.3.2 LLL Sensor Analysis

Recently, DIRSIG has undergone VIS and IR validations by White and Kraska [65-66]. Prior to that, IR validation work was done by Rankin [2]. However, since DIRSIG did not incorporate a LLL sensor, no low-light-level sensor analysis has been performed. The process of analyzing DIRSIG's LLL sensor consists of three main steps. These steps include procuring images of the region of interest, creating a synthetic image of this same region using DIRSIG, and, finally, evaluating the synthetic imagery using the truth imagery.

It should also be noted that this LLL validation is not an end-to-end DIRSIG validation like the ones performed by White, Kraska, or Rankin. For those researchers, the analysis focused on DIRSIG's ability to accurately predict the radiometry for both the visible and thermal bands, as compared to truth data. Evaluation metrics such as rank order correlation (ROC), root mean square error (RMS), and geometric fidelity were employed. Furthermore, a sensitivity analysis was often employed to evaluate temperature, for example. In this research we concern ourselves with modeling the LLL sensor and comparing the results to experimental data. We also implement a laboratory calibration which relates digital counts (DC) to radiance, as a function of sensor gain. Lastly the SIG analysis involves comparing DIRSIG's output to truth data which only involves an RMS error. Furthermore, we numerically compare DIRSIG's integrated output to published literature. This approach disregards the spectral nature of the data.

Chapter 4

4. Ground Truth Collection

4.1 Data Collection Scenario

Ground truth data was collected atop the Center for Imaging Science (CIS) building. Data was collected on two separate evenings, August 19th and September 1st. The days and times of acquisition were determined with the aid of the ephemeris utility. The first collection was taken at night with the moon below the horizon. The second was taken when the moon was approximately 69 percent illuminated, above the horizon. Output from the ephemeris routine can be seen in Figure 4-1 and Figure 4-2. From Figure 4-1, we can see the angular path of the sun and moon plotted as a function of time. Also plotted is the phase fraction of the moon, or percent illuminated. We can see that the optimal time for acquisition on August 19th was between the hours of 9 pm and 4 am. This is when the moon was below the horizon, *i.e.*, the new moon condition. As for September 1st (see Figure 4-2) data was collected between the hours of 9 pm and 2 am. The details of these plots can be seen in Table 4-1 and Table 4-2 which also include moon azimuth information. For the case when the moon was above the horizon we notice that it had a zenith angle between 27 and 10 degrees and a phase fraction of 69 percent, on average.

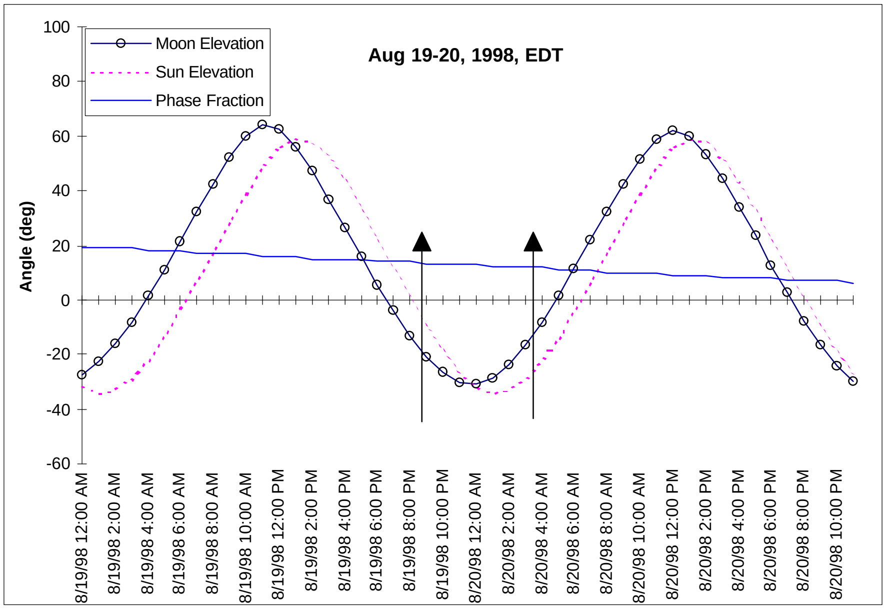

Figure 4-1 Output of ephemeris routine showing optimal data collection times for August 19th – 20th.

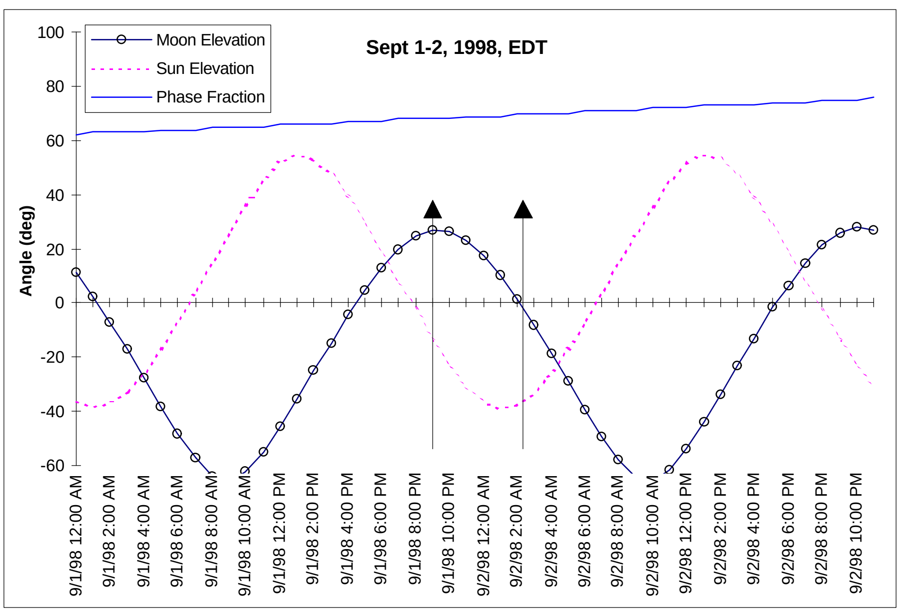

Figure 4-2 Output of ephemeris routine showing optimal data collection times for September 1^{st} – 2^{nd}.

Table 4-1 Output of ephemeris routine showing optimal data collection times for August 19th – 20th.

EDT DATE (UTC - 4)	UTC HOUR	Moon Azimuth	Moon Elevation	Phase Fraction	Sun Zenith
8/19/98 6:00 PM	22	287.9	5.5	14	22.1
8/19/98 7:00 PM	23	297.7	-3.8	14	11.2
8/19/98 8:00 PM	0	308.3	-13.3	14	0.9
8/19/98 9:00 PM	**1**	**320.4**	**-20.9**	**13**	**-9.7**
8/19/98 10:00 PM	**2**	**334**	**-26.7**	**13**	**-18.9**
8/19/98 11:00 PM	**3**	**349.2**	**-30.1**	**13**	**-26.4**
8/20/98 12:00 AM	**4**	**5.1**	**-30.7**	**13**	**-31.8**
8/20/98 1:00 AM	**5**	**20.7**	**-28.4**	**12**	**-34.2**
8/20/98 2:00 AM	**6**	**35.1**	**-23.6**	**12**	**-33.3**
8/20/98 3:00 AM	**7**	**47.8**	**-16.7**	**12**	**-29.3**
8/20/98 4:00 AM	**8**	**59.1**	**-8.3**	**12**	**-22.7**
8/20/98 5:00 AM	9	69.3	1.5	11	-14.2
8/20/98 6:00 AM	10	79	11.3	11	-3.9

Table 4-2 Output of ephemeris routine showing optimal data collection times for September 1st – 2nd.

EDT DATE (UTC - 4)	UTC HOUR	Moon Azimuth	Moon Elevation	Phase Fraction	Sun Zenith
9/1/98 6:00 PM	22	133.8	13.1	67	18.4
9/1/98 7:00 PM	23	146.2	19.9	68	7.5
9/1/98 8:00 PM	0	160.2	24.7	68	-2.1
9/1/98 9:00 PM	**1**	**175.3**	**27**	**68**	**-13.7**
9/1/98 10:00 PM	**2**	**190.7**	**26.5**	**68**	**-23.1**
9/1/98 11:00 PM	**3**	**205.5**	**23.2**	**69**	**-30.9**
9/2/98 12:00 AM	**4**	**218.9**	**17.5**	**69**	**-36.4**
9/2/98 1:00 AM	**5**	**230.8**	**10.1**	**69**	**-38.8**
9/2/98 2:00 AM	**6**	**241.4**	**1.6**	**70**	**-37.6**
9/2/98 3:00 AM	7	251.2	-8.3	70	-33.1
9/2/98 4:00 AM	8	260.5	-18.5	70	-26

The location on top of the Center was chosen for multiple reasons. First was the fact that the Center housed most of the equipment and it was therefor much easier to move around. Secondly, was because of the optimum view angle from atop the Center. From this vantage point, objects and targets were readily visible. Another reason for choosing this location, and perhaps one of the most important, was the fact that the principle investigator was able to have all secondary sources within a radius of approximately 2,000 feet turned off. This was important for controlled illumination purposes, and was accomplished with the help of RIT's physical plant and Campus Safety. Another reason for the site was because it contains a variety of materials including asphalt, concrete, and grass. Figure 4-3 shows a daytime view of the collection site from atop the west face of the CIS building.

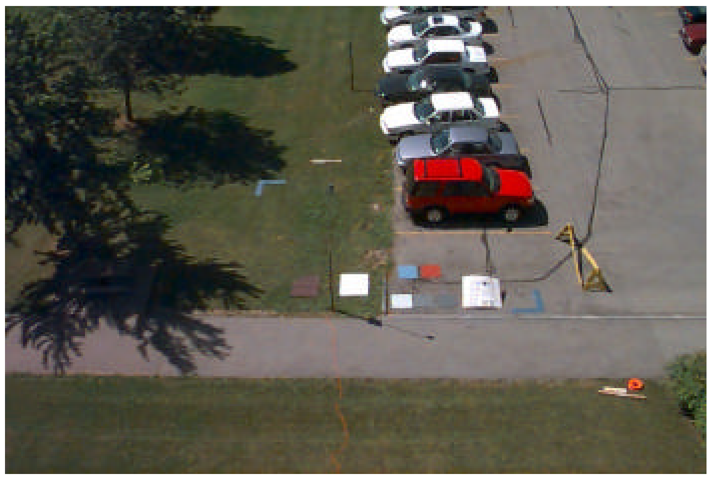

Figure 4-3 View of the collection site from atop of the CIS building.

4.2 Creation of the Truth Scene

Once the site location was selected, a scene had to be created containing relevant targets, secondary sources and objects. The following key features were taken into consideration during the collection. These items are summarized in Table 4-3.

Table 4-3 Summary of targets and objects in scene.

Targets	Secondary Sources and Objects
Black target	40 W tungsten light bulb (in scene)
White target	150 W tungsten light bulb (out of scene)
Blue target	300 W tungsten / halogen light bulb (out of scene)
Red target	
Light gray target	Truck, Sport Utility
Medium gray target	Human, fully clothed (approximately 5’9" tall)
Dark gray target	
Resolution target	
Aluminum angle targets	

Thermal data was also taken along with the low-light-level imagery. Collection of this data could be used in implementing VIS/IR image fusion techniques. When fusing or registering images, it is useful to have some key ground control points (GCP) that are readily visible in both data sets. Since we are dealing with low light and thermal imagery, it would be extremely beneficial to have a target that appeared distinctly in both images. The target used for this purpose was aluminum (see Figure 4-4). Aluminum is useful here because it has a high reflectivity, or low emissivity, in the visible and thermal bands. The aluminum targets were set up to encompass the entire field of view (FOV) of the cameras. They were place at opposite corners of the field of view and set up to form right angles. This was to resemble fiducial marks to aid in registration. From the overhead view of Figure 4-3 one can make out the overall camera’s field of view by noticing the locations of the aluminum fiducial marks.

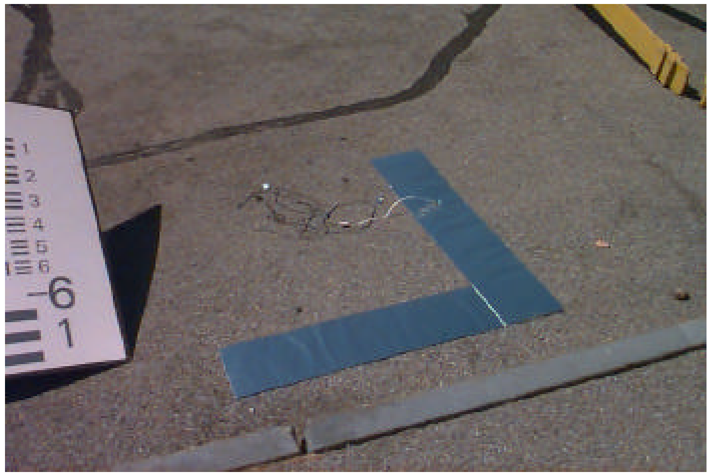

Figure 4-4 Aluminum fiducial mark set up at corners of field of view.

Secondary light sources were also used during the data collection. Two types of sources were used with varying outputs. There were two tungsten bulbs, 40w and 150w, and one 300w tungsten halogen bulb. The 40w tungsten bulb was placed *in the scene* on a pole to resemble a street lamp (see Figure 4-5). Here, the 40w bulb was placed in a steel box which had an aperture below it to control the amount of illumination on the ground. A close-up of this set up can be seen in Figure 4-6.

Figure 4-5 Image of man-made street lamp.

The remaining sources were placed *outside* of the scene. Both the 150w tungsten and 300w tungsten halogen bulbs were placed on a pole about 30 feet from the edge of the camera's field of view, as can be seen in Figure 4-7. Here we see the geometrical relationship between the street lamp and external sources. A close-up of the external sources mounted on the pole can be see in Figure 4-8.

Figure 4-6 Close up of street lamp showing aperture below the bulb.

Figure 4-7 Image of sources placed outside the cameras field of view.

Figure 4-8 Close-up of external sources placed outside cameras field of view.

The last two objects of interest to be considered in the collection were a vehicle and a human. A close-up of the truck can be see in Figure 4-9.

Figure 4-9 Close up of vehicle used in the data collection.

Temperature information was acquired by placing thermisters on various objects throughout the scene. This data was used for in-scene calibration of the imagery. Thermister data was collected just after a thermal image acquisition. This was performed 2-3 times for each data collection. Some of the thermisters can be seen placed on objects in previous Figures.

4.3 Equipment Used

This section describes the equipment used during the collection and any modifications performed on such equipment. Figure 4-10 shows some of the monitoring equipment used during the collection. From left to right, an ohmmeter used to record the gain of the LLL camera, two monitors used to display the outputs from both the IR and LLL cameras, a laptop computer used to digitize and store the signal, and an extra monitor in lieu of the LCD display during poor lighting conditions.

Figure 4-10 Image of digitizing and monitoring equipment**.**

A forward looking infrared (FLIR) camera and a image intensified CCD (IICCD) camera were used during the data collection. These can be seen in Figure 4-11, where the LLL camera is on the left and the IR camera is on the right. The LLL camera used was the AG-5745EF-3 automatic gated intensified CCD manufactured by PULNiX America Inc., located in Sunnyvale, CA. A standard Sony C-mount zoom lens was used in place of the fixed focal (75mm) lens that was shipped with the camera (see Figure 4-12). The fact that the Sony lens was of variable focal length, (16 - 64 mm), helped immensely when trying to match the two camera's FOVs. A variable focal length lens on the LLL camera was desired since the IR camera had a fixed focal length and therefor fixed FOV. The cameras FOVs were best match when using a focal length of around 36 mm. The ICCDs f-number was set to f/5.6 (wide open).

General Description of the ICCD

The gate speed on the camera is controlled from 60 Hz (field mode) or 30 Hz (frame mode) to 100 ns maximum speed continuously. The dynamic range is typically 10^{-4} lux to 50,000 lux at f=1.4 with a smooth and fast response. The internal CCD camera automatic gain control function is also incorporated for optimum picture quality. The overall TV resolution is 400 lines with excellent contrast due to the refined signal processing of the TM-745E. The AG-series have variable edge enhancement for higher definition (factory setting is at min. level). A provision for manual and external gating control is provided by switches and the gate pulse output can be monitored. The AG-5745F is well suited for military, aerospace, RPV, under-water observation, mobile surveillance, and scientific applications. For additional specifications see Appendix A.

Figure 4-11 Images showing LLL (left) and IR (right) cameras.

Figure 4-12 Close up view of IICCD with C-mount zoom lens.

4.3.1 Modifications to the IICCD Camera

The factory settings on the camera proved to be unacceptable for this research. The major problem was with the automatic gain control (AGC) of the intensifier tube. The AGC was always on, as set by the manufacture. However, for this research, it was desired to be able to manually control the gain. With AGC on, the in-scene dynamic ranges is always being rescaled. In this way, the circuitry protects the camera from "over amplification" which can lead to damage of the intensifier tube. This, in turn, creates a nonlinear camera which is very difficult to characterize. Therefore, it was crucial that the ACG be overridden. This proved to be a daunting task that required numerous conversations with the manufacture. However, the end result was some careful modifications to the circuitry, some of which can be seen externally in Figure 4-13.

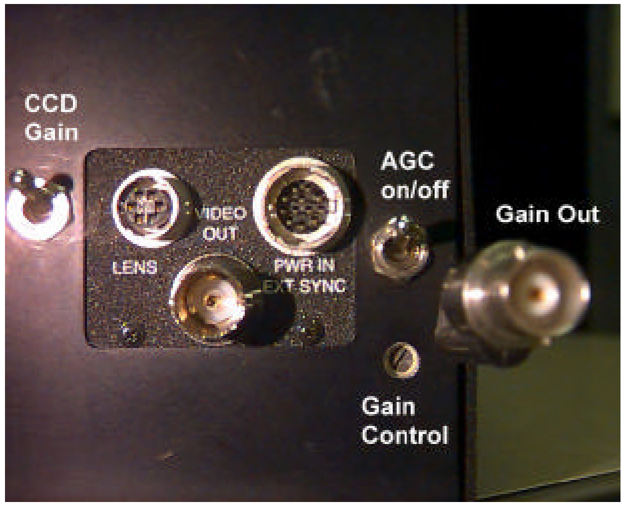

Figure 4-13 Modifications to the ICCD, as seen from the back of the camera.

At the back of the camera are switches to control the gain of the CCD and intensifier tube. When the camera AGC is off, the potentiometer below the switch controls the gain from 0 V to 8 V max. With the camera AGC on, the gain can reach V_{max} = 9 V, which is typically a gain of 15,000. The difference in maximum gain is due to the fact that the 10 kΩ trimmer is only tied to 8 V (which was found on the board) not 9 V. This gain voltage can be monitored via a BNC connector found at the back of the camera. For complete analysis and details of the ICCD camera modifications see Appendix B

4.4 Data Collected

As for the collection itself, images containing various combinations of objects and secondary sources were taken. All the data contained targets while the truck, human, and secondary sources were varied from set to set. Within each data set, the gain of the camera was also varied. Each image was sampled twice so that temporal noise averaging could be performed (if required) and analyzed. Table 4-4 shows a summary of all the combinations used in the collection, while Appendix C contains the actual data from of collection itself, including gain settings used.

Table 4-4 Summary of image scenarios created during the data collection.

Condition	Thermal w/ Human	Thermal w/o Human	LLL w/ Human	LLL w/o Human
No light sources	x	x	x	x
Truck Dome Light On	x	x	x	x
300w Tungsten Halogen On	x	x	x	x
150w Tungsten On	x	x	x	x
40w Street Lamp On	x	x	x	x
Window Open	x	x	x	x
Window Closed	x	x	x	x
Truck Headlights On	x	x	x	x
No Truck/ No Lights	x	x	x	x
No Truck/ St. Lamp On	x	x	x	x
No Truck/ 300w Tung. Hal.	x	x	x	x
No Truck/ 150w Tungsten	x	x	x	x

Reflectivity information from various materials throughout the scene was also measured after the data collection. This data was then used to determine the emissivity of objects. The emissivity data is necessary for the ray tracer. The details of this are covered in section 5.2 entitled DIRSIG Input Files.

4.5 Noise Averaging

This short section is devoted to looking at improvements in image quality. One way to reduce the noise in an image is to simply replace every pixel with the *average* in an N pixel neighborhood around that pixel. The resulting image should have the noise reduced by $(1/N)^{1/2}$. However this process acts like a low-pass filter resulting in a blurred output image. In this light we could also achieve noise reduction by averaging multiple frames of the same image. Here again the noise should be reduced by $(1/N)^{1/2}$, where N is the number of samples averaged. This is possible since there is no motion between frames thus resulting in very accurate registration and lack of spatial blurring. Figure 4-14 shows two images of a noisy low-light-level scene taken moments apart. It is assumed that the noise in each image is random.

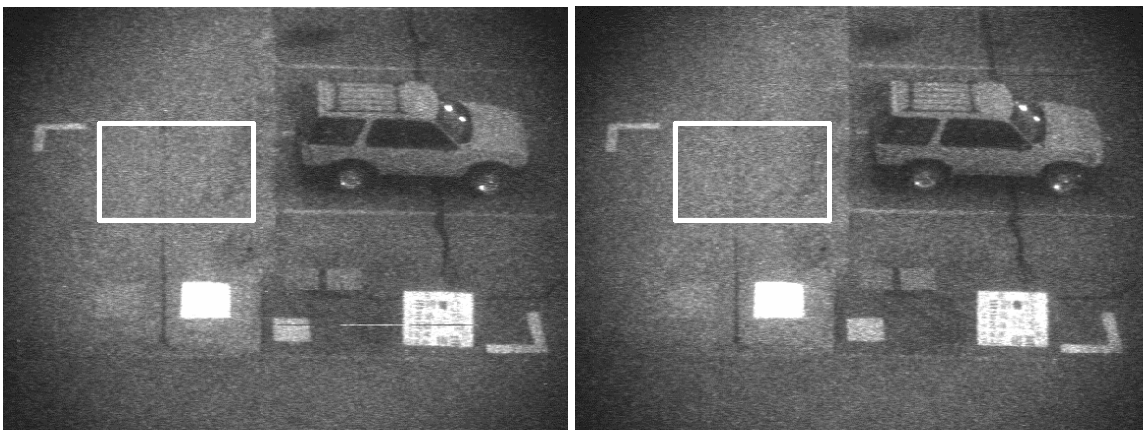

Figure 4-14 Two frames of the same scene taken ten seconds apart.

By just averaging 2 frames we should see a reduction by a factor of 0.707, as see in Figure 4-15. If we look at the statistics in a 150 x 100 pixel window, as shown in Figure 4-14, we see that image a) has $\mu = 129.84$ and $\sigma = 15.71$, while image b) has $\mu = 129.64$ and $\sigma = 15.45$. On average this is $\mu = 129.74$ and $\sigma = 15.58$. If we use the ratio of μ/σ as a kind of signal-to-noise metric we see that, when computed, this value is 8.3.

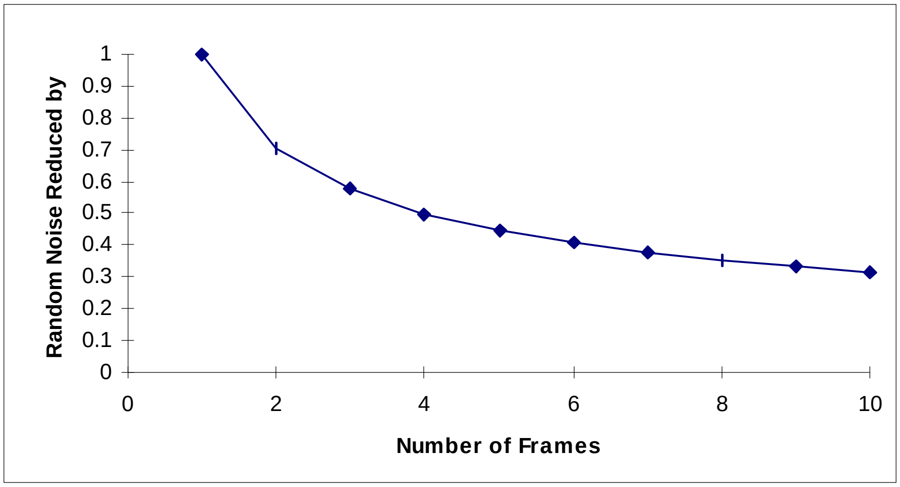

Figure 4-15 Noise reduction by temporal averaging of multiple frames.

Now if we simply add the two frames, with a scale of 2 (divide by) and offset of 0, we get the image in Figure 4-16, which has reduced noise. If we now look at the statistics in the same region as before we have, μ = 129.79 and σ = 12.20. The ratio here is 10.638, which says we have maintained our mean while reducing the standard deviation by 22%. In terms of the expected reduction we should have seen the standard deviation change to $(\sigma_{avg})(0.707) = 11.01$. However, we measured 12.20. Which is to say that we didn't reduce the noise quite as much as expected. This 11% error is pretty good considering that by averaging *only* 2 frames we reduced our noise significantly. Of course this treatment assumed that the regions selected were similar and that the noise was completely random which, in most cases, is not true for real systems.

Figure 4-16 Two frames added together to reduce noise.

Chapter 5

5. DIRSIG Environment

5.1 SIG Scene Creation

After the data collection was completed, a wire-frame model of the site needed to be constructed. Available to the principle investigator were detailed blue-prints of surrounding buildings, parking lots, and other areas of interest. These blue-prints were obtained from RITs physical plant. Elevation information was obtained by measuring objects by hand with a tape measure. Dimensions and locations of other objects such as secondary sources, vehicles, targets, and humans, were also measured by hand and recorded the day of the collection. The scene was recreated using AutoCAD (Windows release 13). A summary of the objects taken into account is shown in Table 5-1. Figure 5-1 shows sample drawings of some of these objects.

It should be noted that the location used for this data collection was also used in a previous validation of DIRSIG [68]. The vantage point at which the scene was viewed, atop the CIS building, was also very similar (i.e., similar FOVs). During that validation, the site was reconstructed in CAD, along with a vehicle, pool, and other miscellaneous objects. However, the recreation was not as accurate as the one presented in this research. It was therefore the principle investigator’s decision to recreate not only the site of the collection at higher detail, but the surrounding area as well. This may prove to be useful to other researchers who may wish to use the roof top of the CIS building for data collections and validations of DIRSIG in the future.

Table 5-1 Objects to be recreated in AutoCAD.

Targets	Secondary Sources and Objects
Black target	40 W tungsten light bulb (in scene)
White target	150 W tungsten light bulb (out of scene)
Blue target	300 W tungsten / halogen light bulb (out of scene)
Red target	
Light gray target	Truck, Sport Utility
Medium gray target	Human, fully clothed (approximately 5’9" tall)
Dark gray target	Grass, Dirt, Concrete Curbs, Parking Lot
Resolution target	Center for Imaging Science Building
Aluminum angle targets	

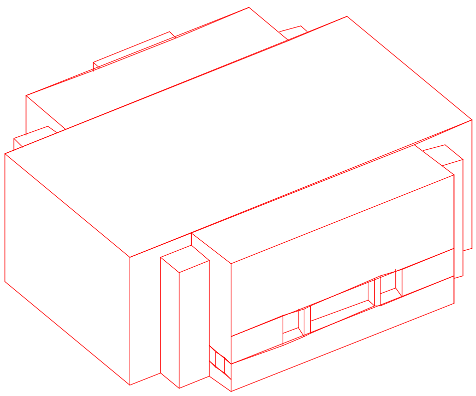

Center for Imaging Science building

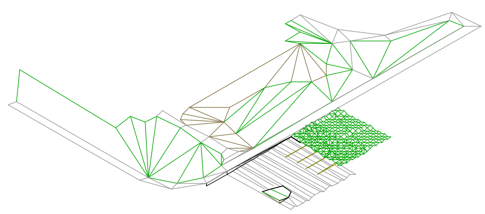

Dirt, Grass, Asphalt, etc.

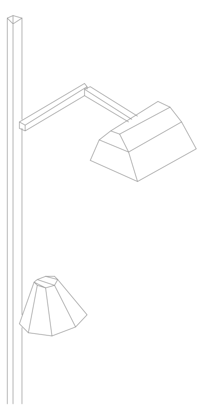

300w tungsten-halogen and 150w tungsten sources

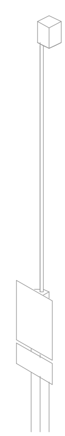

40w tungsten street lamp and sign

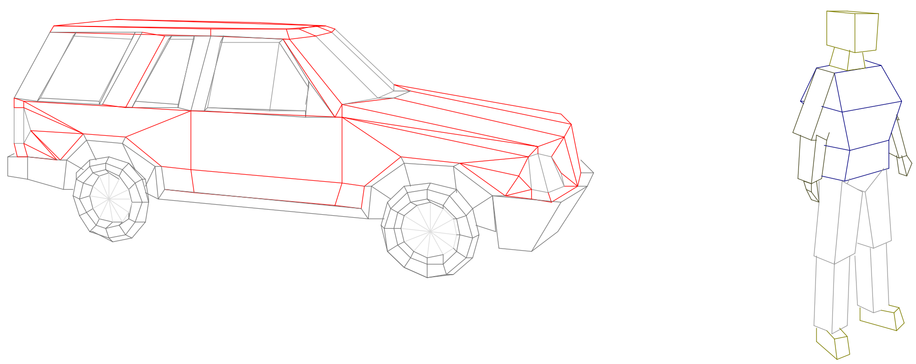

1995 Ford Explorer 5’ 9” Human

Figure 5-1 Objects created using AutoCAD.

Once the individual objects were constructed, the region could be fabricated by assembling each object or part into a new file to form the overall scene. This can be seen in Figure 5-2. This particular scene is made up of 1880 facets. Most of these facets come from the make up of the truck (Ford Explorer, 486 facets) and undulating grass (519 facets). The specific area of interest is actually a subset of this larger scene.

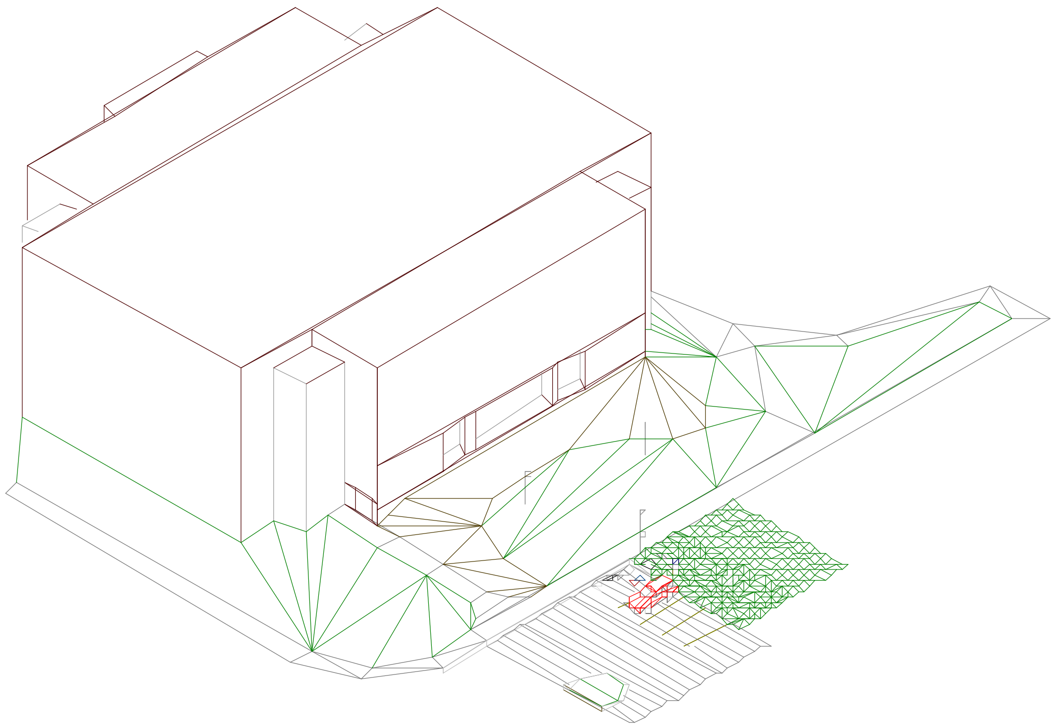

Figure 5-2 Entire scene drawn in AutoCAD.

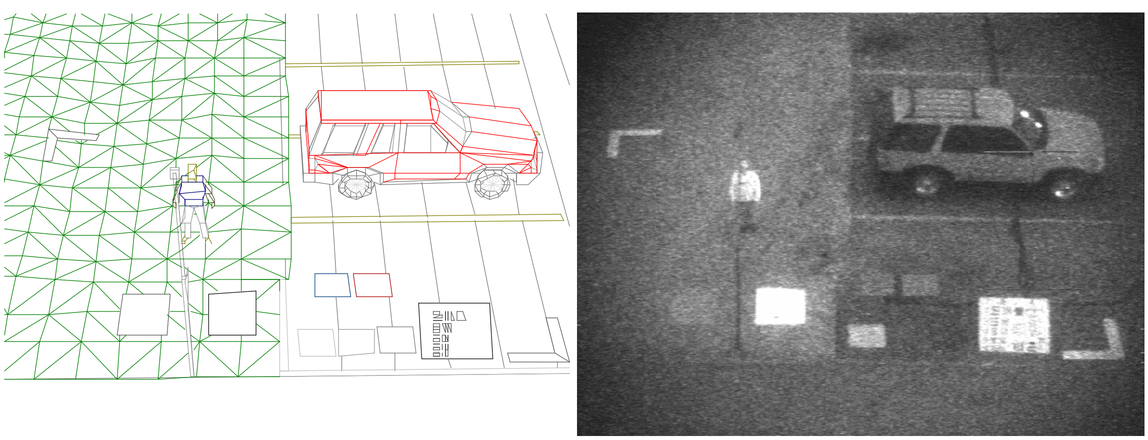

AutoCAD file (left) with same view point as image from IICCD camera.

5.2 DIRSIG Input Files

So far we have collected ground truth data and recreated the scene using AutoCAD. The next logical step is to render the scene using DIRSIG. However, before this can be accomplished we must first *set up* a series of *input files* for the ray tracer to read. For example, the CAD file must be formatted to include facet normals and material attributes. Furthermore, the contents of it needs to be assembled in hierarchical fashion for fast and effective ray tracing of the scene. Some of the steps in the overall SIG process can be outlined as follows:

- Construction of individual parts in AutoCAD
- Assembly of individual parts into objects in AutoCAD
- Assembly of objects into an entire scene in Auto CAD
- Computing the facet normal vectors
- Exporting the scene from AutoCAD into the DIRSIG Geometric Database
- Determining the scene look angle
- Building the radiance data for the scene
- Defining the sensor characteristics
- Running the DIRSIG model on the scene
- Extracting images from the output files
- Making the output images displayable and viewing them

There are several files and databases that are needed to enable DIRSIG to generate accurate results. A list of these can be seen in Table 5-2. Some of these files are generated as a result of running programs, such as *Control7*, *find_min_max_view_angle*, or *build_radiance*. Figure 5-3 illustrates how these programs and input DIRSIG files interact with one another. Not all the files listed in Table 5-2 will be used in this research. In addition to the required files two of the optional files will be used; the weather file and the secondary source file. For a complete description of these files and their contents see Appendix D.

Since we did not collect data via an airborne system, we can omit the platform motion and specification files (*.prf, *.psf). Also, the meteorological conditions on both evenings were such that the atmosphere was fairly clear, so we can also omit radiosonde data (*.rsd). Finally, we can neglect the extinction coefficient (*.ext) and texture files (*.tex) because we do not have any transmissive objects in the scene nor are we going to be adding texture. This leaves us with the weather (*.wth) and secondary sources (*.src) files.

Table 5-2 DIRSIG Input files**.**

File extension	Description of Required Files
*.gdb	Geometric Database containing each facet's location, normal, and material
*.ems	Material emissivities that are a function of the wavelength and look angle
*.mat	Material file containing the physical properties of each material
*.adv	AutoCAD dview file containing the scene and imaging parameter coordinates in AutoCAD units.
*.snd	Scene node file containing the bandpass spectral ranges and the data that relates the scene position to the earth and sun
*.cdk	MODTRAN/LOWTRAN cardeck
*.rad	Radiance file containing the bandpass atmospheric parameters used in DIRSIG
*.sen	Sensor responsivity file containing the spectral response of the sensor
	Description of Optional Files
*.prf	Platform motion profile containing the flight profile of the plane
*.psf	platform specification file containing the imaging system parameters
*.rsd	Radiosonde data that is used by MODTRAN to predict the atmospheric profile
*.wth	Weather file containing 48 hours of weather prior to the imaging time
*.ext	Extinction coefficient file containing coefficients for transmissive materials
*.tex	Texture file contains a picture of the patterned texture that you wish to impose in a scene
*.src	Secondary source file containing insertion point and location of intensity file

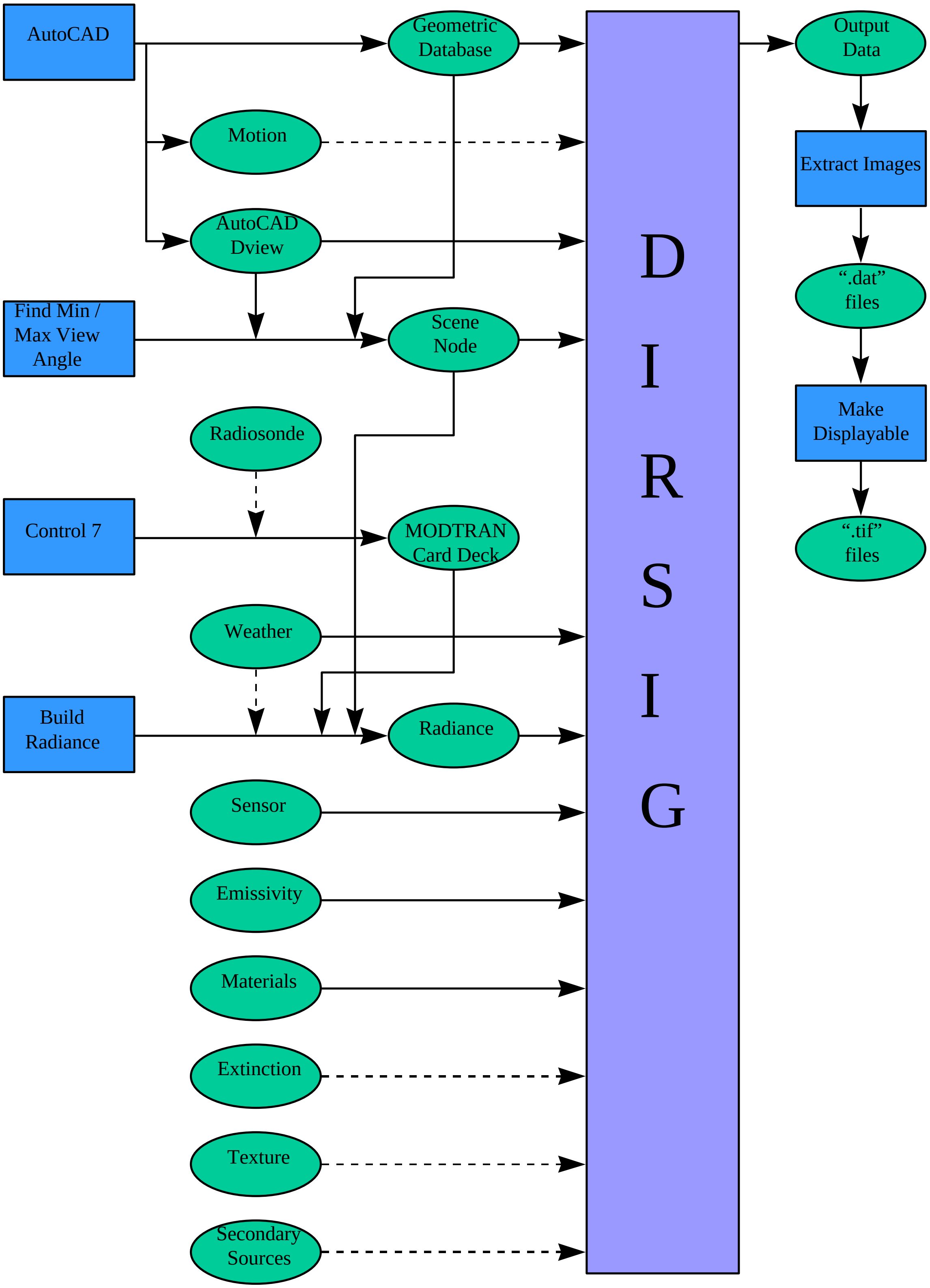

Figure 5-3 Flow chart showing required and optional files needed for DIRSIG input.

The following sub-sections describe the details of creating the input files that were used in this research.

- AutoCAD and the GDB
- Materials and Emissivities
- Dview and Scene Node Files
- Card Decks and Radiance Files
- Weather Files
- Sensor Responsivity Files
- Secondary Source Files
- DIRSIG Batch Files

5.2.1 AutoCAD and the GDB

One of the first steps in the ray tracing process is to prepare the CAD drawing for DIRSIG. In order for DIRSIG to use the drawings created in AutoCAD, some additional preparation of each drawing must be performed. Briefly, these steps include breaking solid objects up into facets, adding normals to these facets, and adding material attributes to these facets.

The scene itself was created in a separate file from that of the truck and human. The latter objects were more complex so they were first drawn in their own respective files then inserted into the larger scene and finally exploded (separated into individual facets). The scene was segmented into layers. This made it much easier to add normals and materials to objects. Table 14-1 in Appendix D lists the layers and materials used in generating the scene Each layer was then saved as a separate drawing file so that normals and materials properties could be added to the facets on the part. Once this step was complete, each "part" was then inserted into a new "object" file. Finally, the "object" was inserted into a new "scene" file. These steps are illustrated in Figure 5-4.

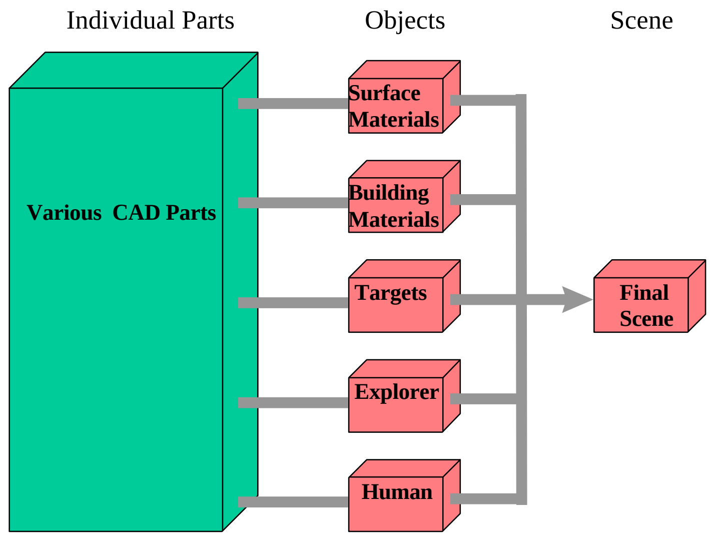

Figure 5-4 Hierarchical structure of AutoCAD scene.

The last step in AutoCAD is to translate the CAD file into a usable DIRSIG data file using the *dirsigdump* LISP routine. It should be noted that the contents of the *.dat file considers AutoCAD DECIMAL units only. In other words, if you created your drawing in some other units such as architectural, you will have to convert them to AutoCAD units. For this research, the drawing was generated using architectural units. Here, 1 inch = 1 AutoCAD unit. This becomes extremely important when entering the dynamic viewing coordinates (DVIEW) in the *.adv file for this file only understands AutoCAD units.

From this point on, the data was handled on a UNIX platform. Here, we format the scene to generate the *.gdb or geometric database file. This database is used by DIRSIG for ray tracing computations.

```
Prompt> dirsigfmt scene_scn.dat
result is scene_scn.gdb
```

5.2.2 Materials and Emissivities

Materials

A diverse set of layers and materials were used ranging from aluminum to human flesh, as can be seen in Table 5-3 and Table 14-1 of Appendix D. In all, a total of 27 materials were defined.

In the ray tracing process, DIRSIG uses a variety of specification pertaining to each material, such as specific heat, thermal conductivity, and mass density, to name a few. A majority of these parameters are used by the thermal sub-model within DIRSIG. The parameters for the visible that are important include optical description, specularity, and emissivity. Materials were given specularity values based on estimates of the surface roughness.

These parameters are contained in a materials file (*.mat). A sample of such a file can be seen in Figure 5-5. Here we only see the header information describing the contents of the file.

Table 5-3 Materials in which emissivity curves and material databases were generated.

Materials	Materials	Materials
black panel	asphalt	light clothes
white panel	yellow line on asphalt	medium clothes
light gray panel	grass	dark clothes
medium gray panel	dirt	red painted truck
dark gray panel	concrete	black area of truck
red panel	brick	plastic molding
blue panel	steel sign	rubber
black bars on resolution target	flesh	regular glass
white back of resolution target		mirrored glass
		polished aluminum

```
# FILE TYPE:    DIRSIG Materials file
# CREATEOR:     `convert_materials' utility
# DATE          Wed Oct  4 12:37:27 EDT 1995
# NOTES:        Entries can be arranged in any order
#               Tags within any entry can be in any order
#               A minimal set of tags are required (see below)
#
# Required Tags:
#       MATERIAL_ENTRY_BEGIN    start an entry
#       MATERIAL_NAME           name of the material
#       MATERIAL_ID             #ID of the material
#       SPECIFIC_HEAT           specific heat (L/cm/°C)
#       THERMAL_CONDUCTIVITY    thermal conductivity (L/cm/hr/°C)
#       MASS_DENSITY            mass density (g/cm³)
#       SPECULARITY             specularity of  material surface (fraction)
#                               0.0 = 100% diffuse and 1.0 = 100% specular
#       VISIBLE_EMISSIVITY      solar/incident emissivity (fraction)
#       THERMAL_EMISSIVITY      thermal/exit emissivity (fraction)
#       EXPOSED_AREA            DCS/THERM surface area term (fraction)
#       OPTICAL_DESCRIPTION     OPAQUE, UNIFORM_TRANSMISSION, or
#                               NONUNIFORM_TRANSMISSION
#       EMISSIVITY_FILE         name of emissivity file
#       THICKNESS               thickness of facet (cm)
#       MATERIAL_ENTRY_END      end of entry
#
# Optional/Additional Tags:
#       EXTINCTION_FILE         extinction file – required for transmission
#       TEXTURE_FILE            name DIRSIG Texture Image file for material
#       USE_GAUSSIAN_TEXTURE    flag to generate gaussian texture
#       TEXTURE_FILE            name DIRSIG Texture Image file for material
#       USE_GAUSSIAN_TEXTURE    flag to generate gaussian texture
```

Figure 5-5 Contents of material file showing various parameters needed for ray tracing.

Since the scene contained a wide variety of materials, many parameters for these materials were not readily available. Parameters of interest include specific heat, thermal conductivity, mass density, specularity, visible emissivity, thermal emissivity, and exposed area. Many of these values came from the DCS technical report on the development of their Thermal Signature Prediction and Analysis Tool (THERM) for the Air Force Infrared Synthetic Image Model (AIRSIM) [69]. Parameters for materials not found in the report were estimated based on similar materials and field measurements. Table 14-2 in Appendix D shows a summary of the material specifications.

Emissivity

Within the materials file there is a reference to an emissivity file. This is, as expected, the spectral emissivity of the material of interest. DIRSIG uses the emissivity parameters of *spectral emissivity*, *specularity*, and *specular emissivity* to describe the characteristics of a material. The specularity value and specular emissivity, for example, describes the magnitude of the specular lobe.

Current users of DIRSIG can reference a standard set of emissivity curves for generic materials, however, some of these curves are not entirely correct in the visible nor are they even available. It was therefore necessary to develop a set of emissivity curves specific to objects in the scene. The spectral regions of interest in this research fall into two bands. They are 0.5 to 0.925 μm and 8 to 12 μm. The former is the spectral response of the photocathode on the IICCD while the latter is the spectral response of the IR camera.

The visible emissivity information was obtained by using a portable spectral radiometer. The Spectra Colorimeter, model PR-650 by Photo Research (see Appendix E for specifications), was used to acquire radiometric data of various objects in the range of 380 - 780 nm in 4 nm increments. This was accomplished by first determining the radiance level from a piece of pressed polytetrafluoroethylene (PTFE) placed in the area of interest. Then by removing the disk, one could measure the sample area underneath. The reflectance was found by dividing the sample spectra by the reference spectra. This is a valid approach because the pressed PTFE exhibits a remarkably high diffuse reflectance over the range of 200 - 2500 nm [70]. Its reflectance is 99% or higher over the spectral range of 350 - 1800 nm. Finally, the emissivity curves are computed since,

$$e(l) = 1 - r(l) \tag{5.1}$$

As mentioned previously, visible emissivity data was only collected up to 0.780μm. The rest of the data came from DIRSIG emissivity databases, the Non-Conventional Exploitation Factors (NEF) database, and other empirical measurements.

The only data that was *not* available for some materials was spectral emissivity in the 8-14μm band. This was not difficult to create, however, since most materials in this band exhibit an emissivity of around 0.90 and higher. One noted exception is that of glass for it has a high Si-O reflectance peak at 8.5μm which is typical of fused silica. The entire family of emissivity curves used in this research can be found in Appendix D.

5.2.3 Dview and Scene Node Files

We now need to determine the look angle as seen by the sensor. This is the angle from which the simulated scene image will be generated. The look angle is found using AutoCAD's dview command which facilitates the creation of a complex camera and target geometry. In this research, only one look angle was used since we only had a single angle during the collection. The AutoCAD dview parameters are placed in a text file (*.adv) for DIRSIG to read in during ray-tracing. The single *.adv file used in this research can be seen in Figure 5-6. The view that is generated as a result of these view parameters is seen in Figure 5-7.

3472.105 2738.860 -0.634	-Target point (x,y,z) in AutoCAD units
3458.405 1954.160 612.597	-Camera point (x,y,z) in AutoCAD units
38.0028 -91.00022 0.0	-Camera angles- elevation, azimuth, and twist
70.0	-Camera focal length in millimeters
128 128	-Output image size - height, width

Figure 5-6 AutoCAD dview (*.adv) file.

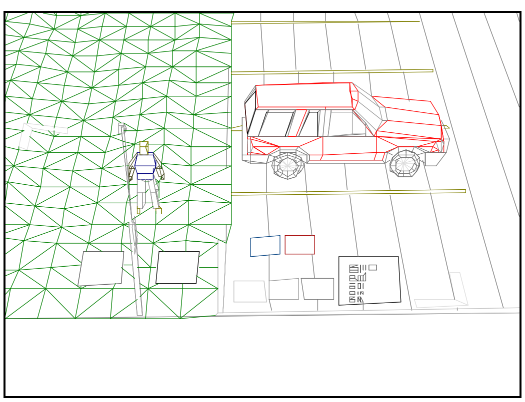

Figure 5-7 AutoCAD view used as input to DIRSIG.

Once the sensor viewing geometry is established we then need to develop radiance information. DIRSIG uses LOWTRAN or MODTRAN (depending on the desired resolution) to simulate atmospheric effects present in real-world, remote sensing systems. The radiometric data that is needed to model the radiation propagation during the ray tracing is generated before DIRSIG (the actual ray tracer) is run. The process of generating this data includes determining the minimum and maximum view angles that the sensor will use and then using LOWTRAN/MODTRAN to generate the radiance data for various rays cast within that solid angle [71]. To start in this process, we have to specify the location of the scene with respect to the sun and earth. This information is placed in a scene node file (*.snd). This file contains the physical location of the scene on the earth using a combination of latitude, longitude, and the sun's location defined by the date and time of day of the simulation. The parameters used for this research can be seen in Figure 5-8.

`0.263`	-Sensor altitude (km)
`2`	-Number of spectral bands
`830.0 1250.0 20.0`	-Min, max, increment, of sensor (cm^{-1}) [8 - 12.04 μm]
`10800.0 20000.0`	-Min, max, increment, of sensor (cm^{-1}) [0.5 - 0.926 μm]
`100.0`	
`23.00 81.00 2.00`	-Min, max, increment for view angle
`9 2 98`	-Month, day, year of simulation, GMT
`02.00`	-Time of day, GMT (decimal)
`4.0`	-Time zone, (hours behind GMT)
`43.16856 77.61583`	-Latitude, longitude

Figure 5-8 Scene node file (*.snd).

5.2.4 Card Decks and Radiance Files

To generate the radiance data that is used during the ray tracing process a LOWTRAN (or MODTRAN) card deck must be generated. This deck, or file, specifies the conditions under which to simulate the *atmospheric contributions* to the imaging process. This is achieved using a program called CONTROL7 which asks a series of questions in formulating the deck. This procedure can be found in Appendix D. We will create a completely synthetic atmosphere with the resultant card deck shown in Figure 5-9.

```
2    2    2    0    0    0    0    0    0    0    0    0    1   0.000   0.00
    1    1    0    1    0    0    5.000     0.000     0.000     0.000     0.218
     0.000     0.000     0.000     0.000     0.000     0.000    0
    1    2    1    0
     0.000     0.000     0.000     0.000     0.000     0.000     0.000     0.000
  5000.000 10000.000    12.626
    0
```

Figure 5-9 MODTRAN/LOWTRAN card deck.

Once the input card deck is complete, we need to compute the radiance. The information found in the scene node and card deck files is used to generate a file containing all the radiance information that is required for the scene simulation. This data is generated by a program called `build_radiance.` The program is written so as to take the scene node and card deck files and create a radiance data file(s) in each bandpass region for a given time, day, and location. It does this by updating the scene node specific fields in the card deck and then runs LOWTRAN or MODTRAN. The output file is then used as an input to DIRSIG to interpolate radiance terms about the hemisphere. Previously sun location, for example, came from LOWTRAN and THERM. As of this research, however, a new program called “ephem” (section 5.3) has been implemented to perform this task. Ephem is based on standards set forth by the National Optical Astronomy Observatories (NOAO).

5.2.5 Weather Files

Weather affects atmospheric modeling and is included in the computation of radiance data. In this regard, the *.wth file provides a time varying value for atmospheric pressure, temperature, and relative humidity (or dew point) as measured at the ground. This offers an improvement over the radiosonde data used, which is collected only twice a day. The main function of the *.wth file during a DIRSIG scene generation, however, is to determine object temperatures [71]. The file is constructed based on the weather conditions 48 hours prior to the collection time, in one hour increments. The weather file that was used for this research can be seen in Appendix D. Usually, weather information is obtained from a source such as the National Oceanic and Atmospheric Administration (NOAA) after collection time. However, weather information for this research was compiled based on the researcher's observations at the time of collection.

5.2.6 Sensor Responsivity Files

The sensor file contains the sensor's gain, offset, and normalized spectral responsivity, $\beta(\lambda)$. The sensor used in this research was the IICCD which had a response from 0.500 - 0.925 μm. The spectral response for this device is seen in Figure 5-10. The file formats used can be found in Appendix D.

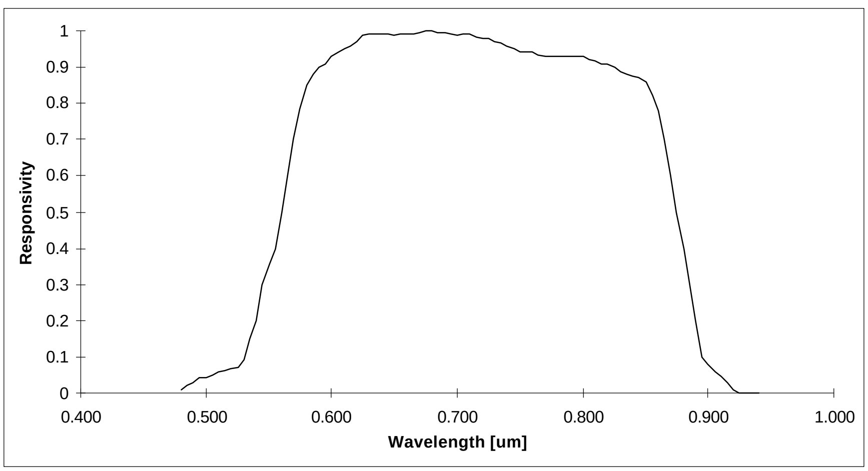

Figure 5-10 IICCD spectral response curve.

5.2.7 Secondary Source Contribution

As a result of this research DIRSIG now has secondary source capability. Furthermore, one can specify a separate spectral intensity distribution for each source. This is illustrated in Figure 5-11.

For a given hit point, DIRSIG calculates the irradiance contribution from the sources in the scene. For this research, spectral intensity curves were generated based on the Planck equation as a function of temperature, which was measured several times for each source. This is a valid approach since we were using tungsten and tungsten-halogen bulbs which closely approximate Planckian blackbody distributions. The derivation of such source distributions can be found in Appendix D.

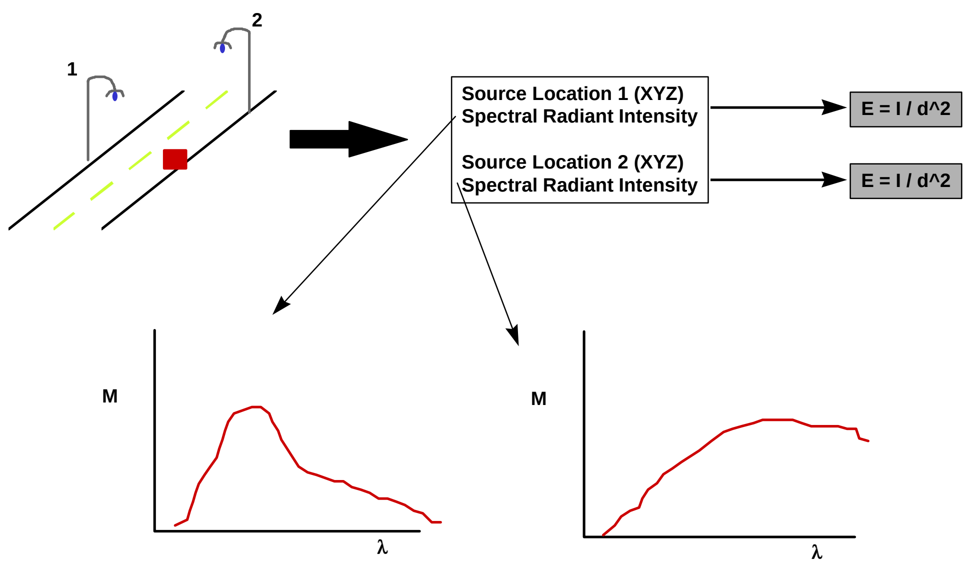

Figure 5-11 Illustration of how secondary sources are handled in DIRSIG.

5.2.8 DIRSIG Batch Files

The final stage is to actually run the ray tracer. This is best handled by a batch file. The batch files that were used for this research can be found in Appendix D.

5.3 Lunar and Sky/Starlight Contribution

Part of the goal of this research is to include secondary source capability into DIRSIG. More than likely, secondary source scenarios occur under conditions of poor illumination, for example street lights on the expressway at night. The other night time source that becomes important in outdoor scenarios is the moon. For example, a moonless, overcast night sky produces a scene illuminance on the order of 10^{-4} lux, whereas a full moon can produce an illuminance of 10^{-1}lux [72].

Previously DIRSIG did not have lunar capability. As of this research, however, MODTRAN has been exploited to produce radiance values based on the conditions of the moon (i.e., phase angle, phase fraction, and location). This lunar (and solar) ephemeris information comes from a program called "ephem". Originally ephem was used to compute optimum ground truth collection dates for this research. However, it has now replaced LOWTRAN and THERM for computing the solar and lunar geometry.

DIRSIG ultimately needs the location(θ, ϕ) and phase fraction(%) of the moon. MODTRAN, however, needs location(θ, ϕ) and phase angle. From the scene node file, ephem can compute solar location(θ, ϕ), lunar location(θ, ϕ), lunar phase angle, and lunar phase fraction(%). This is illustrated in Figure 5-12.

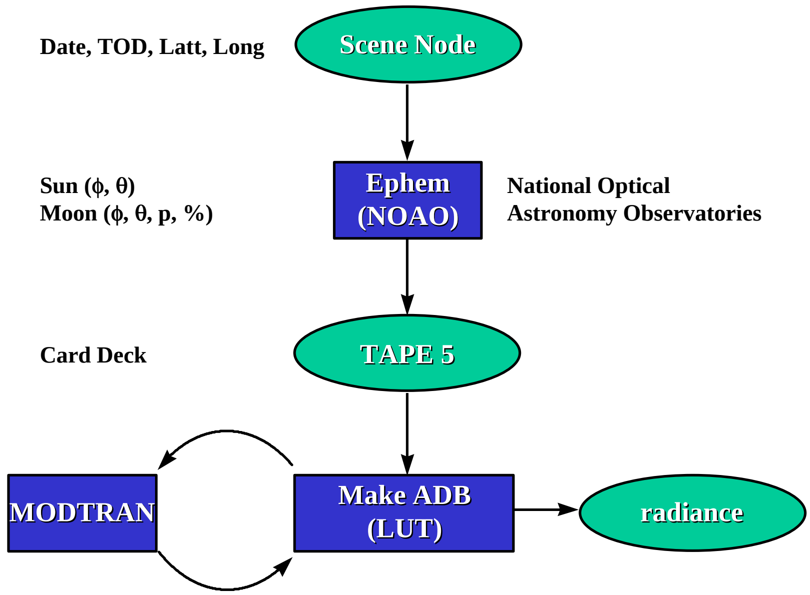

Figure 5-12 Integration of ephem into make ADB.

The phase angle can be computed in one of two ways, based on the illumination percentage (phase fraction) or by taking into account planetary distances. Both forms can be seen below.

$$\cos p = \frac{\text{phase fraction}}{50} - 1 \tag{5.2}$$

$$\cos p = \frac{r^2 + \Delta^2 - R^2}{2r\Delta} \tag{5.3}$$

where:

p = phase angle; angle between sun and earth seen from the planet
r = distance from the moon to the sun
Δ = distance from the moon to the earth
R = distance from the sun to the earth

Ephem is able to compute all of these parameters with only a slight modification to the code (see Appendix F). Some test cases were developed to compare the two methods. The first form is a much easier computation, however, there is some variation between the two as can be see in Figure

5-13. More than likely, the phase calculation incorporating planetary distances is more accurate. Therefore, we will use this method of calculating phase angle for MODTRAN.

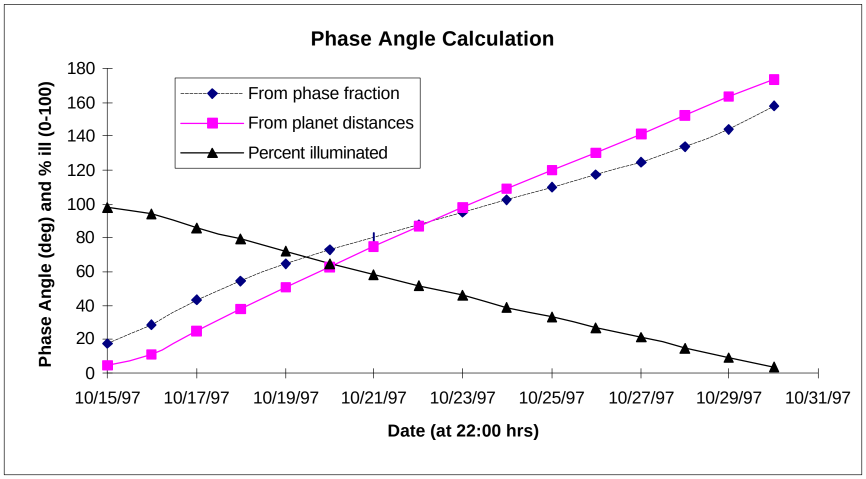

Figure 5-13 Comparison of phase angle calculations.

Sky/Starlight

Sky background and starlight has also been added to DIRSIG. The stars provide approximately 2.2 x 10^{-4} lux (lm m^{-2}) ground illuminance on a clear night. This illuminance is equivalent to about *one-quarter* of the actual light from the night sky with no moon. The greater portion of the natural light of the night sky, the airglow that originates in the upper atmosphere, is produced by the emission from various atoms and molecules. Other minor sources of night illuminance are the aurora and zodiacal light caused by the scattering of sunlight from interplanetary particulate matter [72]. It should be pointed out that except for extremely remote regions of the continents night-time illumination levels are always more or less affected by illumination from artificial light, especially with reflection from clouds under overcast conditions. Table 5-4 and Table 5-5 lists some approximate levels of scene illuminance from the day and night sky under various conditions.

Table 5-4 Natural scene illuminance [72].

Sky Condition	Level of Illuminance lux (lm m^{-2})
Direct sunlight	100,000 - 130,000
Full daylight (not direct sunlight)	10,000 - 20,000
Overcast day	1,000
Very dark day	100
Twilight	10
Deep twilight	1
Full moon	0.1
Quarter moon	0.01
Moonless, clear night sky	0.001
Moonless, overcast night sky	0.0001

Table 5-5 Typical scene illuminance from Pulnix manual.

Sky Condition	Level of Illuminance lux (lm m^{-2})
Clear sunlight	30,000 - 100,000
Overcast day	3,000 - 10,000
Sunrise/sunset	500
Twilight	5
Full moon	0.03 - 0.3
Starlight	0.0007 - 0.003
Overcast night	0.00002 - 0.0002

The atmosphere scatters sunlight, moonlight, and starlight. In addition to this scattered light there is a background observable at night which is due to the sources seen in Table 5-6. An estimate of the average spectral distribution of the night-sky irradiance is plotted in Figure 5-14. This result, in photons per second, is on a horizontal surface of one square meter at sea level in wavelength intervals of 0.050 μm [72]. This is the background spectral curve that will be implemented in DIRSIG. It is assumed that the data already includes the starlight term and that the collection was performed on a clear night. To see the conversion to radiance as well as a verification to published literature, see Appendix G. It is noteworthy that the lower atmosphere emits thermal radiation whose level may be approximated by blackbody radiation at ambient ground temperature though this effect is limited mostly to the far infrared region.

Table 5-6 Observable background sources [73].

15%	Zodiacal
5%	Galactic
40% (avg.)	Luminescence of night sky (fluctuates)
10%	Scattering from the above
30%	Direct and scattered starlight
<1%	Extra-Galactic sources

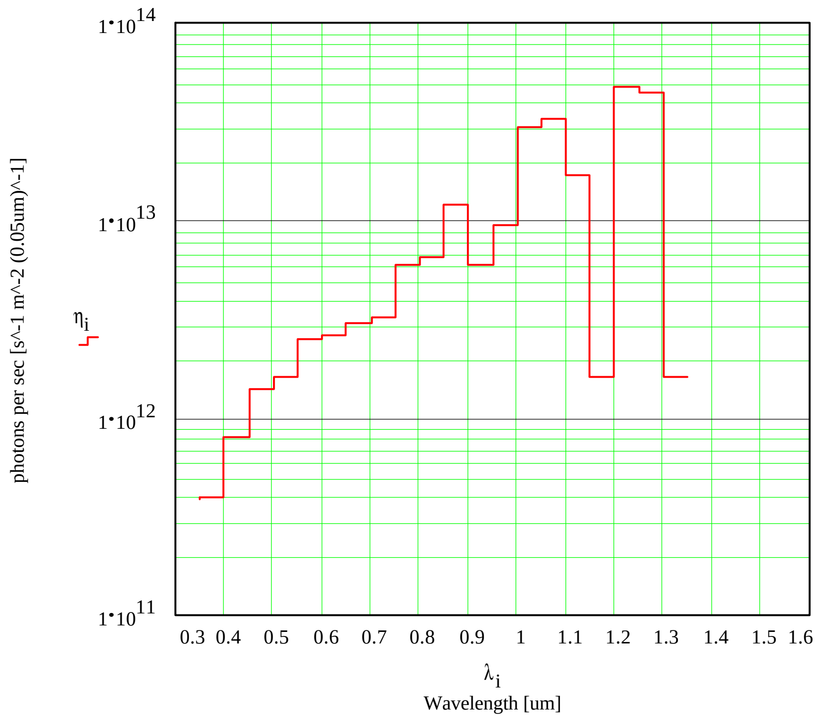

Figure 5-14 Natural night sky spectral irradiance in photons per second.

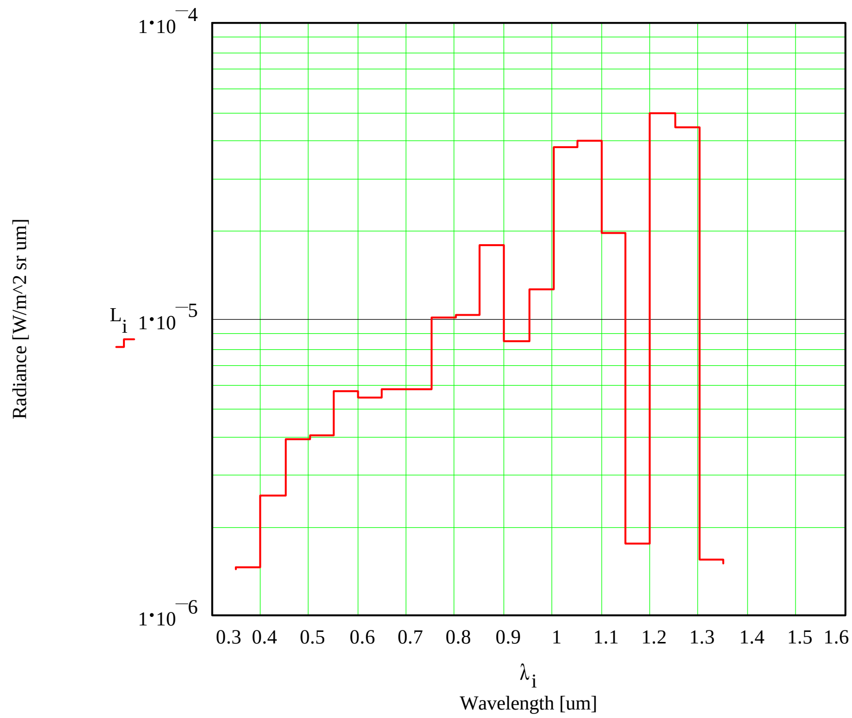

Figure 5-15 Natural night sky spectral radiance in Watts/m^2 sr.

Chapter 6

6. IICCD Modeling

In the following sections we attempt to model many of the artifacts associated with image intensified CCD devices, including photon noise, gain issues, MTF effects, blooming and electronic noise. Though a complete system model is in order (modeling each component separately) we only concern ourselves with generating a model for the "entire system" based on both empirical data and published literature. Here we will attempt to model the operation of an intensifier coupled to a CCD array and apply the above mentioned artifacts to synthetic imagery. Also included are discussions for individual component modeling and the relative importance of these components.

This chapter starts out with a discussion of modeling and what it means to treat the sensor system as an image chain. We then discuss the details of the IICCD systems while describing component MTFs. Finally we comment on the various sources of noise.

6.1 System Modeling: A Chain Approach

The overall approach to synthetic modeling of a low-light-level imaging sensor is illustrated in Figure 6-1. The DIRSIG input parameters include the scene database (objects in scene, thermodynamic and reflectance databases, etc.), the atmospheric databases (path transmissions, scattered radiances, meteorological data) and information on exoatmospheric and man-made sources. The result is a high fidelity radiance field image which is processed by the low-light-level sensor simulator.

The sensor simulation is broken down into the physical elements of a generalized ICCD. Each simulation element reflects a different stage in the processing of the input radiance field. The variability of photon arrival in a low-intensity image is modeled with the appropriate distribution and then passed to the optics model. In the high-sensitivity limit, *i.e*., high gain, it has been shown that the ICCD is photon-noise-limited [74]. That is, once the gain reaches the level at which photon noise is dominant, a change in gain will not affect the signal-to-noise ratio SNR. For small gains, however, contributions from various noise sources become significant. The next stage is to model the input system optics. Here we concern ourselves with the effects due to the entrance pupil and geometric effects due to non-uniformitys in the optics. At this point photoelectrons are incident on the input window of the photocathode, which is part of the II module. The II module is modeled with a subset of components that make up the ICCD device itself (see section 6.2). Key tube components include the photocathode, MCP, and phosphor screen. The input photo-surface generates noise which is filtered by the intensifier phosphors and all the modulation transfer functions that follow. The output of the image intensifier (II) module is usually coupled to a solid state imager via a fiber-optic taper (not shown). The CCD is modeled as a two-dimensional discrete sampling process in both x and y and may include phenomena due to quantum efficiencies or sensor read-out. The radiance image is then processed with pre-amplifier noise from the back-end electronics. The pre-amplifier noise is filtered only by the video processor and the display, which are the last two components to be modeled before the final simulated image is generated.

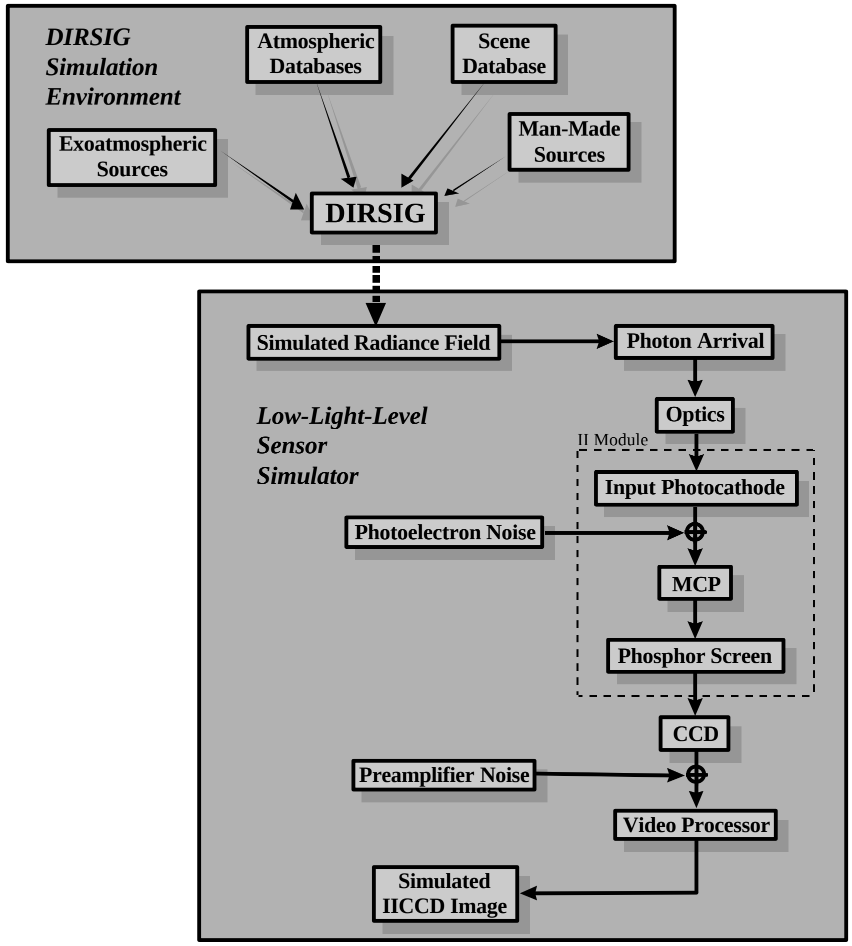

Figure 6-1 The ideal DIRSIG based low-light-level image simulation environment.

6.2 The II Module and CCD Imager

The basic operation of an image intensifier was described in section 2.1.1. A few key points should be mentioned in this section for completeness. Figure 6-2 shows a detailed schematic design of a fiber-optically (FO) coupled IICCD assembly. Here we see an input window, a photocathode, a microchannel plate, a phosphor screen and an output window. We also see a fiber-optic taper, instead of a simple unity magnification FO window. The *photocathode* on the vacuum side of the *input window* converts the input optical image into an electronic image at the vacuum surface of the photocathode in the II. The *MCP* is used to amplify the electron image pixel-by-pixel. The amplified electron image at the output surface of the MCP is reconverted to a visible image using the *phosphor screen* on the vacuum side of the *output window*. This complete process results in an output image which can be as much as 20,000 to 50,000 times brighter than what the unaided eye can perceive [75]. When modeling it should be noted that these proximity focused designs are nearly *distortion-free* with *linear*, i.e., unity gamma, input/output transfer characteristics over wide intrascene dynamic ranges.

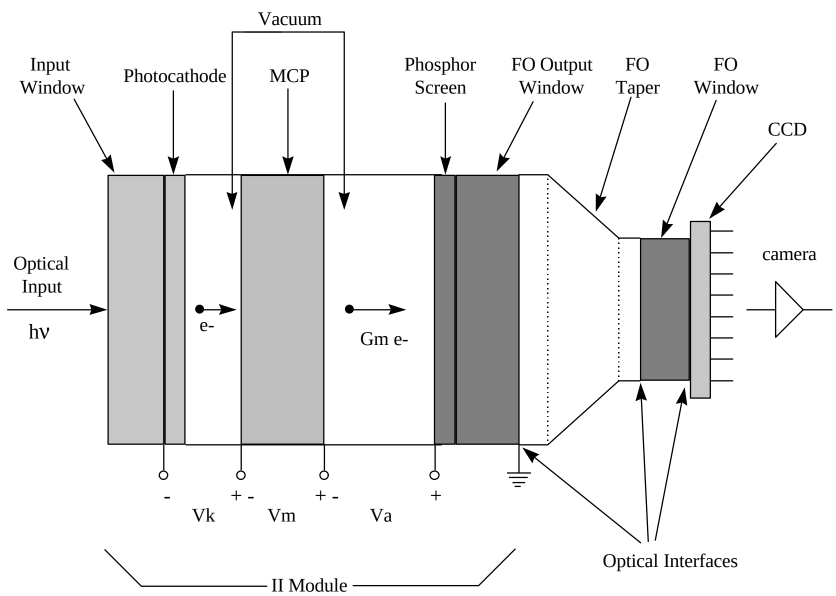

Figure 6-2 Schematic design of a fiber-optically coupled IICCD assembly.

Typically the acceleration voltage at *Vk* is 200 V while the voltage across the MCP (*Vm*) is 800 V. The voltage at *Va is* usually 6000 V which provides enough acceleration across the MCP-to-phosphor screen gap to make the photoelectron strike the aluminized phosphor screen with an energy of about 6 keV. This is enough energy to produce an output image which is many times brighter than the input image. Other dimensions include those mentioned in Table 6-1 which have been found throughout the literature [35, 82].

Table 6-1 Typical IICCD dimensions found in LLL literature.

Photocathode-to-MCP spacing	90 - 170 um
MCP-to-Phosphor spacing	250 - 650 um
MCP thickness	305 um
MCP hole size	5 - 8 um
MCP pitch	6 - 10 um centers
FO hole size	4 - 6 um tapered to 2 - 3 um

6.2.1 Quantum Efficiency (QE) and Spectral Matching

When modeling an IICCD system one needs to take into account the quantum efficiency or spectral sensitivity of the photocathode and sensitivities of the phosphor screen and CCD. The photocathode will dictate the input spectral sensitivity. Typical photocathode QE's and sensitivities can be seen in Figure 2-29 and Figure 2-30 while the one used for this research can be seen in Figure 6-3. It is also important to adequately match the phosphor screen output to the CCD sensitivity. Some typical phosphor screen sensitivities are plotted in Figure 2-3 while the phosphor-CCD combination used in this research can be seen in Figure 6-4. It should be noted that the P20 is selected more often than not because it has a high conversion efficiency and a fast enough decay time for conventional 1/30-s frame times.

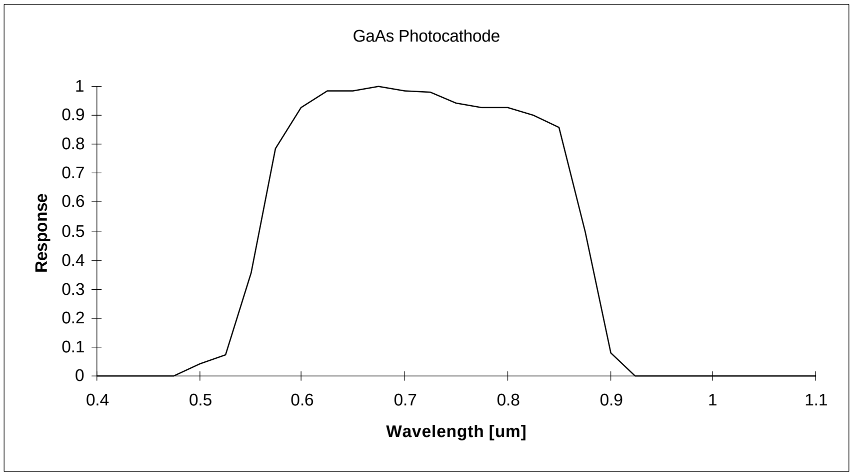

Figure 6-3 Relative spectral responses of the IICCD.

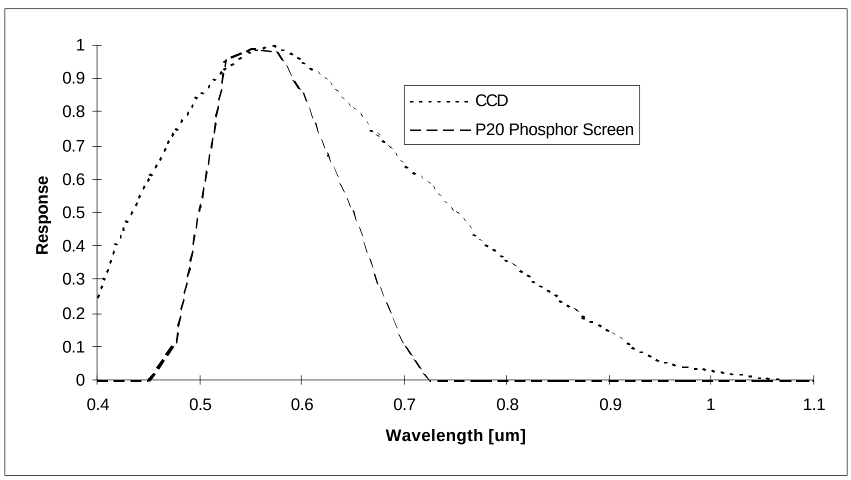

Figure 6-4 Relative spectral response of the phosphor and CCD.

6.2.2 MCP and CCD Imager

When a voltage (*Vm*) is applied across the MCPs input and output electrode, the device produces a low-noise gain *Gm*, as seen in Figure 6-2. The MCP bias current that results from the voltage applied to the MCP sets an upper limit to the maximum linear dynamic range of the MCP. Experimental data indicates that single plates will operate in a linear fashion (i.e., the gain will remain constant over a range of input signal levels) until output current reaches 10 to 15 percent of the bias current [76]. Typical single stage MCPs have bias currents densities on the order of 1 $\mu A/cm^2$ and gains from 10^3 to 10^4, where the gain is described as;

$$Gm = \left(\frac{Vm}{Vc}\right)^g \tag{6.1}$$

where;

Vm = the voltage applied across the MCP [V]
Vc = the crossover voltage for the channel, *i.e.*, it is the MCP applied voltage at which the gain is exactly unity, typically 350-530 V
g = exponential factor, typically 8.5-13

CCD Imager

At the back end of the device is the CCD imager. Here the sensor captures photons and converts them into electrical charges proportional to the amount of illumination. There are basically three sensor architectures most commonly found in digital cameras: full frame, frame transfer and interline transfer. The interline-type image sensor was used for this research. The frame transfer sensor's active pixels and storage pixels are on different sections of the sensor chip. This separation allows the active array area to approach a nearly 100 percent fill factor. Because of this design, the chip is very susceptible to booming (described below). The solution, at the expense of reduced fill factor or sensitivity, is to set aside part of the area at the pixel site with a mask to act as a local storage at the end of an exposure. This provides excellent isolation of adjacent pixels, reducing the possibility of blooming.

6.2.3 Blooming and Auto Gain Control (AGC)

Blooming usually occurs with full frame and frame transfer CCDs and is rarely seen with interline imagers [76]. The situation occurs when there is an overabundance of light entering the system, which may come from bright light sources in the field of view. This causes the CCD potential wells to overfill and spill over to adjacent pixels where a typical CCD pixel full-well charge is on the order of 1 pC or 6.3E^6 electrons. As each pixel in a column from differing lines moves through an extremely bright point, its value can be altered. In an extreme case, *streaking* appears in the form of a white vertical line. If the intensity of illumination exceeds the dynamic range of the sensor, the pixel wells saturate and electrons spill over to adjacent pixels in *both* the X and Y axis which leads to *blooming*. Furthermore, high resolution CCDs with small pixel and electron well capacities have reduced dynamic range and are more susceptible to the blooming and smearing phenomena.

Blooming can also occur within the image intensifier system. As photoelectrons exit the photocathode, they fall on the surface of the MCP. Not all the photoelectrons propagate through a MCP pore, however. About 40% actually hit the spacing between the holes resulting in reflected photoelectrons [77], some of which are at large angles. If we consider 6 μm holes on 8 μm centers, we see that only 58% of the total area constitutes *hole space* while the 42% left makes up the *dead space* between the holes. These reflected photoelectrons propagate back through the MCP and can form a *halo* in the resulting image if the incident number and reflection angle is large enough. The halo diameter will be strongly dependent on the photocathode to MCP spacing, with small MCP spacings decreasing the effect.

This former form of blooming is dominant over a 2nd order effect with occurs at the output of the phosphor screen. Here there are two types of blooming that may occur. The first is the result of high energy photoelectrons which are accelerated across the MCP-phosphor screen gap. These photoelectrons are incident on the phosphor screen surface, (which can also lead to a halo as described above). As a result of this collision, visible photons are formed which fall on a fiber-optic taper with a small amount of spread due to both the gap and phosphor screen interaction. This can be eliminated in some cases by forming the phosphor screen directly onto the FO taper instead of the FO output window. The second form of blooming is due to the decay time inherent in the phosphor screen. This effect is usually minimal but can result in severe blooming or smearing at long decay times.

Auto Gain Control (AGC)

Most manufactures of LLL imaging devices incorporate some method of maximizing scene content while protecting the cameras from burnout. Typically, these methods use either the phosphor screen current or information from the video signal levels to control the gain of the image tube and duty cycle of the gate pulse width. Because the phosphor current is proportional to the average input scene luminance, it can be used to adjust the image tube gain and pulse width duty cycle to an average value. The benefit of using phosphor currents is in instantaneous detection of the phosphor current. Circuits using the video signal levels to correct the exposure level lag the input scene by a minimum of one field integration period [78]. Other types of AGC are also employed such as bright source protection (BSP) or auto signal control (ASC) [77]. Bright source protection puts a resistor in series with the photocathode. When greater cathode current is drawn by the high light inputs from a bright scene, this resistor limits the current in an attempt to extend the operating range of the intensifier while also affording some protection against cathode degradation. This in turn dynamically alters, in a non-linear fashion, the gain of the IIT.

6.2.4 Propagation of a single photon

We end this section by commenting on the propagation of a single photon through the image chain described above. We will do this by looking at the stored charge and number of stored electrons per photoelectron for a *proximity-focused* image intensifier *fiber-optically coupled* to a *CCD*. The general equation [75] for the charge stored in a CCD per input photoelectron from a photocathode with a quantum efficiency, QE_k, [photoelectrons/photon] is

$$Q_{ccd} = e\, G_m\, (V_s - V_d)\, P\, T_{fot}\, T_{CCD}\, QE_{CCD} \quad [coulomb] \tag{6.2}$$

where;

e = e- charge = $1.6E^{-19}$ [coulomb]
G_m = MCP electron gain [e/e]
V_s = MCP-to-screen applied voltage [V]
V_d = phosphor screen "dead-voltage" [V]
P = phosphor screen efficiency [photon/eV]
T_{fot} = transmission of fiber-optic taper
T_{CCD} = transmission of fiber-optic window on the CCD
QE_{CCD} = quantum yield of CCD [e/photon]

Therefore, the number of electrons stored in the CCD per input photoelectron is

$$N_{CCD} = Q_{CCD} / e \quad [e] \tag{6.3}$$

The QE [e/photon] for a GaAs photocathode is typically 25% in the visible (i.e., 4 photons needed to generate 1 electron, on average). All of the above parameters are readily available in published literature or are usually provided by the manufacturer. Other detailed camera modes can be found in [78].

6.3 Component MTFs

We now look at the component MTFs associated with the image chain presented earlier. The *modulation transfer function*, MTF, is essentially a spatial frequency response of an optical imaging system and can be determined in many ways. A method often used involves analysis of the *edge spread function* (ESF). The ESF is useful because the derivative of it with respect to position is called the *line spread function* (LSF) in that direction. Note that for separable systems the LSF(x) is equal to the *point spread function*, PSF(x,0). Furthermore, one line through the 2D MTF is the Fourier transform of the LSF. Strictly speaking, the MTF is the magnitude of the Fourier transform of the PSF. These relationships are seen below;

$$\mathrm{LSF}(x) = \mathrm{PSF}(x,0) = d(\mathrm{ESF})/dx \tag{6.4}$$

$$\mathcal{F}\{\ \mathrm{LSF}(x)\ \} = \mathcal{F}\{\ \mathrm{PSF}(x,0)\ \} = \mathrm{OTF}(x,0) \tag{6.5}$$

$$\mathcal{F}\{\ \mathrm{PSF}(x,y)\ \} = \mathrm{OTF}(\xi,\eta) \tag{6.6}$$

$$|\mathrm{OTF}(x,h)| = \mathrm{MTF}(x,h) \tag{6.7}$$

This system response is in the spatial frequency domain (cyc/mm) rather than the temporal frequency domain (cyc/sec). A spatial variation of light intensity or response is transformed into a set of spatial frequency components. From a visual standpoint, high values of MTF correspond to good visibly, and low values to poor visibility. However, this depends on frequency. Most of the time, these characterizations of resolution are in terms of one-dimensional spatial frequency response, while in reality images are two-dimensional.

The use of one-dimensional frequency responses implies that spatial responses are independent functions of *x* and *y*. Also, the use of Fourier transform theory implies linearity. However, even when independence and linearity conditions are *not met*, the concepts are still used as if they were. In this research we only apply the most important component MTFs with the assumption of circular symmetry. In reality, however, systems do vary in *x* and *y*. When individual components are taken into account, a first order system MTF can be given by

$$MTF_{sys} = MTF_{optics} \bullet MTF_{phocath} \bullet MTF_{MCP} \bullet MTF_{phos} \bullet MTF_{FO} \bullet MTF_{CCD} \bullet MTF_{digitizer} \tag{6.8}$$

Furthermore, the MTF of the intensifier system can be further broken down into sub MTFs which include the MTF of the II-to-CCD coupling, fiber-optic-to-fiber-optic interfaces, fiber-optic-to-CCD interface, etc. Use of the MTF in the characterization of an imaging system requires first a Fourier transform of the object into its spectrum then multiplication of the object spectrum by the appropriate MTF (with a scale factor to match the image) followed by an inverse Fourier transform to obtain the modified profile of the image.

6.3.1 Optics MTF

At the front end of most intensifiers are optics used to collect light while bringing the object to focus at the image plane. Furthermore, the entrance pupil is usually that of a circular pupil of diameter *d*. Therefore, the pupil function can be represented as a 2D *cylinder function*, CYL(r/d) [79].

$$p(r) = CYL\left(\frac{r}{d}\right) \tag{6.9}$$

Assuming Fraunhofer diffraction (far field), the coherent point spread function (PSF) is the Fourier transform of the pupil function.

$$h_{coherent}(r) \propto SOMB\left(\frac{rd}{l z_1}\right) \tag{6.10}$$

where z_1 is the distance from the aperture to the image plane. The optical transfer function (OTF) is the pupil function scaled.

$$H_{coherent}(r) \propto CYL\left(\frac{r\, l z_1}{d}\right) \tag{6.11}$$

The maximum frequency transmitted by this system is $\rho_{max} = d/2\lambda z_1$. The coherent MTF is the modulus of the transfer function. The coherent imaging system with a finite aperture acts as a lowpass filter, *i.e.*, the output image is blurred. Still assuming far field diffraction, the *incoherent* PSF, or airy disk, is the Fourier transform of the pupil function magnitude squared.

$$h_{incoherent}(r) \propto SOMB^2\left(\frac{rd}{l z_1}\right) \tag{6.12}$$

The incoherent transfer function is the autocorrelation of the coherent transfer function. In other words, the incoherent OTF is proportional to the autocorrelation of the pupil function.

$$H_{incoherent}(r) \propto CYL\left(\frac{r\, l z_1}{d}\right) \circ\circ\ CYL\left(\frac{r\, l z_1}{d}\right) \tag{6.13}$$

This latter representation is the transfer function most commonly used. It resembles a circularly symmetric triangle with a cut off frequency twice that found in the coherent case (due to the autocorrelation).

6.3.2 II Tube MTF

The MTF here is representative of the II tube itself. That is, $MTF_{II} = MTF_{phocath} \bullet MTF_{MCP} \bullet MTF_{phos}$. In general, the MTFs associated with intensifier tubes can usually be described by a mathematical function with only two parameters [80-81]. The form of this function in 1D is as follows;

$$MTF_{II} = e^{-\left(\frac{x}{x_c}\right)^n} \tag{6.14}$$

where x_c is the frequency constant and n is the MTF index. The *shape* of the MTF curve is described by the MTF index, and large values of n are associated with a rapid decrease in MTF at the frequency constant x_c. An example of some typical values can be seen in Table 6-2 and graphically illustrated in Figure 6-5. The limiting resolution in the II system is primarily due to the MCP pore size, MCP spacings, and phosphor screen resolution.

Table 6-2 Published values of MTF index and frequency constant.

photocathode, MCP, phosphor screen, reference	Frequency Constant x_c	MTF index n
18mm MCP (proximity) [75]	6.3	1.1
(proximity) [81]	15.0	1.7
[82]	21.5	1.46
S25, 18mm MCP (proximity), P20, [82] (1995)	30	0.85

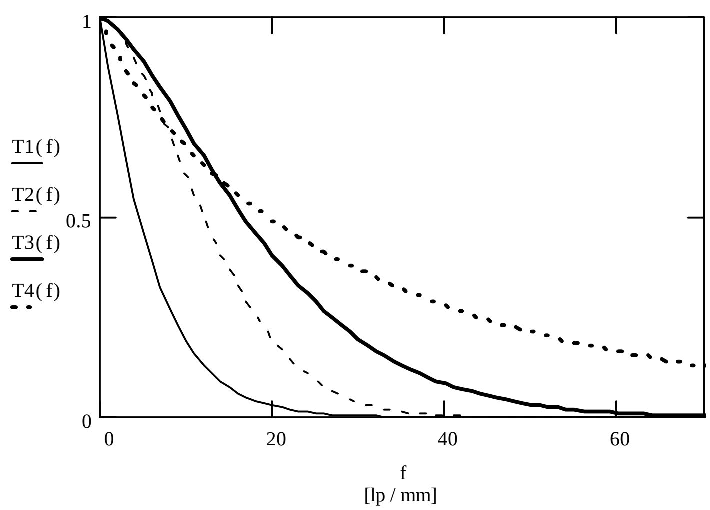

Figure 6-5 Plot of MTF function with varying index and frequency constant.

6.3.3 Fiber Optic MTF

In many of today's IICCDs, the phosphor screen is deposited on a fiber optic bundle which in effect re-samples the image. The bundle is then tapered down to accommodate a CCD. Since the fiber optics are circular in nature we can use the cylinder function to describe the transmittance. The Hankel transform of this yields the sombrero function [79]. Furthermore, the sombrero function can be rewritten in terms of a first-order Bessel function of the first kind;

$$H_0\left\{CYL\left(\frac{r}{d}\right)\right\} = \left|\frac{pd^2}{4}\right| SOMB(dr) \tag{6.15}$$

$$MTF_{FO} = \left|SOMB(dr)\right| = \left|\frac{2J_1(2pdr)}{2pdr}\right| \tag{6.16}$$

where d is the fiber optic coupler's core-to-core pitch and r is the spatial frequency in lp/mm. The Bessel function can then be approximated by a polynomial expansion.

In the interval -3 ≤ x ≤ 3

$$x^{-1}J_1(x)=\frac{1}{2}-0.56249985\left(\frac{x}{3}\right)^2+0.21093573\left(\frac{x}{3}\right)^4-0.03954289\left(\frac{x}{3}\right)^6$$
$$+0.00443319\left(\frac{x}{3}\right)^8-0.00031761\left(\frac{x}{3}\right)^{10}-0.00001109\left(\frac{x}{3}\right)^{12}+e$$

Here $|e|<1.3\times10^{-8}$

In the interval $x \geq 3$

$$J_1(x)=\sqrt{\frac{1}{x}}f_1\cos q_1$$

where

$$f_1=0.79788456+0.00000156\left(\frac{3}{x}\right)+0.01659667\left(\frac{3}{x}\right)^2+0.00017105\left(\frac{3}{x}\right)^3$$
$$-0.00249511\left(\frac{3}{x}\right)^4+0.00113653\left(\frac{3}{x}\right)^5-0.00020033\left(\frac{3}{x}\right)^6+e$$

Here $|e|<4\times10^{-8}$

and

$$q_1=x-2.35619449+0.12499612\left(\frac{3}{x}\right)+0.00005650\left(\frac{3}{x}\right)^2-0.00637879\left(\frac{3}{x}\right)^3$$
$$+0.00074348\left(\frac{3}{x}\right)^4+0.00079824\left(\frac{3}{x}\right)^5-0.00029166\left(\frac{3}{x}\right)^6+e$$

Here $|e|<9\times10^{-8}$

6.3.4 CCD MTF

Solid state imagers have well-defined picture elements, or pixels, which are quantized in both directions and, therefore, are sampled in both directions. A single pixel in the focal plane is of size *b* by *d*, and is modeled in the space domain as a 2D *rectangular function*, RECT(x/b, y/d) [79]. When the camera model samples a scene, the detector element in the sensor system averages the input signal over the detector size in both x and y directions. This is equivalent to convolution of the original 2D image with the 2D RECT function. The sampled signal is obtained by multiplying the averaged signal by the COMB function.

$$f_s(n\Delta x, m\Delta y) = \left\{ f(x,y) ** \left|\frac{1}{bd}\right| RECT\left(\frac{x}{b}, \frac{y}{d}\right)\right\} \bullet \frac{1}{\Delta x \Delta y} COMB\left(\frac{x}{\Delta x}, \frac{y}{\Delta y}\right) \tag{6.17}$$

where:

f_s(nDx, mDy)	= sampled input image defined at coordinated nΔx, mΔy
f(x,y)	= brightness distribution of input image
b, d	= horizontal and vertical widths of the RECT function, respectively
Dx, Dy	= x and y-direction sampling intervals, respectively

If the input spectrum is *bandlimited* at the Nyquist frequency and if the averaged signal is sampled sufficiently to avoid aliasing, (i.e., $\Delta x \le \frac{1}{2x_{\max}}$ and $\Delta y \le \frac{1}{2h_{\max}}$) then the Fourier transform of the sampled signal results in an unaliased spectrum

$$F_s(k\Delta x, l\Delta y) = \left\{ F(x,h) \bullet SINC(bx, dh) \right\} ** COMB(\Delta xx, \Delta yh) \tag{6.18}$$

The DIRSIG images are bandlimited because it simulates a solid state sensor. The spectrum is discrete and has a highest frequency, ξ_{max}, such that ξ_{max}= 1/2Δx. We also see that it satisfies the criterion: F(ξ) = 0 for all frequencies |ξ| > ξ_{max}, therefore, we will not have aliasing.

When the detector MTF in a sensor system is being modeled, the number and arrangement of individual detectors is not considered. The MTF due to the detector blurring is then given by the Fourier transform of the impulse response (PSF) of the detector, which is

$$PSF_{CCD} = \left|\frac{1}{bd}\right| RECT\left(\frac{x}{b}, \frac{y}{d}\right) \tag{6.19}$$

$$MTF_{CCD} = \left| \mathcal{F} \left\{ PSF_{CCD} \right\} \right| = SINC(bx, dh) = \frac{\sin(pxb)}{pxb} \frac{\sin(pxd)}{pxd} \tag{6.20}$$

In summary, we implement an MTF model that takes into account the most prevalent sources of blur. Namely, the "entire" II module, fiber optics, and CCD. The II module is by far the limiting factor in system performance because of its internal makeup. It converts light to electrons, then photons, then back to electrons for the CCD to readout. This degradation is also aided by the fact that there is an axial spacing component between each conversion step, as seen in Figure 6-2. The II module can be further broken down into its MTF components (photocathode, MCP, and phosphor), however, we will not concern ourselves with these components during this treatment. The fiber optic taper and CCD, comparatively speaking, effect system performance to a lesser degree, as will be shown in subsequent sections.

6.4 IICCD System Noise

The signal variations, or noise, are usually characterized by the root mean square (RMS) variation [46] in the instantaneous signal level (S_i) according to

$$N_{RMS} = \left(\frac{\sum_{i=1}^{n} \left(S_i - S_{avg} \right)^2}{n} \right)^{\frac{1}{2}} \quad [V] \tag{6.21}$$

where S_{avg} is the mean signal level and n is the number of samples. However, noise really only becomes significant when is it viewed relative to a corresponding signal. Therefore, the signal-to-noise ratio (SNR) becomes important. Another common parameter used for expressing the concept of noise in *radiometric* input units [*W*] rather then in output signal units [*V*] is noise equivalent power (NEP).

$$NEP(l) = \frac{N}{b(l)} \quad [W] \tag{6.22}$$

where N is the noise and $b(l)$ is the spectral responsivity. From the system NEP and knowing the optical throughput, $G\#$, the noise equivalent radiance can be computed as

$$NER(l) = \frac{NEP(l)}{A_d}(G\#) \tag{6.23}$$

where NER is the amount of radiance or change in radiance on the front of the sensor required to produce a change in sensor output equal to the sensor's noise level [46]. It should also be noted that when determining the sensors NER performance, intrinsic noise sources become much more important than the quantum efficiency.

In the past, the NER has been used in the form of a standard deviation value to generate uncorrelated Gaussian white noise which was then applied to synthetic imagery to model noise artifacts [83]. In this research we will simply create a Gaussian noise distribution with mean μ, and standard deviation σ, which will be added to the final synthetic image. We will not attempt to further investigate the individual sources for it is beyond the scope of this research. However, it should be noted that if the individual noise sources are uncorrelated, they tend to add in quadrature such that

$$N_{total} = \sqrt{N_1^{\ 2} + N_2^{\ 2}} \tag{6.24}$$

where N_1 and N_2 are the noise levels from two uncorrelated noise sources.

In general, the dominant noise sources in IICCD systems are shot noise (photon or quantum noise), and readout noise (see Figure 6-6). The former makes up about 58% of the total noise contribution while the later makes up about 40%. The remaining 2% is representative of all other types [84]. It should also be noted that at high gains the readout noise may become insignificant relative to the shot noise. Lastly, one should consider noise from such sources the MCP, phosphor screen, and ADC quantization. Though a through examination and inclusion of these sources is in order, it is beyond the scope of the this research. Instead we refer the reader to others who have done work in this area [44,84,85].

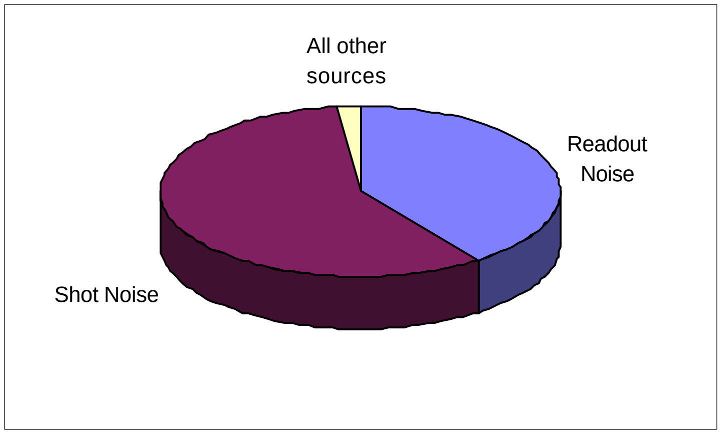

Figure 6-6 Major sources of IICCD noise [84].

6.4.1 Shot Noise

When modeling sensor systems under low light level conditions, one must take into account the arrival rate of photons. As mentioned previously, it has been shown that the IICCD is photon-noise-limited at high gains [86]. For this research we will apply the noise, in a post-processing operation, based on the number of photons for a given pixel radiance.

To see how this works, consider the radiance bar pattern in Figure 6-7a. This bar pattern contains typical radiance values found in LLL SIG imagery (see Table 6-3). For display purposes, the values are scaled up by 10^6 resulting in the those shown in Table 6-4.

Table 6-3 Radiance values found in test pattern [W/m^2 sr].

1.20×10^{-4}	1.65×10^{-4}	2.18×10^{-4}	2.55×10^{-4}
1.00×10^{-5}	2.00×10^{-5}	4.00×10^{-5}	8.10×10^{-5}

Table 6-4 Radiance values scaled up by 10^6 for display purposes.

120	165	218	255

10	20	40	81

We then convert the pixel radiance values to number of photons using the relation below. In doing the calculation, we assume a mean wavelength of 700 nm which results in an approximation due to the fact that the radiance has already been integrated over the bandpass. This is reasonable since the photocathode response of the ICCD is relatively flat from 600 to 800 nm. To perform the calculation correctly, one would have to know the *spectral* distribution of *L*.

$$N_{p\_pixel} = \frac{L\ t\ \ A_{CCD}\ \ a\Omega}{\left(\frac{hc}{l_{700}}\right) N_{pixels}} \qquad (6.25)$$

where:

L = Integrated radiance of a pixel [W/m^2 sr]
τ = Integration time (33ms).
A_{CCD} = Area of CCD
α = Fill factor
N_{pixels} = Number of CCD pixels
Ω = Solid angle [sr]. (A/r^2 = A_{CCD}/focal length^2)
h = Planck's constant (6.6 x 10^{-34} Js)
c = Speed of light (3 x 10^8 m/s)

Next we replace the calculated value for the number of photons with one drawn from a Poisson distribution with mean, N_{p_pixel}. This is done on a pixel-by-pixel basis. Finally the values are converted back to radiances. The results of this can be seen in Figure 6-7b. The "white" radiance value (255) does not provide any visual noise information because of clipping (i.e., we are display limited to 8 bits). From Figure 6-8 we can make out 8 peaks in the histogram due to the various radiance values.

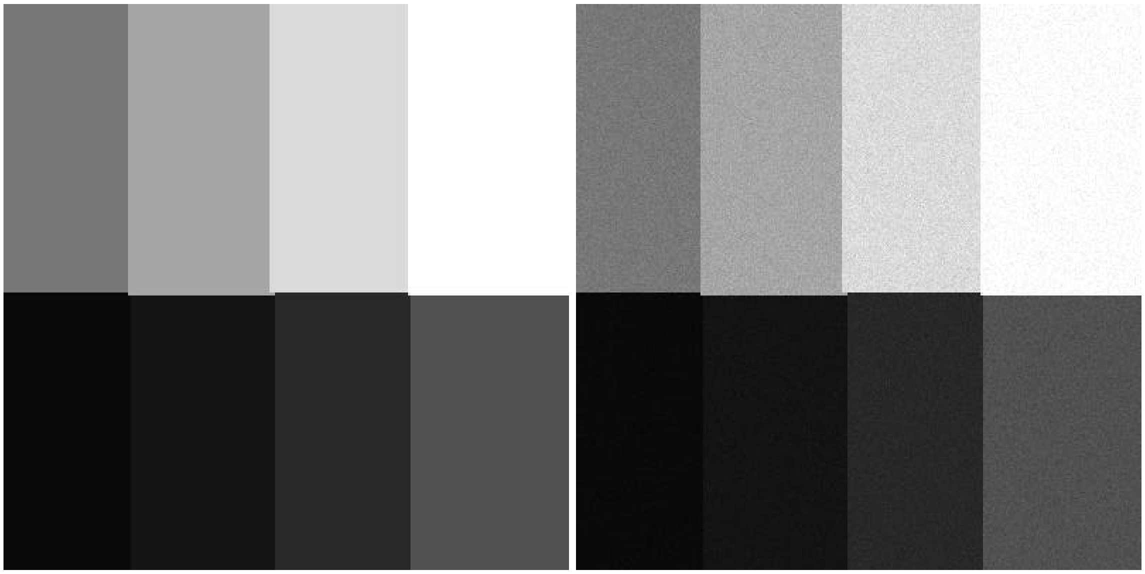

Figure 6-7 a) Bar pattern (400x400). b) Bar pattern with shot noise based number of photons. Both scaled up by factor of 10^6.

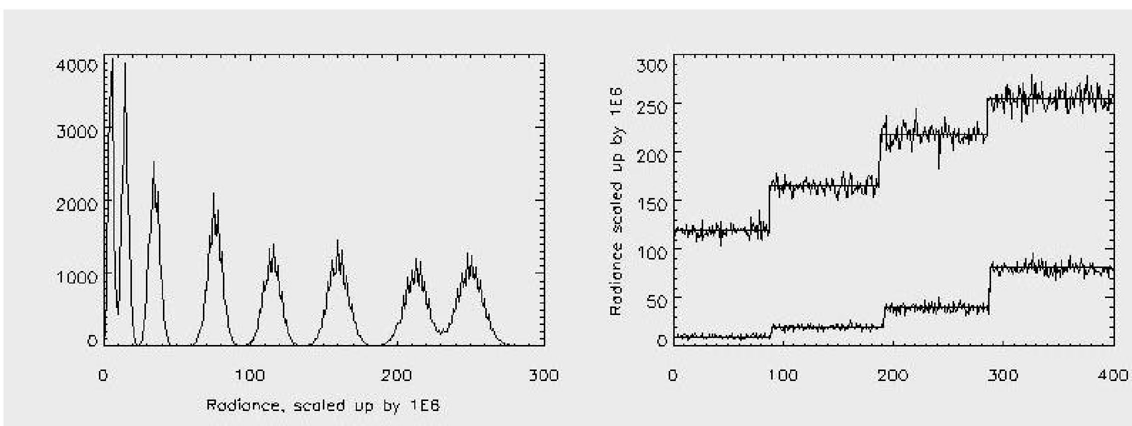

Figure 6-8 a) Histogram of bar pattern with shot noise (notice how radiance values exceed 255) and b) slices through test pattern showing mean radiance values and noise variance.

Photon-noise-limited operation implies that the SNR should be proportional to the square root of the signal (i.e., the mean and variance are equal). If we look at the statistics from the random number generator in terms of SNR we see that this is indeed the case (see Figure 6-9).

One last thing to mention about the noise modeling performed here is that the actual image radiance values span a much larger dynamic range than are shown above. This example illustrates a radiance range from 10^{-4} to 10^{-5}. The actual SIG imagery may contain values from 10^{-3} to 10^{-7}. Visually, this is difficult to analyze in a 2D format for this example because of the limiting display resolutions (*i.e.*, 8 bit color depth).

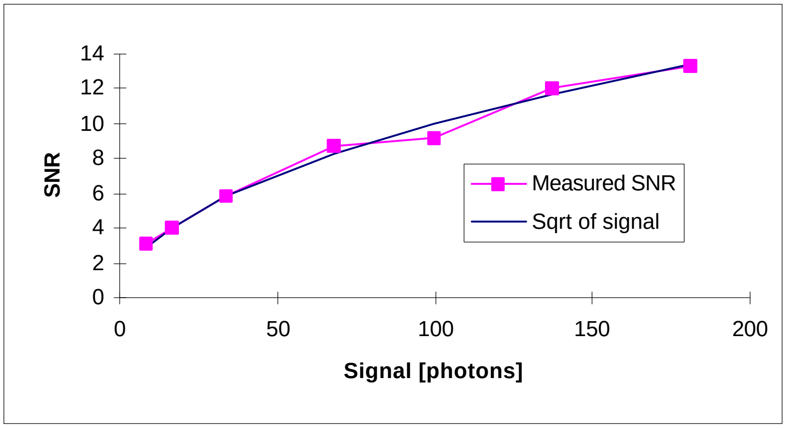

Figure 6-9 Comparison of SNR to ideal case when modeling shot noise.

6.4.2 Pre-Amplifier Noise

Some of the other noise sources that play a significant role in the image chain presented in Figure 6-1, are *photoelectron* and *preamplifier* noise. The photoelectron noise can be thought of as that originating from the photocathode. We have already presented a case for random photon arrival on one side of the photocathode. At the other, is a conversion efficiency and photocathode dark current. Back-end electronics, or pre-amplifier noise, also contribute to the overall noise figure. This may include CCD dark current and readout noise. The approach used here is to treat these noise sources as “additive” Gaussian noise with mean, μ, and standard deviation, σ.

The mean is computed based on the mean value of the image. The standard deviation is computed from a desired signal-to-noise (SNR) ratio. That is, the user defines a SNR and σ is computed as mean/SNR. Finally, the Gaussian distribution is added to the image while the mean value is subtracted back out. This leaves Gaussian (noise) variability in the image.

In summary, we take into account two major sources of system noise. Namely, shot noise and preamplifier noise. We describe the shot noise or quantum with Poisson statistics while using Gaussian statistics for the back-end electronics. The effects of these noise sources on SIG imagery is quite different, as will be demonstrated in subsequent sections.

Chapter 7

7. IICCD Characterization and Implementation

The previous chapter dealt with a detailed mathematical description of the IICCD device. In this section we attempt to characterize the camera by analyzing the modulation transfer function and by performing a laboratory calibration (digital count to radiance). We then use this data to complete the sensor model which includes generating the 2-dimentional filters necessary to account for MTF effects.

7.1 Measured MTF

The camera's MTF was determined at various locations in the IICCD "image chain". Figure 7-1 illustrates the various locations in which the MTF was either measured or referenced from manufactures specifications. Path A is in reference to the II tube only. Here, the MTF was given by the tube manufacture. Path B incorporates everything in the IICCD system including the II tube, fiber optic output, CCD, and video D/A. This path was measured electronically using an oscilloscope. Finally, path C includes everything in path B plus the 8-bit digitizer.

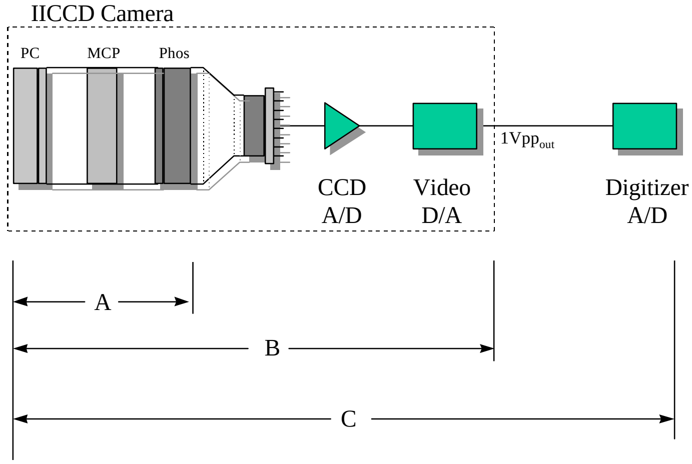

Figure 7-1 Components included in MTF measurement.

7.1.1 Lab set-up and results

The horizontal MTF was measured by imaging a target that contained both a sinusoid and gray scale pattern orientated in the x-direction (horizontal axis). The camera was then calibrated (reflectance vs. voltage or reflectance vs. DC) so as to convert the measured values back to reflectance space. Finally, the MTF was computed based on the actual and measured reflectances. Appendix H contains a detailed analysis of these measurements. The LUT generation for both the digitizer and oscilloscope setups showed that the camera behaved linearly for the given lighting conditions and reflectances presented (see Appendix H). The final MTFs for each path in the above figure can be seen in Figure 7-2.

Additional data from a more recent intensifier tube, the omnibus IV, has also been included in Figure 7-2 as a means of comparison. This tube comes from recent literature (circa, 1999) and has been characterized by the US military [87]. The camera under test for this research was manufactured in 1997. Given the laboratory set-up and equipment used, the data collected is reasonable. Also, given the fact that it is unclear how the MTFs for the omnibus tube and ITT tube were obtained, no additional conclusions can be drawn about the two.

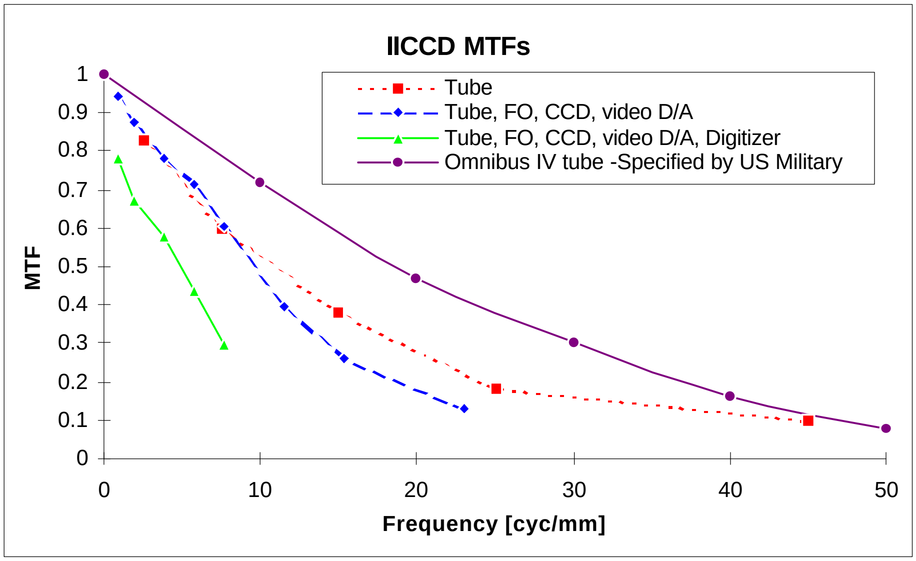

Figure 7-2 Resulting IICCD MTFs for the x-direction at the image plane.

7.2 Radiance Calibration Results

The next section deals with radiometrically calibrating the camera. Here, we wish to relate digital counts to radiance values. This was accomplished by imaging a calibrated light source located in an integrating sphere. The radiance at the cameras input aperture was then reduced by using neutral density filters. The is illustrated in Figure 7-3.

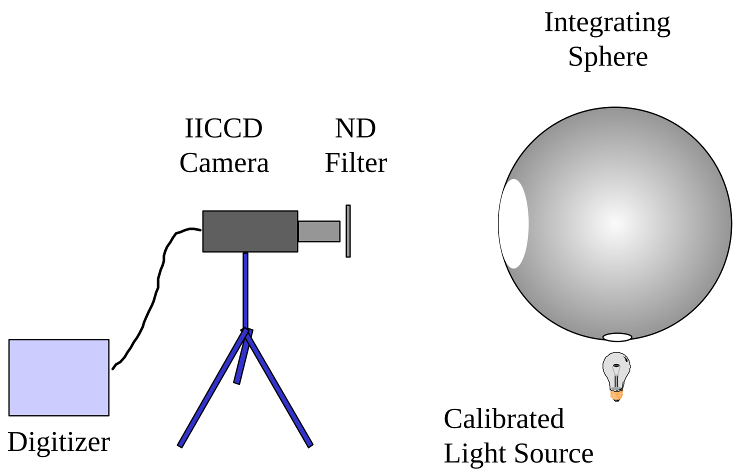

Figure 7-3 Calibration setup using integration sphere.

By knowing the calibrated spectral radiance of the bulb and the transmission of the filters, one can estimate the input radiance to the camera. This radiance was then digitized and a corresponding digital count to radiance look up table (calibration curve) was constructed. Only the results of the calibration are presented here. Complete details can be found in Appendix H.

Three camera gain settings were analyzed; 5.5 V, 6.0 V, and 6.5 V. These camera gains are representative of the settings used at the time of the collection. Implementing the above procedure, the following calibration curves were generated (see Figure 7-4 and Figure 7-5).

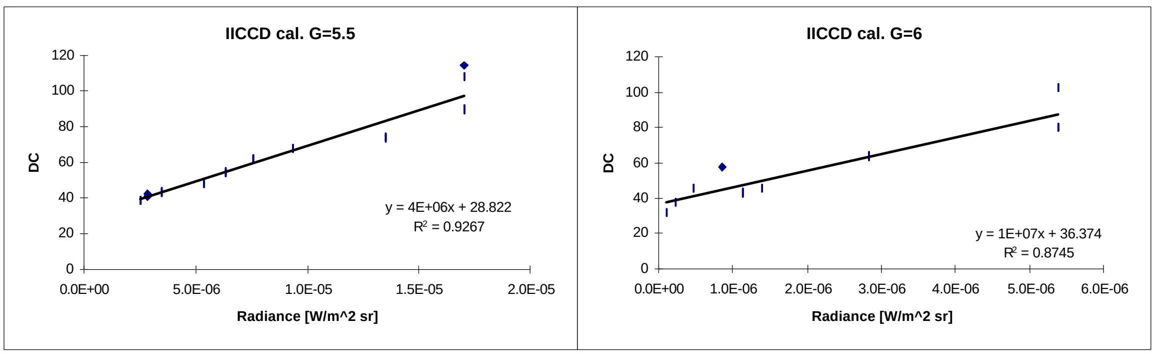

Figure 7-4 Calibration curves for a) gain = 5.5 V and b) gain = 6.0 V.

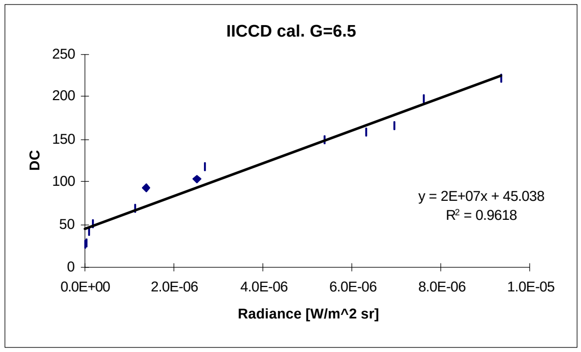

Figure 7-5 Calibration curve for gain = 6.5 V

7.3 Calibration Summary

The last two sections dealt with the characterization of the IICCD camera. The MTF of the tube, tube–video$_{D/A}$, and tube–video$_{D/A}$–digitizer were measured. The ITT tube manufacture provided MTF data without explanation of its origin. Therefore, it was difficult to quantitatively compare this result to anything else. However, relatively speaking, the trends for all the curves were as expected. That is, starting with the ITT tube alone, the measured MTFs should have shown a decreasing trend in performance. This is seen since the video D/A reduced the overall MTF but not nearly as much as the digitizer. Certainly, a better digitizer (more pixels) would have increase image quality significantly. The one used was only 640 x 480. Lastly, included with the measured data was tube data from a more recent device, for relative comparison purposes. Here the *Omnibus IV* MTF was better than the ITT tube MTF. This difference may be due to improvements in tube technology over the last 2 years.

The radiance calibration was performed in order to scale the SIG imagery to a known radiance level. This scaling factor is a function of the camera gain setting. The results of the calibration did not come out as expected. This was due, in part, to laboratory equipment available to the principle investigator. The calibrated bulb used for the collection was 10 W. This was far too bright a source to use for calibrating a device such as an image intensifier. However, it was the only source available during the calibration. Because of this, multiple neutral density filters were used to significantly reduce the light entering the camera. This reduction introduced a fair amount of error due multiple reflections between filters. With the data that was obtained, look-up tables were generated, as a function of camera gain, which related digital counts (DC) to radiance. The noise or error is evident in the data. It is believed that the approach for the calibration is correct. Furthermore, better results would have been obtained if the calibrated source was of lower power.

7.4 Implementation of the Sensor Model

The application of the sensor model is done as a post-processing operation on the radiance imagery. The model itself was written in IDL and is designed to read in a double precision radiance field image (*e.g.*, the output from the DIRSIG ray tracer) and output a copy of the input with some of the artifacts described earlier. The overall procedure is seen below.

$$g(x,y) = \mathcal{F}^{-1}\left\{\left|\mathcal{F}\left\{f(x,y) + n_p(x,y)\right\}\right| \bullet MTF_{II} \bullet MTF_{FO} \bullet MTF_{CCD} \bullet MTF_{digitizer}\right\} + n_g(x,y) \tag{7.1}$$

The first step is implementing the shot noise, $n_p(x,y)$, on the image, $f(x,y)$, (as described in section 6.4.1). We then compute the magnitude of the Fourier transform of this result so that we can multiply it by the MTF of the image intensifier, fiber optic bundle, CCD, and digitizer. Finally, additional pre-amplifier noise is added.

7.4.1 Filters in one dimension

The specification sheet for the camera's II tube (FS9910A) lists the MTF values as a function of frequency (see Table 7-1). From this data, the frequency constant, x_c, and MTF index, n, can be determined for the II analytic function. Figure 7-6 shows the best fit line to the spec sheet data and the values used to obtain such a line.

Table 7-1 MTF values for II tube.

Frequency [lp/mm]	MTF
2.5	0.83
7.5	0.60
15	0.38
25	0.18
45	0.10

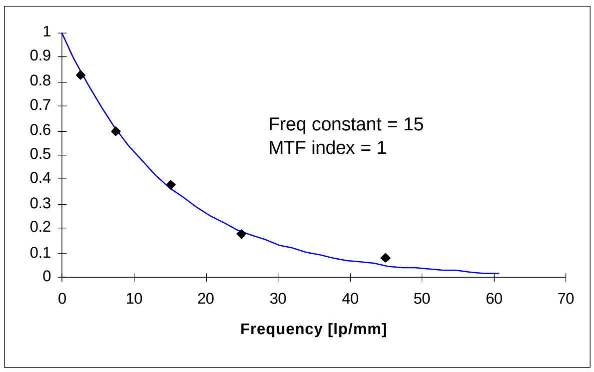

Figure 7-6 Fitting analytic II MTF function to spec sheet data.

The image is then propagated through a fiber optic bundle which is in intimate contact with a CCD. The phosphor side of the fiber optic bundle typically has a core pitch of 6 um (presumably hexagonal packed). Upon exiting the fiber optic bundle, the image falls incident onto the CCD. A typical 1D CCD MTF is usually expressed in cycles/pixel and follows that of a sinc function (section 6.3.4).

$$MTF_{CCD_x} = \left| \mathcal{F}\left\{PSF_{CCD_x}\right\}\right| = SINC(dx) = \frac{\sin(pxd)}{pxd} \qquad (7.2)$$

Here, the Nyquist frequency is half the sampling frequency, or ½ cyc/pixel. However, we need this MTF to be in the same units as the II tube MTF, lp/mm. This is accomplished by the fact that the detector width, *d*, is typically specified in millimeters or microns. If the detector width, *d*, and sampling, *Dx*, are equivalent, we have an effective fill factor of 100%. A fill factor of something less than 100% will result in a reduced modulation at each frequency by a factor of sinc(dξ). Take for example a fill factor of 80%. The sampling, *Dx*, is 22 um while the reduced detector width, *d*, is 18 um. At the Nyquist frequency, 23 cyc/mm, the reduction factor will be :

$$\mathrm{sinc}(dx) = \mathrm{sinc}\left[(0.018\ mm)(23\ \tfrac{cyc}{mm})\right] = 0.75 \tag{7.3}$$

Figure 7-7 illustrates the effect of using a fill factor of 50% in the x and y directions of the CCD. Also included in these plots is the Nyquist frequency for each dimension of the pixel, which shows up as a vertical dotted line.

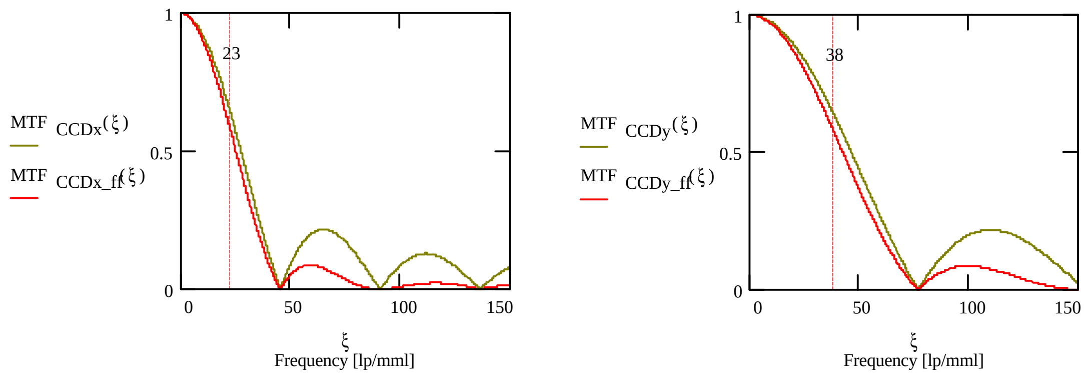

Figure 7-7 MTF for a a) 22 um pixel and b) 11 um pixel with and with out a fill factor of 50%.

Figure 7-8 shows three component MTFs for the x and y directions. The detector modeled is 22 x 13 um with a fill factor of 50%. This results in Nyquist frequencies of 23 and 38 lp/mm, respectively. The fiber optic core pitch modeled is 6 um. The actual pixel dimensions are 11 x 13 um, however, since it is an interline CCD, the effective dimensions change to 22 x 13 um. This is because one row (or column) is used for storage and transfer and does not participle in photon/electron collection.

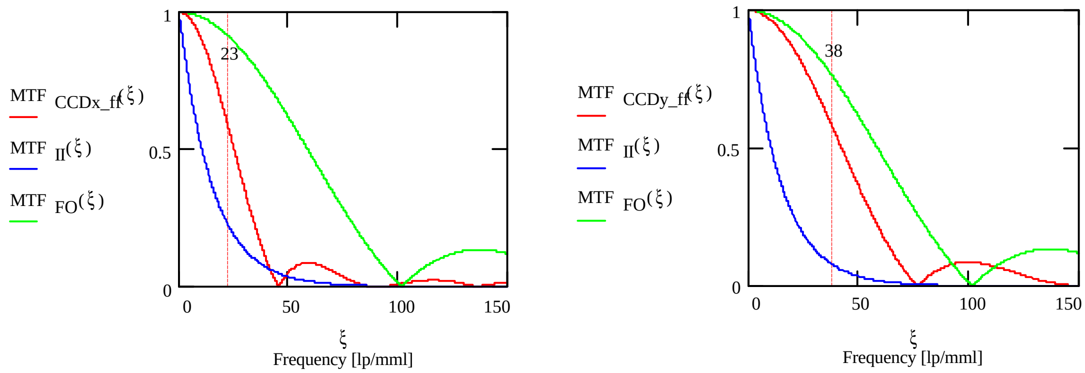

Figure 7-8 MTFs for the II tube, FO, and CCD in the a) x-direction and b) y-directions.

Finally, we sample the curves up to the Nyquist value set forth by the sampling dimension of the CCD. Since the CCD can have varying dimensions, this operation is performed in both the x and y directions. The Nyquist value that is used is that obtained from the *largest* pixel dimension. In this case, 22 um (ξ_{nyq} = 23 lp/mm). This can be seen in Figure 7-9 along with the composite MTF of the ICCD camera system. Clearly we can see that the performance (resolution) of the camera is limited by the intensifier tube.

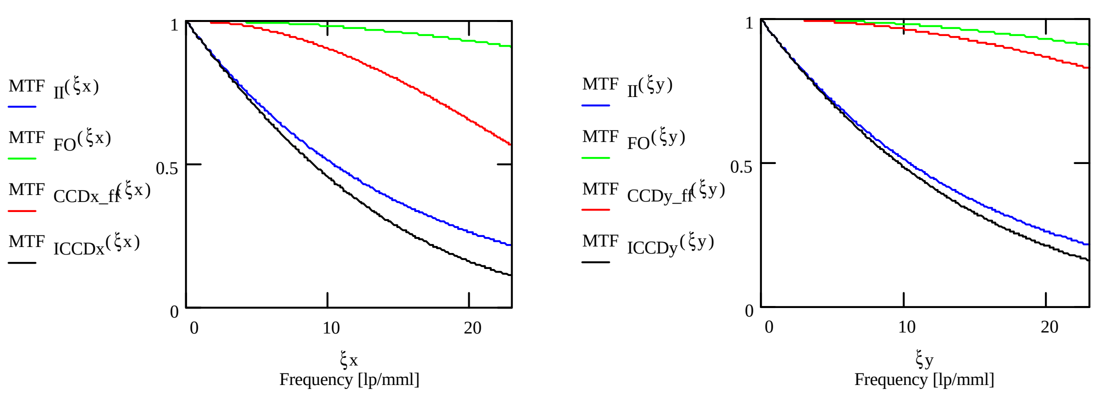

Figure 7-9 1D MTF curves in the x and y direction. Values sampled to the x-direction Nyquist frequency.

We can now compare this theoretical camera MTF (termed MTF_{ICCDx}) to that measured in the laboratory (MTF_elec) for the x-direction. This can be seen in Figure 7-10 along with the II tube MTF (termed MTF_{II}). We can see that by using the values presented above, the theoretical model correlates very well with that which was measured in the laboratory.

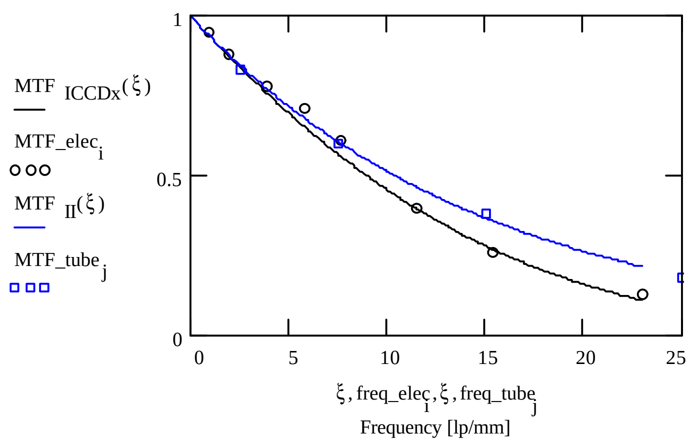

Figure 7-10 Comparison of theoretical camera MTF to measured MTF in the x-direction. MTF_elec and MTF_tube are measured values. MTF_{ICCDx} and MTF_{II} represent the theoretical models.

7.4.2 Filters in Two-Dimensions

The two-dimensional ICCD MTFs are constructed from the 1-D functions presented earlier. It is noticed that the image, f(x,y), is real and even therefore the MTF (through the Fourier transform) will also be real and even. In order to multiply the filter by the image spectrum on a point-by-point basis, the filter must be the same size as the image (*i.e.*, same dimensions/number of pixels). This is done by appropriately sampling the 1D MTF function to the Nyquist value. Since we are computing a DFT on a digital image (band limited with no aliasing), the Nyquist location will always be at the edge of the image in x and y. This illustrated in Figure 7-11.

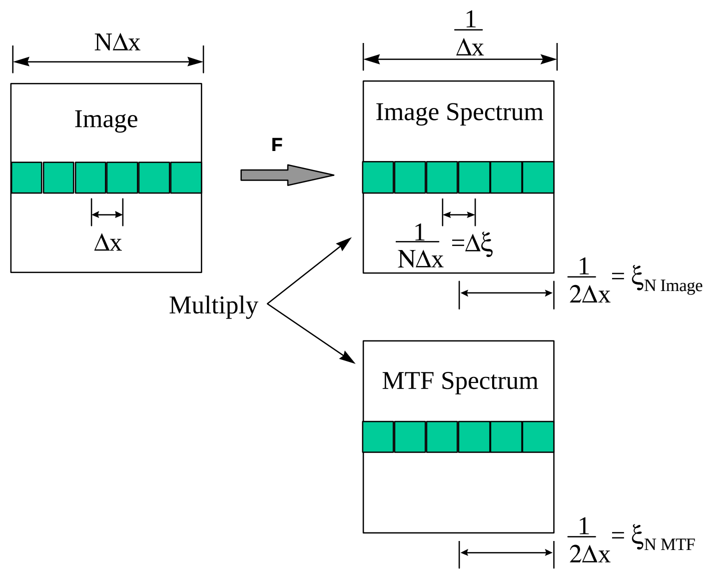

Figure 7-11 Location of Nyquist when computing image DFT.

Once the 1D MTF function is appropriately sampled to the Nyquist, we then convert the function to polar coordinates and rotate it around the z-axis. The result is a *dynamically* sampled MTF that varies with detector width, d, fiber optic core pitch, P, number of samples, N, frequency constant, x_c, and MTF index, n. This result can be seen for the image intensifier tube in Figure 7-12 and for the fiber optic bundle in Figure 7-13.

$$Rscale = \frac{N/2}{x_{NMTF}} \tag{7.4}$$

$$MTF_{II}(r) = e^{-\left(\frac{r/Rscale}{x_c}\right)^n} \tag{7.5}$$

$$r = \sqrt{\left(x - \tfrac{N}{2}\right)^2 + \left(h - \tfrac{N}{2}\right)^2} \tag{7.6}$$

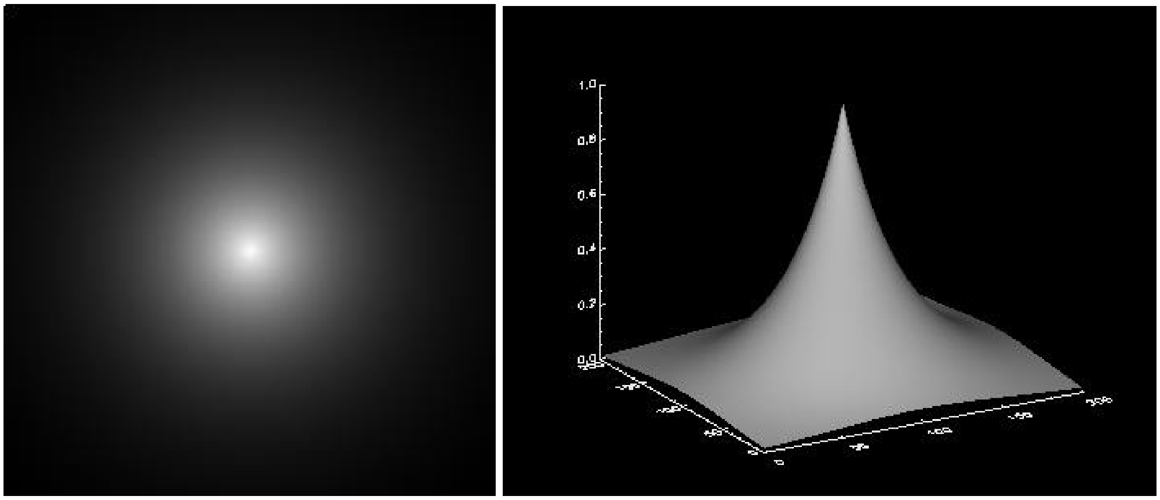

Figure 7-12 a) 2D and b) 3D image tube MTF for ξ_c=15 and n=1. Values sampled to Nyquist.

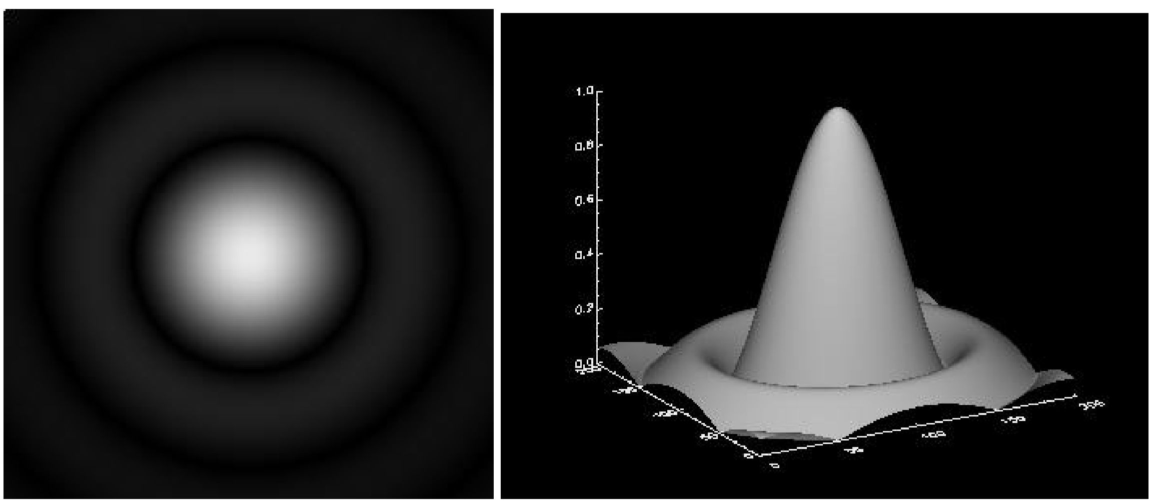

Figure 7-13 a) 2D and b) 3D fiber optic bundle MTF (*not* sampled to Nyquist).

The 2D CCD MTF is treated the same as above except for the fact that it is *not* circularly symmetric and thus is not rotated around the z-axis. Here we compute the sinc function separately in x and y as a function of detector size, *d*, and multiply the result. This result can be seen in Figure 7-14 for an 20um by 28um pixel.

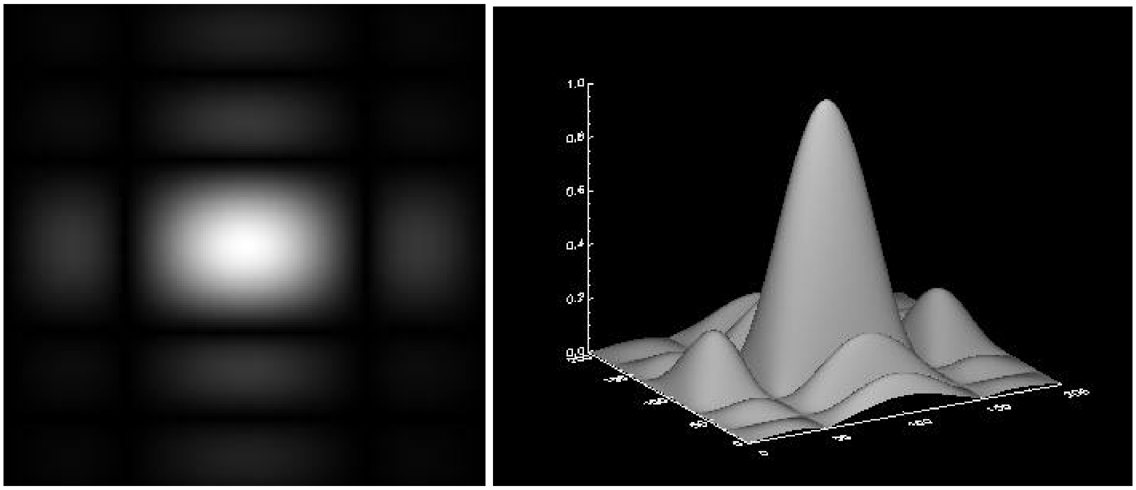

Figure 7-14 a) 2D and b) 3D CCD MTF for a 20 x 28 um pixel (*not* scaled to Nyquist).

Finally, we compute the composite 2D MTF filter which is generated by multiplying the MTFs of the II, FO, and CCD (as seen in Figure 7-15). These individual MTFs are sampled to the Nyquist value, as mentioned previously. The resultant MTF filter is seen in Figure 7-16. Here the effect of the CCDs rectangular shape is seen. The effect is greater attenuation of frequencies along the x axis.

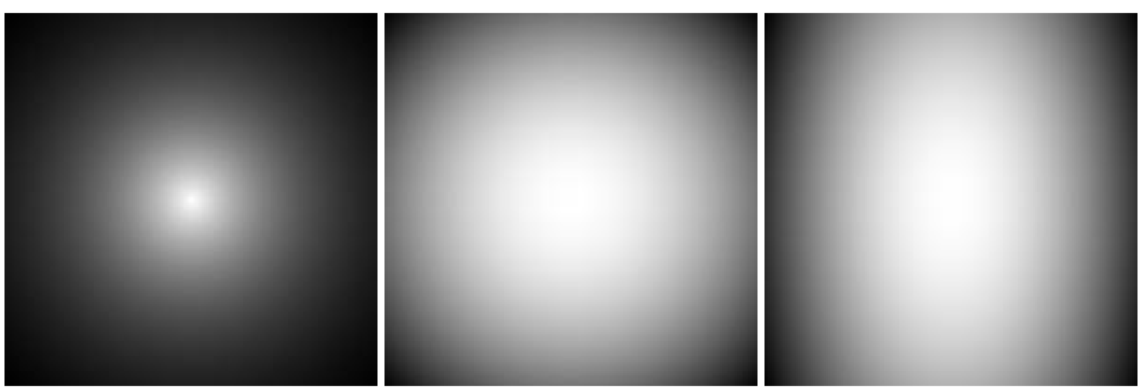

Figure 7-15 Nyquist sampled MTFs for the a) intensifier tube (II), b) fiber optic bundle (FO) and c) CCD.

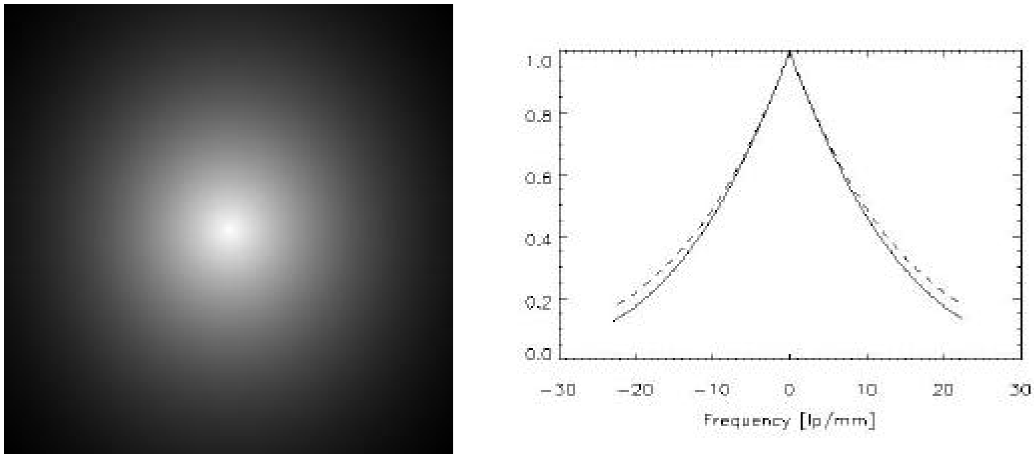

Figure 7-16 Composite Nyquist scaled MTF for ICCD camera (excluding digitizer) and slices along x (solid) and y (dashed) directions.

7.5 Digitizer

The output from the ICCD camera is a standard 1 Vpp video signal. In order to visually assess the data, we sample it with a digitizer and view it on a CRT. It was determined that the digitizers resolution was insufficient for this work. The resolution that was used was around 570 x 480 which degraded the system performance significantly. The overall effect was a significant reduction in the system MTF, as was seen in Figure 7-2. Since this effect is an external one, which can be controlled, the effective system MTF could be increased significantly by means of increased resolution (*i.e.*, more pixels).

We can now compare the measured system MTF (which includes the digitizer MTF) to the theoretical model in the x-direction. This result is seen in Figure 7-17. For reference, the electronic measured (MTF_elec) and theoretical (MTF_{ICCDx}) MTFs have also been included.

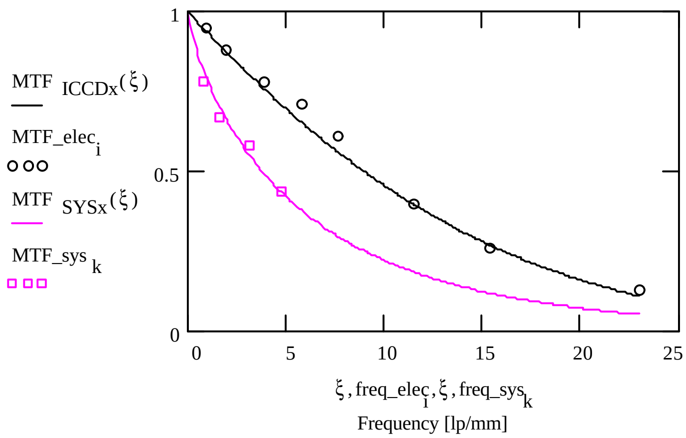

Figure 7-17 MTFs for ICCD camera and entire system which includes the effects from the digitizer.

It is noticed that the data points that are representative of the digitizer can be approximated by a simple analytic function, hence the line-fit in Figure 7-17. This is an important observation for it saves us from computing the filters for the II tube, FO, and CCD separately. Because the II tube plays such a dominant role in the camera MTF, the composite camera MTF will resemble that of the tube. In the end, this will reduce computation time significantly. Therefore, we simply approximate the entire system MTF (which included the digitizer) with an analytic function of the form

$$MTF_{II} = e^{-\left(\frac{x}{6}\right)^{0.8}} \tag{7.7}$$

This is the line-fit that was seen in Figure 7-17. The result for the 2-D case can be seen in Figure 7-18. The approximation assumes that the effects of the digitizer are the same in both the horizontal and vertical directions. Furthermore, we note that ICCD camera MTF does not vary much in the horizontal and vertical directions so we assume that this effect is negligible. This phenomenon is due to the limiting resolution of the intensifier.

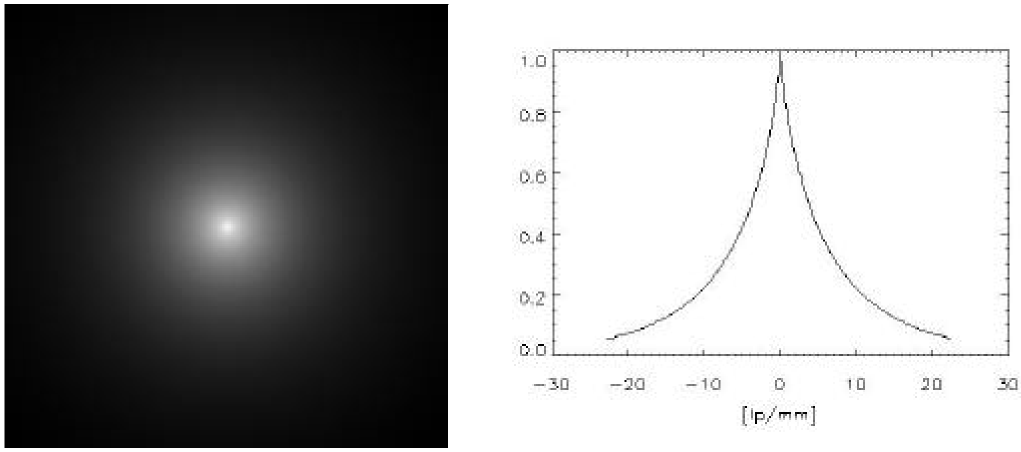

Figure 7-18 Approximation to final system MTF in two dimensions.

Chapter 8

8. Radiance Predictions

In the previous chapters we made an attempt to account for all the possible sources of illumination while predicting how the camera system might behave in the presence of such sources. Before we implement the camera model on the synthetic imagery, we should compute what DIRSIG sees on the ground and compare it to off-line calculations. That is, we will be comparing theory to theory and verifying that DIRSIG does its radiance calculations correctly. If the difference is negligible, we can perform the post-processing with confidence that the radiometry for the background and secondary sources is correct.

8.1 Illumination from a Secondary Source

In this section we determine whether the secondary source model in DIRSIG is giving accurate results. This can be accomplished be comparing its output to truth data. However, since there was no instrument available to measure radiance on the ground at the time of the collection, we have to predict the truth values based on laboratory measurements of a tungsten bulb. This is a valid approach since we can exploit standard radiometric techniques (*e.g.*, inverse square law). Furthermore, the calculation is made simpler because of the fact that we used a 40 W tungsten bulb with a known spectral distribution at a fixed distance. Finally, if the math holds true, we should be able to compare the values calculated to DIRSIGs output. The heart of these predictions is based on the fabricated street lamp modeled in the SIG scene. The question posed is, “what was the radiance on the ground, 14 feet below the source, at the time of the acquisition?” Furthermore, we want to know if DIRSIG is predicting this value.

8.1.1 “Pick a Target in SIG Image and Compare Radiance Values”

The details of the calculations involving the inverse square law, bulb efficiency, modeling of the PR-650 spectrometer, sensor response and bandpass, and spectral intensity for the lamp with no aperture in front of it can be found in Appendix I. Furthermore, the answers obtained in Appendix I are derived from a perfect reflector directly below the source. However, we do not have such an object in the scene. What we do have is grass directly below the source and a white target just off axis, both with known reflectivitys. We will now compute the expected radiance along a path starting from the base of the source and moving outward to the edge of the target (see Figure 8-1). We will compute 5 evenly spaced values along this path.

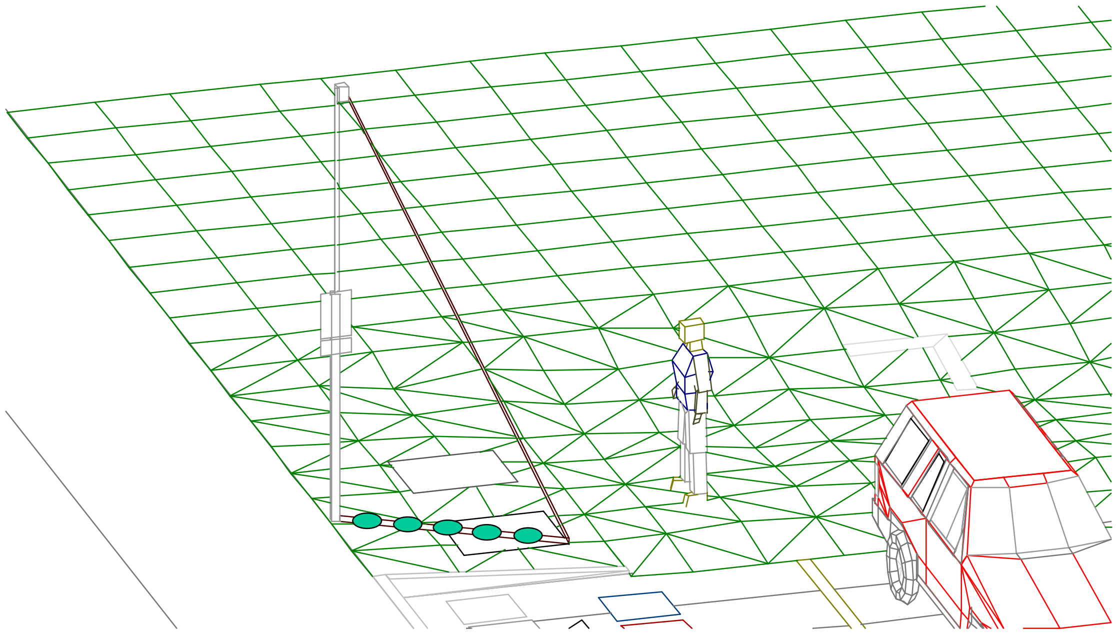

Figure 8-1 Illustration of radiance falloff as we move away from the base of the source. The triangle shape is formed from light to white target, then from white target-to-base of light. The falloff calculated is along the bottom leg of the triangle, with 3 values on the panel and 2 on the grass.

The geometry for the radiometric calculations can be seen in Figure 8-2. The calculation is based on projected area effects. It is first seen that the irradiance from the direct incident ray, E_o, is

$$E_o = \frac{I}{r^2} \qquad \left[\frac{W}{m^2}\right] \tag{8.1}$$

We then compute the irradiance onto a normal surface that is rotated through an angle *q*, as illustrated in Figure 8-2.

$$E_q = E_o \cos q \qquad \left[\frac{W}{m^2}\right] \tag{8.2}$$

Finally, we convert to radiance and factor in the target reflectance, *R*.

$$L_q = \frac{E_q}{p} R \quad = \frac{E_o \cos q}{p} R \quad = \frac{I \cos q}{p\ r^2} R \qquad \left[\frac{W}{m^2 sr}\right] \tag{8.3}$$

Five values of radiance are computed along the *x* leg of the triangle in Figure 8-2. To estimate the value of *q*, the length of each leg in the triangle was measured in AutoCAD. The MathCAD equations below show the implementation of the radiance equation.

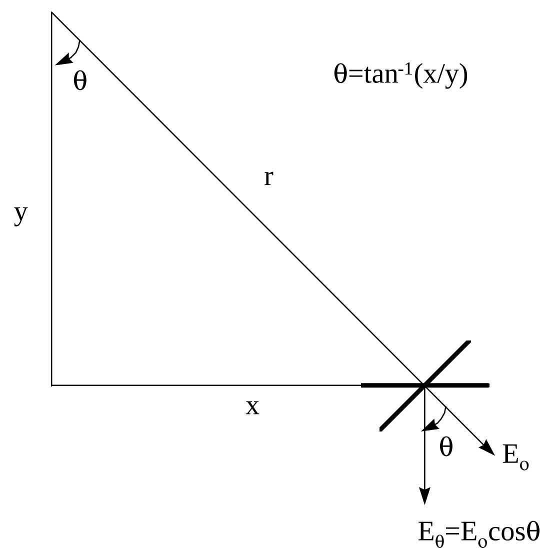

Figure 8-2 Geometric description of projected area effects (cos*q*).

The lengths of each leg in the triangle are shown below along with material reflectances that were used in DIRSIG. The grass reflectance used was 0.35 while the white board was 0.80.

$$r\_vector_j := \begin{array}{|r|}\hline 165.0\,in \\ \hline 167.125\,in \\ \hline 170.75\,in \\ \hline 179.125\,in \\ \hline 188.875\,in \\ \hline \end{array} \quad x\_vector_j := \begin{array}{|r|}\hline 0\cdot in \\ \hline 18.625\,in \\ \hline 39.75\,in \\ \hline 67.125\,in \\ \hline 85.95\,in \\ \hline \end{array} \quad y\_vector_j := \begin{array}{|l|}\hline 165\cdot in \\ \hline 165\cdot in \\ \hline 165\cdot in \\ \hline 165\cdot in \\ \hline 165\cdot in \\ \hline \end{array} \quad R_j := \begin{array}{|l|}\hline 0.35 \\ \hline 0.35 \\ \hline 0.80 \\ \hline 0.80 \\ \hline 0.80 \\ \hline \end{array} \quad angle\_rad_j := \operatorname{atan}\left(\frac{x\_vector_j}{y\_vector_j}\right)$$

The radiance, *Lq1*$_j$, is computed below using mathCAD. The intensity value, *I_bandpass*, comes from the calculation in Appendix I over the bandpass of the ICCD device.

$$L\theta 1_j := \frac{I\_bandpass \cdot \cos\left(angle\_rad_j\right)}{\pi \cdot \left(r\_vector_j\right)^2} \cdot R_j \tag{8.4}$$

We have just predicted the radiance on the ground, including projected area effects, for a point source 13 ft. from the ground as seen by the low-light-level sensor. We can now generate a SIG image and directly read off the radiance pixel values to see if they match what was predicted.

Figure 8-3 shows an unprocessed (*i.e.*, no sensor effects) nighttime SIG image with the only source of illumination being the street lamp. Furthermore, there is no aperture at the bottom of the source, only the housing in which it is encased limits the FOV. We can now select pixels in the image that correspond to the “path” of predicted radiance values and do a direct comparison. Figure 8-4 shows a small segment of radiance pixels just below the source. The bottom left is the shadow from the pole while the gray values are reflectance values from the grass. The white areas are the radiance values from the target, as can be clearly seen in Figure 8-5. The black areas between the grass and white board are shadows.

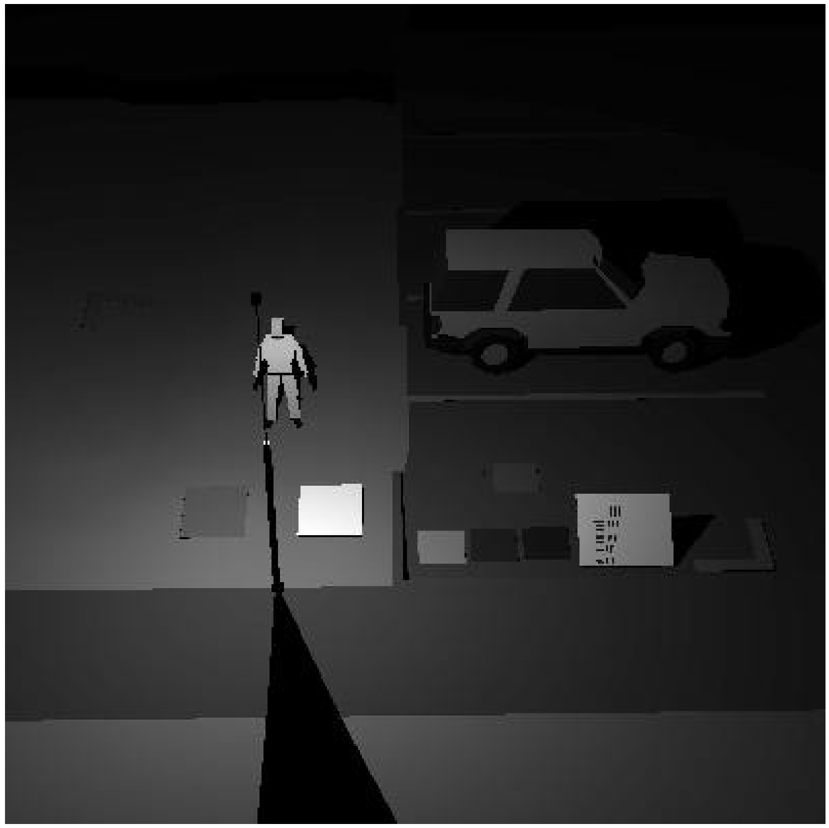

Figure 8-3 Unprocessed SIG image with no moonlight, starlight or limiting aperture.

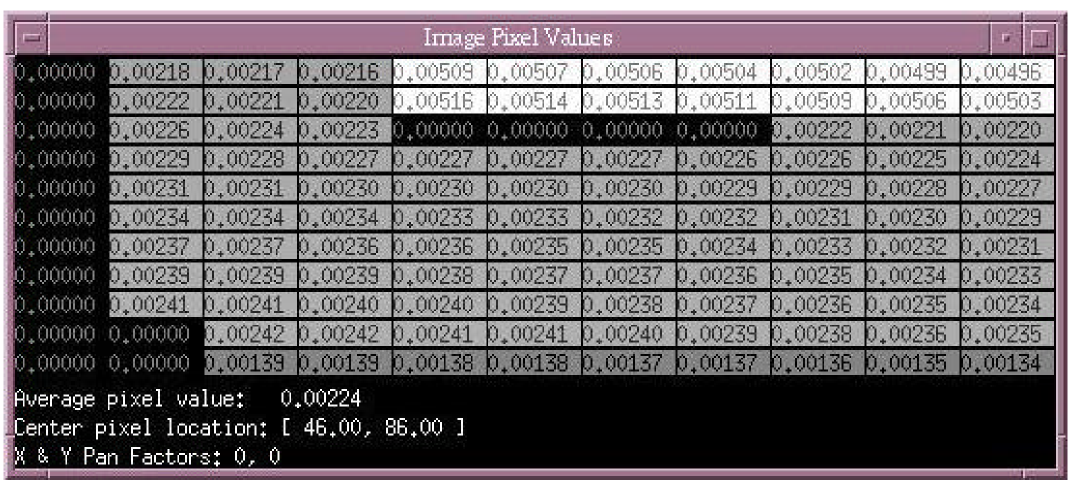

Image Pixel Values

0.00000	0.00218	0.00217	0.00216	0.00509	0.00507	0.00506	0.00504	0.00502	0.00499	0.00496
0.00000	0.00222	0.00221	0.00220	0.00516	0.00514	0.00513	0.00511	0.00509	0.00506	0.00503
0.00000	0.00226	0.00224	0.00223	0.00000	0.00000	0.00000	0.00000	0.00222	0.00221	0.00220
0.00000	0.00229	0.00228	0.00227	0.00227	0.00227	0.00227	0.00226	0.00226	0.00225	0.00224
0.00000	0.00231	0.00231	0.00230	0.00230	0.00230	0.00230	0.00229	0.00229	0.00228	0.00227
0.00000	0.00234	0.00234	0.00234	0.00233	0.00233	0.00232	0.00232	0.00231	0.00230	0.00229
0.00000	0.00237	0.00237	0.00236	0.00236	0.00235	0.00235	0.00234	0.00233	0.00232	0.00231
0.00000	0.00239	0.00239	0.00239	0.00238	0.00237	0.00237	0.00236	0.00235	0.00234	0.00233
0.00000	0.00241	0.00241	0.00240	0.00240	0.00239	0.00238	0.00237	0.00236	0.00235	0.00234
0.00000	0.00000	0.00242	0.00242	0.00241	0.00241	0.00240	0.00239	0.00238	0.00236	0.00235
0.00000	0.00000	0.00139	0.00139	0.00138	0.00138	0.00137	0.00137	0.00136	0.00135	0.00134

Average pixel value: 0.00224
Center pixel location: [46.00, 86.00]
X & Y Pan Factors: 0, 0

Figure 8-4 SIG radiance values [W/m^2 sr] just under the light source (grass values).

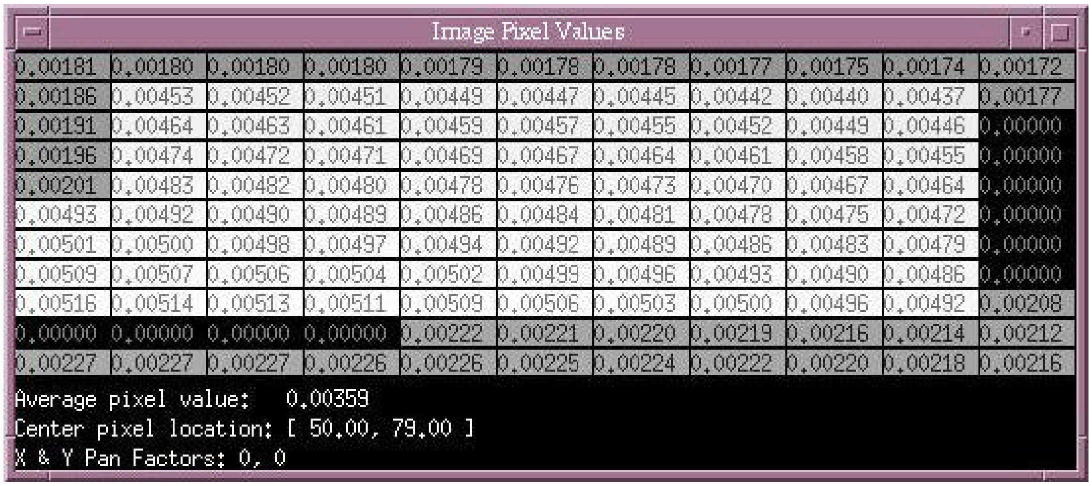

0.00181	0.00180	0.00180	0.00180	0.00179	0.00178	0.00178	0.00177	0.00175	0.00174	0.00172
0.00186	0.00453	0.00452	0.00451	0.00449	0.00447	0.00445	0.00442	0.00440	0.00437	0.00177
0.00191	0.00464	0.00463	0.00461	0.00459	0.00457	0.00455	0.00452	0.00449	0.00446	0.00000
0.00196	0.00474	0.00472	0.00471	0.00469	0.00467	0.00464	0.00461	0.00458	0.00455	0.00000
0.00201	0.00483	0.00482	0.00480	0.00478	0.00476	0.00473	0.00470	0.00467	0.00464	0.00000
0.00493	0.00492	0.00490	0.00489	0.00486	0.00484	0.00481	0.00478	0.00475	0.00472	0.00000
0.00501	0.00500	0.00498	0.00497	0.00494	0.00492	0.00489	0.00486	0.00483	0.00479	0.00000
0.00509	0.00507	0.00506	0.00504	0.00502	0.00499	0.00496	0.00493	0.00490	0.00486	0.00000
0.00516	0.00514	0.00513	0.00511	0.00509	0.00506	0.00503	0.00500	0.00496	0.00492	0.00208
0.00000	0.00000	0.00000	0.00000	0.00222	0.00221	0.00220	0.00219	0.00216	0.00214	0.00212
0.00227	0.00227	0.00227	0.00226	0.00226	0.00225	0.00224	0.00222	0.00220	0.00218	0.00216

Average pixel value: 0.00359
Center pixel location: [50.00, 79.00]
X & Y Pan Factors: 0, 0

Figure 8-5 SIG radiance values [W/m^2 sr] on the white target.

We can visualize the predicted and DIRSIG computed values by creating a plot. This is seen in Figure 8-6. It is noticed that the differences between the two are quite small. However, this was not the case when the analysis first began. It was determined that a cosine term was missing in the source code. The analysis performed here proved to be extremely useful in catching potential errors. Table 8-1 summarizes the differences between the predicted and DIRSIG computed values. The errors are mainly due to the selection of image pixel values in Figure 8-4 and Figure 8-5. Inherent in these values is round-off error.

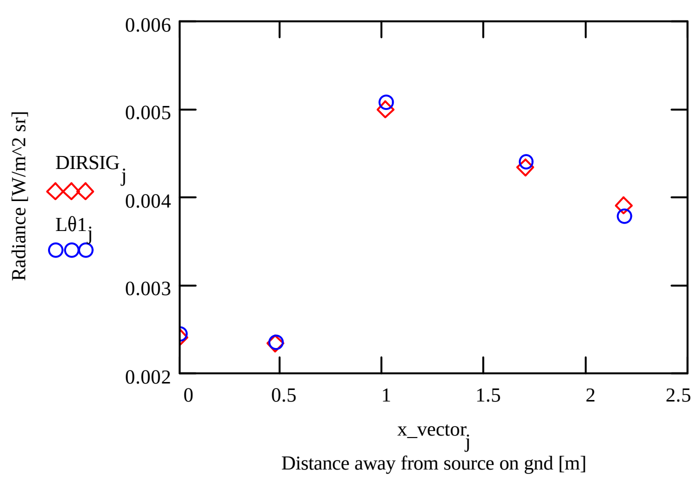

Figure 8-6 Plot showing predicted versus DIRISG computed falloff values.

Table 8-1 Comparison of predicted and DIRSIG computed radiance values.

Location	Calculated radiance [W/m^2 sr]	SIG measured radiance [W/m^2 sr]	Percent Difference [W/m^2 sr]
grass	0.002451	0.00242	1.3
grass	0.002374	0.00236	1.3
panel	0.005087	0.00514	1.8
panel	0.004404	0.00469	1.4
panel	0.003793	0.00442	3.3

8.1.2 Limiting Apertures

We still need to place an aperture in front of the source, as was the case in the real scene. DIRSIG will interpret this aperture as merely limiting the source's field of view and will fail to reduce the irradiance accordingly. This is due to the fact that DIRSIG is a ray tracer and only models *point sources*. Furthermore, it does not know how to handle real or extended sources. However, we can model the output from a extended source by using a collection of point sources. This topic is addressed later. The spectral intensity distribution comes from the Planck equation with color temperature, T. Using this distribution will be incorrect, for the intensity will be too high, compared to truth imagery. The solution is to scale down the intensity.

We can explore the effects of an aperture by measuring the behavior of a real extended source in the laboratory. Appendix I contains a detailed analysis in which the extended source used in this research was modeled as a function of aperture diameter. The results showed that the aperture size used at the time of the collection reduced the irradiance onto a fixed halon disk by a factor of 14.

8.2 Sources of Lunar Illumination

The main sources of nighttime irradiance onto a target can be broken up into four categories; 1) the direct lunar term; 2) the downwelled term; 3) a spectral starlight term and; 4) an airglow term. The latter refers to emissions from various atoms and molecules in the atmosphere.

$$E_{total\,l} = E_{L\,l} + E_{d\,l} + E_{star\,l} + E_{airglow\,l} \tag{8.5}$$

For the present analysis, we will group the starlight and airglow terms as one irradiance factor called E_{sky}. We can examine these three terms to see their effects. First, the lunar irradiance, E_L, onto a target at angle s is

$$_{L\,l} = E_L \ t_{1\,l} \cos s\,'$$

where $E_{L\,l}$

t_1 is the atmospheric transmission along the moon-target path. In addition to the direct lunar irradiance term, there are also lunar photons incident on the target due to scattering from the

derivation that considers scattering from a small volume in the atmosphere [46

total downwelled spectral radiance reaching the target from the s f direction (hemisphere location)

r from zero to the top of the atmosphere according to

$$L_{d\,l}(s \ \ f) = E'_{L\,l} \int_r t_L \ \ t_L \ _l \, b_{sca}(l \ \ q_v)$$

$$E_{dl} = \int \;_{d}\,(s\;\; f)\cos s\;\, d$$

$$E \;\; = \int_{f=}^{2} \;\;^{\frac{p}{2}}_{s=0}\; E'_{\;l} \int_{0} t \;\;_{1l}\, t \quad b \quad (l\;\; q\;)\cos(s \quad \sin(s\,) \quad ds\;\, df$$

For this analysis, we have ignored the effects due to adjacent objects (shape factor) and assume that the target is exposed to the sky dome.

The last term to consider is the spectral starlight irradiance and airglow, which we have

E_{sky}

the night sky with no moon. The remaining portion comes from the atmospheric airglow. This data is usually found in literature as a spectral curve encompassing both starlight and airglow [ ].

To date, DIRSIG computes the solar scattering term but the lunar scattering term as defined above as $_{dl}$

generate all the atmospheric radiances. Prior to simulation, DIRSIG builds up the atmospheric radiance database based on sensor location, FOV, cloud type, time of day, etc. This is

dynamically creates an input file to

card . That is, it creates 84 carddecks containing different parameters which are a function of sensor location, FOV, etc. This card deck specifies the various conditions,

compute the direct terms, downwelled terms, upwelled terms, etc. When MODTRAN computes these parameters for the sun, the card decks are fairly easy to create. The required angle

by an ephemeris utility. However, the input parameters to build the card deck for the moon are quite different. Specifically, the required geometric parameters to compute downwelled radiance.

Therefore, the data presented in this research does not contain the *lunar scattering*

expected that later releases of DIRSIG will implement this lunar scattering term. Additional discussion on this matter can be found in the recommendations section of this thesis. Independent lunar scattering, the results from a separate MODTRAN run can be seen in Figure 8-7. The card deck used is outlined in Appendix K.

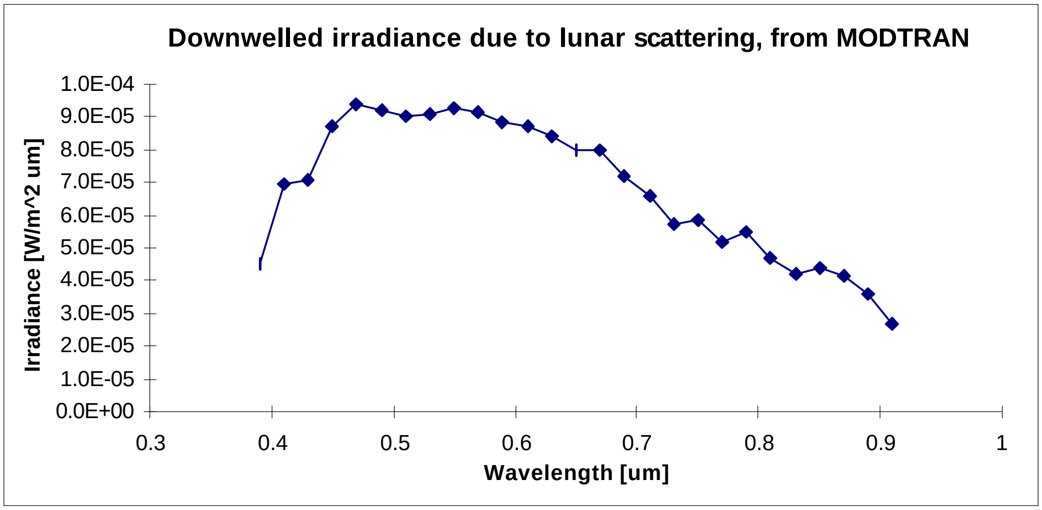

Figure 8-7 Downwelled lunar scattering from MODTRAN.

Though MODTRAN computes scattering, it does not compute starlight radiance. To this end, a spectral sky distribution was implemented which contained starlight and the natural airglow of the atmosphere (see Figure 5-14) with no moon present. When the moon is present, the overall downwelled radiance values in DIRSIG will be too low. This is due to the lack of lunar scattering.

8.3 Analysis of Illumination from Lunar Sources

In the next section we analysis the output of the make_adb utility. This program computes the direct lunar transmission and irradiance (source-to-target path), the sensor transmission and irradiance (target-to-sensor), and integrated hemispherical downwelled radiance. The *integrated* downwelled radiance comes from 84 samples of the sky dome. These samples are computed as separate MODTRAN runs with varying azimuth and zenith. These paths are illustrated in Figure 8-8.

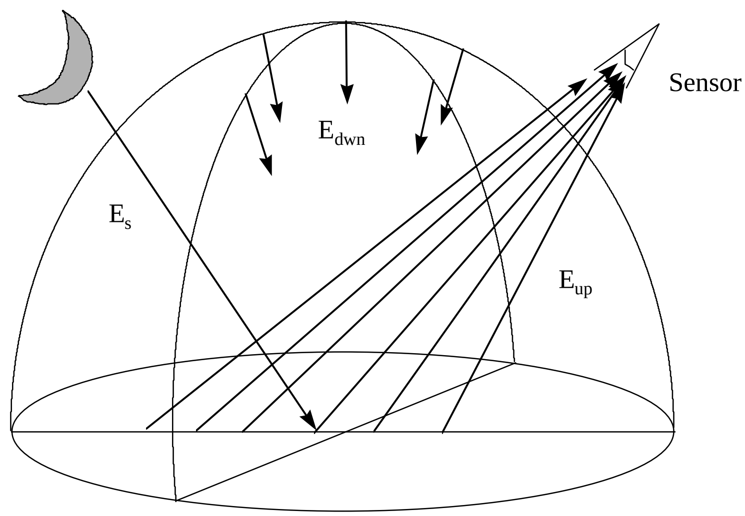

Figure 8-8 Irradiance paths computed by the make_adb utility.

Of interest are the sources of illumination *incident* on the target. That is, the direct solar/lunar and downwelled radiances. For this analysis we will omit the upwelled radiance reaching the sensor.

Once the make_adb utility is run, the output data was compared to that found in published literature. Specifically, the comparison consists of converting the sun, moon, and downwelled spectral irradiance values for a given time of day to illuminance. The only drawback to this approach is that the spectral information lost. We then compare these *illuminance* values to published literature (see Table 5-4 and Table 5-5).

The conversion to illuminance consists of first adding the direct and downwelled terms and then weighting the result by the normalized human visual response curve.

$$\text{Total Illuminance} = \int_{l_{\min}}^{l_{\max}} \left\{ E(l)_{direct}\, t_1(l) + E(l)_{down} \right\} V(l)\, dl \;\; 683 \left[\frac{lm}{W} \right] \quad [\text{lux}] \tag{8.10}$$

where:

$E(l)_{direct}$ = exoatmospheric solar/lunar direct irradiance [W/m^2 sr um]
$t_1(l)$ = atmospheric transmission from source to ground

$E(l)_{down}$ = downwelled sky irradiance [W/m^2 sr um]
$V(l)$ = normalized human visual response

Right away we notice that the downwelled term will *only* contain the skylight distribution (*i.e.*, starlight and airglow). This is because the lunar downwelled scattering is not computed due to reasons stated earlier. The results of the conversion for various times of day can be seen in Table 8-2.

Table 8-2 Tabulated values for sun and moon illuminance. Values are generated with clear sky conditions and good visibility. Output is from DIRSIGs "make_adb" program which builds the hemispherical radiance terms prior to running the ray tracer.

Time	Sun Elev [deg]	Moon Elev [deg]	Phase moon [%]	Sun direct w/trans [lux]	Moon direct w/trans [lux]	Downwelled [lux]	Total Illuminance [lux]
9/6/98 8:00 AM	14	-15		21,866	0	6,297	28,163
9/6/98 10:00 AM	35	-35		61,578	0	15,555	77,133
9/6/98 12:00 PM	50	-50		74,947	0	19,958	94,905
9/6/98 2:00 PM	51	-53		75,708	0	18,383	94,091
9/6/98 4:00 PM	37	-41		64,579	0	21,685	86,263
9/6/98 6:00 PM	17	-22		29,943	0	7,737	37,680
9/6/98 7:00 PM	6	-11		2,540	0	2,562	5,102
9/6/98 7:30 PM	0.4	-6		0	0	507	507
9/6/98 8:00 PM	-5	-1		0	0	17.7	18
9/6/98 9:00 PM	-15	10	96	0	0.0223	0.0012	0.0235
9/6/98 10:00 PM	-25	20	95	0	0.0696	0.0012	0.0707
9/7/98 12:00 AM	-38	36	95	0	0.1129	0.0012	0.1140
9/7/29 2:00 AM	-39	42	94	0	0.1200	0.0012	0.1212
9/7/98 4:00 AM	-27	35	93	0	0.1047	0.0012	0.1059
9/7/98 6:00 AM	-8	18	93	0	0.0555	0.61	0.6628
9/7/98 6:30 AM	-3	13	93	0	0.0346	144	144
9/7/98 7:00 AM	3	8	92	59	0.0124	1,048	1,107
9/7/98 8:00 AM	14	-2		21,339	0	6,195	27,534
9/7/98 9:00 AM	24	-12		46,188	0	10,542	56,731
New moon 9/22/98 1:00 AM	-46	-47	9	0	0	0.0012	0.0012

When comparing these results to those found in Table 5-4 and Table 5-5, we see that the values correlate reasonably well for the various times of day. We first notice that as the sun rises, the total illuminance ranges from 24,000 to 94,000 lux, with the latter occurring at high noon. Here there is a significant amount of downwelled radiance from the sky dome. Even after the sun sets, there is still some downwelled radiance from the sky. The total illuminance here is between 18 and

507 lux. When the sun finally dips below the horizon, the moon turns into the dominant source. The example provided shows the direct lunar term for a 96% moon (i.e., almost full). These full moon values range from 0.020 to 0.120 lux. However, these values should be slightly larger due to the fact that there is no lunar scattering included in the downwelled term.

If we integrate the MODTRAN downwelled irradiance curve from Figure 8-7 and convert it to an illuminance, we get 0.0066 lux. However, it should be noted that this value is only based on one lunar scenario (*i.e.*, time of night). The lunar MODTRAN run that was used was for half-moon conditions. The actual scattering value would change as a function of the moon location, as was seen with sun scattering. However, we can use this value as an approximation as to what the additional irradiance on to the target would be.

The value that does show up as the downwelled term, 0.0012 lux, is simply the integrated skylight curve over the bandpass (i.e., starlight and airglow). It is seen that this value does not change with time of night. This exemplifies the fact that we are not taking into account additional downwelled irradiance due to lunar scattering. Furthermore, we see that downwelled lunar scattering is more significant than starlight and airglow, which seems intuitive. In general the transitions between clear sunlight-sunset-twilight-and night time, seem to correlate very well with published literature values. The comparison is summarized in Table 8-3.

Table 8-3 Comparison of illuminance values for make_adb vs. literature.

Condition	Literature [lux]	make_adb [lux]	With *est.* lunar scattering term
Clear sunlight	30,000 - 100,000	28,000 - 94,000	
Sunrise/sunset	500	507	
Twilight	5 - 10	18	
Full moon	0.030 - 0.300	0.023 - 0.121 *	0.031 - 0.128
Starlight (& airglow)	0.0007 - 0.0030	0.0012	

* Value excludes downwelled lunar scattering.

8.4 Spectral Output of make_adb

In this last section, we look at the spectral distribution of the moon and night sky as computed by DIRSIGs make_adb utility. This data is analyzed in terms of illuminated lunar phase fraction, lunar azimuth, and lunar zenith. Figure 8-9 shows the direct irradiance from the moon (*i.e.*, no transmission attenuation) decreasing slightly as its phase fraction is reduced from 96% to 92%. This trend is expected. When the atmospheric transmission is factored in, as shown in Figure 8-10, we see an immediate decrease in overall illumination, which is also expected. At 9pm, for example, the moon is 96% full which is the largest irradiance value, as shown in Figure 8-9. However, at 9pm the moon was very low in the sky (elevation of 10°) thus leading to an increased path length to the target. This increased atmospheric path dramatically attenuates the irradiance, as seen in Figure 8-10.

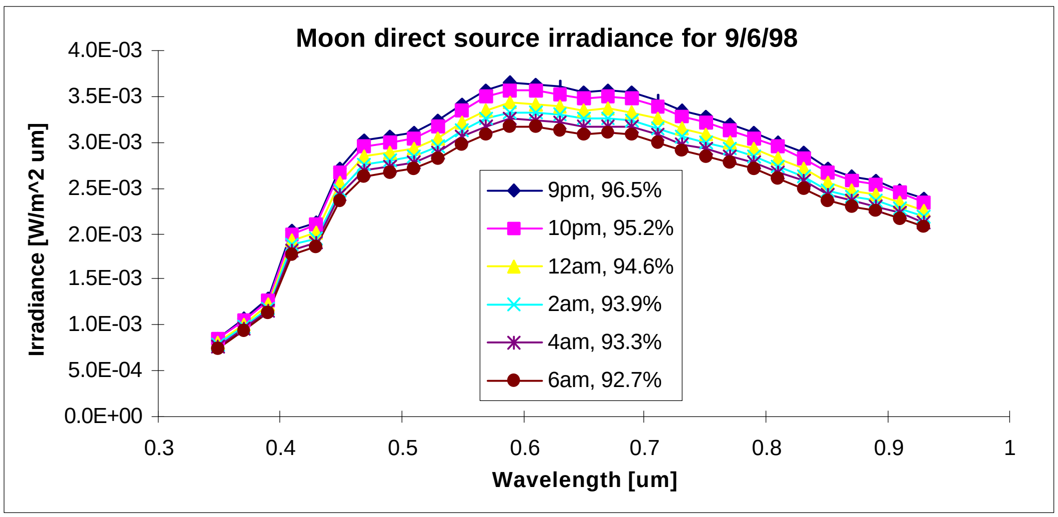

Figure 8-9 Direct lunar irradiance as a function of time of night.

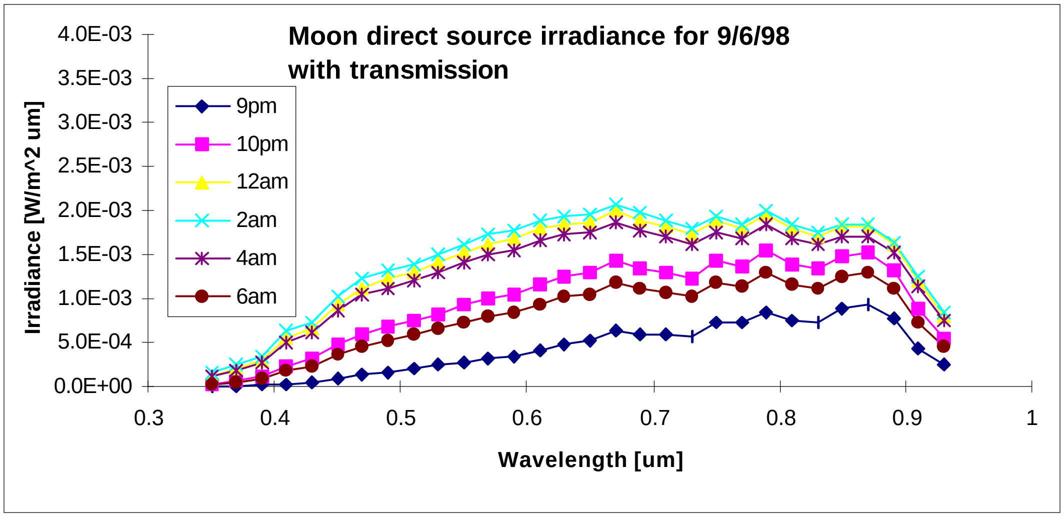

Figure 8-10 Direct lunar irradiance scaled by the atmospheric transmission.

For relative comparison purposes, we have included the direct solar and solar scaled distributions (see Figure 8-11). One can immediately see the magnitude differences between the solar and lunar sources. The same effect described above, however, can also be seen with the solar source. That is, the atmosphere significantly reduces the overall irradiance. This effect is greater at shorter wavelengths.

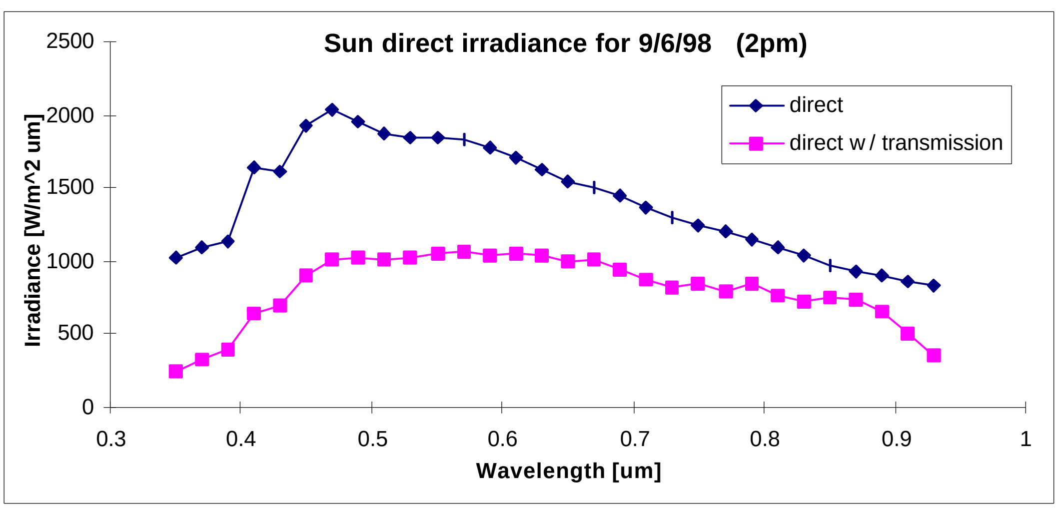

Figure 8-11 Direct solar irradiance at 2pm.

Finally, we explore the distributions for starlight, airglow, and lunar scattering. From looking at Figure 8-12, one can see the *input* skylight distribution to the make_adb utility (*i.e.*, starlight and airglow). This is the curve that was obtained from literature in section 5.3 and is used as a fixed constant for the skylight term in DIRSIG. The other distribution shown is that from the *output* of make_adb. We see that both of these distributions, sampling aside, are the same and that the skylight distribution is being implemented correctly in make_adb. Lastly, there is the issue of lunar scattering. As mentioned section 8.2, we have already discussed make_adbs inability to include the lunar scattering term. In Figure 8-12 the lunar scattering for a particular moon geometry, as computed by MODTRAN, has been included for comparison (see Appendix K for card deck used). The conditions are such that we are looking down onto a target from an altitude of 1700 feet. Furthermore, the moon phase angle is 90 degrees. This yields a phase fraction of 50. We can see how much more significant lunar scattering is in the visible, when compared to skylight. In the near IR, however, the effect is reversed.

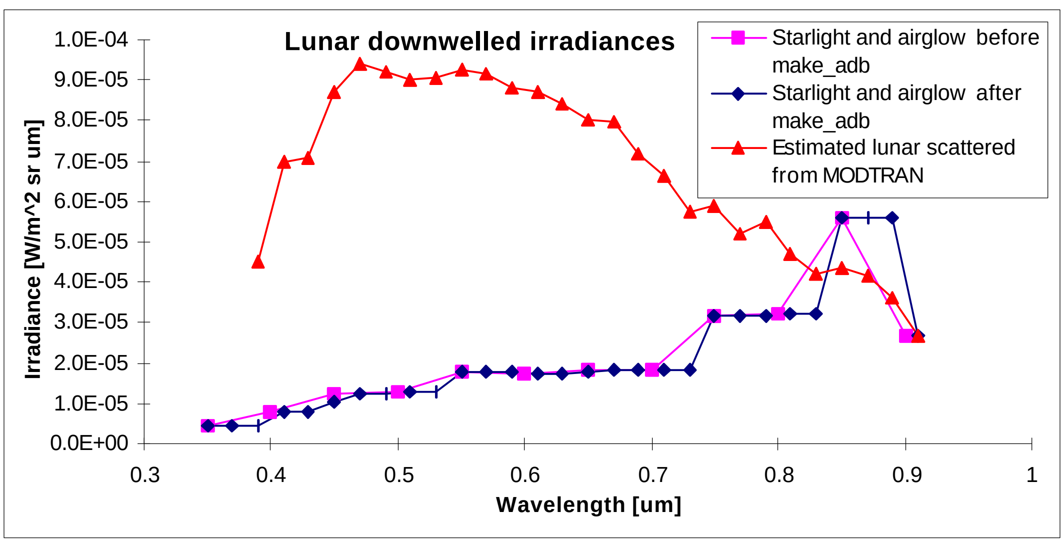

Figure 8-12 Night time downwelled radiance.

8.5 Radiance Prediction Summary

The calculation involving secondary sources showed that DIRSIG is indeed computing the correct irradiance fall-off due to the inverse square law. This analysis proved to be extremely useful for it was determined earlier on that a cosine term was missing from the DIRSIG source code.

It was also found that DIRSIG was not computing the downwelled lunar scattering term. This was due, in part, to the difficulty in creating the input card decks for MODTRAN. When looking at make_adbs output, overall, it was found that the illuminance values correlated well with published literature for all times of the day and night. This is a particularly pleasing result. However, the night time values for sky downwelled were too low and unchanging due to the lack of lunar scattering. Typical lunar scattering is around 0.0066 lux compared to the skylight term (starlight and airglow) which is only 0.0012 lux. This difference was further emphasized when the two spectral distributions were compared.

Chapter 9

9. SIG Image Results

In the previous chapters we generated a low-light-level sensor model and verified that the energy from the introduction of secondary sources such as street lights, the moon, and the stars was reasonable. With the inclusion of these new sources of illumination in DIRSIG, we can generate synthetic imagery and apply the sensor model while comparing the results to truth data.

9.1 SIG Images with Background and Extraterrestrial Sources

To start, a series of SIG images were generated that only included radiation from the sky (*i.e.*, starlight and airglow) and varying phase fractions of the moon. The conditions for these test cases are see in Table 9-1. In all cases, the *sun* was at least 19 degrees below the horizon. As it turns out, the solar downwelled radiance term becomes significant when the sun is at or at least 12 degrees below the horizon. By keeping the sun below this position, we avoid adding in the solar downwelled term.

Table 9-1 Image conditions for sky background and extraterrestrial source test cases.

	GMT Date	GMT Time	Local Time	Moon Elevation	Moon Azimuth	Moon Fraction	Sun Elevation	Sun Azimuth
				Deg	Deg	%	Deg	Deg
Full moon	9-6-98	0300	11pm EDT	31.10	146.81	97.32	-32.33	321.15
¾ moon	9-9-98	0600	2am EDT	46.22	143.46	78.5	-40.04	17.04
½ moon	9-12-98	0900	5am EDT	57.76	139.65	55.1	-19.41	64.10
¼ moon	11-13-98	1000	6am EDT	35.33	119.69	34.9	-22.02	94.39
New moon	9-22-98	0500	1am EDT	-47.31	334.18	9.36	-46.43	358.79

The standard atmosphere make-up was that of a clear sky with 23 km visibility. Since the path length to the sensor is short, and we have clear skys, we neglect *multiple* scattering effects which saves on computation time. All of the SIG imagery for this research was created with only single scattering effects (*i.e*., no multiple bounces in the atmosphere). More importantly, SIG imagery that is created with *multiple* scattering effects would look no different than *single* scattering imagery. This is because of make_adbs inability to compute the lunar scattering term which is only computed when MODTRAN is run in multiple scattering mode. Additionally, the images also include bi-directional effects.

The SIG results for the lunar test cases can be seen in Figure 9-1 and Figure 9-2. All the images have been scaled up by a factor of $2E^6$ for ease of comparison. This scaling is relative to the full moon image. A scale factor of $2E^6$ for the full moon case displays a reasonable amount of dynamic range with a small amount of clipping at the high end. The actual radiance values typically range from $1x10^{-10}$ up to $1x10^{-4}$ [W/cm^2 sr]. This is 6 orders of magnitude. One would need a significant number of bits to display this information. For this research, however, we conform to an 8 bit display for presentation purposes.

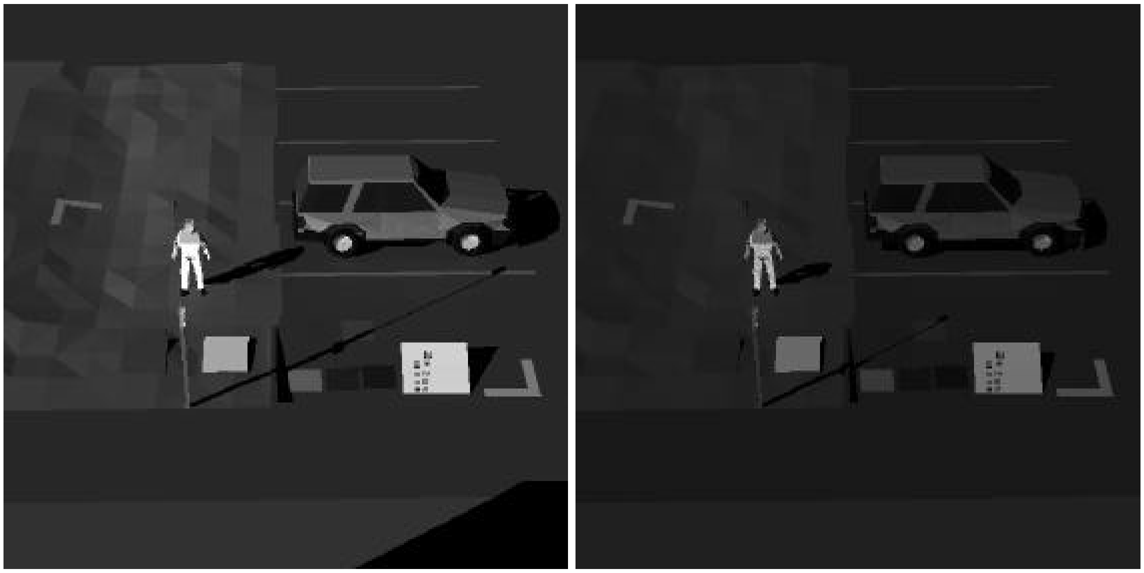

Figure 9-1 a) Full moon (97%) and b), ¾ moon (78%). Both with gain = $2E^6$ and bias = 0.

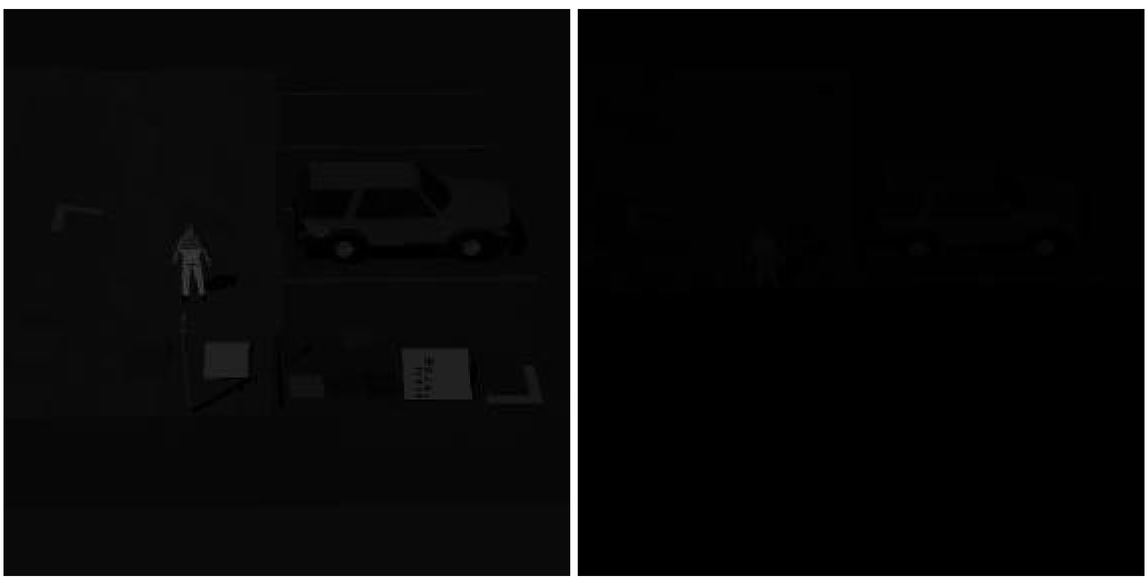

Figure 9-2 a) ½ moon (55%) and b), ¼ moon (35%). Both with gain = $2E^6$ and bias = 0.

The obvious trend in decreased illumination is present in the above sequence. However, it is most difficult to assess what is going on using this level of scaling. Therefore, we linearly auto- scale the images to fill an 8 bit dynamic range. These images are seen in Figure 9-3 through Figure 9-5.

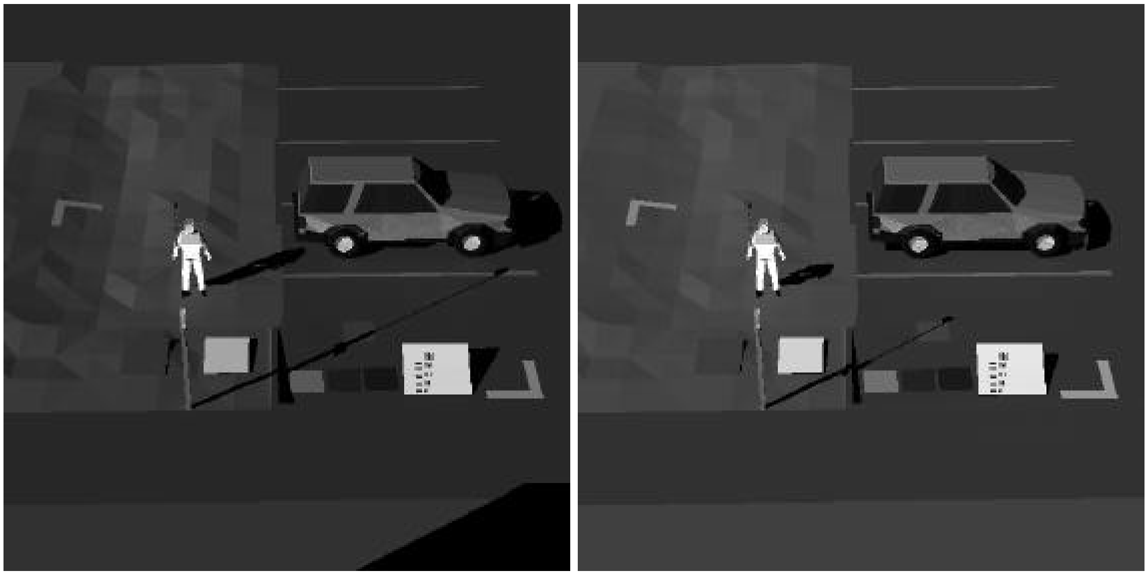

Figure 9-3 a) Full moon (97%) gain = $2E^6$ and b) ¾ moon (78%) gain = $4E^6$.

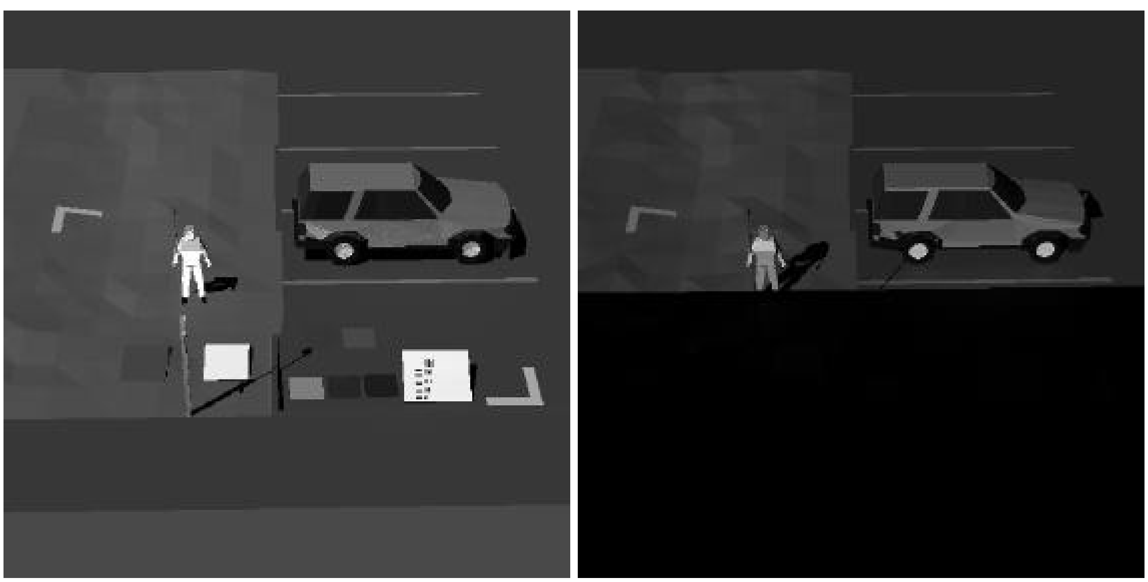

Figure 9-4 a) ½ moon (55%) gain = $14E^6$ and b) ¼ moon (35%) gain = $48E^6$.

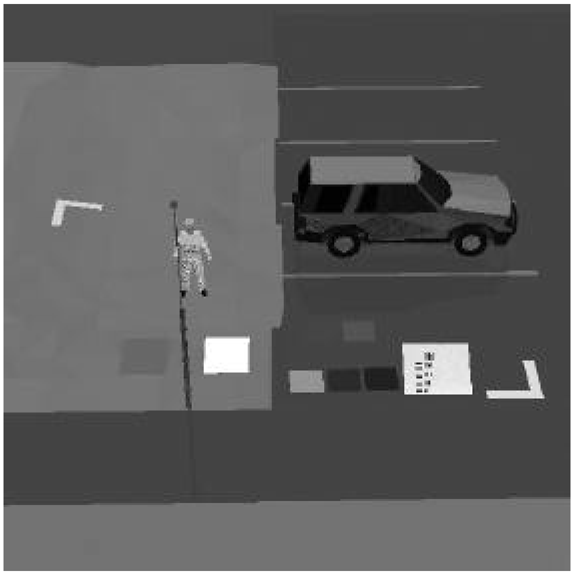

Figure 9-5 New moon case, gain = $80E^8$.

In the full moon case there is a noticeable shadow in the lower right hand corner of the image. This shadow is from the corner of the CIS building. The shadow is gone in the ¾ moon case because the elevation has been increased by 15 degrees, however, the two azimuth's are similar. The general reflectance for the various objects is as expected.

An interesting artifact in the ¼ moon case is the long shadow through the middle of the image. This is from the roof-edge of the CIS building. The top part of the image is illuminated by both moon light and skylight (starlight and airglow) while the bottom half is illuminated by skylight only. This area, however, would be brighter if lunar scattering were present. Finally, we have the new moon case, which has been scaled significantly. The only source of illumination here is from the skylight term. The grass appears to be brighter than in previous images because the integration is that of the skylight curve only. In other words, in the bandpass, the skylight distribution and grass distribution have similar characteristics. They both have a slight increase in the near-IR (see Appendix D). When integrated with the moon's spectral distribution, the overall signal is slightly reduced. This is due to the lower output of the moon at these longer wavelengths. Again the reflectance's of various objects are as expected. The scaling difference between the moon lit imagery and new moon case is around two orders of magnitude. This order of magnitude is as expected. The scaling factor becomes obvious when comparing the spectral distributions of the moon and skylight (see section 8.4).

Also seen in Figure 9-5, is a reflection of the truck in the asphalt immediately next to it. This is due to rays from the sensor-to-target path that actually hit the side of the truck and not the background sky. Those rays that trace to the sky (*i.e.*, miss the truck) from the asphalt are seen as being brighter. Conversely, those that hit the truck *do not* see the sky, but rather the side of the vehicle which is significantly darker than the sky thus creating the shadow region.

9.2 SIG Imagery with Secondary Sources

We now attempt to recreate collected truth imagery, which contains secondary sources. The conditions for the selected ground truth imagery are seen in Table 9-2. The first scenario to look at is one where the sources of illumination are that from the moon, skylight, and distant city lights. This is termed the “nolight” case (see truth images in Figure 9-6 and Figure 9-7). The gain value shown here is representative of the voltage setting used on the camera, which had a maximum setting of 7.8 V. The camera voltage gain is proportional to the overall amplification of the viewed image. The other scenarios include a tungsten halogen source off axis out of the field of view and a fabricated street lamp illuminating the ground below (stlamp).

Table 9-2 Night time conditions for selected truth images.

	GMT Date	GMT Time	Local Time	Moon Elevation	Moon Azimuth	Moon Fraction	Sun Elevation	Sun Azimuth
				Deg	Deg	%	Deg	Deg
nolight	9-2-98	0100	9pm EDT	27.00	175.31	68.1	-13.70	295.23
tghg	9-2-98	0400	12am EDT	17.54	218.90	69.0	-36.39	338.20
stlamp	9-2-98	0430	12:30am EDT	14.01	225.03	69.1	-38.02	347.30

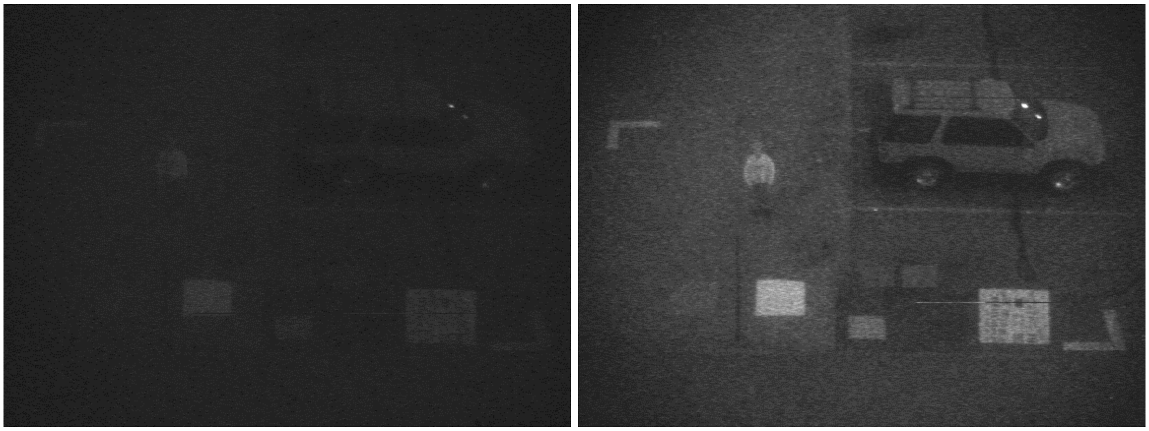

Figure 9-6 Truth images for “nolight” scenario. a) gain = 5 V and b) gain = 6 V.

Figure 9-7 Truth images for “nolight” scenario. a) gain = 6.5 V and b) gain = 7 V.

The previous radiance images that came out of DIRSIG were for *ideal* night time atmospheric conditions, *i.e*., clear skies with high transmission. However, at the time of the collection, it was partly cloudy. This introduced a condition that is presently beyond DIRSIGs capabilities. Namely, to model clouds as well as multiple scattering effects at night. In an attempt to compensate for an overcast sky, in which the 68% moon was nearly absent, the atmospheric transmission was reduced by 75 percent (see Figure 9-8). The reduction value chosen will be discussed in subsequent sections. This reduction did, however, preserve the spectral character of the night sky. Unfortunately, there exist strong shadows in the SIG imagery caused by the clear sky conditions and lack of downwelled scattering. The reduction of the atmospheric transmission was accomplished by manually altering the lunar transmission values in the make_adb output file. To fully compensate, we would have to run a cloud model with multiple scattering present, which would decrease the direct source term while increasing the lunar downwelled scattering term. Obviously, this can not be performed due to the reasons mentioned earlier.

The general premise for the comparison of SIG data to truth imagery, is that of a qualitative one. Since the actual conditions can not be simulated at the present time, we take the approach of simply trying to match the overall contrast of the imagery (*i.e.*, ranking the brightness). Similarly, we attempt to implement characterized values for MTF and noise on the SIG imagery. The end result is SIG data that exhibits common artifacts found in LLL sensor systems. These are then compared to similar truth images taken under similar conditions (*i.e.*, street light on, no moon, etc.).

The first set of images to compare can be seen in Figure 9-9. Because LLL imagery is difficult to assess, due to its sheer nature of being dark, a contrast enhanced version of Figure 9-9 can be seen in Figure 9-10. Here we have a SIG image on the left and its truth equivalent on the right. We are comparing the SIG image to a truth image that was captured with a camera voltage setting of 6V. From this, the calibration (section 7.2) tells us that we need to implement a scale factor of $40E^6$ and bias of 36 DC on the radiance data in order to compare the two images in digital count space. Of course this scale factor would be different for this image had we chosen a different percentage to reduce the lunar transmission by. Seen in the SIG image is a rather long shadow extending to the right of the human. This is due to the moons irradiance. Similarly, we see a shadow cast by the resolution target and light pole.

At this point a short digression is in order which addresses the ambiguity associated with the calibration and lunar transmission reduction factor. If the calibration was absolutely correct, than this would suggest that the lunar transmission factor could be found, for a fixed gain and bias, by computing a series of SIG images with varying percent reductions, say 50 to 90 percent. An RMS error between the truth and SIG image could then be computed by selecting solid areas in the imagery and computing a mean. The “reduction” image with the lowest RMS error, for example, as compared to truth data, would yield the appropriate transmission factor. This was how the 75 percent reduction factor came about for this research. Rather than make a random guess as to what the percentage should be, we let the value rest on the validity of the calibration. Again, the emphasis here is on the relative contrast between the two images.

Figure 9-8 DIRSIG image for "nolight" scenario with direct source irradiance reduced by 75%. The gain = $40E^6$ with bias = 36, which closely resembles a camera gain of 6 V.

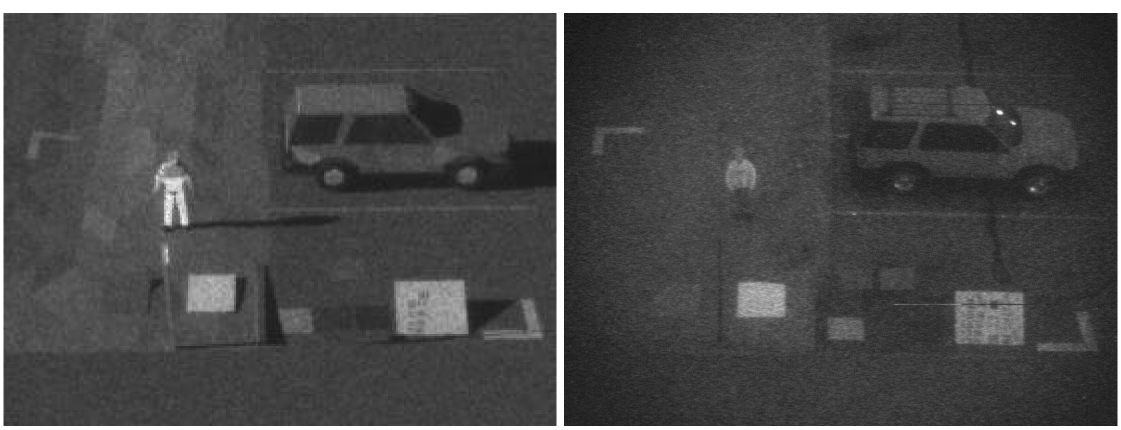

Figure 9-9 DIRSIG image for "nolight" scenario and corresponding truth image. Gain = $40E^6$, bias = 36.

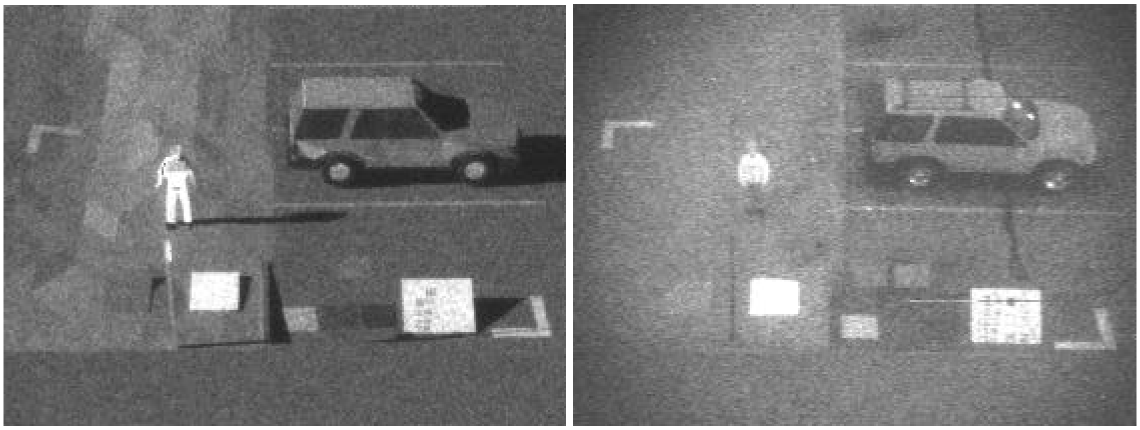

Figure 9-10 Contrast enhanced DIRSIG image for "nolight" scenario and corresponding truth image. Gain = 40E^6, bias = 36.

The images above were created by first applying the shot noise model, with a fill factor of 50%, to the raw radiance data (as discussed in section 6.4.1). This resultant image was then processed with an MTF model using an MTF index of 0.8 and a frequency constant of 6. The image was then processed with Gaussian noise with a SNR of 8. Finally we downsample the image (bi-cubic interpolation) to the size of the truth imagery (576 x 430). Since the aspect ratios between the SIG and truth images were different, some cropping was implemented on the SIG imagery.

We can now perform a quick evaluation by computing an RMS error as a function of local area brightness between the two images. This evaluation consists of measuring four uniform areas, differing in brightness, within each image in terms of mean and standard deviation. Table 9-3 shows which areas in the truth image were measured as well as the resulting RMS statistics. The areas of interest in the truth image were the white panel, light gray panel, asphalt, and grass. It is seen that the initial SIG image (raw radiance) had a reasonably low RMS error with the gain and bias setting stated. Furthermore, the standard deviation is high because the SIG image has yet to contain variance due to noise. Table 9-4 show the RMS error with shot noise implemented on the SIG imagery. The fill factor used here is 50%. We see that the mean RMS has decreased slightly. The standard deviation, however, has increased dramatically. This is due to the extreme variation associated with the noise model. Table 9-5 show the results of a SIG image that contain gain, bias, shot noise, and blur. This is the stage where we implement our MTF filter function. This process is performed as a convolution. Intuitively enough, the operation of convolution highly correlates the noise by reducing the variance, as can be seen in the table. The standard deviation RMS error is now fairly low. One of the last sources of noise to add is Gaussian noise. The results of this can be seen in Table 9-6. Here we have included the effects due to back-end electronics. The noise factor implemented is associated with an SNR factor of 8. The results of this have increased the standard deviation slightly while maintaining the overall mean value. Lastly we downsample the SIG image. This RMS results for this can be seen in Table 9-7. The process of downsampling is done by interpolation. In this case we used a bi-cubic interpolation. Again, this process correlates neighboring pixels resulting in a decrease in variance, as seen in the table. Overall the average RMS errors for the mean and standard deviation are low.

What we have done here is to pick reasonable values for fill factor, MTF index, MTF frequency constant, and SNR, then run the SIG image and see how it compared to the truth image. The values were chosen so as to generate high visual correlation between the truth and SIG image. On average, the relative means and noise variances of a few objects in the SIG scene match that of the truth image. We could have generated a better correlation had we included more uniform areas in the analysis. However, it was deemed that four regions were adequate for this treatment.

Table 9-3 RMS error for SIG image with gain and bias only.

Gain=6V nolight12.bmp solid areas	Truth meas mean	Truth meas stddev	*Original G=40 B=36 sig mean*	*sig stddev*	*mean RMS*	*stddev RMS*
wht panel	159.6	12.0	172	0	12.4	12.0
lt gray	98.7	9.2	106	0	7.3	9.2
asphalt	61.7	6.5	64	0	2.3	6.5
grass	71.3	7.2	78	0	6.7	7.2
Total RMS error:					7.2	8.7

Table 9-4 RMS error for SIG image with gain, bias, and shot noise.

Gain=6V nolight12.bmp solid areas	Truth meas mean	Truth meas stddev	*with Shot fill=0.5 sig mean*	*sig stddev*	*mean RMS*	*stddev RMS*
wht panel	159.6	12.0	168.8	56.2	9.3	44.2
lt gray	98.7	9.2	104.9	47.2	6.2	38.0
asphalt	61.7	6.5	64.4	31.6	2.8	25.1
grass	71.3	7.2	79.6	38.4	8.3	31.2
		Total RMS error:			6.6	34.6

Table 9-5 RMS error for SIG image with gain, bias, shot noise, and blur.

Gain=6V nolight12.bmp solid areas	Truth meas mean	Truth meas stddev	*with Blur xi=6 sig mean*	*sig stddev*	*mean RMS*	*stddev RMS*
wht panel	159.6	12.0	165.0	11.7	5.4	0.3
lt gray	98.7	9.2	99.5	8.6	0.8	0.6
asphalt	61.7	6.5	64.3	5.5	2.6	1.0
grass	71.3	7.2	78.8	7.0	7.5	0.2
		Total RMS error:			4.1	0.5

Table 9-6 RMS error for SIG image with gain, bias, shot noise, blur, and Gaussian noise.

Gain=6V nolight12.bmp solid areas	Truth meas mean	Truth meas stddev	*with Gauss SNR=8 sig mean*	*sig stddev*	*mean RMS*	*stddev RMS*
wht panel	159.6	12.0	165.9	12.6	6.3	0.6
lt gray	98.7	9.2	99.9	9.8	1.2	0.7
asphalt	61.7	6.5	64.1	7.6	2.4	1.1
grass	71.3	7.2	77.9	8.3	6.6	1.1
		Total RMS error:			4.1	0.9

Table 9-7 RMS error for SIG image with gain, bias, shot noise, blur, Gaussian noise, and downsampling.

Gain=6V nolight12.bmp solid areas	Truth meas mean	Truth meas stddev	*after dwn sample sig mean*	*sig stddev*	*mean RMS*	*stddev RMS*
wht panel	159.6	12.0	166.6	12.2	7.0	0.2
lt gray	98.7	9.2	100.7	8.5	2.0	0.7
asphalt	61.7	6.5	63.8	6.8	2.2	0.3
grass	71.3	7.2	79.1	7.8	7.8	0.6
Total RMS error:					4.7	0.5

9.2.1 Tungsten-Halogen Source Off-Axis

The next set of SIG images deal with the inclusion of secondary sources. The first scenario is one that contains a 300 W tungsten halogen lamp, off axis, out of the field of view of the camera. We will term this scenario “tghg”. The truth images for this are shown in Figure 9-11 and Figure 9-12.

Figure 9-11 Truth images for “tghg” scenario. a) gain = 4 V and b) gain = 5 V.

Figure 9-12 Truth images for “tghg” scenario. a) gain = 5.5 V and b) gain = 6 V.

In the truth images above we see saturation and blooming at gains higher than 5 V. This saturation is not present in the “nolight” cases. With this in mind we attempt to simulate the 5 V truth image. This is shown in Figure 9-13. The conditions for the simulation are the same as presented above, that is, a fill factor of 50%, frequency constant of 10, and a SNR of 8. The only difference is in the image scaling. The gain and bias used were $10E^6$ and 20, respectively.

Figure 9-13 DIRSIG image and truth image for tungsten-halogen source off axis. Gain=$10E^6$, bias=20.

The main *geometric* aspects of the truth image have been faithfully reproduced. This includes geometric orientation and shadowing. Light source coordinates were measured in the truth scene and entered in the SIG scene database. It is seen from Figure 9-13 that the SIG shadowing of the street lamp, vehicle, and human lye in the same locations as those in the truth image. However, the source was moved about 1 foot east in order to obtain higher correlation between the truth and SIG image.

Another important observation is that of the specular nature of various objects in the truth scene. It is seen from Figure 9-13b, that the vehicle, grass, and resolution target have a more pronounced specular aspect to them than is reproduced in the SIG imagery. At first glance, this is more than likely due to the reasons mentioned earlier in this chapter. However, water may have formed on various objects during the course of the evening, in the form of dew, giving the appearance of increased specularity. This is more commonly seen with grass. DIRSIG does, however, posses the capability to model specular objects, though we will not explore this area in this research.

9.2.2 Street Lamp Scenario

The next set of images is that from the street lamp scenario. Here we have a tungsten 40 watt bulb in an enclosed box with an aperture on it. The light is approximately 15 feet above the ground suspended by a piece of conduit. The truth images for this scenario can be seen in Figure 9-14 and Figure 9-15.

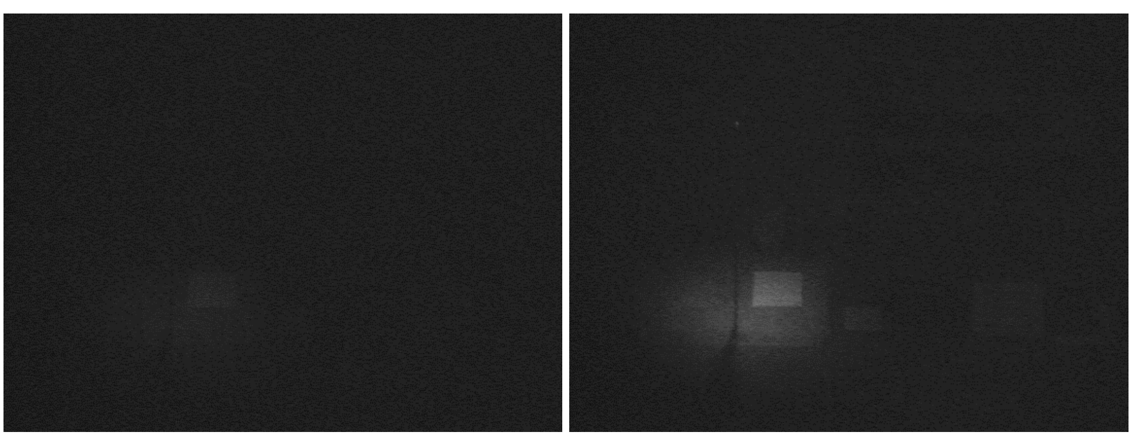

Figure 9-14 Truth images for “streetlamp” scenario. a) gain = 3 V and b) gain = 4 V.

Figure 9-15 Truth images for “streetlamp” scenario. a) gain = 5 V and b) gain = 5.2 V.

The representative SIG image for a 5 V simulation can be is seen in Figure 9-16. Of interest are the sharp transitions on the ground defined by the aperture on the source above. This is due to the fact that DIRSIG only performs computations based on ideal point sources and is unaware of realistic extended sources. Because DIRSIG is a ray tracer, which leads to modeling using geometrical optics, other phenomena such as diffraction can not be modeled. An approach can be used, however, that simulates an extended source. This entails placing multiple point sources in the SIG lamp housing, each having a different location. This effect, when processed, can be seen in Figure 9-16. In order to achieve this, 5 point sources were placed in the lamp housing, one on top of the other, spaced 1 inch apart. Each point source drew upon the same spectral distribution. Therefore, in order to maintain the overall intensity, each point source distribution was scaled by one-fifth. Upon generation of the radiance field image, LLL sensor effects were added which included shot noise, blur, and electronic noise. It is obvious that more point sources would do a better job at approximating the extended source. However, for this treatment we only used five.

Figure 9-16 DIRSIG image and truth image for street lamp scenario. Gain=10E^6, bias=20.

One last observation is that because DIRSIG lacks the ability to model path scattering, such as fog as seen from a car's headlights, we do not see some of the side effects due to secondary sources. For example, if we look at the 5 V case for the nolight truth scenario and compare it to the 5 V street lamp truth scenario we notice two major differences, only one of which DIRSIG models (see Figure 9-17). The first is the fact that there is a light source in one of the images, the second, which DIRSIG does not account for, is the fact that there is additional radiation incident on the truck and surround due to scattering from the light source. Figure 9-17 shows contrast enhanced versions of both of these truth images. The vehicle in the street lamp case shows up with more detail due to scattering from the light source. The DIRSIG equivalent images do not exemplify this effect.

Figure 9-17 Contrast enhanced truth images for a) nolight and b) street lamp scenarios. Both with camera gains of 5 V. The vehicle in the street lamp case shows up with more detail due to scattering from the light fixture.

9.3 Additional LLL SIG Imagery Examples

In this section we present SIG imagery for display purposes only. Unlike previous sections, where we compared SIG data to truth data, here we simply demonstrate the potential for adding secondary sources to pre-existing CAD scenes. The first example shows a runway and airplane hanger with six 2800 K light sources in it (see Figure 9-18). The surrounding illumination is due to a half moon. This image, unlike previous ones, contains texture maps for the grass, runway, and building.

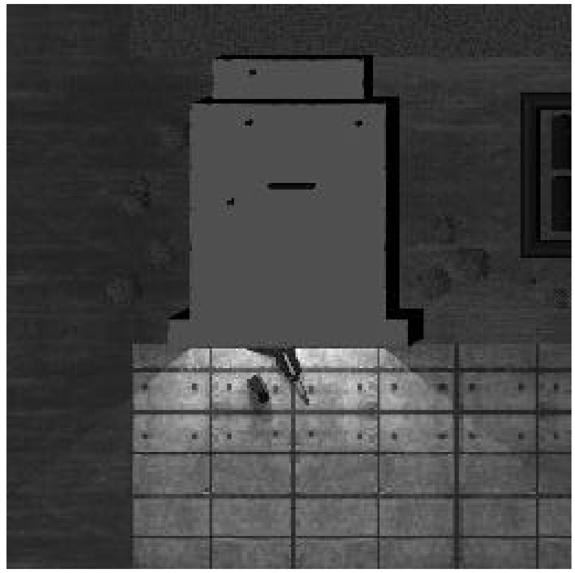

Figure 9-18 SIG scene under half moon illumination.

9.3.1 CCD Streaking

Here we use the above SIG scene to demonstrate how one might implement CCD streaking, as described in section 6.2.3. As previously mentioned, streaking is most commonly seen in full frame CCD imagers and less likely found in interline devices. The phenomenon manifests itself when saturation occurs in pixel wells along a vertical (or horizontal) line. The excess electrons spill over to neighboring pixels possibly filling them up as well.

The general algorithm (see Appendix L) consists of first sorting all the amplified pixel values in a given line (or row). The brightest pixel value is then compared to a user specified saturation level. If this pixel value exceeds the saturation level, the overflow is passed on to the neighboring pixels. The line is then resorted, and the overflow test repeated until there are no pixels over the threshold. The results of this can be seen in Figure 9-19.

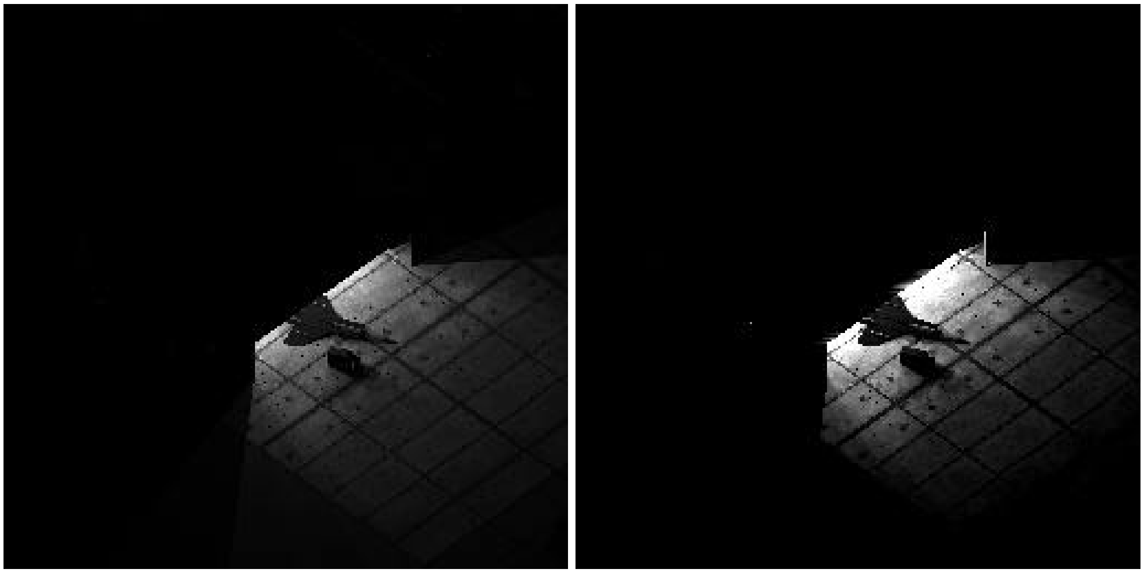

Figure 9-19 Foxbat SIG scene viewed off axis under new moon conditions a) with out any sensor effects and b) with modeled CCD streaking.

It is evident from Figure 9-19b that we have implemented saturation at the entrance to the hanger. The original image was scaled by a user defined gain value which lead to saturation. This saturation was spread over the neighborhood according to the algorithm in Appendix L.

9.4 Aerial Resolution

Finally we make some observations on resolving power using the resolution target in truth images. The target used was the 1951 United States Air Force chart (USAF). This target was designed for checking lenses used in aerial photography. The spatial resolution of a lens is normally expressed in terms of line pairs per millimeter (lp/mm) in the *image plane*. We can calculate the resolution, at the *target*, by using the following equation

$$resolving\ power = 2^{m + \frac{n-1}{6}} \qquad [lp / mm] \tag{9.1}$$

where *m* is the group number and *n* is the element number. By factoring in the magnification, we can calculate the resolution at the *image plane*.

Since we included such a target in the collection imagery, we can calculate the limiting resolution for a couple truth scenarios. Using the above equation to compute resolving power, we can see that in the “nolight” scenario, for a gain of 6.52 V, the limiting resolution was around 0.015 lp/mm at the target which corresponds to 15.73 lp/mm at the focal plane. Similarly, if we look at the tungsten-halogen test case, which has a slightly lower gain of 5 V, we see the limiting resolution was around 17.62 lp/mm at the focal plane. The latter is slightly higher because of the lower gain, resulting in less saturation and possibly less noise. The ICCD tube manufacture claims that the intensifier tube has a limiting resolution of 45 lp/mm which is significantly greater than the measured values above. This is expected since the A/D, video D/A, and digitizer degrade the signal dramatically, as shown earlier. If we take the “limiting” frequency as the value of the MTF at 10 percent, we see that our analytic function representing the entire camera system (Figure 7-17) yields a value of 17 lp/mm which coincides with what was calculated from the USAF target. Furthermore, after the addition of noise and MTF, the SIG images yield target resolution values on the same order as the truth images.

Chapter 10

10. Conclusions and Recommendations

Overall, the main objectives of this research have been met. That is, synthetic simulation and modeling of IICCDs. However, to fully implement the model, we needed to first generate a low-light-level simulation environment. By exploring the behavior of lunar sources, starlight, secondary sources, and the detailed workings of an image-intensified CCD device, we have successfully integrated a low-light-level sensor model into a multispectral simulation environment, DIRSIG. The additions to the DIRSIG model have been made to improve the radiometric accuracy and realism for low-light-level imaging conditions. This includes the incorporation of the moon as an additional exoatmospheric source, star light and man-made sources. Similarly, a generic low-light-level sensor model has been developed that allows the user to model a variety of IIT and IICCD components and instruments.

10.1 SIG Environment Conclusions and Recommendations

Since the completion of this report, many improvements have been made to the SIG model. For example, the creation of separate scene node and dview files, as generated in this research, are no longer needed. All information, including the geometric database, time of run, location, atmospheric database, sensor type and location, output image size, bandpass, source types, etc. are contained in one configuration file. Furthermore, there are new tools available to debug the CAD scene. These include changing materials, material properties, facet attributes, and facet normals.

The integration of skylight, lunar and secondary sources proved to be extremely successful. The secondary source calculations were verified by generating a SIG image which contained such a source. The output was then compared to calculated values which exhibited a high correlation (only after it was discovered that a cosine term was missing in the SIG model). The lunar direct term was then qualitatively compared to published literature. This also exhibited high correlation. However, the values were slightly off due to make_adb's lack of lunar scattering.

The SIG data that was generated *visually* correlated well with truth data. This was evaluated in terms of an RMS error. Difficulties arose with the fact that truth data was collected when it was cloudy. This proved problematic for it was difficult to simulated the atmospheric conditions at the time of the collection. An attempt was made to simulate the reduction in radiance by manually reducing the transmittance by 75%. Resulting SIG imagery demonstrated that lunar scenarios as well as secondary source scenarios could be generated in a simulation environment with added effects from a low light level sensor model.

Can not view sources

Though the SIG environment was successfully demonstrated, there is still room for improvement. First and foremost is the fact that you can't actually look at a secondary light source. The sources are defined in terms of x, y, and z coordinates, however, aiming the sensor directly at this location produces no visible image of the source itself. You can only see its effect after light has encountered a surface or facet. The solution is rather simple. One only needs to perform a geometric test to determine if the point source falls in the field of view of a pixel. If it does, check to see that it is not blocked by a facet. If all is well here, the point source will fill one pixel and its irradiance will be determined via the inverse square law.

No lunar scattering

Mentioned throughout this research is the fact that make_adb, the radiance builder for DIRSIG, did not take into account lunar downwelled scattering. The lunar scattering only plays a major role when the moon is in the night sky. It was demonstrated that this downwelled term can be quite significant when compared to the skylight background (*i.e.*, starlight and airglow). This was accomplished for a particular lunar geometry by running MODTRAN off-line in multiple scattering mode. The problem shows up in the creation of the card deck for the downwelled radiance case. As mentioned previously, the downwelled radiance is computed by sampling the above hemisphere 84 times. Each sample is a MODTRAN run. The parameters that must be used to build the card deck are shown in Figure 10-1. These options differ from that of the solar downwelled case. What needs to be calculated is the zenith angle and azimuth angle between the observer line of sight and observer to moon path for every sample of the sky dome. The problem manifests itself again for the computation of the upwelled radiance to the sensor.

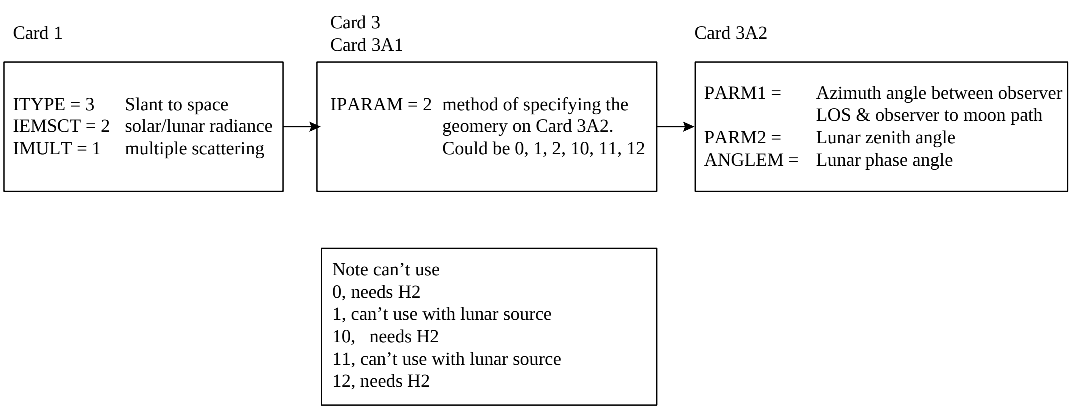

Figure 10-1 Required card deck parameters for computing the downwelled lunar radiance.

No particle scattering

Since DIRSIG is a *ray* tracer, it is inept at modeling particle scattering, such as that from car headlights on a foggy evening. This is a realism that is seen at night rather than during the day. The scattering mentioned here differs from that mentioned above only in that, here we are talking about path scattering from a car headlight to a building wall, for example. We saw the effects of this in the tungsten halogen truth images (Figure 9-17). Both images used the same camera gain. However, the vehicle stands out more in the image that contained a light source than the one without a source. This is clearly due to scattered light from the fixture illuminating the vehicle. At the present time, it is not clear that the ray tracer can actually model this phenomena. However, what would have to be done is to consider each pixel illuminated under the lamp as another secondary source. Each pixel on the truck then would have to trace to each illuminated pixel under the secondary source. This approach requires an enormous amount of calculation. Similarly, if we were to model haze, we would have to include a MODTRAN run for each path from the truck to the "second" secondary source.

DIRSIG Runtimes

The generation of one SIG image used for this research required 15 hours of computation time running on an DEC Alpha 533 under Linux OS. Each image was 1024 x 1024 and also included shape factor. Unfortunately, due to the nature of the physics and the sheer number of calculations to be performed, the run times are typical of DIRSIG images (see Figure 10-2). This is certainly an area that can always be improved by streamlining the code or running the application on a faster machine.

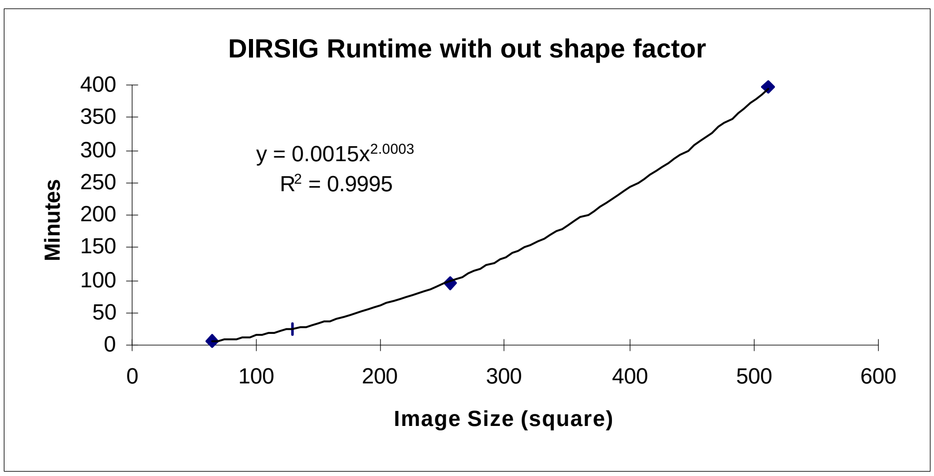

Figure 10-2 Typical DIRSIG run times excluding shape factor.

Possible error in make_adb for computation of solar/lunar altitude

An error that was found in the DIRSIG environment was in the calculation of the solar and lunar altitude. Make_adb uses an ephemeris utility to compute the relative positions of the sun and moon. However, when the two were compared off-line, it was noticed that there exists a difference in the calculation of altitude. The calculation for azimuth and moon phase fraction were O.K. The error increased as the extraterrestrial source got closer to the horizon (see Table 10-1). When the source was below the horizon, the error was zero. It is unclear as to the source of this error. One can only speculate that the atmospheric temperature and pressure are not being considered in make_adb utility. These are parameters that are specified in the ephem program and should be taken into account in make_adb.

Table 10-1 Ephem vs. make_adb off line for computation of solar/lunar elevation.

	Sun altitude				Moon altitude		
Time	EPHEM	make_adb	% difference		EPHEM	make_adb	% difference
9/6/98 8:00 AM	13.76	13.69	0.5		-14.73	-14.73	0
9/6/98 10:00 AM	34.66	34.64	0.1		-34.68	-34.68	0
9/6/98 12:00 PM	50.19	50.18	0.0		-49.98	-49.98	0
9/6/98 2:00 PM	51.47	51.46	0.0		-52.85	-52.85	0
9/6/98 4:00 PM	37.37	37.35	0.1		-40.86	-40.86	0
9/6/98 6:00 PM	16.38	16.77	2.3		-21.68	-21.68	0
9/6/98 7:00 PM	5.98	5.84	2.4		-11.16	-11.16	0
9/6/98 8:00 PM	-4.61	-4.98	7.4		0.16	-0.53	69.8
9/6/98 9:00 PM	-15.34	-15.34	0		10	9.91	0.9
9/6/98 10:00 PM	-24.79	-24.79	0		19.85	9.80	0.5
9/7/98 12:00 AM	-38.28	-38.28	0		35.96	35.94	0.1
9/7/29 2:00 AM	-39.35	-39.35	0		42.18	42.16	0.0
9/7/98 4:00 AM	-27.32	-27.32	0		34.79	34.77	0.1
9/7/98 6:00 AM	-8.13	-8.13	0		18.23	18.18	0.3
9/7/98 7:00 AM	2.84	2.58	10.1		8.39	8.29	1.2
9/7/98 8:00 AM	13.56	13.50	0.4		-0.73	-2.02	63.9
9/7/98 9:00 AM	24.29	24.26	0.1		-12.38	-12.38	0

Detailed analysis of spectral sky distributions

Part of the goal of this research was to demonstrate a low-light-level, nighttime simulation environment. This entailed generating a spectral night time sky distribution. The one used in this research only came from one source of literature. Furthermore, no other literature sources were found that contained such a distribution. This certainly needs to be investigated further. It is believed, however, that the distribution obtain is a reasonable one for the principle investigator has spoken with colleagues at other research institutions that reference the same literature source.

SIG Validation

No model is complete if it does not imitate the real world. This would entail a rigorous validation. Throughout this research, we simply aimed at comparing the relative contrast between the truth and SIG images. The validation could not go much beyond that for we did not have the appropriate radiometric instruments measuring data at the time of the collection (*i.e.*, actual radiance of objects in the truth scene). Therefore, a more rigorous validation is in order. DIRSIG had been validated in the past but not for low light level imaging conditions. The approach used here would be very similar to what was used in this research; calibration of the camera and image capture system. Then a data collection could be performed while comparing truth to SIG imagery. Other suggestions for the data collection would include choosing a *very* remote location in which there were no additional sources of stray light such as from city lights.

10.2 Calibration Conclusions and Recommendations

In an attempt to understand the workings of the IICCD camera and to override the auto gain control feature (AGC), modifications to the device were made. This proved to be extremely helpful in characterizing the camera. The MTF of the camera system, including the CCD A/D and video D/A, were measured. Similarly, the MTF of the digitizer and image intensifier tube were also obtained. These were then compared to literature MTFs for similar devices. The results showed that the measured values were as expected, with the digitizer being the limiting factor.

The radiance calibration proved to be moderately successful at best. This was due, in part, to the extreme sensitivity of the IICCD device and laboratory equipment available to the principle investigator. The data that was collected related scene radiance to digital counts. Look- up tables were generated and gain and bias values were obtained. These values were ultimately applied to SIG imagery for scaling purposes.

Higher resolution in frame grabber

One of the limiting factors in the performance of the imaging system was the resolution of the frame grabber. The grabber that was used was that of 8 bits with a maximum spatial resolution of 640 by 480. It is evident from the above discussion that more resolution would have been extremely helpful.

MTF in two-dimensions

The MTFs in this research were only measured in one dimension. It was assumed that the difference between the x and y MTFs was negligible. This may not have been a safe assumption, however. More often than not, the MTFs are different, such as that from non-square CCDs. Therefore, this y-dimension information should be evaluated and compared to what has already been measured.

Lower wattage light source for calibration

The characterization performed in this research was fairly noisy due to the fact that the calibrated light source was too intense. To achieve adequate light levels for the camera, a series of neutral density filters were used. However, errors were induced when ND filters of 3.00 and higher were used. This was due to the stacking of two filters and interference problems found at the interface. Therefore, It was extremely difficult to obtain repeatable values under high gain situations. This error ultimately showed up in the overall calibration of the device. To circumvent this problem, we would need a much lower, calibrated, source than the 10 watt one used in this research. This would certainly eliminate the need for multiple ND filters. Another solution is to used the inverse square law.

10.3 Camera Modeling Conclusions and Recommendations

The camera model presented in this research attempted to model some of the main characteristics found in many of today's image intensified devices. These included shot noise, MTF, and pre-amplifier noise. SIG imagery was created with the sensor model applied. The values for the sensor model came from laboratory measurements and off-line calculations. The results showed that the current sensor model qualitatively reproduced image intensifier artifacts found in similar truth imagery.

Expand sensor model

The sensor model presented in this research is by no means complete. It simply demonstrates that a basic LLL model incorporating MTF and noise, is capable of modeling a large percentage of what the end user sees. One of the main artifacts found in LLL devices is the phenomena of *blooming*. For this research we demonstrated how one dimensional blooming or streaking could be modeled. Similarly, we laid some ground-work as to the possible sources of localized, two-dimensional blooming. Certainly, for this model to be more complete, one would have to include such effects. Another part of the model that might be deemed important, is the *optics model*. Here we are referring to the optics in front of the input or photocathode window. Again, we omitted this module to limit the overall scope of this research. However, information has been presented in the flavor of linear systems theory as to what the point spread function and MTF would be. There are other, more subtle, components to consider in the LLL imaging chain as well. These include modeling the *microchannel plate*, *phosphor screen*, *photocathode*, *fiber optics*, other sources of *noise*, and losses due to *optical interfaces*. Again, this research documents some of the theory behind these phenomena. Lastly, we touch upon the topic of modeling other types of LLL devices. The research presented here only takes into account one particular flavor of image intensifier. There are many on the market today that have different designs. Modeling these other types of IICCDs, which might contain different photocathode sensitivities, MTFs, noise, etc., could expand the validity or robustness of the model presented in this research.

10.4 Recommendation Summary and Future Efforts

In this last section we simply summarize the problems encountered through out this research and suggested solutions. These recommendations are summarized in tabular form.

- Work involved in the viewing of secondary sources
- Incorporate lunar scattering
- Simulate particle scattering
- Investigate ambiguities between make_adb and ephem
- Detailed analysis of spectral sky distributions
- More rigorous validation of LLL environment
- Add texture maps to SIG imagery
- Integrate LLL SIG imagery with IR data for image fusion (see section 10.5)
- Be sure to use high resolution frame grabbing devices
- Measure MTF in two-dimensions
- Use lower wattage light source when performing calibration
- Expand sensor model to separately include
    - Blooming, optics, MCP, phosphor screen, photocathode, fiber optics
    - Losses due to optical interfaces
- Model other types of LLL devices

10.5 Addendum: Preliminary Work on Image Fusion

This section, along with Appendix M, describes some background and preliminary work that was performed in the area of VIS/IR image fusion in addition to the presented research. The goal for VIS/IR sensor fusion is to provide a composite image that can be easily and intuitively exploited to rapidly extract the relevant information contained in both of the independent acquisitions of the scene. The remote sensing community readily uses this technique [88]. Here, fusion is used for multispectral image sharpening, for example.

A fall-out from the research presented in this thesis is the potential to merge low-light-level and IR imagery. More advance hybrid imaging systems acquire imagery from an intensified imager and thermal IR (TIR) imager simultaneously. By doing so, real-time or post processing techniques can be utilized to fuse the two image products to gain the specific advantages of each sensor type. For instance, the fused image product might utilize the ability of the thermal sensor to resolve the horizon and suppress the effects of “blooming” by the ICCD while still providing the visible cues such as lighting and shadows intuitive to the common observer. Real-time fusion of LLL-VIS/IR image fusion has been performed to generate hybrid imagery useful for collision avoidance or improved situational awareness [89]. A group at MITs Lincoln Labs has been performing real time image fusion with this in mind. Their work involves the real time (low latency) fusion of low-light visible and thermal IR imagery by combining the sensor’s complementary information into a single color video stream for display to the user. Although this technique can significantly improve the interpretability of the imagery, the governing radiometry for the process is simplified. More elaborate techniques might need to be devised that use physical based algorithms that can produce even better hybrid imagery. Perhaps, alternative bands (other than the visible or thermal IR regions) can be utilized for other applications (*i.e*., monitoring plant stress or water quality).

To aid in the improvement of current fusion algorithms and the development of new ones, a high fidelity simulation environment, such as DIRSIG, proves to be extremely useful. Some synthetically fused data has been generated using the DIRSIG environment. The fusion algorithms, however, are far from sophisticated. The data set that is presented used a simple addition technique (see Appendix M). Future work may involve the exploration or improvement of other potential VIR/IR fusion techniques using the DIRSIG simulation environment.

11. Appendix A

11.1 IICCD Specifications

Additional Specification on the PULNiX AG-5745EF-3 automatic gated intensified CCD. Manufacture date is June 3, 1997.

Table 11-1 Intensifier Tube Specifications.

Type	18mm gated, proximity focus
Input	1in (18mm diameter)
Output	2/3in (tapered-fiber coupled to CCD)
Photocathode	GaAs
Phosphor Screen	P20
Gain	15,000 (typical)
Resolution	64 lp/mm
Distortion	N/A
EBI	3.5×10^{-11} lm/cm^2
Spectral resolution	500 nm - 925 nm
Magnification	1
Tube Life	Est. 20,000 hrs.

Table 11-2 CCD Camera Specifications.

Imager	2/3in. interline transfer CCD
Pixel	768 (H) x 493 (V)
Cell size	11 µm x 13 µm
Scanning	525 lines 60 Hz, 2:1 interlace
Sync	Internal/external auto switch HD/VD, 4.0 Vpp impedance 4.7kΩ VD = interlace/non-interlace
TV resolution	570 (H) x 359 (V)
S/N ratio	50 dB min.
Min Illumination	0.5 lux f-1.4 without IR cut filter
Video output	1.0 Vpp composite video, 75Ω
AGC	ON
Gamma	1.0

Table 11-3 AG Series Specifications.

Max. gating speed	100 ns, 10 ns w/ext. gate
Gain control	Variable
Min. Sensitivity	1 x 10^{-6} lux at face plate
Min. Illumination	1 x 10^{-4} lux f = 1.4
Lens mount	C-mount standard. Use 1in. format lenses
Power req.	12V DC (11.5 V to 15 V), 600mA, 6W typical
Size (L ´W ´ H)	171mm x 70mm x 78 mm
Weight	3 lbs., 2 ounces (1.429 kg)
Power cable	12P-02 or KC-10
Power supply	PD-12 or K25-12V
Operating temp.	-10° C to 50° C

12. Appendix B

12.1 Details of ICCD modifications

This section includes addition information to that which was mentioned in section 4.3.1. The inside of the camera can be seen in Figure 12-1 as viewed from the top and BNC side. The camera circuitry consists of 4 printed circuit boards (PCB) stacked on top of one another. The top board controls the gain for the intensifier tube while the second board down from the top controls the CCD gain. Normally, the tube gain is controlled via a low voltage signal form the top board. This signal ranges from 0 V to 9 V. This is the white wire connected to the pad labeled “gain cont”. To bypass the continuous gain control, a 10 kΩ trimmer connected to 8 V and ground was used. In this way the voltage can manually be set (see Figure 12-2). A change in output signal is usually only seen when the voltage is set to 3.5 V and higher.

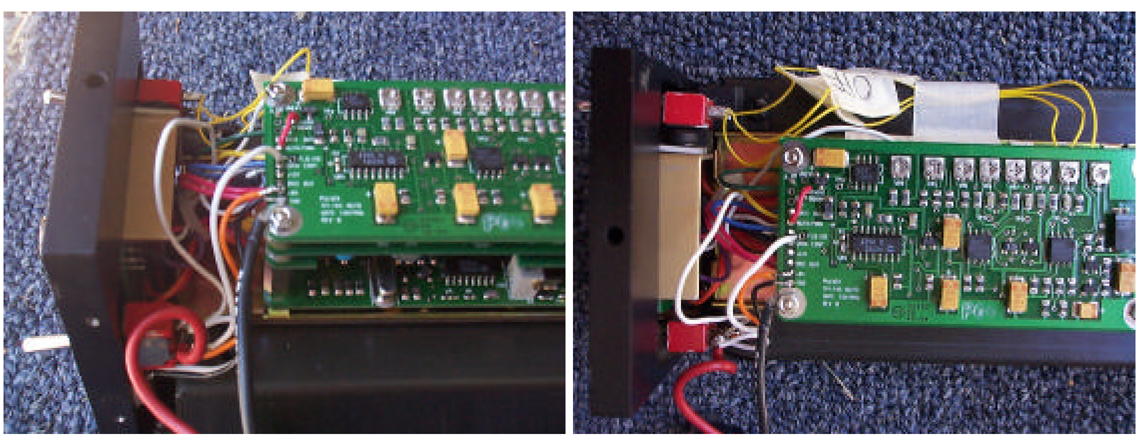

Figure 12-1 Modified ICCD camera circuitry as viewed from the a) right and b) top.

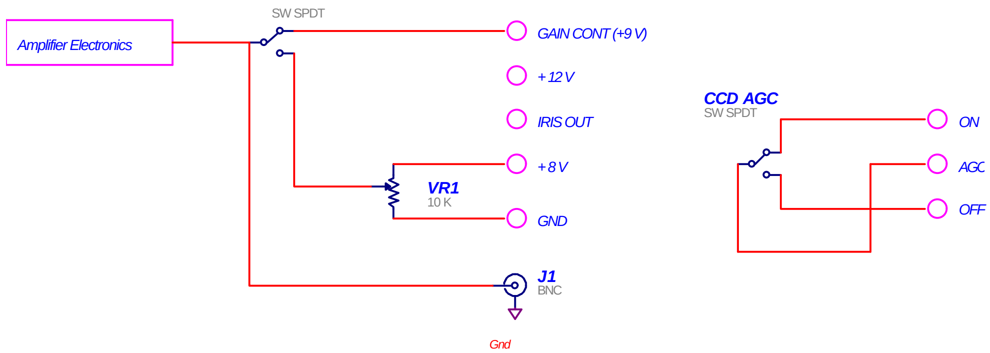

Figure 12-2 Wiring diagram used to over ride the ICCD tube and CCD AGC.

To modify the CCD gain, a single-pole-double-throw switch was used. This can also be seen in Figure 12-2. Figure 12-3 shows the wires coming from the switch and going to the second PCB. The switch simply toggles the CCD AGC on and off. The other end of the yellow wires are soldered to pads on the second board labeled "ON", "AGC", and "OFF". Also seen in Figure 12-3 is the back of the ICCD which contains the switches, trim pot, and BNC output.

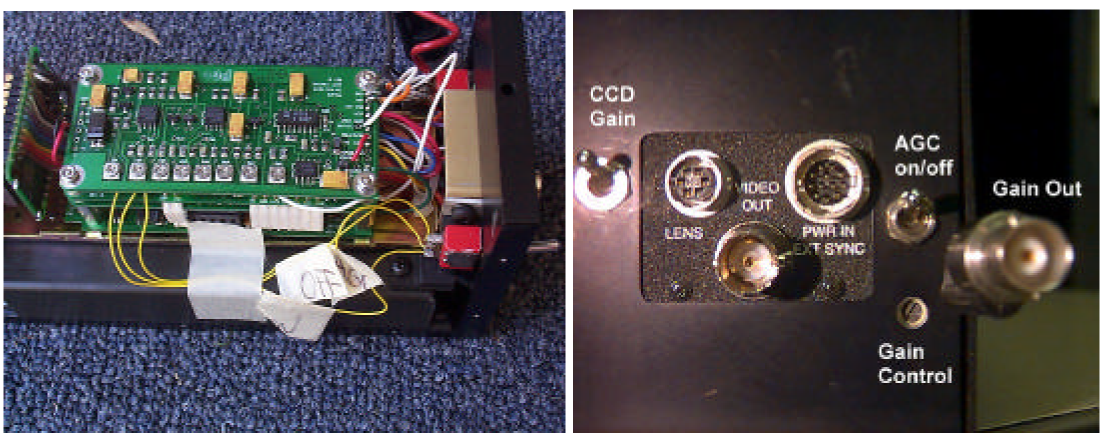

Figure 12-3 Modified ICCD camera circuitry as seen from the a) left and b) back of device.

13. Appendix C

Data was collected on two evenings, August 19th and September 1st. In case one, the moon was below the horizon while in case two the moon was 69% illuminated. Thermister data was collected periodically through out the evening in both cases. Furthermore, it was collected immediately following a thermal image frame grab. Each numerical entry in a data table corresponds to “suffix” of an image file name. For example, if the thermal image entries were 02, 03, the file names would be Nolight02.bmp and Nolight03.bmp.

13.1 Day 1 Collection (Aug 19th - 20th)

Moon below the horizon.

Time = 12:06am -12:15am No Secondary Sources	Gain Setting (v)	Thermal w/ Human	Thermal w/o Human	LLL w/ Human	LLL w/o Human
	6.04	02, 03	00, 01	04, 05	06, 07
File Convention:	7.01			10, 11	08, 09
NolightXX.bmp	7.99			12, 13	14, 15

Time = 12:22am -12:29am Truck Dome Light On	Gain Setting (v)	Thermal w/ Human	Thermal w/o Human	LLL w/ Human	LLL w/o Human
	2.00			18, 19	16, 17
File Convention:	4.04			20, 21	22, 23
NolightXX.bmp	5.01			26, 27	24, 25
	5.95			28, 29	30, 31

Time = 12:35am Thermister Data	Object	Thermister Number	Thermister Reading (kΩ)
	Truck Tire	16	4.137
	Truck Glass	11	4.285
	Truck Body	4	4.062
	Asphalt	2	3.193
	Aluminum Asphalt		3.745
	Aluminum Grass		4.404
	Grass		3.870
	Panel		4.407
	Sidewalk		3.420

Time = 12:51am -12:56am 300w Tungsten Halogen	Gain Setting (v)	Thermal w/ Human	Thermal w/o Human	LLL w/ Human	LLL w/o Human
	3.00			02, 03	00, 01
File Convention:	3.99			04, 05	06, 07
TgHgXX.bmp	5.02			10 11	08, 09
	6.02			12, 13	14, 15

Time = 12:58am -1:15am 150w Tungsten	Gain Setting (v)	Thermal w/ Human	Thermal w/o Human	LLL w/ Human	LLL w/o Human
	2.05	20, 21	22, 23	02, 03	00, 01
File Convention:	3.00			04, 05	06, 07
TgXX.bmp	4.08			10, 11	08, 09
	5.06			12, 13	14, 15
	6.05			18, 19	16, 17

Time = 1:25am Thermister Data	Object	Thermister Number	Thermister Reading (kΩ)
Outside Temp ~57 F	Truck Tire	16	4.278
	Truck Glass	11	4.511
	Truck Body	4	4.148
	Asphalt	2	3.259
	Aluminum Asphalt		3.820
	Aluminum Grass		4.416
	Grass		4.153
	Panel		dead
	Sidewalk		3.529

Time = 3:02am - 3:09am 40w Street Lamp	Gain Setting (v)	Thermal w/ Human	Thermal w/o Human	LLL w/ Human	LLL w/o Human
	3.02			02, 03	00,01
File Convention:	4.14			04, 05	06, 07
LampXX.bmp	5.03			10, 11	08, 09
	5.38			12, 13	14, 15

Time = 3:17am - 3:18am 40w Street Lamp	Gain Setting (v)	Thermal w/ Human	Thermal w/o Human	LLL w/ Human	LLL w/o Human
		02, 03	00, 01		
File Convention:					
LampthXX.bmp					

Time = 3:20am Thermister Data	Object	Thermister Number	Thermister Reading (kΩ)
Outside Temp ~54 F	Truck Tire	16	4.563
	Truck Glass	11	4.736
	Truck Body	4	4.472
	Asphalt	2	3.570
	Aluminum Asphalt		4.072
	Aluminum Grass		4.736
	Grass		4.086
	Panel		dead
	Sidewalk		3.840

Time = 3:38am - 3:44am Misc	Gain Setting (v)	Thermal w/ Human	Thermal w/o Human	LLL w/ Human	LLL w/o Human
Window Open	4.43				00, 01
Window Closed	4.43				02, 03
Truck Headlights On	2.78				04, 05
File Convention:					
WinopeXX.bmp					

Time = 3:47am - 3:47am Misc	Gain Setting (v)	Thermal w/ Human	Thermal w/o Human	LLL w/ Human	LLL w/o Human
3 Minutes After Truck Left			00, 01		
File Convention:					
TrucklXX.bmp					

Time = 3:51am - 3:52am No Truck/ No Lights	Gain Setting (v)	Thermal w/ Human	Thermal w/o Human	LLL w/ Human	LLL w/o Human
File Convention:	5.07			00, 01	
NotrucXX.bmp	6.07			02, 03	
	6.82			04, 05	

Time = 3:53am - 3:55am No Truck/ St. Lamp On	Gain Setting (v)	Thermal w/ Human	Thermal w/o Human	LLL w/ Human	LLL w/o Human
File Convention:	3.07				06,07
NotrucXX.bmp	4.05				08, 09
	5.06				10, 11
	5.46				12, 13

Time = 4:03am - 4:05am No Truck/ 300w Tung. Hal.	Gain Setting (v)	Thermal w/ Human	Thermal w/o Human	LLL w/ Human	LLL w/o Human
File Convention:	4.04				14, 15
NotrucXX.bmp	4.90				16, 17
	5.44				18, 19
	6.06				20, 21

Time = 4:07am - 4:08am No Truck/ 300w Tung. Hal.	Gain Setting (v)	Thermal w/ Human	Thermal w/o Human	LLL w/ Human	LLL w/o Human
File Convention:	4.04			23, 24	
NotrucXX.bmp	4.82			25, 26	
	5.48			27, 28	
Notruc22.bmp = junk					

Time = 4:09am - 4:10am No Truck/ 150w Tungsten	Gain Setting (v)	Thermal w/ Human	Thermal w/o Human	LLL w/ Human	LLL w/o Human
File Convention:	4.05				29, 30
NotrucXX.bmp	5.00				31, 32
	5.60				33, 34
	6.35				35, 36

Time = 4:11am - 4:12am No Truck/ 150w Tungsten	Gain Setting (v)	Thermal w/ Human	Thermal w/o Human	LLL w/ Human	LLL w/o Human
File Convention:	4.01			37, 38	
NotrucXX.bmp	4.73			39, 40	
	5.31			41, 42	
	5.82			43, 44	

13.2 Day 2 Collection (Sept. 1^{st} - 2^{nd})

Moon 69 percent illuminated

Time = 10:03pm - 10:13pm No Secondary Sources	Gain Setting (v)	Thermal w/ Human	Thermal w/o Human	LLL w/ Human	LLL w/o Human
File Convention:	3.99	00, 01	02, 03	04, 05	06, 07
nolighXX.bmp	4.99			10, 11	08, 09
	6.00			12, 13	14, 15
	6.52			18, 19	16, 17
	7.02			20, 21	22, 23

Time = 10:20pm Thermister Data	Object	Thermister Number	Thermister Reading (kΩ)
Outside Temp ~67 F	Truck Tire	16	3.2501
	Truck Glass	11	3.3329
	Truck Body	4	3.1830
	Asphalt	2	2.8440
	Aluminum Asphalt		2.9371
	Aluminum Grass		3.4752
	Grass		3.1061
	Panel	6	3.2603
	Sidewalk		2.7928

Time = 10:55pm - 11:04pm Truck Dome Light On	Gain Setting (v)	Thermal w/ Human	Thermal w/o Human	LLL w/ Human	LLL w/o Human
File Convention:	1.99	01, 02	03, 04	07, 08	05, 06
domeXX.bmp	4.03			09, 10	11, 12
	5.04			17, 18	13, 14
	6.00			20, 21	22, 23
00, 15, 16, 19 = junk					

Time = 11:49pm - 12:01am 300w Tungsten Halogen	Gain Setting (v)	Thermal w/ Human	Thermal w/o Human	LLL w/ Human	LLL w/o Human
File Convention:	3.03	22, 23	20, 21	00, 01	02, 03
tghgXX.bmp	3.99			06, 07	04, 05
	5.00			08, 09	10, 11
	5.48			16, 17	18, 19
	6.03			14, 15	12, 13

Time = 12:06an Thermister Data	Object	Thermister Number	Thermister Reading (kΩ)
Outside Temp ~65 F	Truck Tire	16	3.2928
	Truck Glass	11	3.4164
	Truck Body	4	3.2305
	Asphalt	2	2.9261
	Aluminum Asphalt		2.9714
	Aluminum Grass		3.4340
	Grass		3.0366
	Panel	6	3.2333
	Sidewalk		2.9015

Time = 12:27am - 12:35am 40w Street Lamp	Gain Setting (v)	Thermal w/ Human	Thermal w/o Human	LLL w/ Human	LLL w/o Human
File Convention:	3.01	22, 23	20, 21	04, 05	06, 07
stlmpXX.bmp	4.10			10, 11	08, 09
	5.04			12, 13	14, 15
	5.23			18, 19	16, 17
00, 01, 02, 03 = junk					

Time = 12:37am - 12:38pm 40w Street Lamp	Gain Setting (v)	Thermal w/ Human	Thermal w/o Human	LLL w/ Human	LLL w/o Human
Human pushing on pole	4.92			24, 25	
Human directly under pole	4.92			26, 27	
File Convention:					
stlmpXX.bmp					

Time = 12:55am - 1:08am No Truck / St. Lamp On	Gain Setting (v)	Thermal w/ Human	Thermal w/o Human	LLL w/ Human	LLL w/o Human
File Convention:	5.03			02, 03	00, 01
ntstlpXX.bmp	4.14			04, 05	06, 07
	5.00			10, 11	08, 09
	5.82	18, 19	20, 21	12, 13	14, 15
16, 17, = junk					

Time = 1:15am - 1:25am No Truck / 300w Tung. Hal.	Gain Setting (v)	Thermal w/ Human	Thermal w/o Human	LLL w/ Human	LLL w/o Human
File Convention:	3.07	20, 21	22, 23	02, 03	00, 01
nttghgXX.bmp	4.00			04, 05	06, 07
	4.94			10, 11	08, 09
	5.25			12, 13	14, 15
	5.60			18, 19	16, 17
Human reflected in Al panel		24			

Time = 1:35am Thermister Data	Object	Thermister Number	Thermister Reading (kΩ)
Outside Temp ~63 F	Truck Tire	16	NA
	Truck Glass	11	NA
	Truck Body	4	NA
	Asphalt	2	3.0090
	Aluminum Asphalt		3.0260
	Aluminum Grass		3.4030
	Grass		3.0770
	Panel	6	3.1935
	Sidewalk		2.9550

14. Appendix D

Actual DIRSIG Input Files

This section contains the actual DIRSIG input files as well as other information pertaining to the construction of such files.

14.1 AutoCAD and the GDB

Table 14-1 Layers used in the AutoCAD drawings.

Layer Name	Definition	Material ID and Name	Object Grouping
face_al_panel	aluminum fiducial panels	#27 polished_aluminum	targets
face_arm	arm of human	#18 lt_clothes	human
face_asphalt	asphalt parking lot	#10 asphalt	surface
face_black_panel	black panel	#1 blk_panel	targets
face_blue_panel	blue panel	#7 blue_panel	targets
face_building	CIS building	#15 brick	building
face_concrete	concrete curbs	#14 concrete	surface
face_dirt	dirt	#13 dirt	surface
face_dk_gray_panel	dark gray panel	#5 dk_gray_panel	targets
face_foot	human foot	#20 dk_clothes	human
face_frame	body of truck	#21 red_truck	explorer
face_frame_blk	black part of body on truck	#22 blk_truck	explorer
face_glass_mir_cis	mirrored glass on CIS building	#26 mirrored_glass	building
face_glass_mir_trk	mirrored glass on explorer	#26 mirrored_glass	explorer
face_glass_trk	regular glass on explorer	#25 glass	explorer
face_grass	grass	#12 grass	surface
face_head	head of human	#17 flesh	human

face_leg	legs of human	#19 md_clothes	human
face_lt_gray_panel	light gray panel	#3 lt_gray_panel	targets
face_med_gray_panel	medium gray panel	#4 md_gray_panel	targets
face_molding	molding of truck	#23 molding	explorer
face_red_panel	red panel	#6 red_panel	targets
face_res_target_blk	bars on resolution target	#9 res_trgt_blk	targets
face_res_target_wht	back board on resolution target	#8 res_trgt_wht	targets
face_rim	rims on truck	#27 polished_aluminum	explorer
face_sign_light	sign and secondary sources	#16 sign	building
face_tire	tire on truck	#24 rubber	explorer
face_waist_chest	waist and chest of human	#18 lt_clothes	human
face_white_panel	white panel	#2 wht_panel	targets
face_yellow_line	parking lot lines	#11 yellow_line	surface
wire_arm	arm of human	NA	NA
wire_asphalt	parking lot asphalt	NA	NA
wire_building	CIS building	NA	NA
wire_calf	calf of human	NA	NA
wire_concrete	concrete curbs	NA	NA
wire_dirt	dirt	NA	NA
wire_foot	foot of human	NA	NA
wire_head	head of human	NA	NA
wire_res_target	bars on resolution target	NA	NA
wire_sign_light	sign and secondary sources	NA	NA
wire_thigh	thigh of human	NA	NA
wire_waist	waist of human	NA	NA

Summary of procedure used in the development of the geometric database.

- Save all parts in the full scene drawing as separate files (.dwg)
    - Hide and lock layer of interest, turn on all the rest and delete all facets.

    - Save remaining parts of interest as desired part.
    - Purge all unused layers, views, and blocks
- Run addnorms LISP routine
    - assign a part name (i.e., part name: asphalt)
    - save as asphalt_norm.dwg
- Run pick LISP routine
    - assign a material ID and name
    - save as asphalt_atts.dwg
- Create objects
    - insert all parts with 0, 0, 0 insertion point
    - save as explorer_obj.dwg, for example
- Create scene
    - insert objects with 0, 0, 0 insertion point
    - save as scene_scn.dwg
- Run dirsigdump LISP routine to generate scene_scn.dat file
    - Rename to scene_scn.dump so as not to get confused with DIRSIG output

14.2 Material files

Table 14-2 Summary of material specifications. Bold values come from the DCS Corp. database while non-bold values are estimated from DCS tables and field measurements.

Material and ID	SpHt	Thm Con	Mass Dens	Specu-larity	Vis ems	Them ems	Exp A
1 blk_panel	0.2	0.5	0.2	0.15	0.95	0.95	-0.5
2 wht_panel	0.2	0.5	0.2	0.15	0.18	0.18	-0.5
3 lt_gray_panel	**0.6689**	**1.10**	**0.400**	0.10	0.56	**0.90**	-0.5
4 md_gray_panel	**0.6689**	**1.10**	**0.400**	0.10	0.85	**0.90**	-0.5
5 dk_gray_panel	**0.6689**	**1.10**	**0.400**	0.10	0.88	**0.90**	-0.5
6 red_panel	**0.6689**	**1.10**	**0.400**	0.10	0.89	**0.90**	-0.5

7 blue_panel	**0.6689**	**1.10**	**0.400**	0.10	0.76	**0.90**	-0.5
8 res_trgt_wht	0.2	0.5	0.2	0.15	0.28	0.28	-0.5
9 res_trgt_blk	0.2	0.5	0.2	0.15	0.82	0.82	-0.5
10 asphalt	**0.2200**	**5.93**	**2.114**	0.10	0.89	**0.93**	-0.5
11 yellow_line	**0.2200**	**5.93**	**2.114**	0.15	0.81	**0.93**	-0.5
12 grass	**1.0**	**5.0**	**1.0**	0.10	0.80	0.93	-0.5
13 dirt	**0.2000**	**2.88**	**1.350**	0.10	0.94	**0.90**	-0.5
14 concrete	**0.1600**	**15.48**	**1.600**	0.10	0.83	**0.88**	-0.5
15 brick	**0.2098**	**8.17**	**0.768**	0.10	0.84	**0.93**	-0.5
16 sign	**0.1111**	**464.40**	**7.833**	0.10	0.94	0.94	-0.5
17 flesh	1.0	50.0	1.0	0.10	0.78	0.55	-0.5
18 lt_clothes	**0.3799**	**2.15**	**1.160**	0	0.41	**0.77**	-0.5
19 md_clothes	**0.3799**	**2.15**	**1.160**	0	0.61	**0.77**	-0.5
20 dk_clothes	**0.3799**	**2.15**	**1.160**	0	0.96	**0.77**	-0.5
21 red_truck	**0.1111**	**464.40**	**7.833**	0.40	0.88	**0.10**	-0.5
22 blk_truck	**0.1111**	**464.40**	**7.833**	0.20	0.90	**0.90**	-0.5
23 molding	**0.0400**	**64.50**	**1.400**	0.10	0.94	**0.72**	-0.5
24 rubber	**0.2986**	**1.30**	**1.198**	0.05	0.96	**0.99**	-0.5
25 glass	**0.2000**	**12.04**	**2.600**	0.20	0.70	**0.79**	-0.5
26 mirrored_glass	**0.2000**	**12.04**	**2.600**	0.90	0.05	**0.79**	-0.5
27 polished_aluminum	**0.2198**	**1754.40**	**2.390**	0.50	**0.10**	**0.04**	-0.5

```
## Materials file for LLL DIRSIG work
# Created by Emmett Ientilucci
# 10-15-98
#
# FILE TYPE:    DIRSIG Materials file
# CREATEOR:     `convert_materials' utility
# DATE          Wed Oct  4 12:37:27 EDT 1995
# NOTES:        Entries can be arannged in any order
#               Tags within any entry can be in any order
#               A minimal set of tags are required (see below)
#
# Required Tags:
#      MATERIAL_ENTRY_BEGIN                    start an entry
#      MATERIAL_NAME                           name of the material
#      MATERIAL_ID                             #ID of the material
#      SPECIFIC_HEAT                           specific heat
```

```
#    THERMAL_CONDUCTIVITY          thermal conductivity
#    MASS_DENSITY                  mass desnity
#    SPECULARITY                   specularity of the material surface
#                                  0.0 = 100% diffuse and 1.0 = 100% specular
#    VISIBLE_EMISSIVITY            solar/incident emissivity
#    THERMAL_EMISSIVITY            thermal/exit emissivity
#    EXPOSED_AREA                  DCS/THERM surface area term
#    OPTICAL_DESCRIPTION           OPAQUE, UNIFORM_TRANSMISSION, or
#                                  NONUNIFORM_TRANSMISSION
#    EMISSIVITY_FILE               name of emissivity file
#    THICKNESS                     thickness [cm]
#    DOUBLE_SIDED                  if true, puts normal on both sides of facet
#    MATERIAL_ENTRY_END            end of entry
#
# Optional/Additional Tags:
#    EXTINCTION_FILE               extiction file -- required for transmission
#    TEXTURE_FILE                   name DIRSIG Texture Image file for material
#    USE_GAUSSIAN_TEXTURE          flag to generate gaussian texture
#
# Materials are
# 1 blk_panel          10 asphalt       18 lt_clothes
# 2 wht_panel          11 yellow_line   19 md_clothes
# 3 lt_gray_panel      12 grass         20 dk_clothes
# 4 md_gray_panel      13 dirt          21 red_truck
# 5 dk_gray_panel      14 concrete      22 blk_truck
# 6 red_panel          15 brick         23 molding
# 7 blue_panel         16 sign          24 rubber
# 8 res_trgt_wht       17 flesh         25 glass
# 9 res_trgt_blk                        26 mirrored_glass
#                                       27 polished_aluminum
```

#--- # Painted Wood Targets etc. #--- #1-----Black Construction Board----- #-----Guess based on DCS tables # -----and ems data collected MATERIAL_ENTRY_BEGIN MATERIAL_NAME = blk_panel MATERIAL_ID = 1 SPECIFIC_HEAT = 0.2 THERMAL_CONDUCTIVITY = 0.5 MASS_DENSITY = 0.2 SPECULARITY = 0.15 VISIBLE_EMISSIVITY = 0.95 THERMAL_EMISSIVITY = 0.95 EXPOSED_AREA = -0.5 THICKNESS = 1.0 OPTICAL_DESCRIPTION = OPAQUE EMISSIVITY_FILE = blk_panel.ems DOUBLE_SIDED = TRUE MATERIAL_ENTRY_END	#2-----White Construction Board----- #-----Guess based on DCS tables # -----and ems data collected MATERIAL_ENTRY_BEGIN MATERIAL_NAME = wht_panel MATERIAL_ID = 2 SPECIFIC_HEAT = 0.2 THERMAL_CONDUCTIVITY = 0.5 MASS_DENSITY = 0.2 SPECULARITY = 0.15 VISIBLE_EMISSIVITY = 0.25 THERMAL_EMISSIVITY = 0.90 EXPOSED_AREA = -0.5 THICKNESS = 1.0 OPTICAL_DESCRIPTION = OPAQUE EMISSIVITY_FILE = wht_panel.ems DOUBLE_SIDED = TRUE MATERIAL_ENTRY_END	#3-----Emulates: Wood-Green Paint, DCS MATERIAL_ENTRY_BEGIN MATERIAL_NAME = lt_gray_panel MATERIAL_ID = 3 SPECIFIC_HEAT = 0.6689 THERMAL_CONDUCTIVITY = 1.10 MASS_DENSITY = 0.400 SPECULARITY = 0.10 VISIBLE_EMISSIVITY = 0.56 THERMAL_EMISSIVITY = 0.90 EXPOSED_AREA = -0.5 THICKNESS = 1.0 OPTICAL_DESCRIPTION = OPAQUE EMISSIVITY_FILE = lt_gray_panel.ems DOUBLE_SIDED = TRUE MATERIAL_ENTRY_END
#4----Emulates: Wood-Green Paint, DCS MATERIAL_ENTRY_BEGIN MATERIAL_NAME = md_gray_panel MATERIAL_ID = 4 SPECIFIC_HEAT = 0.6689 THERMAL_CONDUCTIVITY = 1.10 MASS_DENSITY = 0.400 SPECULARITY = 0.10 VISIBLE_EMISSIVITY = 0.85 THERMAL_EMISSIVITY = 0.90 EXPOSED_AREA = -0.5 THICKNESS = 1.0 OPTICAL_DESCRIPTION = OPAQUE EMISSIVITY_FILE = md_gray_panel.ems DOUBLE_SIDED = TRUE	#5----Emulates: Wood-Green Paint, DCS MATERIAL_ENTRY_BEGIN MATERIAL_NAME = dk_gray_panel MATERIAL_ID =5 SPECIFIC_HEAT = 0.6689 THERMAL_CONDUCTIVITY = 1.10 MASS_DENSITY = 0.400 SPECULARITY = 0.10 VISIBLE_EMISSIVITY = 0.88 THERMAL_EMISSIVITY = 0.90 EXPOSED_AREA = -0.5 THICKNESS = 1.0 OPTICAL_DESCRIPTION = OPAQUE EMISSIVITY_FILE = dk_gray_panel.ems DOUBLE_SIDED = TRUE	#6----Emulates: Wood-Green Paint, DCS MATERIAL_ENTRY_BEGIN MATERIAL_NAME = red_panel MATERIAL_ID = 6 SPECIFIC_HEAT = 0.6689 THERMAL_CONDUCTIVITY = 1.10 MASS_DENSITY = 0.400 SPECULARITY = 0.10 VISIBLE_EMISSIVITY = 0.89 THERMAL_EMISSIVITY = 0.90 EXPOSED_AREA = -0.5 THICKNESS = 1.0 OPTICAL_DESCRIPTION = OPAQUE EMISSIVITY_FILE = red_panel.ems DOUBLE_SIDED = FALSE

MATERIAL_ENTRY_END	MATERIAL_ENTRY_END	MATERIAL_ENTRY_END
#7----Emulates: Wood-Green Paint, DCS MATERIAL_ENTRY_BEGIN MATERIAL_NAME = blue_panel MATERIAL_ID =7 SPECIFIC_HEAT = 0.6689 THERMAL_CONDUCTIVITY = 1.10 MASS_DENSITY = 0.400 SPECULARITY = 0.10 VISIBLE_EMISSIVITY = 0.76 THERMAL_EMISSIVITY = 0.90 EXPOSED_AREA = -0.5 THICKNESS = 1.0 OPTICAL_DESCRIPTION = OPAQUE EMISSIVITY_FILE = blue_panel.ems DOUBLE_SIDED = FALSE MATERIAL_ENTRY_END	#--- # Resolution Target (Wht and Blk Areas) #--- #8----Guess based on DCS tables # -----and ems data collected MATERIAL_ENTRY_BEGIN MATERIAL_NAME = res_trgt_wht MATERIAL_ID = 8 SPECIFIC_HEAT = 0.2 THERMAL_CONDUCTIVITY = 0.5 MASS_DENSITY = 0.2 SPECULARITY = 0.15 VISIBLE_EMISSIVITY = 0.28 THERMAL_EMISSIVITY = 0.92 EXPOSED_AREA = -0.5 THICKNESS = 0.25 OPTICAL_DESCRIPTION = OPAQUE EMISSIVITY_FILE = res_trgt_wht.ems DOUBLE_SIDED = TRUE MATERIAL_ENTRY_END	#9----Guess based on DCS tables # -----and ems data collected MATERIAL_ENTRY_BEGIN MATERIAL_NAME = res_trgt_blk MATERIAL_ID = 9 SPECIFIC_HEAT = 0.2 THERMAL_CONDUCTIVITY = 0.5 MASS_DENSITY = 0.2 SPECULARITY = 0.15 VISIBLE_EMISSIVITY = 0.82 THERMAL_EMISSIVITY = 0.92 EXPOSED_AREA = -0.5 THICKNESS = 0.25 OPTICAL_DESCRIPTION = OPAQUE EMISSIVITY_FILE = res_trgt_blk.ems DOUBLE_SIDED = TRUE MATERIAL_ENTRY_END
#--- # Surface / Soil / Materials #--- #10 -----Emulates: Asphalt (2), DCS # MATERIAL_ENTRY_BEGIN # MATERIAL_NAME = asphalt # MATERIAL_ID = 10 # SPECIFIC_HEAT = 0.2200 # THERMAL_CONDUCTIVITY = 5.93 # MASS_DENSITY = 2.114 # SPECULARITY = 0.10 # VISIBLE_EMISSIVITY = 0.89 # THERMAL_EMISSIVITY = 0.93 # EXPOSED_AREA = -0.5 # OPTICAL_DESCRIPTION = OPAQUE # EMISSIVITY_FILE = asphalt.ems # DOUBLE_SIDED = TRUE # MATERIAL_ENTRY_END	#10 MATERIAL_ENTRY_BEGIN MATERIAL_NAME = asphalt MATERIAL_ID = 10 SPECIFIC_HEAT = .7 THERMAL_CONDUCTIVITY = 23.0 MASS_DENSITY = 2.114 SPECULARITY = 0.05 VISIBLE_EMISSIVITY = 0.95 THERMAL_EMISSIVITY = 0.65 EXPOSED_AREA = 0.20 THICKNESS = 2.0 OPTICAL_DESCRIPTION = OPAQUE EMISSIVITY_FILE = asphalt.ems DOUBLE_SIDED = TRUE MATERIAL_ENTRY_END	#11---Yellow Parking Lot Lines on Asphalt---- -- # -----Emulates: Asphalt (2), DCS MATERIAL_ENTRY_BEGIN MATERIAL_NAME = yellow_line MATERIAL_ID = 11 SPECIFIC_HEAT = 0.4650 THERMAL_CONDUCTIVITY = 20.9300 MASS_DENSITY = 1.0000 SPECULARITY = 0.10 VISIBLE_EMISSIVITY = 0.95 THERMAL_EMISSIVITY = 0.65 EXPOSED_AREA = 0.40 THICKNESS = 4.0 OPTICAL_DESCRIPTION = OPAQUE EMISSIVITY_FILE = yellow_line.ems DOUBLE_SIDED = FALSE MATERIAL_ENTRY_END
#12---Emulates: Grass Dry, Summer, DCS # but the grass had dew on it so, # vis em 0.91 -> 0.80 (refl goes up) # thm em 0.88 -> 0.93 (refl goes dwn) # MATERIAL_ENTRY_BEGIN # MATERIAL_NAME = grass # MATERIAL_ID = 12 # SPECIFIC_HEAT = 1.000 # THERMAL_CONDUCTIVITY = 5.00 # MASS_DENSITY = 1.000 # SPECULARITY = 0.10 # VISIBLE_EMISSIVITY = 0.80 # THERMAL_EMISSIVITY = 0.93 # EXPOSED_AREA = -0.5 # OPTICAL_DESCRIPTION = OPAQUE # EMISSIVITY_FILE = grass.ems # DOUBLE_SIDED = TRUE # MATERIAL_ENTRY_END	#12 MATERIAL_ENTRY_BEGIN MATERIAL_NAME = grass MATERIAL_ID = 12 SPECIFIC_HEAT = 1.8000 THERMAL_CONDUCTIVITY = 20.0000 MASS_DENSITY = 1.0000 SPECULARITY = 0.00 VISIBLE_EMISSIVITY = 0.65 THERMAL_EMISSIVITY = 0.90 EXPOSED_AREA = 0.45 THICKNESS = 4.0 OPTICAL_DESCRIPTION = OPAQUE EMISSIVITY_FILE = grass.ems DOUBLE_SIDED = TRUE MATERIAL_ENTRY_END	#13-----Emulates: Dirt-Dry, DCS # if damp, vis ems and thm ems go up MATERIAL_ENTRY_BEGIN MATERIAL_NAME = dirt MATERIAL_ID = 13 SPECIFIC_HEAT = 0.2000 THERMAL_CONDUCTIVITY = 2.88 MASS_DENSITY = 1.350 SPECULARITY = 0.10 VISIBLE_EMISSIVITY = 0.94 THERMAL_EMISSIVITY = 0.90 EXPOSED_AREA = -0.5 OPTICAL_DESCRIPTION = OPAQUE EMISSIVITY_FILE = dirt.ems DOUBLE_SIDED = TRUE MATERIAL_ENTRY_END
#14-----Emulates: Concrete - Smooth, DCS MATERIAL_ENTRY_BEGIN MATERIAL_NAME = concrete MATERIAL_ID = 14 SPECIFIC_HEAT = 0.1600 THERMAL_CONDUCTIVITY = 15.48 MASS_DENSITY = 1.600 SPECULARITY = 0.10 VISIBLE_EMISSIVITY = 0.83 THERMAL_EMISSIVITY = 0.88 EXPOSED_AREA = -0.5 THICKNESS = 4.0	#15-----RIT Red Brick----- #-----Emulates: Brick-Red, Rough, DCS MATERIAL_ENTRY_BEGIN MATERIAL_NAME = brick MATERIAL_ID = 15 SPECIFIC_HEAT = 0.2098 THERMAL_CONDUCTIVITY = 8.17 MASS_DENSITY = 0.768 SPECULARITY = 0.10 VISIBLE_EMISSIVITY = 0.84 THERMAL_EMISSIVITY = 0.93 EXPOSED_AREA = -0.5	#16------Green Parking Signs----- #-----Emulates: Carbon Steel-ForstGrn, DCS MATERIAL_ENTRY_BEGIN MATERIAL_NAME = sign MATERIAL_ID = 16 SPECIFIC_HEAT = 0.1111 THERMAL_CONDUCTIVITY = 464.40 MASS_DENSITY = 7.833 SPECULARITY = 0.10 VISIBLE_EMISSIVITY = 0.94 THERMAL_EMISSIVITY = 0.94 EXPOSED_AREA = -0.5

OPTICAL_DESCRIPTION = OPAQUE EMISSIVITY_FILE = concrete.ems DOUBLE_SIDED = TRUE MATERIAL_ENTRY_END	OPTICAL_DESCRIPTION = OPAQUE EMISSIVITY_FILE = brick.ems DOUBLE_SIDED = TRUE MATERIAL_ENTRY_END	THICKNESS = 1.0 OPTICAL_DESCRIPTION = OPAQUE EMISSIVITY_FILE = sign.ems DOUBLE_SIDED = FALSE MATERIAL_ENTRY_END
#--- # Human Attributes #--- # Guess at parameters # vis ems = avg of ems from .38-.652 #17 thm ems = from data looks lower at .78 MATERIAL_ENTRY_BEGIN MATERIAL_NAME = flesh MATERIAL_ID = 17 SPECIFIC_HEAT = 1.0 THERMAL_CONDUCTIVITY = 50.0 MASS_DENSITY = 1.0 SPECULARITY = 0.10 VISIBLE_EMISSIVITY = 0.78 THERMAL_EMISSIVITY = 0.55 EXPOSED_AREA = -0.5 THICKNESS = 4.0 OPTICAL_DESCRIPTION = OPAQUE EMISSIVITY_FILE = flesh.ems DOUBLE_SIDED = FALSE MATERIAL_ENTRY_END	#18-----Emulates: Nylon Cloth, DCS MATERIAL_ENTRY_BEGIN MATERIAL_NAME = lt_clothes MATERIAL_ID = 18 SPECIFIC_HEAT = 0.3799 THERMAL_CONDUCTIVITY = 2.15 MASS_DENSITY = 1.160 SPECULARITY = 0.0 VISIBLE_EMISSIVITY = 0.41 THERMAL_EMISSIVITY = 0.77 EXPOSED_AREA = -0.5 THICKNESS = 4.0 OPTICAL_DESCRIPTION = OPAQUE EMISSIVITY_FILE = lt_clothes.ems DOUBLE_SIDED = FALSE MATERIAL_ENTRY_END	#19-----Emulates: Nylon Cloth, DCS MATERIAL_ENTRY_BEGIN MATERIAL_NAME = md_clothes MATERIAL_ID = 19 SPECIFIC_HEAT = 0.3799 THERMAL_CONDUCTIVITY = 2.15 MASS_DENSITY = 1.160 SPECULARITY = 0.0 VISIBLE_EMISSIVITY = 0.61 THERMAL_EMISSIVITY = 0.77 EXPOSED_AREA = -0.5 THICKNESS = 4.0 OPTICAL_DESCRIPTION = OPAQUE EMISSIVITY_FILE = md_clothes.ems DOUBLE_SIDED = TRUE MATERIAL_ENTRY_END
#20-----Emulates: Nylon Cloth, DCS MATERIAL_ENTRY_BEGIN MATERIAL_NAME = dk_clothes MATERIAL_ID = 20 SPECIFIC_HEAT = 0.3799 THERMAL_CONDUCTIVITY = 2.15 MASS_DENSITY = 1.160 SPECULARITY = 0.0 VISIBLE_EMISSIVITY = 0.96 THERMAL_EMISSIVITY = 0.77 EXPOSED_AREA = -0.5 THICKNESS = 4.0 OPTICAL_DESCRIPTION = OPAQUE EMISSIVITY_FILE = dk_clothes.ems DOUBLE_SIDED = FALSE MATERIAL_ENTRY_END	#--- # 1995 Red Explorer #--- #21-----Painted Red Body----- #-----Emulates: Carbon Steel-Cleaned, DCS MATERIAL_ENTRY_BEGIN MATERIAL_NAME = red_ truck MATERIAL_ID = 21 SPECIFIC_HEAT = 0.1111 THERMAL_CONDUCTIVITY = 464.40 MASS_DENSITY = 7.833 SPECULARITY = 0.40 VISIBLE_EMISSIVITY = 0.88 THERMAL_EMISSIVITY = 0.70 EXPOSED_AREA = -0.5 THICKNESS = 0.2 OPTICAL_DESCRIPTION = OPAQUE EMISSIVITY_FILE = red_truck.ems DOUBLE_SIDED = FALSE MATERIAL_ENTRY_END	#22-----Painted Black Parts----- #-----Emulates: Carbon Steel-Black, DCS MATERIAL_ENTRY_BEGIN MATERIAL_NAME = blk_truck MATERIAL_ID = 22 SPECIFIC_HEAT = 0.1111 THERMAL_CONDUCTIVITY = 464.40 MASS_DENSITY = 7.833 SPECULARITY = 0.20 VISIBLE_EMISSIVITY = 0.90 THERMAL_EMISSIVITY = 0.90 EXPOSED_AREA = -0.5 THICKNESS = 0.2 OPTICAL_DESCRIPTION = OPAQUE EMISSIVITY_FILE = blk_truck.ems DOUBLE_SIDED = FALSE MATERIAL_ENTRY_END
#23-----Plastic Molding----- #-----Emulates: Plastic Sheet, DCS MATERIAL_ENTRY_BEGIN MATERIAL_NAME = molding MATERIAL_ID = 23 SPECIFIC_HEAT = 0.0400 THERMAL_CONDUCTIVITY = 64.50 MASS_DENSITY = 1.400 SPECULARITY = 0.10 VISIBLE_EMISSIVITY = 0.94 THERMAL_EMISSIVITY = 0.72 EXPOSED_AREA = -0.5 THICKNESS = 1.0 OPTICAL_DESCRIPTION = OPAQUE EMISSIVITY_FILE = molding.ems DOUBLE_SIDED = FALSE MATERIAL_ENTRY_END	#24-----Emulates: Rubber-Tire, DCS MATERIAL_ENTRY_BEGIN MATERIAL_NAME = rubber MATERIAL_ID = 24 SPECIFIC_HEAT = 0.2986 THERMAL_CONDUCTIVITY = 1.30 MASS_DENSITY = 1.198 SPECULARITY = 0.05 VISIBLE_EMISSIVITY = 0.96 THERMAL_EMISSIVITY = 0.99 EXPOSED_AREA = -0.5 THICKNESS = 1.0 OPTICAL_DESCRIPTION = OPAQUE EMISSIVITY_FILE = rubber.ems DOUBLE_SIDED = FALSE MATERIAL_ENTRY_END	#--- # Misc. Glass and Aluminum #--- #25-----Regular Glass----- #-----Emulates: Glass, DCS MATERIAL_ENTRY_BEGIN MATERIAL_NAME = glass MATERIAL_ID = 25 SPECIFIC_HEAT = 0.2000 THERMAL_CONDUCTIVITY = 12.04 MASS_DENSITY = 2.600 SPECULARITY = 0.20 VISIBLE_EMISSIVITY = 0.70 THERMAL_EMISSIVITY = 0.79 EXPOSED_AREA = -0.5 THICKNESS = 0.5 OPTICAL_DESCRIPTION = OPAQUE EMISSIVITY_FILE = glass.ems DOUBLE_SIDED = FALSE MATERIAL_ENTRY_END

#26-----Mirrored Glass, Truck and CIS-----
#-----Emulates: Glass, DCS
MATERIAL_ENTRY_BEGIN
MATERIAL_NAME = mirrored_glass
MATERIAL_ID = 26
SPECIFIC_HEAT = 0.2000
THERMAL_CONDUCTIVITY = 12.04
MASS_DENSITY = 2.6000
SPECULARITY = 0.90
VISIBLE_EMISSIVITY = 0.05
THERMAL_EMISSIVITY = 0.79
EXPOSED_AREA = -0.5
THICKNESS = 0.5
OPTICAL_DESCRIPTION = OPAQUE
EMISSIVITY_FILE = glass.ems
DOUBLE_SIDED = FALSE
MATERIAL_ENTRY_END
	#27-----Polished Aluminum, Truck Rims-----
	#-----Emulates: Aluminum Polished, DCS
	MATERIAL_ENTRY_BEGIN
	MATERIAL_NAME = polished_aluminum
	MATERIAL_ID = 27
	SPECIFIC_HEAT = 0.2198
	THERMAL_CONDUCTIVITY = 1754.40
	MASS_DENSITY = 2.390
	SPECULARITY = 0.50
	VISIBLE_EMISSIVITY = 0.10
	#THERMAL_EMISSIVITY = 0.04
	THERMAL_EMISSIVITY = 0.84
	EXPOSED_AREA = -0.5
	THICKNESS = 0.2
	OPTICAL_DESCRIPTION = OPAQUE
	EMISSIVITY_FILE = polished_alum2.ems
	DOUBLE_SIDED = FALSE
	MATERIAL_ENTRY_END	

14.3 Emissivity Curves

Emissivity files are constructed as illustrated in Figure 14-1. The first value in the file is the number of curves contained in the file. The next 90 values represent the angular falloff. Since the SIG image formed was from one look angle only as well as being synthesized at night, the angular falloff was made the same for all materials, as seen in Figure 14-2. All the emissivity files for this research contained data from 0.4 μm to 14 μm. These curves can be seen below.

```
1                      #number of emissivity curves in file
1.00                   #start of angular fall off (0-90deg)
0.99
.
.
0.87
0.85
CURVE_BEGIN            #beginning of emissivity data
0.380  0.98            #wavelength, emissivity
0.384  0.95
.
.
12.30  0.93
12.34  0.94
```

Figure 14-1 Example of emissivity file.

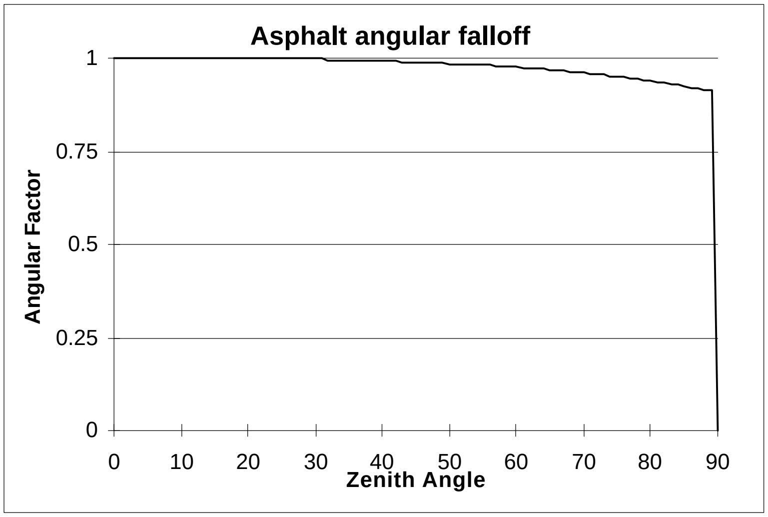

Figure 14-2 Generic angular falloff.

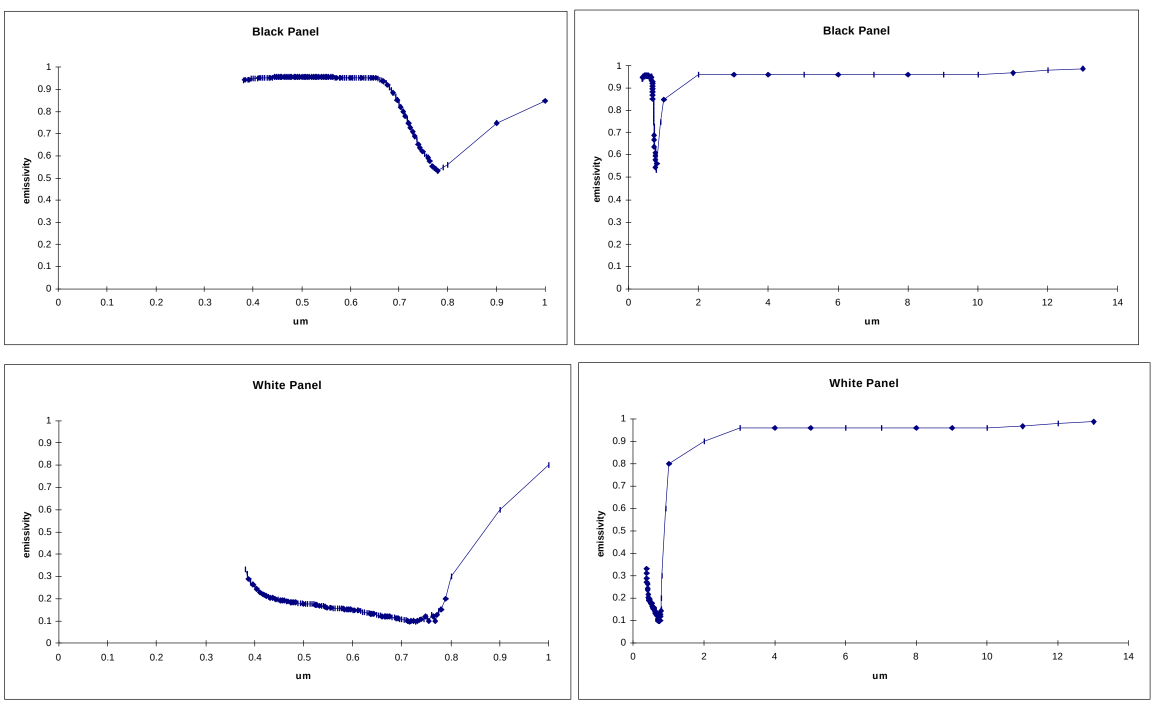

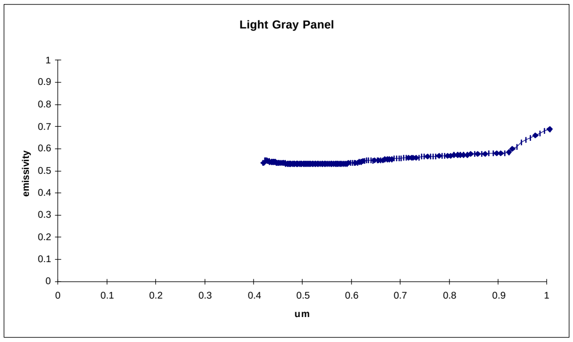
Light Gray Panel
emissivity
um

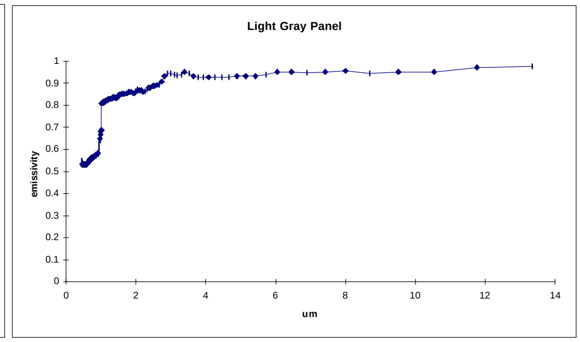
Light Gray Panel
emissivity
um

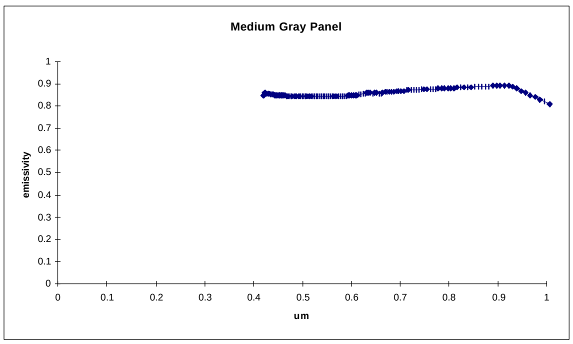
Medium Gray Panel
emissivity
um

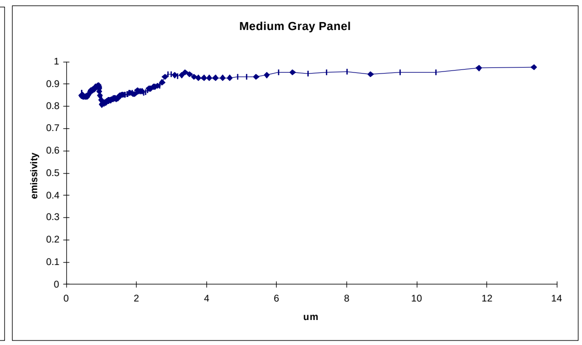
Medium Gray Panel
emissivity
um

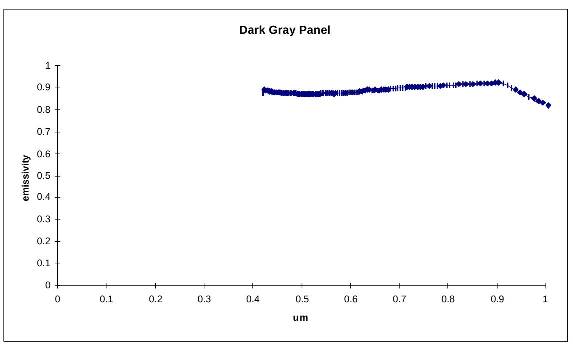
Dark Gray Panel
emissivity
um

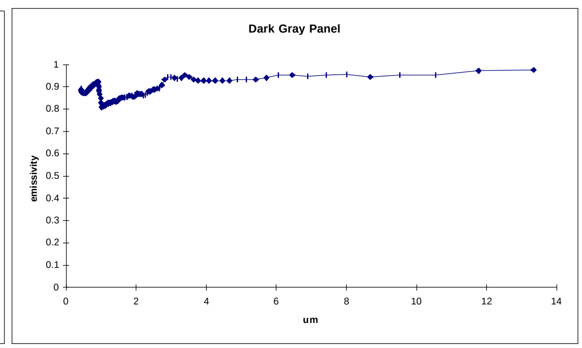
Dark Gray Panel
emissivity
um

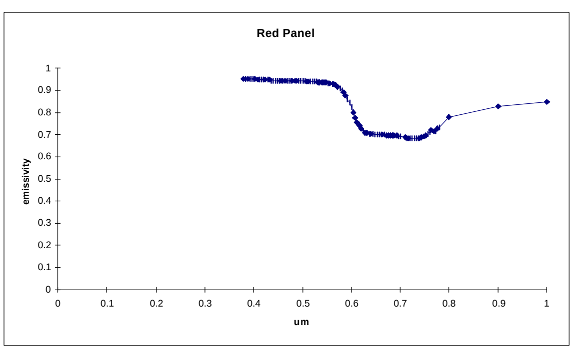
Red Panel
emissivity
um

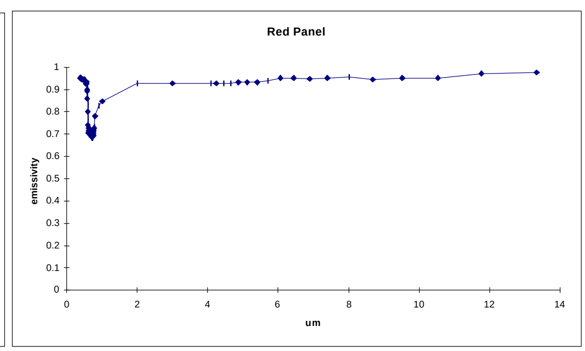
Red Panel
emissivity
um

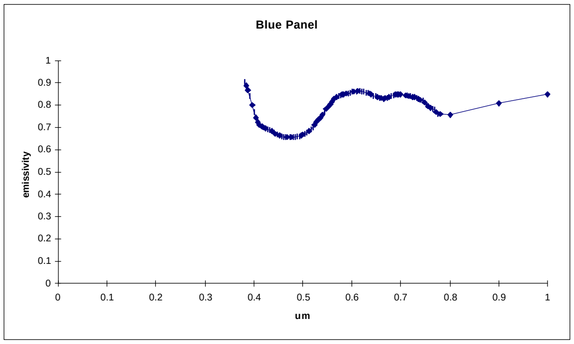
Blue Panel
emissivity
1 0.9 0.8 0.7 0.6 0.5 0.4 0.3 0.2 0.1 0
0 0.1 0.2 0.3 0.4 0.5 0.6 0.7 0.8 0.9 1
um

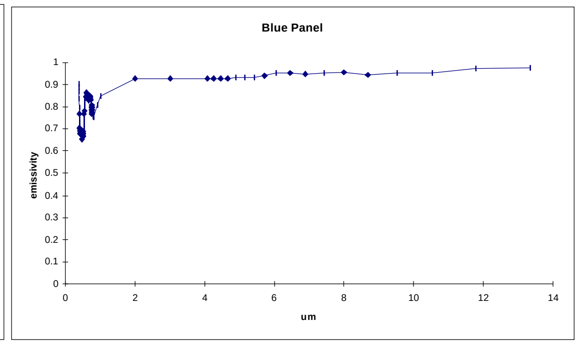
Blue Panel
emissivity
1 0.9 0.8 0.7 0.6 0.5 0.4 0.3 0.2 0.1 0
0 2 4 6 8 10 12 14
um

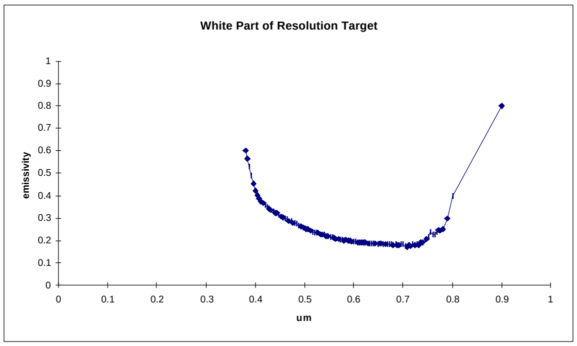
White Part of Resolution Target
emissivity
1 0.9 0.8 0.7 0.6 0.5 0.4 0.3 0.2 0.1 0
0 0.1 0.2 0.3 0.4 0.5 0.6 0.7 0.8 0.9 1
um

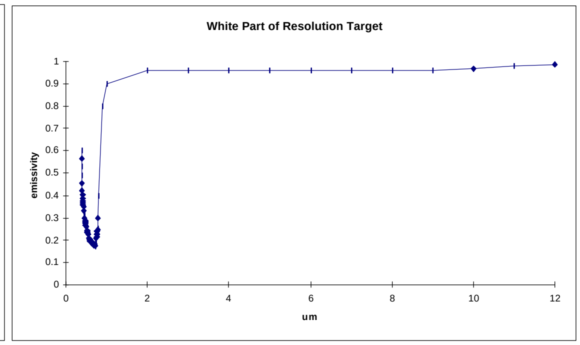
White Part of Resolution Target
emissivity
1 0.9 0.8 0.7 0.6 0.5 0.4 0.3 0.2 0.1 0
0 2 4 6 8 10 12
um

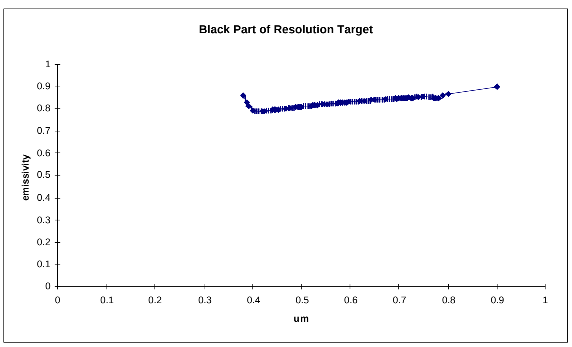
Black Part of Resolution Target
emissivity
1 0.9 0.8 0.7 0.6 0.5 0.4 0.3 0.2 0.1 0
0 0.1 0.2 0.3 0.4 0.5 0.6 0.7 0.8 0.9 1
um

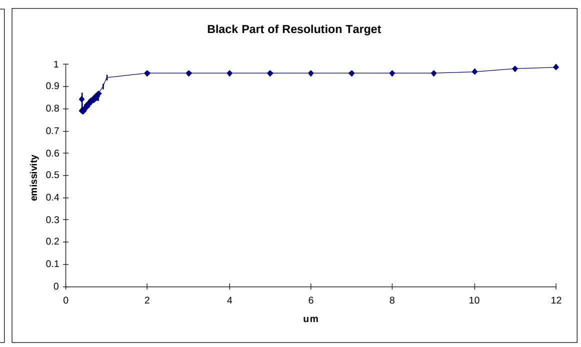
Black Part of Resolution Target
emissivity
1 0.9 0.8 0.7 0.6 0.5 0.4 0.3 0.2 0.1 0
0 2 4 6 8 10 12
um

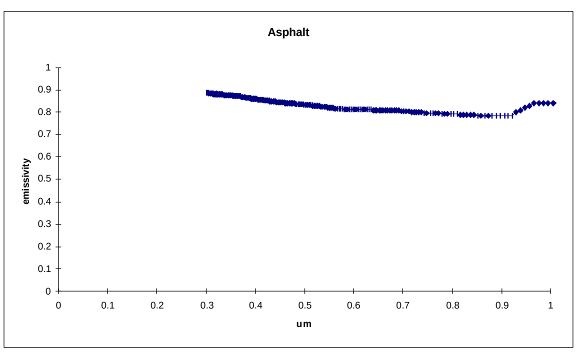
Asphalt
emissivity
1 0.9 0.8 0.7 0.6 0.5 0.4 0.3 0.2 0.1 0
0 0.1 0.2 0.3 0.4 0.5 0.6 0.7 0.8 0.9 1
um

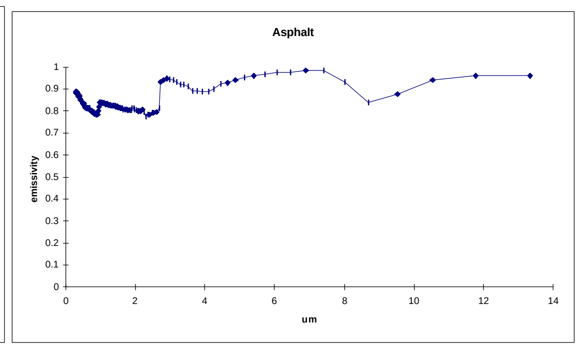
Asphalt
emissivity
1 0.9 0.8 0.7 0.6 0.5 0.4 0.3 0.2 0.1 0
0 2 4 6 8 10 12 14
um

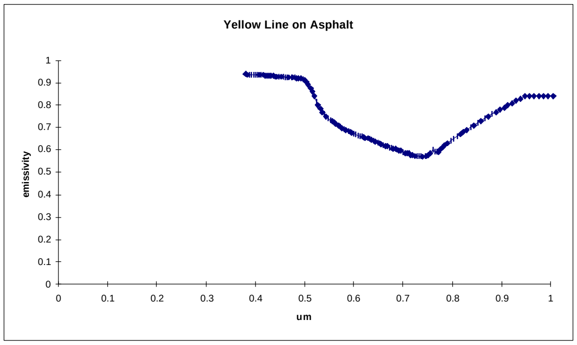
Yellow Line on Asphalt
emissivity
0 0.1 0.2 0.3 0.4 0.5 0.6 0.7 0.8 0.9 1
0 0.1 0.2 0.3 0.4 0.5 0.6 0.7 0.8 0.9 1
um

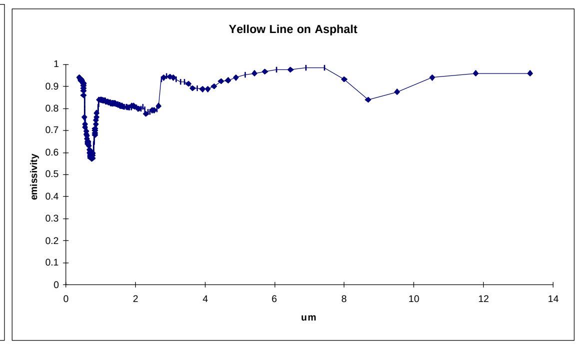
Yellow Line on Asphalt
emissivity
0 0.1 0.2 0.3 0.4 0.5 0.6 0.7 0.8 0.9 1
0 2 4 6 8 10 12 14
um

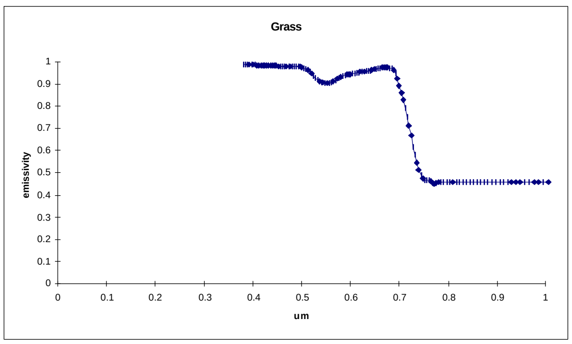
Grass
emissivity
0 0.1 0.2 0.3 0.4 0.5 0.6 0.7 0.8 0.9 1
0 0.1 0.2 0.3 0.4 0.5 0.6 0.7 0.8 0.9 1
um

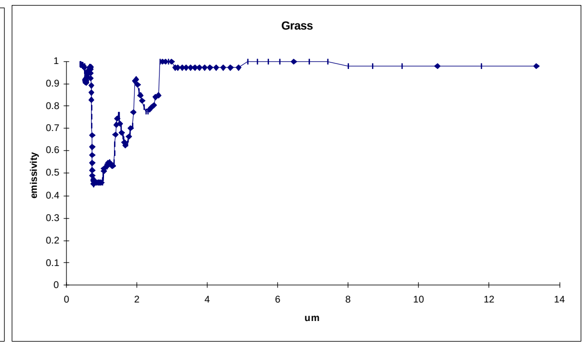
Grass
emissivity
0 0.1 0.2 0.3 0.4 0.5 0.6 0.7 0.8 0.9 1
0 2 4 6 8 10 12 14
um

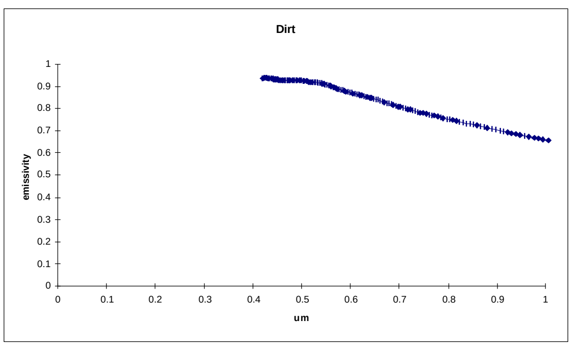
Dirt
emissivity
0 0.1 0.2 0.3 0.4 0.5 0.6 0.7 0.8 0.9 1
0 0.1 0.2 0.3 0.4 0.5 0.6 0.7 0.8 0.9 1
um

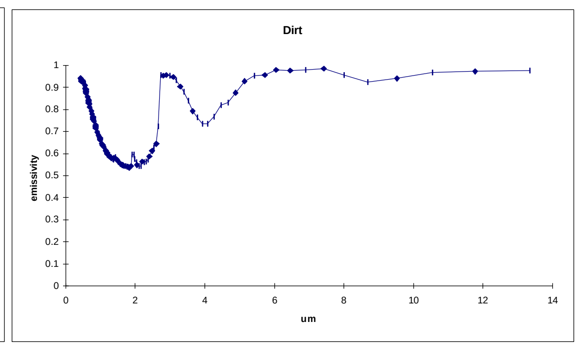
Dirt
emissivity
0 0.1 0.2 0.3 0.4 0.5 0.6 0.7 0.8 0.9 1
0 2 4 6 8 10 12 14
um

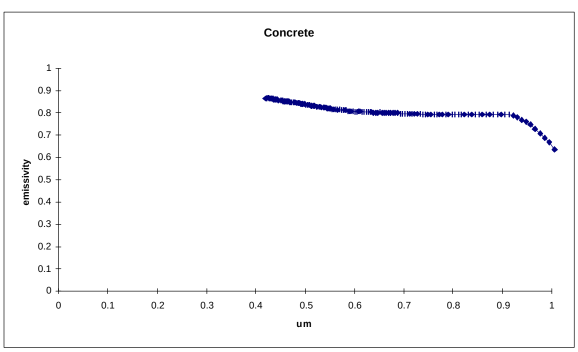
Concrete
emissivity
0 0.1 0.2 0.3 0.4 0.5 0.6 0.7 0.8 0.9 1
0 0.1 0.2 0.3 0.4 0.5 0.6 0.7 0.8 0.9 1
um

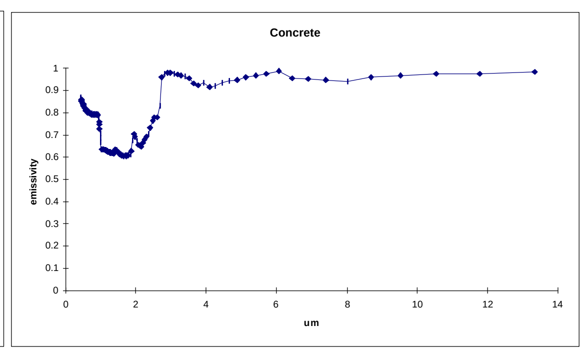
Concrete
emissivity
0 0.1 0.2 0.3 0.4 0.5 0.6 0.7 0.8 0.9 1
0 2 4 6 8 10 12 14
um

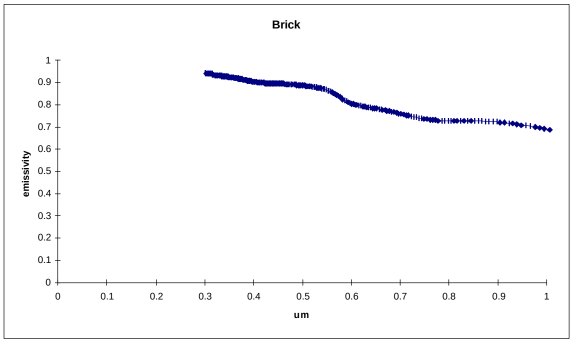
Brick
emissivity
um

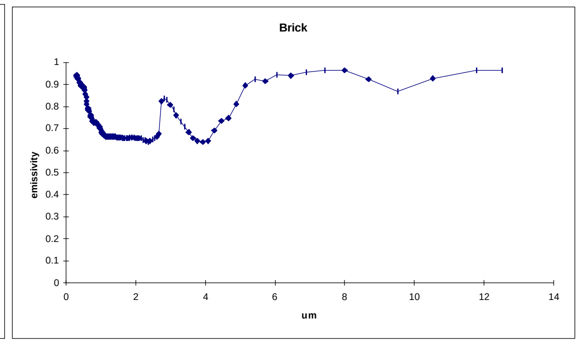
Brick
emissivity
um

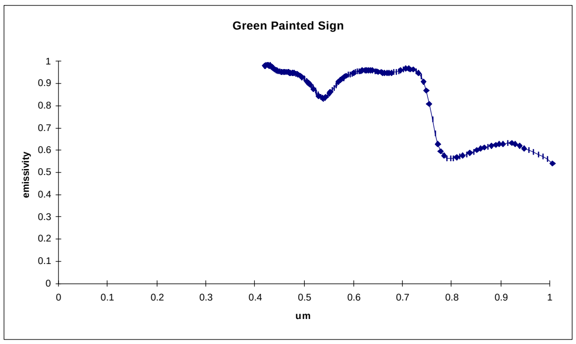
Green Painted Sign
emissivity
um

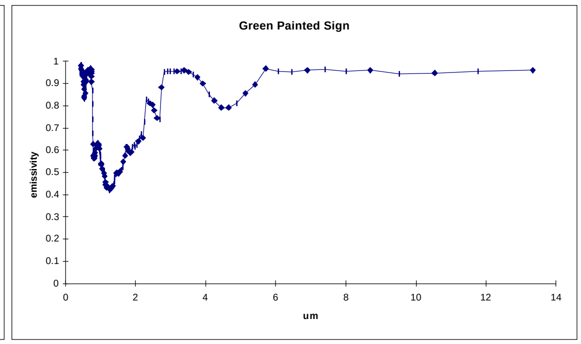
Green Painted Sign
emissivity
um

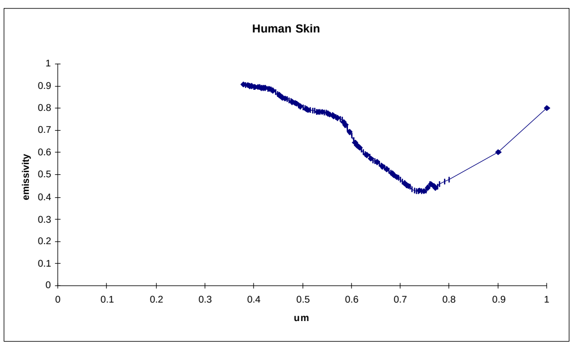
Human Skin
emissivity
um

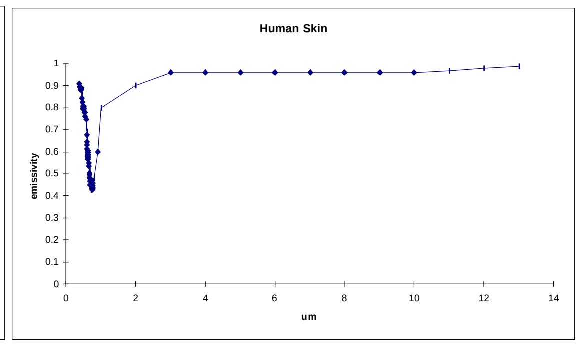
Human Skin
emissivity
um

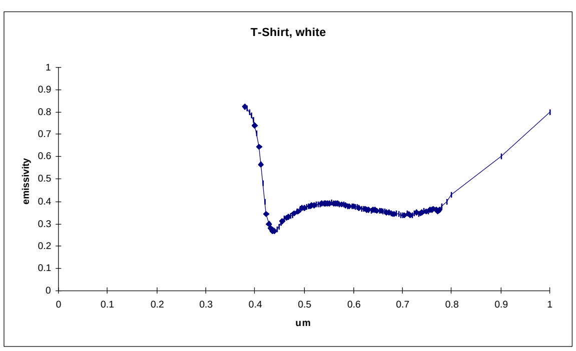
T-Shirt, white
emissivity
um

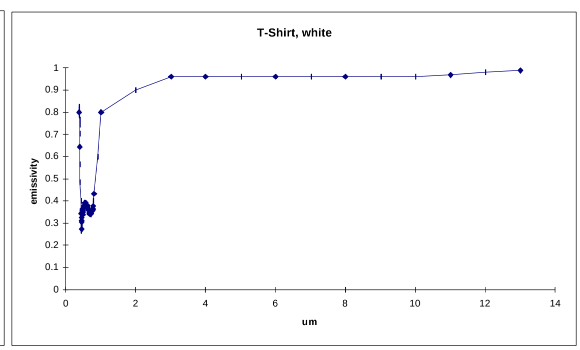
T-Shirt, white
emissivity
um

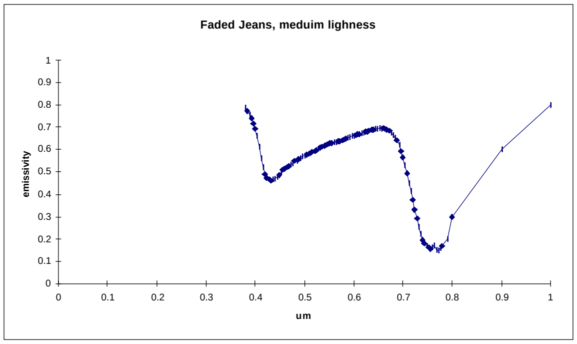
Faded Jeans, meduim lighness
emissivity
0 0.1 0.2 0.3 0.4 0.5 0.6 0.7 0.8 0.9 1
0 0.1 0.2 0.3 0.4 0.5 0.6 0.7 0.8 0.9 1
um

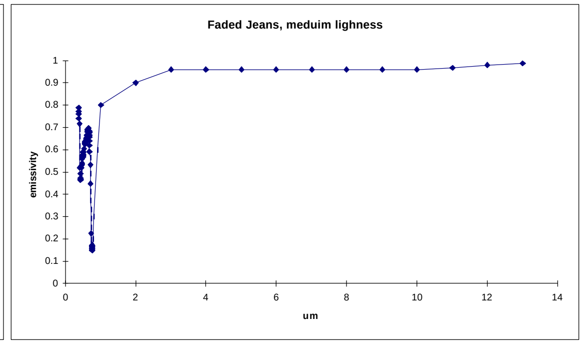
Faded Jeans, meduim lighness
emissivity
0 0.1 0.2 0.3 0.4 0.5 0.6 0.7 0.8 0.9 1
0 2 4 6 8 10 12 14
um

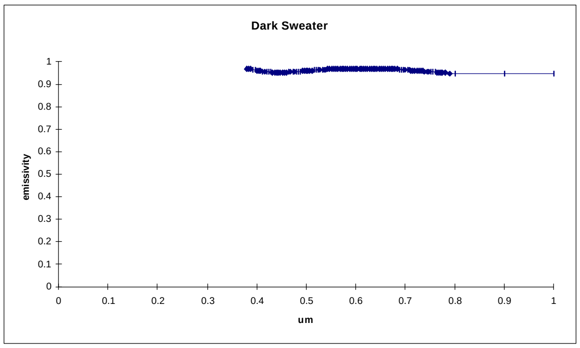
Dark Sweater
emissivity
0 0.1 0.2 0.3 0.4 0.5 0.6 0.7 0.8 0.9 1
0 0.1 0.2 0.3 0.4 0.5 0.6 0.7 0.8 0.9 1
um

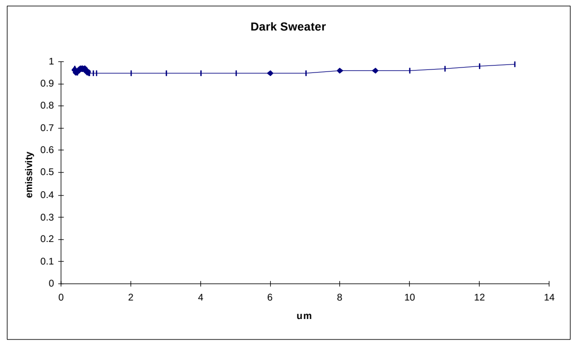
Dark Sweater
emissivity
0 0.1 0.2 0.3 0.4 0.5 0.6 0.7 0.8 0.9 1
0 2 4 6 8 10 12 14
um

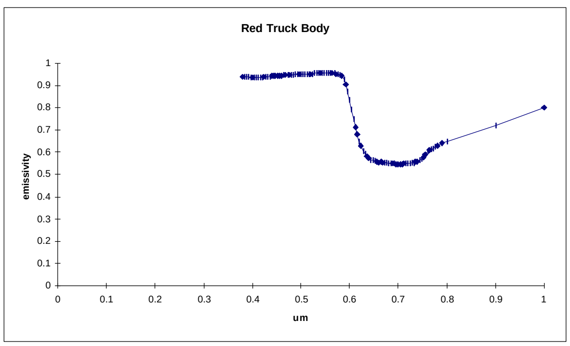
Red Truck Body
emissivity
0 0.1 0.2 0.3 0.4 0.5 0.6 0.7 0.8 0.9 1
0 0.1 0.2 0.3 0.4 0.5 0.6 0.7 0.8 0.9 1
um

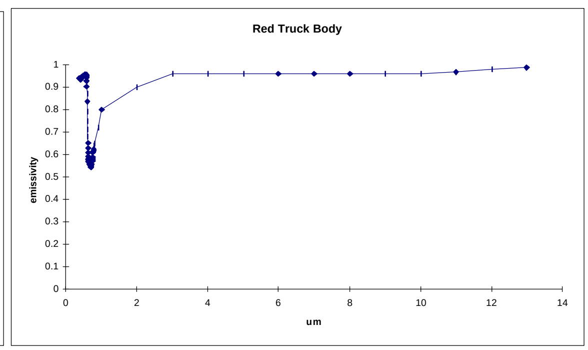
Red Truck Body
emissivity
0 0.1 0.2 0.3 0.4 0.5 0.6 0.7 0.8 0.9 1
0 2 4 6 8 10 12 14
um

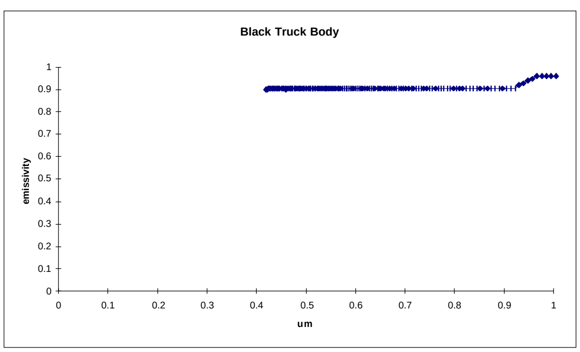
Black Truck Body
emissivity
0 0.1 0.2 0.3 0.4 0.5 0.6 0.7 0.8 0.9 1
0 0.1 0.2 0.3 0.4 0.5 0.6 0.7 0.8 0.9 1
um

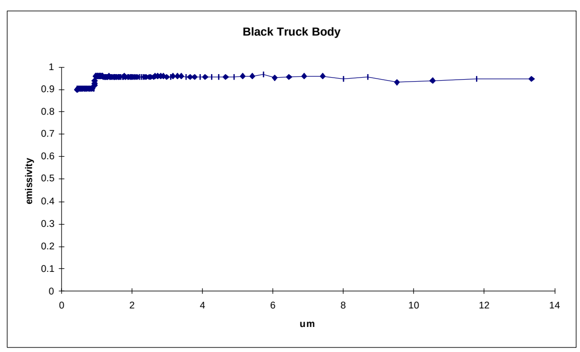
Black Truck Body
emissivity
0 0.1 0.2 0.3 0.4 0.5 0.6 0.7 0.8 0.9 1
0 2 4 6 8 10 12 14
um

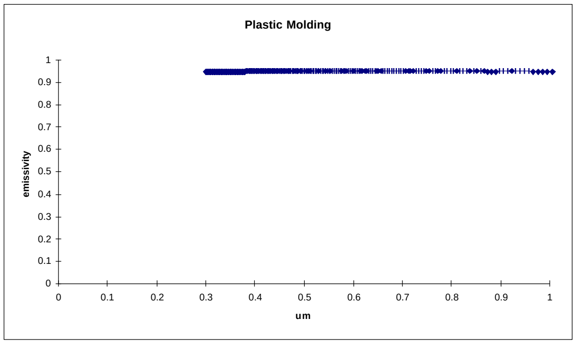
Plastic Molding
emissivity
um
0
0.1
0.2
0.3
0.4
0.5
0.6
0.7
0.8
0.9
1

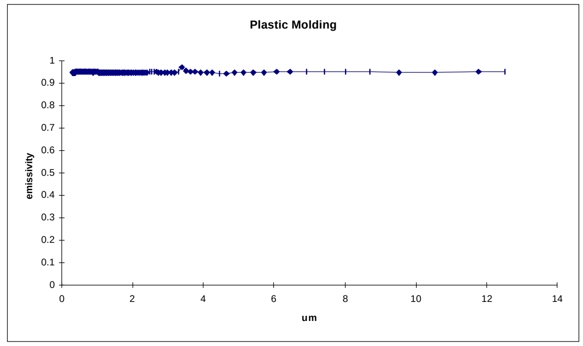
Plastic Molding
emissivity
um
0
2
4
6
8
10
12
14

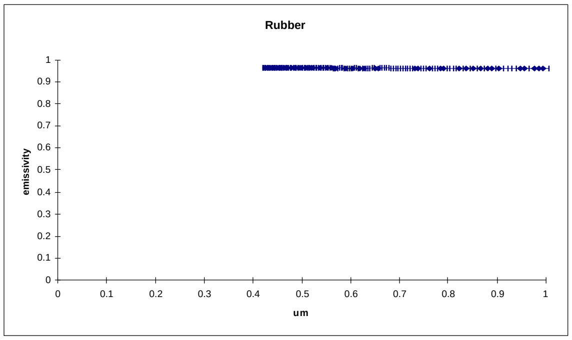
Rubber
emissivity
um

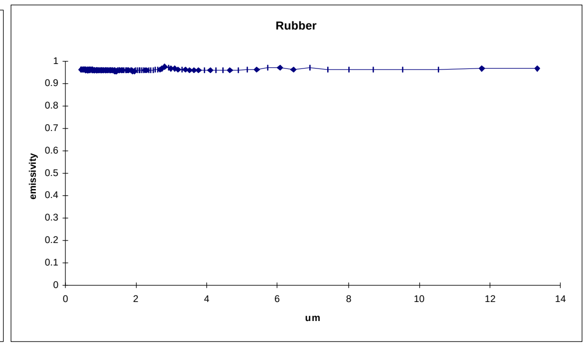
Rubber
emissivity
um

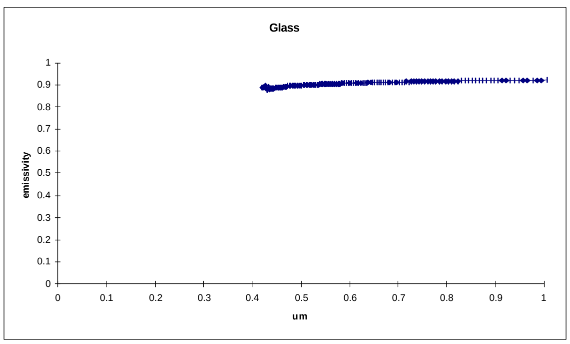
Glass
emissivity
um

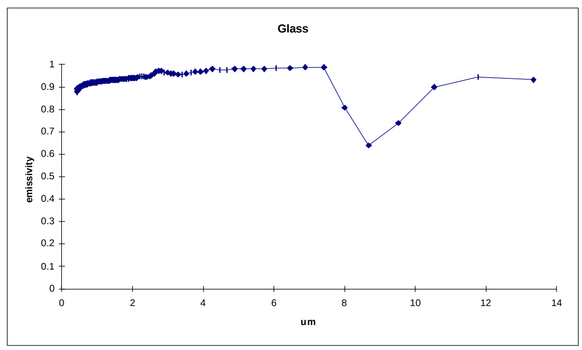
Glass
emissivity
um

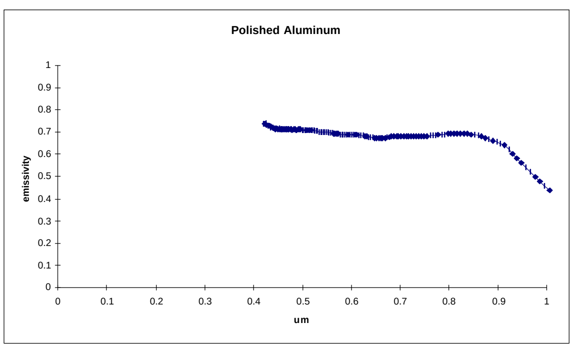
Polished Aluminum
emissivity
um

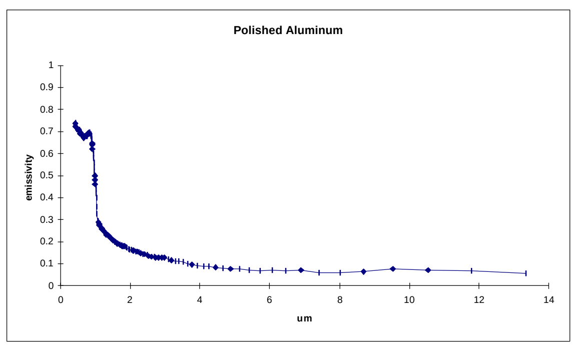
Polished Aluminum
emissivity
um

14.4 CONTROL7 Output for Creation of Card Deck

titan.cis.rit.edu> **control7**
ENTER FILE NAME FOR PRODUCED CARD DECK:
scene_scn.cdk

*** CARD 1 ***
INPUT ATMOSPHERIC MODEL TYPE
MODEL= 0 IF METEOROLOGICAL DATA ARE SPECIFIED (HORIZONTAL PATH ONLY)
1 TROPICAL ATMOSPHERE
2 MID-LATITUDE SUMMER
3 MID-LATITUDE WINTER
4 SUB-ARCTIC SUMMER
5 SUB-ARCTIC WINTER
6 1976 U.S. STANDARD ATMOSPHERE
7 NEW MODEL ATMOSPHERE (RADIOSONDE DATA)
CHOOSE A MODEL NUMBER:
2

INPUT THE TYPE OF ATMOSPHERIC PATH
ITYPE= 1 FOR A HORIZONTAL (CONSTANT PRESSURE) PATH
2 VERTICAL OR SLANT PATH BETWEEN TWO ALTITUDES
3 VERTICAL OR SLANT PATH TO SPACE
CHOOSE A TYPE:
2

PROGRAM EXECUTION MODE
IEMSCT= 0 PROGRAM EXECUTION IN TRANSMITTANCE MODE
1 PROGRAM EXECUTION IN RADIANCE MODE
2 PROGRAM EXECUTION IN RADIANCE MODE
WITH SOLAR/LUNAR SCATTERED RADIANCE INCLUDED
3 DIRECT SOLAR IRRADIANCE
ENTER EXECUTION MODE:
2

MULTIPLE SCATTERING EXECUTION MODE
IMULT= 0 PROGRAM EXECUTED W/OUT MULTIPLE SCATTERING
1 PROGRAM EXECUTED WITH MULTIPLE SCATTERING
MULTIPLE SCATTERING MODE:
0 (since we have a very short path length and relatively clear sky)

DO YOU WANT TO MODIFY THE DEFAULT ALTITUDE PROFILES OF TEMPERATURE AND PRESSURE (Y OR N)? **n**
DO YOU WANT TO MODIFY THE DEFAULT ALTITUDE PROFILE OF WATER VAPOR (Y OR N)? **n**
DO YOU WANT TO MODIFY THE DEFAULT ALTITUDE PROFILES OF OZONE (Y OR N)? **n**
DO YOU WANT TO MODIFY THE DEFAULT SEASONAL DEPENDENCE OF CH4 (Y OR N)? **n**
DO YOU WANT TO MODIFY THE DEFAULT SEASONAL DEPENDENCE OF N2O (Y OR N)? **n**
DO YOU WANT TO MODIFY THE DEFAULT SEASONAL DEPENDENCE OF CO (Y OR N)? **n**
DO YOU WANT TO PRINT THE ATMOSPHERIC PROFILES (Y OR N)? **n**

WHAT IS THE TEMPERATURE OF THE EARTH (BOUNDARY LAYER)
IN DEGREES K (0.0 USES THE FIRST RADIOSONDE READING)? **0**

ENTER THE SURFACE ALBEDO (0.00 IS A BLACKBODY) **0**

*** CARD 2 ***
SELECT AN AEROSOL EXTINCTION
IHAZE= 0 NO AEROSOL ATTENUATION INCLUDED IN CALCULATION
1 RURAL EXTINCTION, 23-KM VIS.
2 RURAL EXTINCTION, 5-KM VIS.
3 NAVY MARITIME EXTINCTION, SETS OWN VIS.
4 MARITIME EXTINCTION, 23-KM VIS.
5 URBAN EXTINCTION, 5-KM VIS.
6 TROPOSPHERIC EXTINCTION, 50-KM VIS.
7 USER DEFINED AEROSOL EXTINCTION COEFFICIENTS

TRIGGERS READING IREG FOR UP TO 4 REGIONS
OF USER DEFINED EXTINCTION ABSORPTION AND
ASSYMETRY
8 ADVECTION FOG EXTINCTION, 0.2-KM VIS.
9 RADIATION FOG EXTINCTION, 0.5-KM VIS.
10 DESERT EXTINCTION SETS OWN VISIBILITY FROM WIND SPEED
CHOOSE AEROSOL EXTINCTION TYPE:
1

SELECT A SEASON
ISEASN= 0 DEFAULT SEASON FOR MODEL
(SUMMER FOR MODELS 0,1,2,4,6,7)
(WINTER FOR MODELS 3,5)
1 SPRING-SUMMER
2 FALL-WINTER
CHOOSE A SEASON:
1

SELECT A VOLCANIC AEROSOL EXTINCTION
IVULCN= 0 DEFAULT TO STRATOSPHERIC BACKGROUND
1 STRATOSPHERIC BACKGROUND
2 AGED VOLCANIC TYPE/MODERATE VOLCANIC PROFILE
3 FRESH VOLCANIC TYPE/HIGH VOLCANIC PROFILE
4 AGED VOLCANIC TYPE/HIGH VOLCANIC PROFILE
5 FRESH VOLCANIC TYPE/MODERATE VOLCANIC PROFILE
6 BACKGROUND STRATSPHERIC TYPE/MODERATE VOLCANIC PROFILE
7 BACKGROUND STRATSPHERIC TYPE/HIGH VOLCANIC PROFILE
8 FRESH VOLCANIC TYPE/EXTREME VOLCANIC PROFILE
CHOOSE A VOLCANIC EXTINCTION:
0

SPECIFY CLOUD/RAIN RATE MODEL
ICLD = 0 NO CLOUDS OR RAIN
1 CUMULUS CLOUD BASE .66KM TOP 2.7KM
2 ALTOSTRATUS CLOUD BASE 2.4KM TOP 3.0KM
3 STRATUS CLOUD BASE .33KM TOP 1.0KM
4 STRATUS/STRATO CUMULUS BASE .66KM TOP 2.0KM
5 NIMBOSTRATUS CLOUD BASE .16KM TOP .66KM
6 2.0MM/HR DRIZZLE (MODELED WITH CLOUD 3)
RAIN 2.0MM/HR AT 0KM TO .22MM/HR AT 1.5KM
7 5.0MM/HR LIGHT RAIN (MODELED WITH CLOUD 5)
RAIN 5.0MM/HR AT 0KM TO .2MM/HR AT 1.5KM
8 12.5MM/HR MODERATE RAIN (MODELED WITH CLOUD 5)
RAIN 12.5MM/HR AT 0KM TO .2MM/HR AT 2.0KM
9 25.0MM/HR HEAVY RAIN (MODELED WITH CLOUD 1)
RAIN 25.0MM/HR AT 0KM TO .2MM/HR AT 3.0KM
10 75.0MM/HR EXTREME RAIN (MODELED WITH CLOUD 1)
RAIN 75.0MM/HR AT 0KM TO .2MM/HR AT 3.5KM
11 USER DEFINED CLOUD EXTINCTION, ABSORPTION, AND AEROSOL
EXT. COEFFICIENTS' TRIGGERS READING IREG FOR UP TO 4
REGIONS OF EXTINCTION ABSORPTION + ASSYMETRY
18 STANDARD CIRRUS MODEL
19 SUB VISUAL CIRRUS MODEL
20 NOAA CIRRUS MODEL (LOWTRAN 6)
CHOOSE A CLOUD MODEL:
0

DO YOU WANT TO USE ARMY VERTICAL STRUCTURE ALGORITHM FOR AEROSOLS IN BOUNDARY LAYER? **n**
DO YOU WANT TO OVERRIDE THE DEFAULT VISIBILITY (Y OR N)? **y**
VISIBILITY (KM)? **5**

WHAT IS THE RAIN RATE? (MM/HR) **0**
WHAT IS THE GROUND ALTITUDE ABOVE SEA LEVEL? (KM) **0.218**

*** CARD 3 ***

ENTER H1, INITIAL ALTITUDE (KM) (OBSERVER POSITION): **0 (from scene node)**
ENTER H2, FINAL ALTITUDE (KM): **0 (assumes ground)**

ENTER INITIAL ZENITH ANGLE (DEGREES) AS MEASURED FROM INITIAL ALTITUDE
(NOTE: 0 LOOKS STRAIGHT UP, 180 STRAIGHT DOWN): **0 (loads range in scene node)**

ENTER PATH (RANGE) LENGTH (KM): **0 (calculated by DIRSIG)**
ENTER EARTH CENTER ANGLE SUBTENDED BY H1 AND H2 (DEGREES): **0 (calculated)**
DO YOU WANT TO OVERRIDE THE DEFAULT EARTH RADIUS (Y OR N)? **n**
USE THE SHORT PATH FROM OBSERVER'S TO FINAL ALTITUDE (Y OR N)? **y**

```
*** CARD 3A1 ***
 SPECIFY THE GEOMETRY OF THE OBSERVATION
 IPARM =        0  SPECIFY 1 OBSERVER LATITUDE
                   2 OBSERVER LONGITUDE
                   3 SOURCE LATITUDE
                   4 SOURCE LONGITUDE
 IPARM =        1  SPECIFY 1 OBSERVER LATITUDE
                   2 OBSERVER LONGITUDE
 IPARM =        2  SPECIFY 1 AZIMUTHAL ANGEL
                   2 ZENITH ANGLE OF THE SUN
CHOOSE A TYPE OF GEOMETRY SPECIFICATION:
1

 IPH =   0  HENYEY-GREENSTEIN AEROSOL PHASE FUNCTION
         1  USER SUPPLIED AEROSOL PHASE FUNCTION
         2  MIE GENERATED DATA BASE OF AEROSOL PHASE FUNCTIONS FOR THE LOWTRAN MODELS
ENTER PHASE FUNCTION TYPE:
2
```

ENTER THE DAY OF THE YEAR (I.E. FROM 1 TO 365): **1 (loaded from scene node)**

*** CARD 3A2 ***
ENTER OBSERVER LATITUDE (-90 TO 90): **0 (loaded from scene node)**
ENTER OBSERVER LONGITUDE (0 TO 360): **0 (loaded from scene node)**
ENTER TIME OF DAY IN DECIMAL HOURS: **0 (loaded from scene node)**
ENTER PATH AZIMUTH AS DEGREES EAST OF NORTH: **0 (loaded from scene node)**

*** CARD 4 ***
WHAT UNITS ARE YOU USING FOR WAVELENGTH? (MICRONS OR NANOMETERS) **microns**
INPUT STARTING AND ENDING WAVELENGTH ON BANDPASS **1 2 (loaded from scene node)**
HOW MANY INTERVALS ACROSS BANDPASS? (MAXIMUM 396) **396**

```
*** CARD 5 ***
IRPT= 0   TO END LOWTRAN 6 RUN
    1   TO READ ALL DATA CARDS AGAIN
    3   TO READ ONLY CARD 3 AGAIN (GEOMETRY DATA)
    4   TO READ ONLY CARD 4 AGAIN (WAVELENGTH RANGE)
SELECT IRPT:
0
=====================================================================
```

14.5 Weather file

Table 14-3 Weather file used for simulation on September 01, 1998.

time (hr)	Temp (C)	Press (mbars)	Hum (frac)	DewPt (C)	Wind (m/s)	Dir Ins	Indir Ins	Sky	Cloud	rain	rain	rain
48	1											
0	17	1030	-1	10	2	0	0	1	0	0	0	0
1	16	1030	-1	11	0	0	0	1	0	0	0	0
2	16	1030	-1	11	2	0	0	1	0	0	0	0
3	15	1029	-1	10	2	0	0	1	0	0	0	0
4	13	1029	-1	8	1	0	0	1	0	0	0	0
5	13	1029	-1	8	1	0	0	1	0	0	0	0
6	12	1028	-1	8	0	0	0	1	0	0	0	0
7	12	1029	-1	8	0	73	2	0.9	5	0	0	0
8	13	1030	-1	8	2	81	3	0.9	5	0	0	0
9	16	1030	-1	9	2	85	4	0.9	5	0	0	0
10	17	1030	-1	8	2	88	5	0.9	5	0	0	0
11	19	1030	-1	9	2	89	5	1	0	0	0	0
12	21	1029	-1	10	3	89	5	1	0	0	0	0
13	23	1027	-1	12	2	88	5	1	0	0	0	0
14	24	1026	-1	11	2	86	4	1	0	0	0	0
15	26	1025	-1	11	2	82	3	0.9	5	0	0	0
16	26	1023	-1	11	4	75	2	0.9	5	0	0	0
17	26	1023	-1	11	2	54	1	0.8	5	0	0	0
18	23	1022	-1	12	4	0	0	0.7	5	0	0	0
19	22	1022	-1	12	3	0	0	0.8	5	0	0	0
20	20	1022	-1	11	3	0	0	0.8	5	0	0	0
21	18	1022	-1	11	3	0	0	0.9	5	0	0	0
22	18	1024	-1	11	2	0	0	1	0	0	0	0
23	17	1024	-1	10	2	0	0	1	0	0	0	0
24	17	1024	-1	10	2	0	0	1	0	0	0	0
25	16	1024	-1	11	3	0	0	0.9	5	0	0	0
26	16	1024	-1	11	3	0	0	0.9	5	0	0	0
27	15	1024	-1	10	3	0	0	0.9	5	0	0	0
28	13	1024	-1	8	2	0	0	0.9	5	0	0	0
29	13	1024	-1	8	2	0	0	0.9	5	0	0	0
30	12	1024	-1	8	2	0	0	0.9	5	0	0	0
31	12	1025	-1	8	2	73	2	0.8	5	0	0	0
32	13	1025	-1	8	2	81	3	0.8	5	0	0	0
33	16	1029	-1	9	2	85	4	0.8	5	0	0	0
34	16	1029	-1	8	3	88	5	0.7	5	0	0	0
35	18	1028	-1	10	4	89	5	0.7	5	0	0	0
36	19	1026	-1	10	3	89	5	0.8	5	0	0	0
37	21	1025	-1	10	4	88	5	0.9	5	0	0	0
38	23	1022	-1	9	2	86	4	0.9	5	0	0	0

39	23	1019	-1	8	2	82	3	0.9	5	0	0	0
40	24	1016	-1	7	4	75	2	1	0	0	0	0
41	24	1015	-1	6	2	54	1	1	0	0	0	0
42	23	1014	-1	7	2	0	0	1	0	0	0	0
43	21	1014	-1	8	2	0	0	1	0	0	0	0
44	19	1013	-1	8	2	0	0	1	0	0	0	0
45	18.1	1014	-1	10	3	0	0	0.9	1	0	0	0
46	**17.79**	**1014**	**-1**	**10**	**3**	**0**	**0**	**0.9**	**1**	**0**	**0**	**0**
47	17.7	1013	-1	10	3	0	0	0.7	1	0	0	0
48	17.53	1013	-1	9	2	0	0	0.2	1	0	0	0

14.6 Sensor spectral responsivity files

```
DIRSIG_RSP

BAND {
    MINIMUM_WAVELENGTH = 0.480
    MAXIMUM_WAVELENGTH = 0.940
    DELTA_WAVELENGTH = 0.020
}

GAIN = 10000.0
BIAS = 0.0
TYPE = INTEGRATED

RESPONSE {
    0.480000        0.010000
    0.485000        0.020000
    0.490000        0.030000
    0.495000        0.040000
    0.500000        0.042882
    0.505000        0.050000
    0.510000        0.057118
    0.515000        0.064237
    0.520000        0.068000
    0.525000        0.071612
    0.530000        0.090000
    0.535000        0.150000
    0.540000        0.200000
    0.545000        0.300000
    0.550000        0.357204
    0.555000        0.400000
    0.560000        0.500000
    0.565000        0.600000
    0.570000        0.700000
    0.575000        0.786021
    0.580000        0.850000
    0.585000        0.880000
    0.590000        0.900000
    0.595000        0.910000
    0.600000        0.927959
```

0.605000	0.940000
0.610000	0.950000
0.615000	0.960000
0.620000	0.970000
0.625000	0.986278
0.630000	0.990000
0.635000	0.990000
0.640000	0.990000
0.645000	0.990000
0.650000	0.986278
0.655000	0.990000
0.660000	0.992000
0.665000	0.993000
0.670000	0.994000
0.675000	1.000000
0.680000	0.998000
0.685000	0.996000
0.690000	0.994000
0.695000	0.993000
0.700000	0.986278
0.705000	0.990000
0.710000	0.990000
0.715000	0.985000
0.720000	0.980000
0.725000	0.977702
0.730000	0.970000
0.735000	0.965000
0.740000	0.960000
0.745000	0.950000
0.750000	0.943396
0.755000	0.940000
0.760000	0.940000
0.765000	0.935000
0.770000	0.930000
0.775000	0.928388
0.780000	0.930000
0.785000	0.930000
0.790000	0.930000
0.795000	0.930000
0.800000	0.928388
0.805000	0.920000
0.810000	0.915000
0.815000	0.910000
0.820000	0.910000
0.825000	0.900515
0.830000	0.890000
0.835000	0.880000
0.840000	0.876000
0.845000	0.870000
0.850000	0.857633
0.855000	0.820000
0.860000	0.780000
0.865000	0.700000
0.870000	0.600000
0.875000	0.500000
0.880000	0.400000
0.885000	0.300000

0.890000	0.200000
0.895000	0.100000
0.900000	0.077187
0.905000	0.060000
0.910000	0.045000
0.915000	0.030000
0.920000	0.010000
0.925000	0.000000
0.930000	0.000000
0.935000	0.000000
0.940000	0.000000

}

14.7 Derivation of spectral source distributions

Need to generate Planck intensity distributions from 0.3 to 4.0um, in [W/sr um], for various temperatures, T.

First lets convert exitance, M to intensity, I.

$M = \Theta / A$

$\Theta = MA$

$I = \Theta / \Omega \quad = MA / \Omega \quad = M$ (surf. area of filament) / 4π sr

$I = (M\ 2\pi rh) / 4\pi$

$I = Mrh / 2$ [W/m sr]

$h := 6.6260755 \cdot 10^{-34} \cdot \text{joule} \cdot \text{sec}$ $\qquad k := 1.380658 \cdot 10^{-23} \cdot \dfrac{\text{joule}}{\text{K}}$

$c := 299792458 \dfrac{\text{m}}{\text{sec}}$ $\qquad T := 2669\,\text{K}$

$r\_filament := 0.5 \cdot \text{mm}$ $\qquad h\_filament := 5 \cdot \text{mm}$

$\mu\text{m} := 10^{-6} \cdot \text{m}$ $\qquad \dfrac{\text{watt}}{\text{m}} = 1 \cdot 10^{-6} \cdot \dfrac{\text{watt}}{\mu\text{m}}$

$$I(\lambda) := \frac{2 \cdot \pi \cdot h \cdot c^2}{\lambda^5 \cdot \left(\exp\left(\dfrac{h \cdot c}{\lambda \cdot k \cdot T} \right) - 1 \right)} \cdot \frac{r\_filament \cdot h\_filament}{2} \cdot 10^{-6}$$ [W/sr um]

$\lambda := 0.300 \cdot \mu m, 0.320 \cdot \mu m .. 4.000 \cdot \mu m$

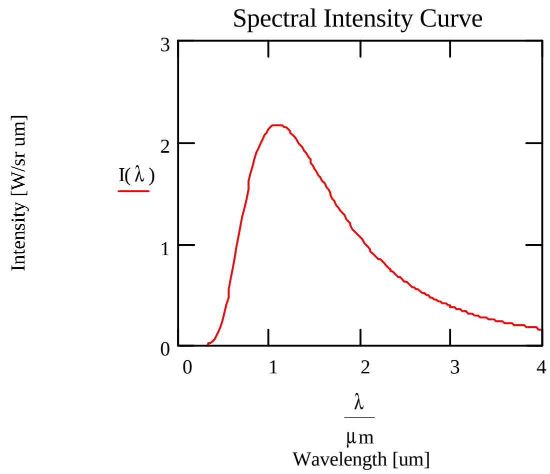

$\mathrm{WRITEPRN}(\mathrm{int\_wave}) := \frac{\lambda}{\mu m}$

$\mathrm{WRITEPRN}(\mathrm{intensity}) := I(\lambda)$

Intensity file for 2669 °K tungsten source, for example

0.280	0.0000000
0.300	0.0030241
0.320	0.0067327
0.340	0.0133936
0.360	0.0242839
0.380	0.0407554
0.400	0.0640984
0.420	0.0954132
0.440	0.1355071
0.460	0.1848312
0.480	0.2434557
0.500	0.3110814
0.520	0.3870788
0.540	0.4705451
0.560	0.5603709
0.580	0.6553083
0.600	0.7540358
0.620	0.8552156
0.640	0.9575417
0.660	1.0597780
0.680	1.1607860
0.700	1.2595440
0.720	1.3551590
0.740	1.4468690

0.760	1.5340450
0.780	1.6161840
0.800	1.6929030
0.820	1.7639280
0.840	1.8290850
0.860	1.8882860
0.880	1.9415230
0.900	1.9888480
0.920	2.0303730
0.940	2.0662530
0.960	2.0966810
0.980	2.1218760
1.000	2.1420800
1.020	2.1575520
1.040	2.1685590
1.060	2.1753740
1.080	2.1782700
1.100	2.1775220
1.120	2.1733980
1.140	2.1661600
1.160	2.1560620
1.180	2.1433500
1.200	2.1282570
1.220	2.1110080
1.240	2.0918150
1.260	2.0708770
1.280	2.0483850
1.300	2.0245150
1.320	1.9994330
1.340	1.9732940
1.360	1.9462420
1.380	1.9184110
1.400	1.8899230
1.420	1.8608940
1.440	1.8314280
1.460	1.8016210
1.480	1.7715620
1.500	1.7413320
1.520	1.7110050
1.540	1.6806470
1.560	1.6503190
1.580	1.6200760
1.600	1.5899690
1.620	1.5600400
1.640	1.5303300
1.660	1.5008750
1.680	1.4717060
1.700	1.4428510
1.720	1.4143350
1.740	1.3861780
1.760	1.3584000
1.780	1.3310170
1.800	1.3040410
1.820	1.2774850
1.840	1.2513570
1.860	1.2256650
1.880	1.2004150

1.900	1.1756110
1.920	1.1512570
1.940	1.1273540
1.960	1.1039020
1.980	1.0809020
2.000	1.0583520
2.020	1.0362490
2.040	1.0145920
2.060	0.9933765
2.080	0.9725988
2.100	0.9522543
2.120	0.9323381
2.140	0.9128448
2.160	0.8937689
2.180	0.8751044
2.200	0.8568451
2.220	0.8389845
2.240	0.8215162
2.260	0.8044335
2.280	0.7877294
2.300	0.7713972
2.320	0.7554299
2.340	0.7398204
2.360	0.7245619
2.380	0.7096472
2.400	0.6950694
2.420	0.6808214
2.440	0.6668965
2.460	0.6532876
2.480	0.6399880
2.500	0.6269909
2.520	0.6142896
2.540	0.6018776
2.560	0.5897483
2.580	0.5778954
2.600	0.5663125
2.620	0.5549934
2.640	0.5439320
2.660	0.5331224
2.680	0.5225585
2.700	0.5122348
2.720	0.5021454
2.740	0.4922848
2.760	0.4826476
2.780	0.4732285
2.800	0.4640221
2.820	0.4550236
2.840	0.4462277
2.860	0.4376297
2.880	0.4292247
2.900	0.4210082
2.920	0.4129755
2.940	0.4051221
2.960	0.3974438
2.980	0.3899363
3.000	0.3825954
3.020	0.3754171

3.040	0.3683974
3.060	0.3615324
3.080	0.3548185
3.100	0.3482519
3.120	0.3418291
3.140	0.3355466
3.160	0.3294009
3.180	0.3233887
3.200	0.3175069
3.220	0.3117523
3.240	0.3061217
3.260	0.3006122
3.280	0.2952208
3.300	0.2899448
3.320	0.2847813
3.340	0.2797277
3.360	0.2747812
3.380	0.2699394
3.400	0.2651997
3.420	0.2605597
3.440	0.2560171
3.460	0.2515694
3.480	0.2472144
3.500	0.2429500
3.520	0.2387740
3.540	0.2346843
3.560	0.2306788
3.580	0.2267557
3.600	0.2229129
3.620	0.2191486
3.640	0.2154609
3.660	0.2118481
3.680	0.2083084
3.700	0.2048402
3.720	0.2014417
3.740	0.1981113
3.760	0.1948475
3.780	0.1916488
3.800	0.1885136
3.820	0.1854405
3.840	0.1824281
3.860	0.1794750
3.880	0.1765798
3.900	0.1737413
3.920	0.1709582
3.940	0.1682291
3.960	0.1655530
3.980	0.1629285
4.000	0.1603546

14.8 DIRSIG Batch Files

```
#!/bin/csh
#*****************************************************************************
#   Run-time variables
#*****************************************************************************
# -t NO therm
# -s NO shape factor
# -d NO debug images
# -i convert GDB from IN to KM
# -f convert GDB from FT to KM
# -c convert GDB from CM to KM
# -o convert GDB from GDB coords to KM
setenv DIRSIG_EMISSIVITY   ../dirsig_lib/emissivity
setenv DIRSIG_TRANSMISSION /dirs/lib/data/transmission
#setenv SRC_FILE cis.src
setenv DBL_FILE default.dbl

/usr/bin/time dirsig -tsdi \
   scene_scn.adv \
   scene_scn.snd \
   ../dirsig_lib/weather/sept0198.wth \
   ../dirsig_lib/materials/lll_scene.mat \
   scene_scn_wbottom.gdb \
   scene_scn.adb \
   ../dirsig_lib/sensor/sensor_visible.sen \
   scene_scn.dat \
>& DIRSIG.LOG
```

15. Appendix E

15.1 Spectral Radiometer

The PR-650 is a fast scanning, spectroradiometric telecolorimeter that acquires the spectrum of optical radiation from 380nm to 780nm simultaneously in parallel under CMOS microcomputer control.

Spectral Range	380 - 780 nm
Spectral Bandwidth	8 nm (fwhm)
Wavelength Resolution	less than 3.5 nm/pixel
Luminance Accuracy	± 4% of calculated luminance at 2856K @ 23°C, ± 1 digit (resolution 0.01 units)
Sensitivity Range	< 1.0 fL (3.4 cdm^{-2}) to > 10,000 fL (34,000cdm^{-2}) for 2856° K source @ 23°C
Spectral Accuracy	± 2 nm
Digital Resolution	14 bit A/D

16. Appendix F

16.1 Modified Ephemeris Code

```
/*  This routine prints out all kinds of stuff....
 *  You give it Month, Day, Year, Hour, and Min
 *  Temp, Press, Lat, Long, HtSealevel...
 *  It prints out..
 *  tons..
 *  Emmett Ientilucci  10/98
 */

#include <stdio.h>
#include <math.h>
#include "astro.h"
#include "circum.h"
#include "screen.h"

void
bye(void)
{
        exit(0);
}

void cal_mjd(int, double, int, double *) ;

void
main(void)
{
        Now             curtime;
        Sky             pos;
        double          TempInF, TempInC;
        double          PressInInch, PressInmBar;
        double          LatInDeg, LatInRad, LngInDeg, LngInRad;
        double          HeightFt, HeightER;
        double          PhAngleDeg;
        int             Month, Year;
        double          Day, Time, FracOfDay, Hour, Min, LocalHour;
        double          r, D, R, D_Au, p, NewPhase;

/*      time_fromsys(&curtime); this is for using current CPU time */

/* USER SPECIFIED TIME */
        Month   = 9;    /* This is UTC time, not local (UTC=GMT=Zulu, all the same) */
        Day     = 2;    /* so 6pm EDT local = 1800 -> 1800+4 = 22 GMT */
        Year    = 1998;
        Hour    = 02;
        Min     = 00;

        FracOfDay  = (Hour/24.0) + (Min/(24.0*60.0));


/*      MJD is the Modified Julian Data.
 *      To enter date you need the number of
 *      days SINCE 12/31.5/1899 (noon of that day).
 */
        cal_mjd(Month, Day, Year, &(curtime.n_mjd));

        curtime.n_mjd += FracOfDay;

/* POSSIBLE INPUTS
 * n_mjd;   modified Julian date, ie, days since
 *              Jan 0.5 1900 (== 12 noon, Dec 30, 1899), utc.
 *              enough precision to get well better than 1 second.
 *              N.B. if not first member, must move NOMJD inits.
```

```
 * n_lat;      latitude, >0 north, rads
 * n_lng;      longitude, >0 east, rads
 * n_tz;       time zone, hrs behind UTC
 * n_temp;     atmospheric temp, degrees C
 * n_pressure; atmospheric pressure, mBar
 * n_height;   height above sea level, earth radii
 * n_epoch;    desired precession display epoch as an mjd, or EOD
 * n_tznm[4];          time zone name; 3 chars or less, always 0 at end
 */

/* USER SPECIFIED DATA */
        TempInF      = 45.0;
        PressInInch  = 29.5;
        LatInDeg     = 43.16856; /*=43deg 10min */
        LngInDeg     = -77.61583; /*=77deg 36min, Neg makes it deg West */
        HeightFt     = 800;
        curtime.n_tz    = 4.0;  /* 5hrs behind GMT in EST, 4 in EDT */

/* CONVERSIONS */
        TempInC     = (5./9.) * (TempInF - 32.0);
        PressInmBar = 33.86 * PressInInch;
        LatInRad    = degrad(LatInDeg);
        LngInRad    = degrad(LngInDeg);
        HeightER    = (HeightFt / 2.093e7);

        curtime.n_temp     = TempInC;
        curtime.n_pressure = PressInmBar;
        curtime.n_lng      = LngInRad;
        curtime.n_lat      = LatInRad;
        curtime.n_height   = HeightER;
        curtime.n_epoch    = EOD;

/* Possible outputs
 * s_ra;               ra, rads (precessed to n_epoch)
 * s_dec;              dec, rads (precessed to n_epoch)
 * s_az;               azimuth, >0 e of n, rads
 * s_alt;              altitude above topocentric horizon, rads
 * s_sdist;            dist from object to sun, au
 * s_edist;            dist from object to earth, au (moon is in km)
 * s_elong;            angular sep between object and sun, >0 if east
 * s_hlong;            heliocentric longitude, rads
 * s_hlat;             heliocentric latitude, rads
 * s_size;             angular size, arc secs
 * s_phase;            phase, %
 * s_mag;              visual magnitude
 */
/** Info about the MOON **/
        body_cir(MOON, 0.0, &curtime, &pos);

        PhAngleDeg = raddeg(acos((pos.s_phase / 50.0) - 1.0));

/* PRINT OUTPUT STUFF */
        printf("\n\n");
        printf("\n\n");
        printf("\n\n");
        printf("****************** Ephemeris DATA for the MOON and SUN *****************\n");
        printf("Emmett Ientilucci  9/98");
        printf("\n\n");

        LocalHour   = Hour - curtime.n_tz;
        if( LocalHour < 0.0 ){
                LocalHour= 12 + LocalHour;
        }

        printf("----------USER DEFINED PARAMETERS:----------\n");
        printf("Latitude          = %.1f deg\n", raddeg(curtime.n_lat));
        printf("Longitude         = %.1f deg ( NEG puts us W of prime meridian)\n", raddeg(curtime.n_lng));
        printf("Ht above sea level = %f er[ft] %5.1f feet \n", curtime.n_height, HeightFt);
        printf("Temperature       = %.1f C %15.1f F\n", curtime.n_temp, TempInF );
        printf("Pressure          = %.1f mBar %10.1f inHg\n", curtime.n_pressure, PressInInch);
        printf("Hr behind UTC     = %.1f (5hr behind GMT in EST, 4hr in EDT)\n", curtime.n_tz);
        printf("Current GMT Set   = %d-%.0f-%d, %2.0f:%2.0f  \n", Month, Day, Year, Hour, Min);
        printf("Local Time        = %2.0f:%2.0f  \n", LocalHour, Min );

        printf("Which is a MJD    = %f \n", curtime.n_mjd);
```

```
        printf("\n\n");

        printf("----------MOON DATA FOR CURRENT TIME IS:---------\n");
        printf("Moon Right Ascension, R.A.      = %.3f rad %8.1f deg     %5.2f hrs\n", pos.s_ra, raddeg(pos.s_ra), radhr(pos.s_ra));
        printf("Moon Declination, Dec           = %.3f rad %8.1f deg\n", pos.s_dec, raddeg(pos.s_dec));
        printf("Moon azimuth, Az                = %.3f rad %8.2f deg\n", pos.s_az , raddeg(pos.s_az ) );
        printf("Moon alt. from horz, Alt (Zen)  = %.3f rad %8.2f deg\n", pos.s_alt, raddeg(pos.s_alt) );
        printf("Moon Heliocentric lng           = %.2f deg\n", raddeg(pos.s_hlong));
        printf("Moon Heliocentric lat           = %.2f deg\n", raddeg(pos.s_hlat));
        printf("Dist from moon to earth, Ea Dst = %.2f km %.2f mi\n", pos.s_edist, (pos.s_edist/1.609344));
        printf("Dist from moon to sun, Sn Dst   = %f au\n", pos.s_sdist);
        printf("< sep btwn obj & sun, Elong     = %.1f deg?\n", pos.s_elong);
        printf("< size of obj, Size             = %.0f arc seconds\n", pos.s_size);
        printf("Moon Visual magnitude, VMag     = %.0f \n", pos.s_mag);
        printf("Moon phase fraction, Phs        = %.2f percent illuminated\n\n", pos.s_phase);
        printf("Moon phase angle, angle betwn\n");
        printf("earth and sun from obj (moon)   = %.2f rad %6.3f deg\n", degrad(PhAngleDeg), PhAngleDeg);

        r        = pos.s_sdist; /* in Au */
        D        = pos.s_edist; /* in km */
        D_Au     = D / 1.495979e8; /* conv km to Au */

        body_cir(SUN, 0.0, &curtime, &pos);

        R        = pos.s_edist; /* in Au */
        p        = ((r*r) + (D_Au*D_Au) - (R*R)) / (2.0*r*D_Au) ;
        NewPhase= raddeg( acos(p) );

        printf("\n");
        printf("Dist from moon to sun, r        = %f \n", r);
        printf("Dist from moon to earth, D_Au   = %f \n", D_Au);
        printf("Dist from sun to earth, R       = %f \n", R);
        printf("p                               = %f Au\n", p);
        printf("New Phase Angle                 = %.3f deg \n", NewPhase);
        printf("different formula, more accurate\n");
        printf("\n\n");
/** Info about the SUN **/
        printf("----------SUN DATA FOR CURRENT TIME IS:----------\n");
        printf("Sun Right Ascension, R.A.      = %.3f rad %8.1f deg     %5.2f hrs\n", pos.s_ra, raddeg(pos.s_ra), radhr(pos.s_ra));
        printf("Sun Declination, Dec           = %.3f rad %8.1f deg\n", pos.s_dec, raddeg(pos.s_dec));
        printf("Sun azimuth, Az                = %.3f rad %8.2f deg\n", pos.s_az , raddeg(pos.s_az ) );
        printf("Sun alt. from horz, Alt (Zen)  = %.3f rad %8.2f deg\n", pos.s_alt, raddeg(pos.s_alt) );
        printf("Sun Heliocentric lng           = %.2f deg\n", raddeg(pos.s_hlong));
        printf("Sun Heliocentric lat           = %.2f deg\n", raddeg(pos.s_hlat));
        printf("Sun Visual magnitude, VMag     = %.0f \n", pos.s_mag);
        printf("\n\n");
}
```

17. Appendix G

17.1 Starlight spectral conversions

Read off values from reference [72].

An estimate of the average spectral distribution of the night-sky irradiance is shown below. This result, in photons per second, is on a horizontal surface of one square meter at sea level in wavelength intervals of 0.050 um. The lower atmosphere emits thermal radiation whose level may be approximated by blackbody radiation at ambient ground temperature. This effect is limited mostly to the far infrared region.

$N := 21 \quad i := 1..N$

[um] $\lambda_i :=$	Lum eff $V_i :=$	[s^{-1} m^{-2} $(0.05um)^{-1}$] $\eta_i :=$
0.350	0	$4.0 \cdot 10^{11}$
0.400	0.000396	$8.0 \cdot 10^{11}$
0.450	0.038	$1.4 \cdot 10^{12}$
0.500	0.323	$1.6 \cdot 10^{12}$
0.550	0.995	$2.5 \cdot 10^{12}$
0.600	0.631	$2.6 \cdot 10^{12}$
0.650	0.107	$3.0 \cdot 10^{12}$
0.700	0.0041	$3.2 \cdot 10^{12}$
0.750	0.00012	$6.0 \cdot 10^{12}$
0.800	0	$6.5 \cdot 10^{12}$
0.850	0	$1.2 \cdot 10^{13}$
0.900	0	$6.0 \cdot 10^{12}$
0.950	0	$9.5 \cdot 10^{12}$
1.000	0	$3.0 \cdot 10^{13}$
1.050	0	$3.3 \cdot 10^{13}$
1.100	0	$1.7 \cdot 10^{13}$
1.150	0	$1.6 \cdot 10^{12}$
1.200	0	$4.7 \cdot 10^{13}$
1.250	0	$4.4 \cdot 10^{13}$
1.300	0	$1.6 \cdot 10^{12}$
1.350	0	$1.6 \cdot 10^{12}$

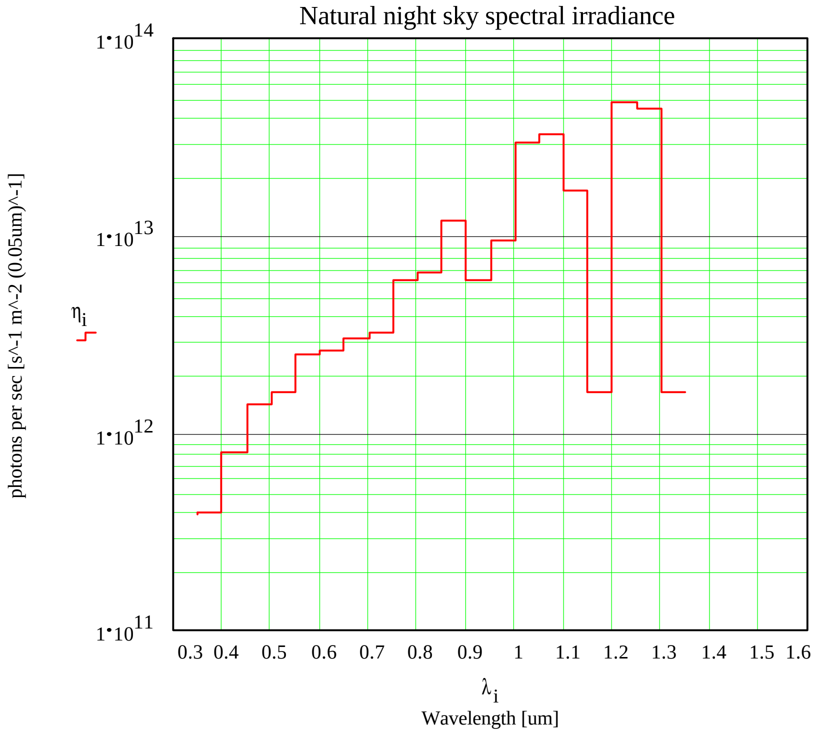

We now convert η(λ) (photons per second) to exitance, M(λ) or E

$h := 6.62607551 0^{-34}$ [Js]

$c := 29979245$ [m/s]

$Mtemp_i := \eta_i \cdot \frac{h \cdot c}{\lambda_i \cdot 10^{-6}}$ $Mtemp_4 = 6.3$ [W m^{-2} 0.05um^{-1}]

There are 20, 0.05um in 1um

$M_i := Mtemp_i \cdot 20$ $M_4 = 1.2$ [W m^{-2} um^{-1}]

Find the radiance

$L_i := \frac{M_i}{\pi}$ $L_4 = 4.0$ [W m^{-2} um^{-1} sr^{--1}]

Convert to cm^{-2}

$m^2 = 1 \cdot 10^4$

$Lcm_i := \frac{L_i}{10000}$ $Lcm_1 = 1.4$ [W cm^{-2} um^{-1} sr^{-1}]

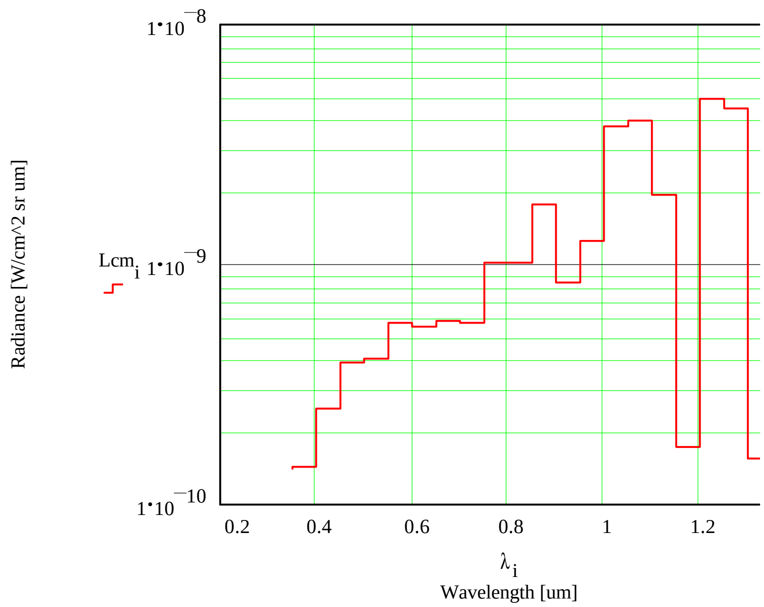

WRITEPRN(nightsky) $:= Lcm_i$

WRITEPRN(nightwave) $:= \lambda_i$

Convert to illuminance and luminance then compare to published night sky data.

$\lambda min := \lambda_1$

$\lambda max := \lambda_N$ $\Delta\lambda := \frac{\lambda max - \lambda min}{N - 1}$ $\Delta\lambda = 0.050$ [um]

[W m^{-2} um^{-1}] • [um] • [lm W^{-1}] = [lm m^{-2}] = [lux]

$Illuminance\_E := \left(\sum_{i=1}^{N} M_i \cdot \Delta\lambda \cdot V_i\right) \cdot 683$ $Illuminance\_E = 0.0012$ [lux] = [lm / m^2]

Reference [58] says that starlight is around 0.00022 [lux], which is ¼ of the actual light from the sky with NO moon. This means that the total sky illuminance is 0.00088 [lux]. Additionally, reference [58] says the moon-less clear sky is 0.00100 [lux]. We have calculated 0.00120 [lux].

$Luminance\_L := \left(\sum_{i=1}^{N} L_i \cdot \Delta\lambda \cdot V_i\right) \cdot 683$ $Luminance\_L = 0.0004$ [cd /m^2] = [nit] = [lm / m^2 sr]

Wavelength [μm]	Radiance [W/cm^2 sr μm]
0.350	1.445E-10
0.400	2.529E-10
0.450	3.934E-10
0.500	4.047E-10
0.550	5.748E-10
0.600	5.48E-10
0.650	5.837E-10
0.700	5.781E-10
0.750	1.012E-9
0.800	1.027E-9
0.850	1.785E-9
0.900	8.431E-10
0.950	1.265E-9
1.000	3.794E-9
1.050	3.974E-9
1.100	1.954E-9
1.150	1.759E-10
1.200	4.953E-9
1.250	4.451E-9
1.300	1.556E-10
1.350	1.499E-10

18. Appendix H

18.1 Electronic MTF

The gray scale on the sine wave target (see Figure 18-1) was imaged first so as to create a look up table of reflectance vs. voltage (see Table 18-1). The reflection densities (D_r), frequency's (cyc/mm) and input modulation vales were given and can also be seen in Figure 18-1. The results of the calibration can be seen in Figure 18-2. It is noticed that the ICCD output (voltage) is fairly linear over the range of reflection densities.

The camera gain was then set to 4.4 V at f/1.8 with the room lights off and a hall door ajar. The lens focal length was 75 mm and the distance to the target was 4597 mm. This produced a magnification of f/distance = 75 mm/4597 mm = 61.

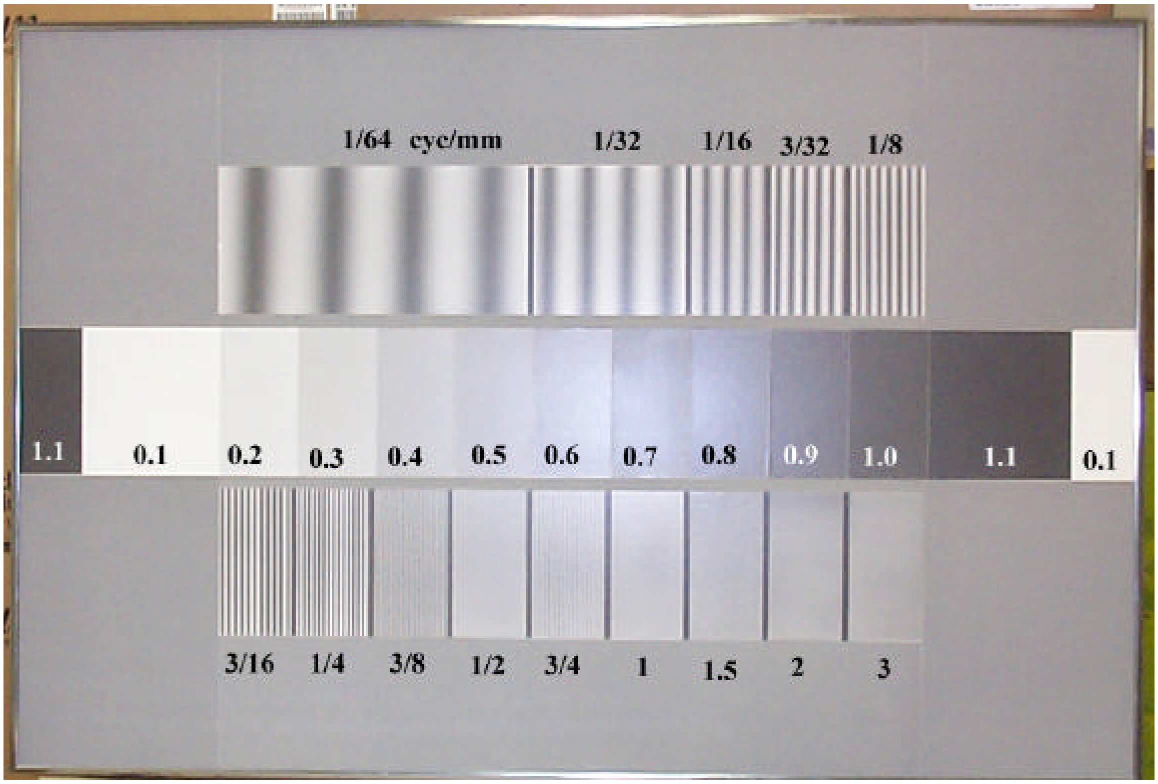

Figure 18-1 Sine wave target used to calculate ICCD MTF.

Table 18-1 Camera voltage as a function of reflectance.

Actual reflection density, D_r	Measured voltage [V]	Calculated reflectance $R = 10^{-D_r}$
0.1	0.2484	0.794
0.2	0.1985	0.631
0.3	0.15	0.501
0.4	0.1141	0.398
0.5	0.08906	0.316
0.6	0.0625	0.251
0.7	0.03438	0.200
0.8	0.02031	0.158
0.9	0.003125	0.126
1	-0.009375	0.100
1.1	-0.01875	0.079

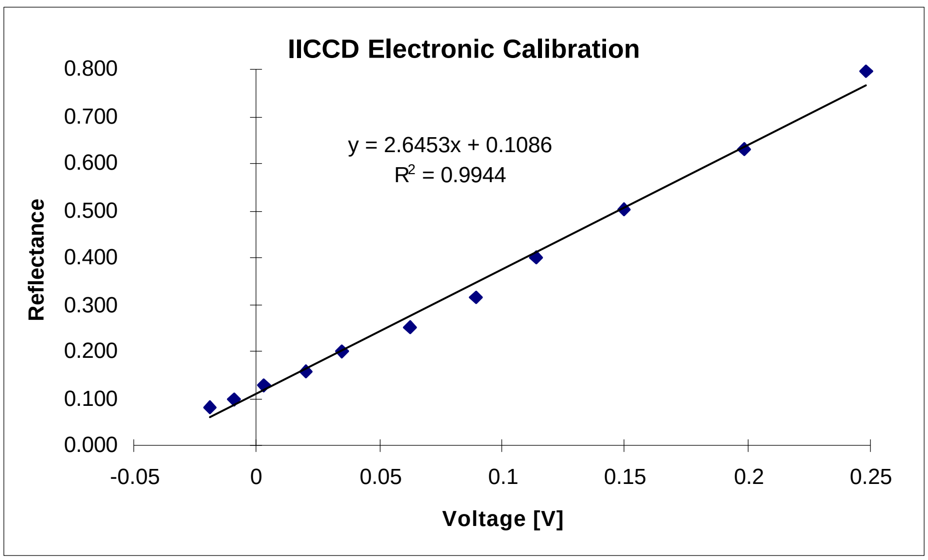

Figure 18-2 IICCD electronic MTF calibration curve.

Next, the sine wave target was imaged. Actually, the target had a variety sine wave patterns with in it ranging form 1/64 to 3.0 cyc/mm. Only some of these were used in the calculation (see Table 18-2). This produced a sin wave-like pattern on the oscilloscope that was representative of the frequency imaged. For each frequency, the minimum and maximum voltages were measured.

Using the linear equation determined from the calibration, the voltages were converted to reflectance's. From this the output modulation was computed using

$$Modulation_{out} = \frac{R_{\max} - R_{\min}}{R_{\max} R_{\min}}$$

The input modulation values were already computed (and listed on the target) using a similar technique. The modulation transfer was finally computed by simply computing a ratio of the input and output modulations.

$$MTF = \frac{Modulation_{out}}{Modulation_{in}}$$

The final relationship of modulation vs. frequency (at the image plane) for the electronic measurement can be seen in Figure 18-3.

Table 18-2 Measured electronic IICCD MTF.

Period [mm]	Frequency obj plane [cyc/mm]	Mag	Frequency img plane [cyc/mm]	Min V	Max V	Min refl	Max refl	Mod. out	Mod. in	MTF
64.00	0.02	61.30	0.96	0	0.1109	0.109	0.402	0.575	0.608	**0.95**
32.00	0.03	61.30	1.92	0.007812	0.1203	0.129	0.427	0.535	0.611	**0.88**
16.00	0.06	61.30	3.83	0.004688	0.09219	0.121	0.352	0.489	0.624	**0.78**
10.67	0.09	61.30	5.75	0.01094	0.08906	0.138	0.344	0.429	0.6	**0.71**
8.00	0.13	61.30	7.66	0.01875	0.08281	0.158	0.328	0.349	0.575	**0.61**
5.33	0.19	61.30	11.49	0.0463	0.09531	0.231	0.361	0.219	0.552	**0.40**
4.00	0.25	61.30	15.32	0.04688	0.07812	0.233	0.315	0.151	0.582	**0.26**
2.67	0.38	61.30	22.99	0.06719	0.08594	0.286	0.336	0.080	0.608	**0.13**

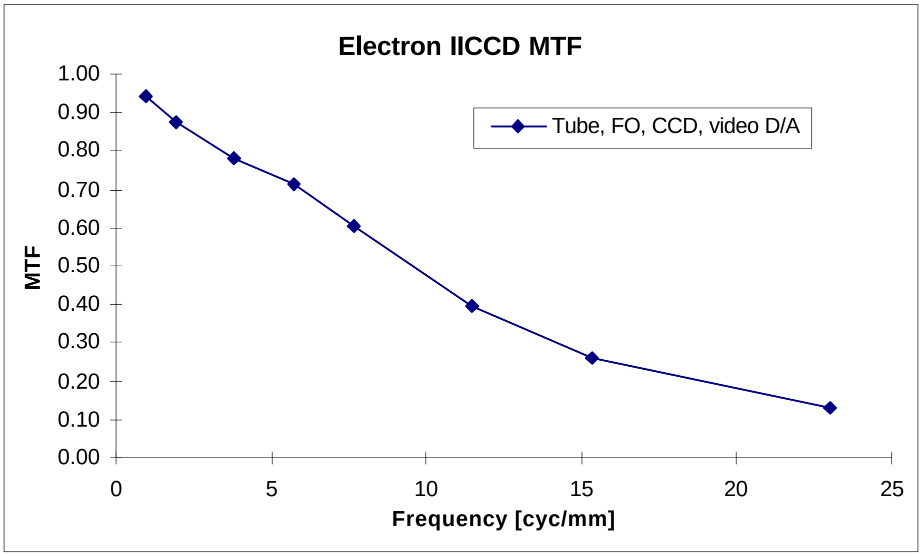

Figure 18-3 Electronic MTF curve.

18.2 Digitizer MTF

The other technique for the measuring the cameras MTF, was to include the effects of the 8 bit digitizer. Again, a look up table was created that related measured digital counts to reflectance (see Table 18-3). Here we see that the digitizer does not add any non-linearity's to the system. The system behaves linearly for the given conditions and with in the set of reflectance's presented.

Finally, the output modulation values were computed thus enabling the computation of the digitized MTF. This can be seen in Figure 18-5. Notice how much poorer the digitized MTF is compared to the electronically measured MTF.

Table 18-3 Digital count as a function of reflectance.

Actual reflection density, D_r	Measured digital count	Calculated reflectance $R = 10^{-Dr}$
0.1		0.794
0.2	159.92	0.631
0.3	146.52	0.501
0.4	124.71	0.398
0.5	111.39	0.316
0.6	97.79	0.251
0.7	86.9	0.200
0.8	79.29	0.158
0.9	71.6	0.126
1	67.74	0.100
1.1	63.04	0.079

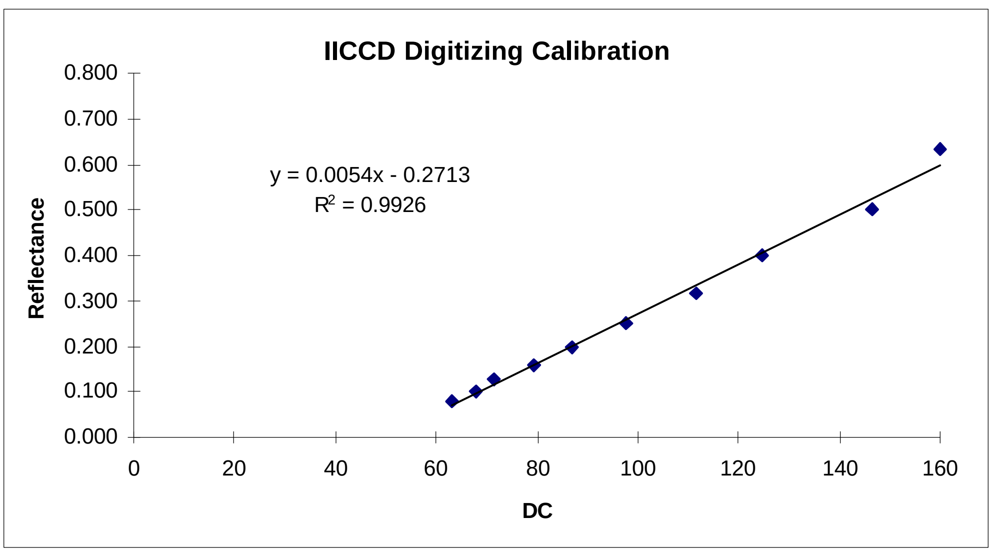

Figure 18-4 IICCD digitized MTF calibration curve.

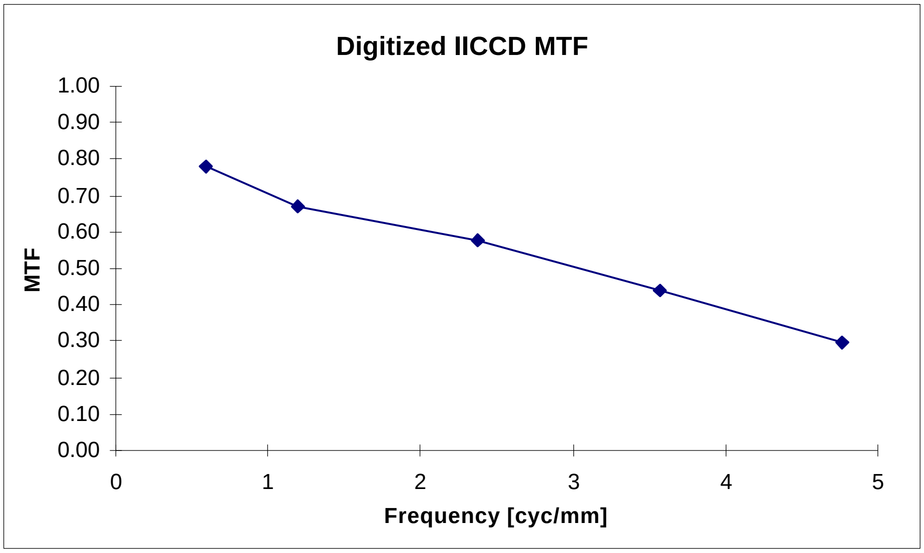

Figure 18-5 Digitized MTF curve.

18.3 Manufacture MTF

The specification sheet for the cameras II tube (FS9910A) lists the following MTF values as a function of frequency (see Figure 18-6). Contact with the manufacture revealed no additional information about distances or laboratory lighting conditions during the time of collection.

Table 18-4 Manufactures MTF values for II tube.

Frequency [lp/mm]	MTF
2.5	0.83
7.5	0.60
15	0.38
25	0.18
45	0.10

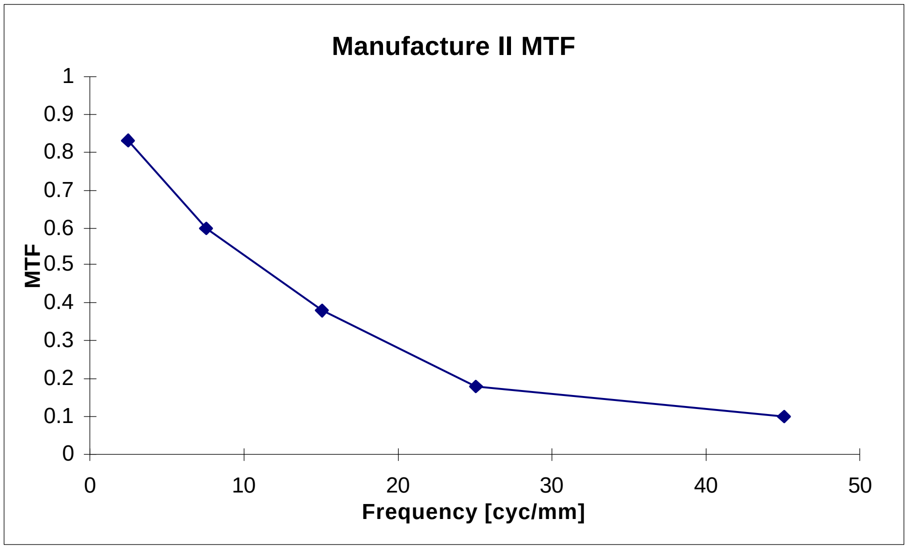

Figure 18-6 Manufacture MTF curve for II tube.

18.4 IICCD Radiometric Calibration

The IICCD camera was set up to image the entrance port of an integrating sphere. The sphere contained a calibrated 10 W tungsten halogen bulb. The spectral distribution for some of the bulbs contained in the integration sphere can be seen in Figure 18-7. The region of interest is between 480 and 940 nm. We generate a broad band radiance value over this region with the assumption that the spectral distribution is fairly constant. This integration yields a radiance of 5.5085 [W/m^2 sr]. It is this value that will get reduced via an ND filter and then digitized.

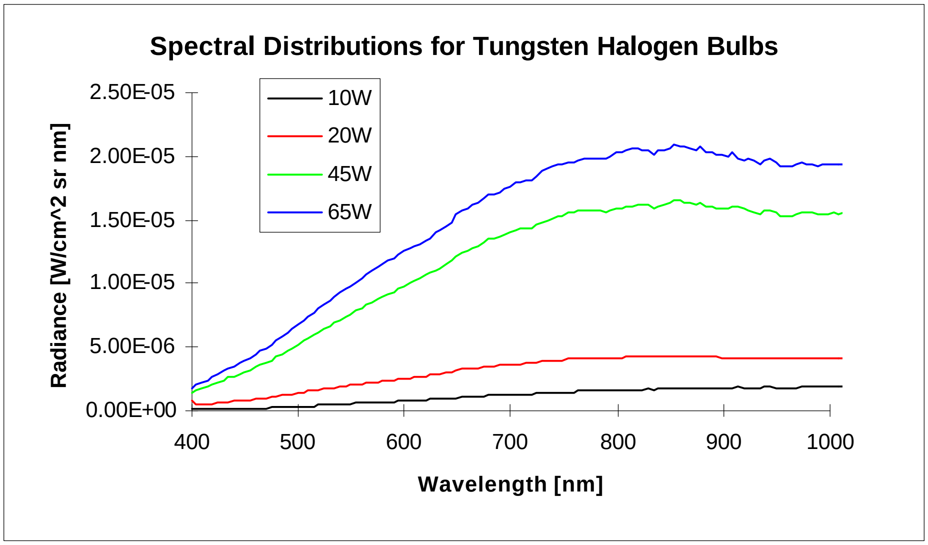

Figure 18-7 Distribution of bulbs used in integration sphere.

A series of ND filters were measured using a transmission densitometer and then subsequently placed in front of the camera to reduce the over light level. The resulting signal (uniform field of light) was then digitized. The reduced radiance was then computed by converting the transmission density to transmittance (see Table 18-5). This value was then used to modulate the integrated radiance value. This analysis was then performed for a series of camera gains. The results of this can be seen in Figure 18-8 - Figure 18-10.

Table 18-5 IICCD radiometric calibration for gain = 5.5 V.

Gain = 5.5V File name	Mean DC	Stddev	Filter 1	Filter 2	Transmission density, D_τ	Transmission $\tau=10^{-D\tau}$	Reduced radiance [W/m^2 sr]
g55_fll01	42.24	3.84	3.92	2.37	6.29	5.13E-07	2.82E-06
g55_fll02	40.89	3.72	3.92	2.37	6.29	5.13E-07	2.82E-06
g55_fll03	38.48	3.27	3.57	2.77	6.34	4.57E-07	2.52E-06
g55_fll04	38.38	3.26	3.57	2.77	6.34	4.57E-07	2.52E-06
g55_fll05	43.08	3.97	3.83	2.37	6.2	6.31E-07	3.47E-06
g55_fll06	43.55	3.97	3.83	2.37	6.2	6.31E-07	3.47E-06
g55_fll07	48.18	4.71	3.24	2.77	6.01	9.77E-07	5.38E-06
g55_fll08	48.81	4.65	3.24	2.77	6.01	9.77E-07	5.38E-06
g55_fll09	54.53	4.95	3.57	2.37	5.94	1.15E-06	6.32E-06
g55_fll10	54.9	5.07	3.57	2.37	5.94	1.15E-06	6.32E-06
g55_fll11	62.25	4.88	3.92	1.94	5.86	1.38E-06	7.6E-06
g55_fll12	62.02	4.86	3.92	1.94	5.86	1.38E-06	7.6E-06
g55_fll13	67.55	4.9	3.83	1.94	5.77	1.7E-06	9.35E-06
g55_fll14	68.04	4.87	3.83	1.94	5.77	1.7E-06	9.35E-06
g55_fll15	74.63	6.06	3.24	2.37	5.61	2.45E-06	1.35E-05
g55_fll16	73.67	6.11	3.24	2.37	5.61	2.45E-06	1.35E-05
g55_fll17	114.22	8.5	3.57	1.94	5.51	3.09E-06	1.7E-05
g55_fll18	88.96	6.69	3.57	1.94	5.51	3.09E-06	1.7E-05
g55_fll19	108.05	8.29	3.57	1.94	5.51	3.09E-06	1.7E-05
g55_fll20	90.17	6.4	3.57	1.94	5.51	3.09E-06	1.7E-05

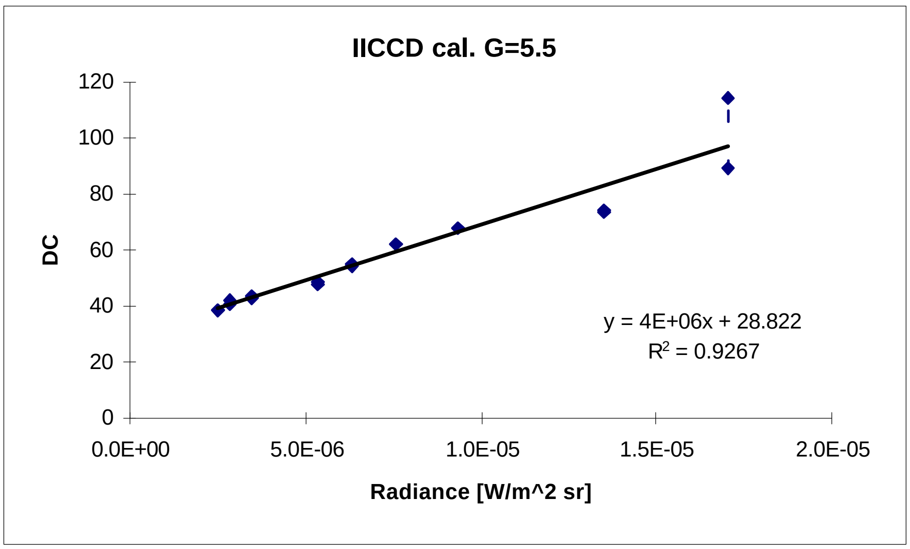

Figure 18-8 Calibration curve for gain = 5.5 V.

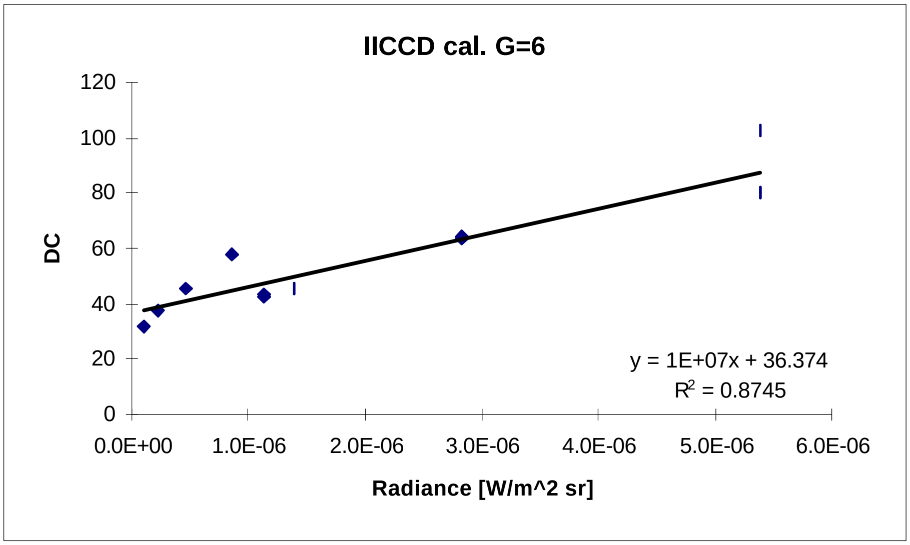

Figure 18-9 Calibration curve for gain = 6.0 V.

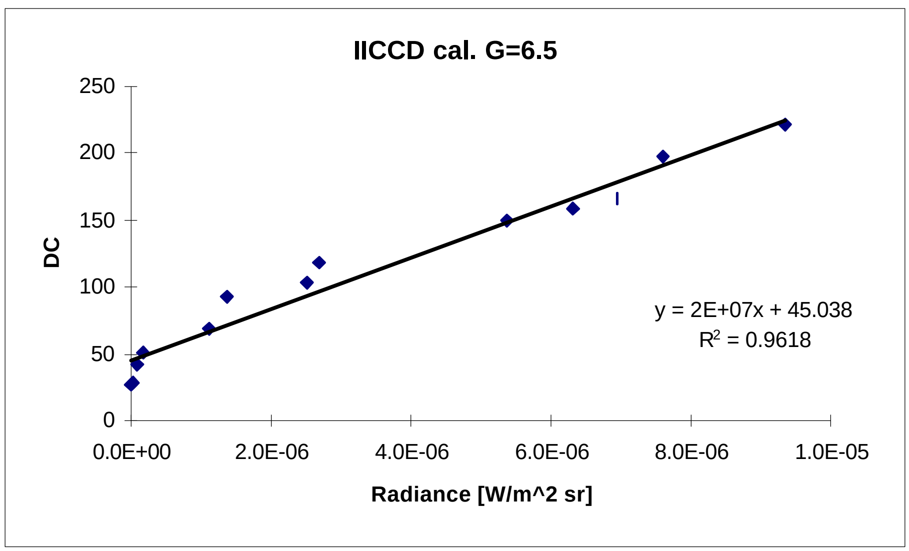

Figure 18-10 Calibration curve for gain = 6.5 V.

The above data was collected with an aperture setting of f/11. However, the f-number at the time of the collection was f/5.6 or 2 stops up. We therefore compensate by factoring 4 times as much light into the gain values (see Table 18-6, Figure 18-11 and Figure 18-12). It is this gain that we apply to the SIG radiance imagery to simulate the various camera gain settings. In Figure 18-11, we show a linear interpolation between data points. This *may* be valid for camera gains from 5.5 to 6.5 V, but clearly it is not valid outside this range. The gain associated with 5 V calibration was estimated because of the lack of data.

Table 18-6 Camera and image gain values.

Camera gain [V]	Gain for f/11	est. Gain for f/5.6	Bias
*5.0	2×10^6	8×10^6	20
5.5	4×10^6	16×10^6	29.822
6.0	10×10^6	40×10^6	36.374
6.5	20×10^6	80×10^6	45.038

* estimated

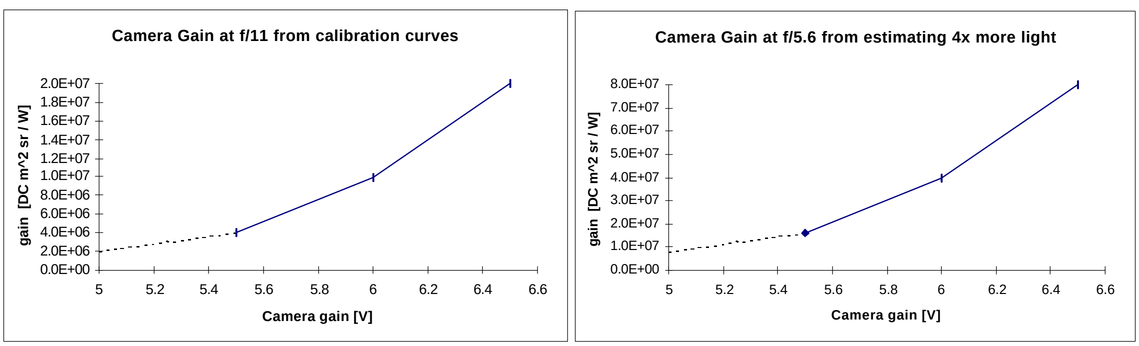

Figure 18-11 Camera gain as a function of image gain value.

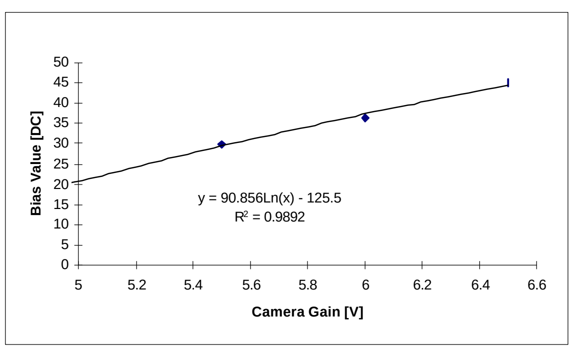

Figure 18-12 Image bias as a function of camera gain.

19. Appendix I

19.1 Inverse Square Law Predictions (no aperture)

As mentioned before, we will base all the calculations on the street lamp source which contained a 40 W tungsten bulb in an enclosed housing. First we will consider the case with out the aperture in front of the source. We will deal with the aperture case latter. We start with some laboratory measured radiance and distance data. These were collected using a halon disk and the PR-650 radiometer. We now ask the question, what is the radiance on the ground if the source was 13' 9" away (which is the bottom of the source)?

$r\_1 := 60.96\,cm$ $\quad r\_2 := 109\cdot cm$ $\quad r\_distance := 13\cdot ft + 9\cdot in$ $\quad sr := 1$

$L\_1 := 0.239\dfrac{watt}{m^2\cdot sr}$ $\quad L\_2 := 0.079\dfrac{watt}{m^2\cdot sr}$ $\quad L=?$

Use the inverse square law to find the <u>radiance, (really the irradiance)</u> for 2 cases (we're pretty far away from the source). Furthermore, there are no cos θ falloff effects (i.e., tilted halon disk).

$$Lcase1 := \frac{L\_1\cdot r\_1^2}{r\_distance^2} \qquad Lcase2 := \frac{L\_2\cdot r\_2^2}{r\_distance^2}$$

$$Lcase1 = 0.005057\frac{watt}{m^2\cdot sr} \qquad Lcase2 = 0.005344\frac{watt}{m^2\cdot sr}$$

Since we have two data points, we can do a cross check to see it the inverse square law is holding up by using set 1 to compute the predicted radiance at the distance in set 2, then compare.

$L2cross\_check := \frac{L\_1 \cdot r\_1^2}{r\_2^2}$ $L2cross\_check = 0.074754 \frac{watt}{m^2 \cdot sr}$

$error := \frac{L\_2 - L2cross\_check}{L\_2} \cdot 100$ $error = 5.37$ $mW := 10^{-3} \cdot watt$

The radiance we predicted was smaller by $L\_2 - L2cross\_check = 4.245934 m^{-2} \cdot mW$. This difference is around 5% which is tolerable since, maybe, we are not "totally" in the inverse square law region yet. Therefore, we will use the second data set for the $r\_distance = 13.75 \cdot ft$ radiance prediction which "is" in the inverse square law region.

There are 3 fundamental problems with these answers. 1) these answers are only integrated from 0.380 to 0.780 μm (due to the measuring instrument). DIRSIG radiance values will be integrated from 0.500 to 0.925 μm, which is the sensors range. 2) the sensor response is not taken into account. 3) we do not take into account source information, such as the area of the filament, transmission of the glass bulb, etc.

19.1.1 Bulb Efficiency

With the measured data we can calculate the efficiency of the 40 W tungsten source. Since the efficiency of tungsten sources is well known, this calculation will serve as a (sanity) check to make sure the above data is in the ball park.

eff = (Pout / Pin)* 100

$\Theta = E A$ $E = L \pi$ (r = 1) (using Halon reflector, i.e., lambertian)

$A = 4 \pi r^2$

$\Theta = 4 \pi^2 \cdot L\_1 r\_1^2$

$Pout = \Theta$

$i := 0.326 amp$

$v := 118 volt$

$$Pin := i \cdot v$$

$$Pout = 3.506 \cdot watt$$

$$Pin = 38.468 \cdot watt$$

$$eff := \frac{Pout}{Pin} \cdot 100 \qquad eff = 9.11$$

Typical efficiency's are around 7% in the visible. This is slightly higher because the bulb was in an enclosed housing. This means that our collected data is very reasonable.

19.1.2 Use Planck Equation to Reproduce PR-650 Data

Another way to calculate the radiance at some distance is to use the Planck equation. This is valid since tungsten and tungsten-halogen sources both have spectral exitance distributions that closely match that of a blackbody with color temperature, T. First we recreate the previous set of radiance answers from the radiometer using a measured color temperature. If all is well, the values will be the same. We can then introduce the correct integrated response interval, the sensor response, and the area of the filament, for example. The geometry we will use in the predictions is illustrated in Figure 19-1.

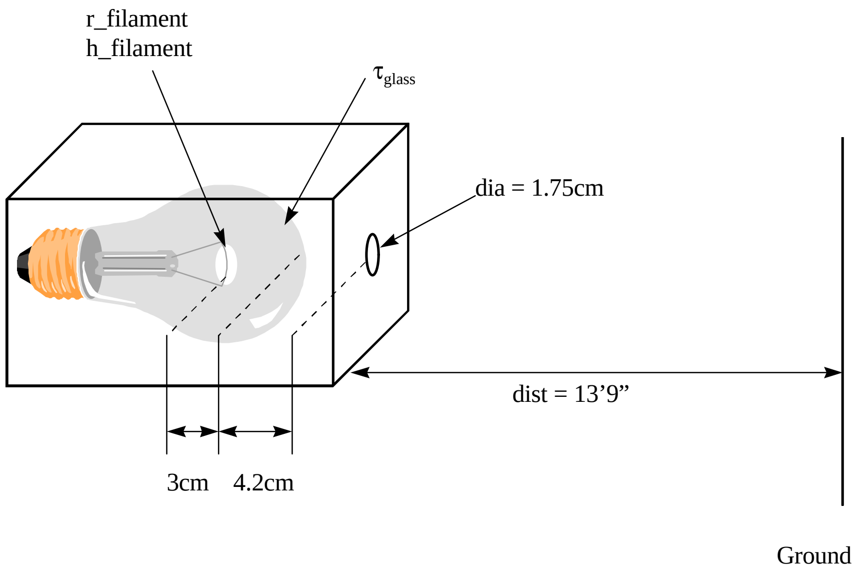

Figure 19-1 Geometric parameters of light the source to be considered for radiometric predictions.

$h := 6.6260755 \cdot 10^{-34} \cdot \mathrm{joule} \cdot \mathrm{sec}$ $k := 1.380658 \cdot 10^{-23} \cdot \frac{\mathrm{joule}}{K}$ $\mu m := 10^{-6} \cdot m$

$c := 299792458 \frac{m}{\mathrm{sec}}$ $T := 2669 K$ (avg. of 6 measurements)

$\lambda 1 := 0.380 \cdot \mu m$ $r\_filament := 0.5 \cdot mm$

$\lambda 2 := 0.780 \cdot \mu m$ $h\_filament := 5 \cdot mm$

$$M(\lambda) := \frac{2\,\pi\,h\,c^2}{\lambda^5 \cdot \left(\exp\left(\frac{h.c}{\lambda\,k\,T}\right) - 1\right)} \text{[W/m^3]}$$

$$\lambda := \lambda 1, (\lambda 1 + 0.010 \mu m) .. \lambda 2$$

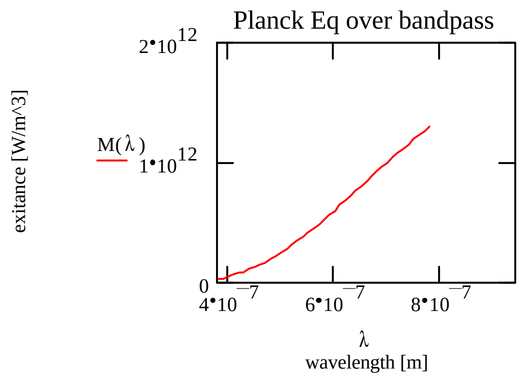

$$\text{Mbandpass} := \int_{\lambda 1}^{\lambda 2} M(\lambda)\, d\lambda$$

$\Theta\text{total} := \text{Mbandpass} \cdot 2 \cdot \pi \cdot \text{r\_filament} \cdot \text{h\_filament}$
(lateral surface area, cylinder =2πrh)

The efficiency flux was $\text{Pout} = 3.51 \cdot \text{watt}$.
The total here is $\Theta\text{total} = 3.6 \cdot \text{watt}$

$$E := \frac{\Theta\text{total}}{4 \cdot \pi \cdot \text{r\_distance}^2}$$
(surface area, sphere =4πr^2)

$$L1 := \frac{E}{\pi}$$

$L1 = 0.005188 \dfrac{\text{watt}}{m^2 \cdot sr}$ $\qquad$ $\text{Lcase2} = 0.005344 \dfrac{\text{watt}}{m^2 \cdot sr}$

This answer is very close to the measured Lcase2 value. Therefore, we have successfully reproduced the radiometers results. The math looks good.

19.1.3 Include and Sensor Response and Correct Bandpass

In order to see the same radiance as DIRSIG predicts, we need to change the bandpass and include the sensor response.

$N := 92$ $\qquad$ $i := 0..N$ $\qquad$ We really have $N + 1 = 93$ data points in our sensor file, as defined by the scene node file (*.snd).

$\lambda := \mathrm{READPRN}(\text{wavelength})\cdot m \qquad \lambda min := \lambda_0 \qquad \lambda min = 0.48\cdot\mu m$

$\beta := \mathrm{READPRN}(\text{beta}) \qquad \lambda max := \lambda_N \qquad \lambda max = 0.94\cdot\mu m$

Our actual interval is from 0.500 to 0.925um. The values at the ends get diminished, so its effectively the same. We need .48 - .94um to get 93 values spaced at .005um.

$$M_i := \frac{2\cdot\pi\cdot h\cdot c^2}{\left(\lambda_i\right)^5\cdot\left(\exp\left(\frac{h\cdot c}{\lambda_i\cdot k\cdot T}\right)-1\right)}$$

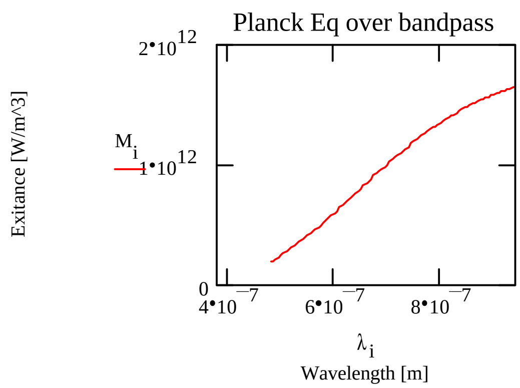

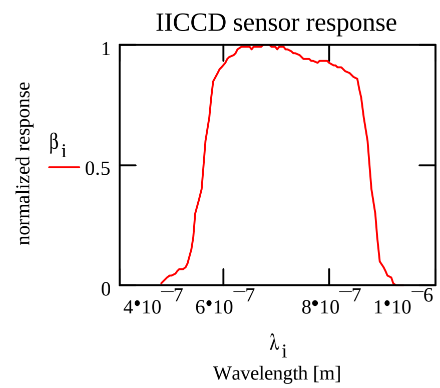

$\Delta\lambda := \frac{\lambda max - \lambda min}{N+1} \qquad \Delta\lambda = 0.005\cdot\mu m \qquad T = 2669\,K$

Compute radiance just as before except now we are using a discrete integral while changing the bandpass and including the IICCD response.

$$Lcorrected1 := \frac{\sum_{i=0}^{N} M_i\cdot\Delta\lambda\cdot\beta_i\cdot(2\cdot\pi\cdot r\_filament\cdot h\_filament)}{\pi\cdot\left(4\cdot\pi\cdot r\_distance^2\right)}$$

$Lcorrected1 = 0.0070795028\frac{watt}{m^2\cdot sr} \qquad L1 = 0.0051881248\frac{watt}{m^2}$ Uncorrected

19.1.4 Compute as Intensity Instead of Exitance

Technically, DIRSIG reads in **spectral intensity** values from a file then computes the radiance at a given distance. The answers obtained here should be exactly the same as before. This is how DIRSIG predicts the radiance on the ground.

First we convert exitance [M] to intensity [I].

$M = \Theta / A$
$\Theta = MA$

$I = \Theta / \Omega$
$I = MA / \Omega$
$I = M$ (surf. area of filament) / 4π sr -(4π sr in a sphere)
$I = (M\, 2\pi rh) / 4\pi$
$I = Mrh / 2$ [W/m sr]

$$I_i := \frac{2\cdot\pi\cdot h\cdot c^2}{\left(\lambda_i\right)^5\cdot\left(\exp\left(\frac{h\cdot c}{\lambda_i\cdot k\cdot T}\right)-1\right)}\cdot\frac{r\_filament\cdot h\_filament}{2} \quad \text{[W/sr m]}$$

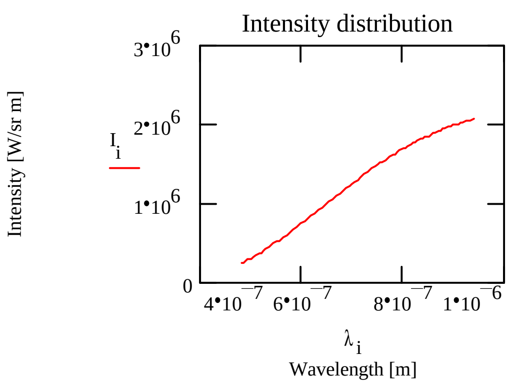

$\lambda min = 0.48\cdot\mu m$
$\lambda max = 0.94\cdot\mu m$
$\Delta\lambda = 0.005\cdot\mu m$

$$I\_bandpass := \sum_{i=0}^{N} I_i\cdot\Delta\lambda\cdot\beta_i$$

$$E := \frac{I\_bandpass}{r\_distance^{2}}$$

$$Lnew := \frac{E}{\pi}$$

Computing using M or I results in the same value. This is good.

$$Lnew = 0.0070795028 \frac{watt}{m^{2} \cdot sr} \qquad Lcorrected1 = 0.0070795028 \frac{watt}{m^{2} \cdot sr}$$

19.2 Radiance Including Aperture

We have successfully predicted the radiance on the ground and shown that it agrees with DIRSIG's results. However, the actual radiance on the ground will be lower when an aperture is placed in front of the source. We will now calculate the radiance on the ground with this aperture in place. Finally we will reduce the value generated by DIRSIG to this amount.

Some measured data to see the behavior of aperture area, distance, and radiance.

$j := 0..4 \quad i := 0..2$

$d\_aperture56_j :=$

$1.25 \cdot cm$
$1.5 \cdot cm$
$2 \cdot cm$
$2.5 \cdot cm$
$3 \cdot cm$

$L56\_76_j :=$

$0.00969 \, watt \cdot m^{-2} \cdot sr^{-1}$
$0.0134 \, watt \cdot m^{-2} \cdot sr^{-1}$
$0.0255 \, watt \cdot m^{-2} \cdot sr^{-1}$
$0.0425 \, watt \cdot m^{-2} \cdot sr^{-1}$
$0.0623 \, watt \cdot m^{-2} \cdot sr^{-1}$

$d\_aperture105_i :=$

$2 \cdot cm$
$2.5 \cdot cm$
$3 \cdot cm$

$L105\_102_i :=$

$0.00777 \, watt \cdot m^{-2} \cdot sr^{-1}$
$0.01330 \, watt \cdot m^{-2} \cdot sr^{-1}$
$0.01830 \, watt \cdot m^{-2} \cdot sr^{-1}$

$$A\_aperture56_j := \pi \cdot \left(\frac{d\_aperture56_j}{2} \right)^2$$

$$A\_aperture105_i := \pi \cdot \left(\frac{d\_aperture105_i}{2} \right)^2$$

$m56 := slope(A\_aperture56, L56\_76)$

$m105 := slope(A\_aperture105, L105\_102)$

$b56 := intercept(A\_aperture56, L56\_76)$

$b105 := intercept(A\_aperture105, L105\_102)$

$$m56 = 91.102 \cdot \frac{watt}{m^4}$$

$$m105 = 26.681 \cdot \frac{watt}{m^4}$$

$$b56 = -0.002 \cdot \frac{watt}{m^2}$$

$$b105 = -0.000323 \cdot \frac{watt}{m^2}$$

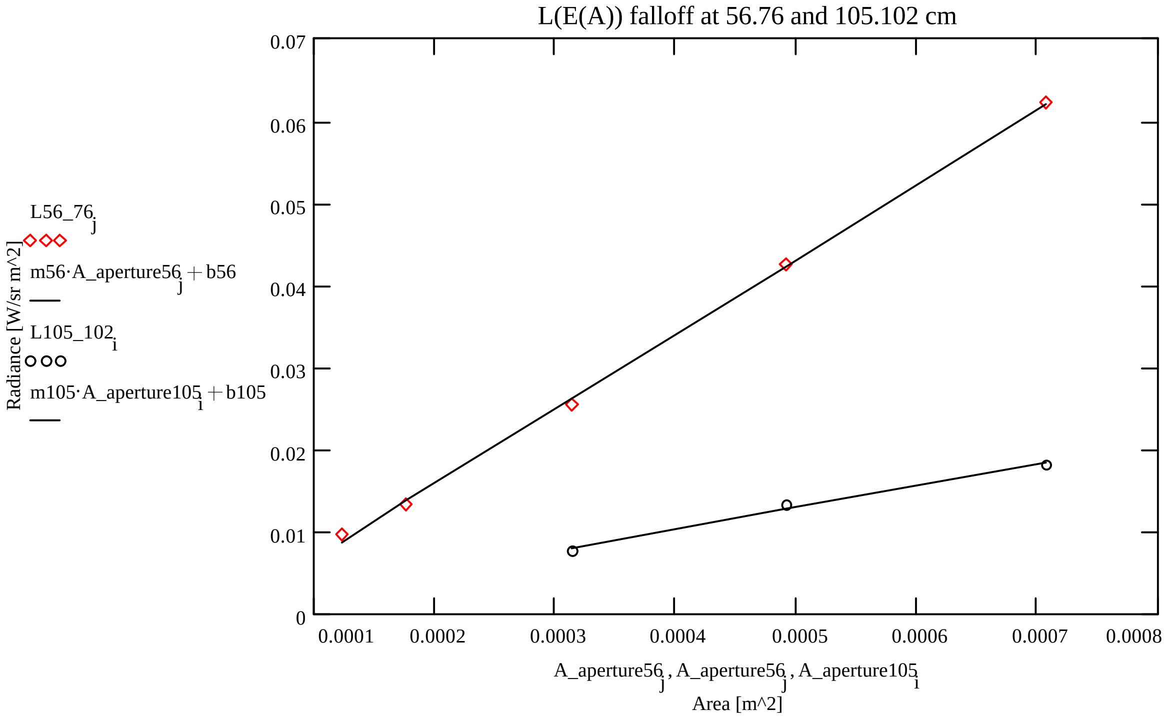

We know how the irradiance changes, via the inverse square law, as a function of distance. Once at a given distance, the variation in irradiance is linear with aperture diameter, as expected. Therefore to predict the radiance at 13ft for a given aperture diameter, we actually predict the slope (and intercept) of the aperture first, construct a linear equation with m and b, and compute L. This is illustrated below.

$13 \cdot ft + 9 \cdot in = 419.1 \cdot cm$

Using r= 56.76 cm data.

$$m419\_1 := \frac{m56 (56.76cm)^2}{(419.1 \cdot cm)^2}$$

$$m419\_1 = 1.671006 \frac{watt}{m^4}$$

$$b419\_1 := \frac{b56 \cdot (56.76cm)^2}{(419.1 \cdot cm)^2}$$

Using r= 105.102 cm data.

$$m419\_2 := \frac{m105 (105.102cm)^2}{(419.1 \cdot cm)^2}$$

$$m419\_2 = 1.677956 \frac{watt}{m^4}$$

$$b419\_2 := \frac{b105 \cdot (105.102cm)^2}{(419.1 \cdot cm)^2}$$

$b419\_1 = -0.0000426 \frac{watt}{m^2}$

$b419\_2 = -0.0000203 \frac{watt}{m^2}$

$Ap\_dia := \frac{11}{16} \cdot in$

$Ap\_dia = 1.746 \cdot cm$

$Ap\_area := \pi \cdot \left(\frac{Ap\_dia}{2}\right)^2$

$L419\_1 := m419\_1 \cdot Ap\_area + b419\_1$

$L419\_2 := m419\_2 \cdot Ap\_area + b419\_2$

$L419\_1 = 0.000358 \frac{watt}{m^2}$

$L419\_2 = 0.000382 \frac{watt}{m^2}$

These are based on what would be seen by the PR-650, not DIRSIG (which has a different sensor response and bandpass).

19.2.1 Recreate Aperture Data From PR-650

We now recreate the radiometers results, once again. If all is well, the values will match. We then implement the correct bandpass and sensor response. Finally, we change DIRSIGs output to match this value and modify the cos(θ) falloff.

$\sigma := 5.6676 \cdot 10^{-8} \cdot \frac{watt}{m^2 \cdot K^4}$

$r\_filament := 0.5 \cdot mm$

$\tau\_glass := .85$

$h := 6.6260755 \cdot 10^{-34} \cdot joule \cdot sec$

$h\_filament := 5 \cdot mm$

$T := 2669 K$

$c := 299792458 \frac{m}{sec}$

$r\_bulb := 3 \cdot cm$

$dist := 13 \cdot ft + 9 \cdot in$

$k := 1.380658 \cdot 10^{-23} \cdot \frac{joule}{K}$

$d\_aperture := \frac{11}{16} \cdot in$

$\mu m := 10^{-6} \cdot m$

If we integrated all the area under the Planck function, for a given T, we will get the total exitance of that source. We then can use our filament area terms to get the total flux. If the filament terms are correct, we should get the rated wattage for the bulb.

$$M\_bulb := \sigma \cdot T^4$$

$$A\_filament := 2 \cdot \pi \cdot (r\_filament) \cdot (h\_filament)$$

$$\Theta\_bulb := (M\_bulb) \cdot (A\_filament)$$

$$\Theta\_bulb = 45.18 \cdot watt$$

(Not bad)

$$M(\lambda) := \frac{2 \cdot \pi \cdot h \cdot c^2}{\lambda^5 \cdot \left(\exp\left(\frac{h \cdot c}{\lambda \cdot k \cdot T} \right) - 1 \right)}$$ [W/m^3]

$$\lambda 1 := 0.380 \cdot \mu m$$
$$\lambda 2 := 0.780 \cdot \mu m$$

$$Mbandpass := \int_{\lambda 1}^{\lambda 2} M(\lambda)\, d\lambda$$

$$\Theta total := Mbandpass \cdot 2 \cdot \pi \cdot r\_filament \cdot h\_filament$$

$$A\_bulb := 4 \cdot \pi \cdot r\_bulb^2$$

(Surface area of bulb)

$$E\_on\_bulb\_glass := \frac{\Theta total}{A\_bulb}$$

Treat the coated bulb glass as a diffuser

$$M\_bulb := (E\_on\_bulb\_glass) \cdot (\tau\_glass)$$

Assume the aperture is “just beyond” the diffuser (i.e., the “lambertian” disk fills the entire aperture).

$$A\_aperture := \pi \cdot \left(\frac{d\_aperture}{2} \right)^2$$

$\Theta := M\_bulb \cdot A\_aperture$

$I := \frac{\Theta}{\pi}$

$E := \frac{I}{dist^2}$

$L2 := \frac{E}{\pi}$

This derived answer correlates extremely well with the values derived empirically. The math looks good.

$L2 = 0.000374 \frac{watt}{m^2}$

$L419\_1 = 0.000358 \frac{watt}{m^2}$

$L419\_2 = 0.000382 \frac{watt}{m^2}$

19.2.2 Include Sensor Response and Bandpass to Correct DIRSIGs Output

Like before, we need to adjust these values for they don't have the corrects bandpass and lack the sensor response.

$N := 92$ $\quad$ $i := 0..N$

$\lambda := READPRN(wavelength) \cdot m$ $\quad$ $\lambda min := \lambda_0$ $\quad$ $\lambda min = 0.48 \cdot \mu m$

$\beta := READPRN(beta)$ $\quad$ $\lambda max := \lambda_N$ $\quad$ $\lambda max = 0.94 \cdot \mu m$

$$M_i := \frac{2 \cdot \pi \cdot h \cdot c^2}{\left(\lambda_i\right)^5 \cdot \left(\exp\left(\frac{h \cdot c}{\lambda_i \cdot k \cdot T}\right) - 1\right)}$$

$\Delta\lambda := \frac{\lambda max - \lambda min}{N + 1}$ $\quad$ $\Delta\lambda = 0.005 \cdot \mu m$ $\quad$ $T = 2669 K$

$$\text{Lcorrected2} = \frac{\sum_{i=0}^{N} M_i\, \Delta\lambda\, \beta_i\, (2\pi\ \text{rfilament hfilament})\ \tau\text{glass Aaperture}}{\pi^2\ \text{Abulb}\ \ \text{dist}^2}$$

$$\text{Lcorrected2} = 0.0005097204\,\frac{\text{watt}}{\text{m}^2\cdot\text{sr}}$$

Uncorrected

$$\text{L2} = 0.0003735422\,\frac{\text{watt}}{\text{m}^2}$$

19.2.3 Compute as Intensity Instead of Exitance, again…

Technically, DIRSIG reads in **spectral intensity** values from a file then computes the radiance at a given distance. The answers obtained here should be exactly the same as before. This is how DIRSIG predicts the radiance on the ground.

I = Mrh / 2 [W/m sr]

$$I_i := \frac{2\cdot\pi\cdot h\cdot c^2}{\left(\lambda_i\right)^5\cdot\left(\exp\left(\frac{h\cdot c}{\lambda_i\cdot k\cdot T}\right)-1\right)}\cdot\frac{\text{r\_filament}\cdot\text{h\_filament}}{2} \qquad \text{[W/sr m]}$$

$$\text{I\_bandpass} := \sum_{i=0}^{N} I_i\, \Delta\lambda\beta_i$$

$$\text{E\_glass} := \frac{\text{I\_bandpass}}{\text{r\_bulb}^2}$$

$$\text{M\_glass} := \text{E\_glass}\cdot\tau\text{\_glass}$$

$$\Theta\text{\_aperture} := \text{M\_glass}\cdot\text{A\_aperture}$$

$$I := \frac{\Theta\text{\_aperture}}{\pi}$$

$$\text{E\_gnd} := \frac{I}{\text{dist}^2}$$

$$\text{Lnew} := \frac{\text{E\_gnd}}{\pi}$$

AGAIN, Computing using M or I results in the same value. This is good.

$$\text{Lnew} = 0.0005097204\,\frac{\text{watt}}{\text{m}^2} \qquad \text{Lcorrected2} = 0.0005097204\,\frac{\text{watt}}{\text{m}^2\cdot\text{sr}}$$

19.3 Secondary Source Radiance Prediction Summary

It can be seen from Table 19-1 that the radiometer model was fairly accurate. This radiometer model was developed because the measuring instrument did not have the correct bandpass or sensor response as DIRSIG. We then developed a corrected model and compared the values, including reflectance's, to DIRSIGs output, (see Table 8-1). The DIRSIG corrected values are slightly higher than the measured radiometer results because we integrate more of the peak of the Planck curve. The sensor response reduction, however, does not out weigh the added energy introduced by the new bandpass.

In the real scene, there was an aperture in front of the source. This severely limits the amount of light reaching the ground. We therefore developed a second detailed model to take into account such parameters as bandpass, sensor response and aperture size. From Table 19-2, we see that the model correlates extremely well with measured data. The introduction of the aperture reduced the radiance directly below the source from 5188 to 374 μW/sr m^2, for the PR-650 cases. This is a factor of 14. The introduction of the aperture reduced the radiance directly below the source from 7080 to 510 μW/sr m^2, for the DIRSIG corrected cases. This is also factor of 14. From this it is estimated that the *irradiance* on the ground directly below the source was around 1.6 mW/m^2.

As of this writing DIRSIG lacks the ability to deal with broad band or extended sources. When a source with an aperture is used, the program merely restricts the field of view with out any regard to the reduction in energy. We can see that such a reduction is significant for small apertures (factor of 14).

Table 19-1 Radiance prediction summary for NO aperture case, at a fixed distance.

Actual measured data	$Lcase2 = 0.005344 m^{-2} \cdot watt$	actual measured
Modeled PR-650 radiance	$L1 = 0.005188 m^{-2} \cdot watt$	modeling radiometer using Planck
DIRSIG corrected	$Lcorrected1 = 0.007080 m^{-2} \cdot watt$	includes bandpass, sensor response

Table 19-2 Radiance prediction summary for aperture case, at a fixed distance.

measured data	$L419\_1 = 0.000358 m^{-2} \cdot watt$	actual measured
measured data	$L419\_2 = 0.000382 m^{-2} \cdot watt$	actual measured
Modeled PR-650 radiance	$L2 = 0.000374 m^{-2} \cdot watt$	modeling radiometer using Planck
DIRSIG corrected	$Lcorrected2 = 0.000510 m^{-2} \cdot watt$	includes bandpass, sensor response

20. Appendix J

20.1 ICCD Simulator

Program:	iiccd_simulator.pro
Description:	Program is designed to read in a DIRSIG radiance field image. The program then computes quantum or shot noise based on the number of photons. It then computes the appropriate intensifier tube MTF based on two parameters. Next it computes the CCD FO MTF based on a sinc function. It then generates a composite filter, computes the FFT of the image and multiplies the magnitudes of the image and filter. Next the inverse FFT is computed and finally Gaussian noise is added in the form of a user defined SNR. The output is linearly scaled.
Author	Emmett Ientilucci
Modification:	6/99

```
FUNCTION LinScl, image, gain, bias,n
	scaled = gain * image + bias
	;need to do the clipping at 8bit, or else IDL will do a reversal.
	FOR col=0, n-1 DO BEGIN
		FOR row=0, n-1 DO BEGIN
			IF scaled(col,row) GT 255.0 THEN scaled(col,row)= 255.0
			IF scaled(col,row) LT 0.0   THEN scaled(col,row)= 0.0
		ENDFOR
	ENDFOR
	RETURN, scaled
END



FUNCTION num_values, end_value, resolution
	answer = ((end_value / resolution)*2 )
	RETURN, answer
END



FUNCTION sinc1d,x,img_sz
	MTF = x
	abs_x = ABS(x)
	FOR col=0, img_sz-1 DO BEGIN
		FOR row=0, img_sz-1 DO BEGIN
			IF (abs_x(col,row) EQ 0.0) THEN BEGIN
				MTF(col,row) = 1.0
			ENDIF ELSE BEGIN
				MTF(col,row) = ABS( sin(!PI*abs_x(col,row)) / (!PI*abs_x(col,row)) )
			ENDELSE
		ENDFOR
	ENDFOR
	RETURN, MTF
END


FUNCTION sinc2d, x, y, img_sz
	MTF2d = sinc1d(x, img_sz) * sinc1d(y,img_sz)
	RETURN, MTF2d
END
```

```
FUNCTION chkbrd,x,y
        checkerboard = make_array(x, y, /long, /index)
        checkerboard = double((-1.)^(checkerboard mod x)*(-1.)^(checkerboard/x))
        RETURN, checkerboard
END




PRO IICCD_simulator

;************************* Get f_of_x ****************************
;openr, lun, 'stlamp_normal_inten_50per.img', /get_lun  ;256
;openr, lun, 'stlamp_scldwn_inten_regadb.img', /get_lun ;256
;openr, lun, 'stlamp_scldwn_inten_90per.img', /get_lun
;openr, lun, 'tghg3110_scldwn300.img', /get_lun
;openr, lun, '78.img', /get_lun
openr, lun, 'test256.img', /get_lun
print, 'Reading in image........'
;openr, lun, 'nolight_90per.img', /get_lun
N = 256.0
Header  = bytarr(8)
Image   = dblarr(N,N)
readu, lun, Header
readu, lun, Image
free_lun, lun
print, 'Image: min=', min(Image), ' max=', max(Image)
print, 'done.'
;************************* END Get f_of_x *************************


Image = rotate(Image,7)


Gain = 8.0E7
Bias = 20.
ImageScaled = LinScl(Image, Gain, Bias, N)
;print, 'OutputImageScaled: Min=', min(OutputImageScaled), ' Max=', max(OutputImageScaled)
window,/free, xsize=N, ysize=N, title='FinalImageScaled'
tv, ImageScaled




;Pixel size
delta_x_noise = 133.0E-6
delta_y_noise = 133.0E-6
delta_x = 133.0E-6
delta_y = 133.0E-6
;Number of pixels
x_number = N ;768
y_number = N ;493



;******* IMPLEMENT SHOT NOISE BASED ON NUM OF PHOTONS ************
print, 'Generating shot noise................'
Npixels  = x_number*y_number
```

```
x_length = x_number*delta_x_noise
y_length = y_number*delta_y_noise
Accd     = x_length*y_length
IntTime  = 0.033
f        = 30.0E-3
omega    = Accd/f^2
h        = 6.6E-34
c        = 3.0E8
lamda    = 500.0E-9


NpCCD   = (Image*Accd*IntTime*omega) / ((h*c)/lamda)
NpPIXEL = NpCCD/Npixels

NpRand = NpPIXEL
FOR ROW=0, N-1 DO BEGIN
        FOR COL=0, N-1 DO BEGIN
                NpRand[COL,ROW] = RANDOMn(seed, 1, POISSON=NpPIXEL[COL,ROW])
        ENDFOR
ENDFOR

ImageShot = (NpRand*Npixels*((h*c)/lamda)) / (Accd*IntTime*omega)

;need to do the clipping at 8bit, or else IDL will do a reversal.
;FOR col=0, N-1 DO BEGIN
;       FOR row=0, N-1 DO BEGIN
;               IF ImageShot(col,row) GT 255.0 THEN ImageShot(col,row)= 255.0
;       ENDFOR
;ENDFOR

print, 'NpPixel:   min=', min(NpPIXEL),   ' max=', max(NpPIXEL)
print, 'NpRand:    min=', min(NpRand),    ' max=', max(NpRand)
print, 'ImageShot: min=', min(ImageShot), ' max=', max(ImageShot)

;window,/free,xsize=N, ysize=N, title='ImageShot'
;tvscl, ImageShot
print, 'done.'
;************************ END SHOT NOISE ************************



;Gain = 60.0E6
;Bias = 0.0
;ImageShotScaled = LinScl(ImageShot, Gain, Bias, N)
;print, 'ImageShotScaled: Min=', min(ImageShotScaled), ' Max=', max(ImageShotScaled)
;window,/free, xsize=N, ysize=N, title='ImageShotScaled'
;tv, ImageShotScaled

;WRITE_TIFF, 'ImageScaled.tif',     ImageScaled
;WRITE_TIFF, 'ImageShot.tif',       ImageShot
;WRITE_TIFF, 'ImageShotScaled.tif', ImageShotScaled




;******************** MAKE II MTF FUNCTION **********************
print, 'Generating II MTF function...........'
delta_x = delta_x*1.0E3  ;puts it in [mm]
delta_y = delta_y*1.0E3  ;puts it in [mm]

nyquist_x = 1.0/(2.0*delta_x)
nyquist_y = 1.0/(2.0*delta_y)

Rscale   = (N/2.0) / nyquist_x
```

```
print, 'CCD Nyquist_x = ',nyquist_x, ' [lp/mm]'
print, 'CCD delta x = ',delta_x, ' [mm]

II_MTF = dblarr(N,N)

freq_const = 15
MTF_index  = 1.0

FOR x=0, N-1 DO BEGIN
        FOR y=0, N-1 DO BEGIN
                r = sqrt(((x-(N/2))^2 + ((y-N/2))^2))
                temp_val = ((r/Rscale)/freq_const)^MTF_index
                II_MTF(x,y) = exp( -temp_val )
        ENDFOR
ENDFOR

x_axis = findgen(N+1) - N/2.0           ;Create and array from -N/2 to +N/2
x_axis_scaled = x_axis * ((2.0*nyquist_x)/N)            ;Scale it to go from -Nyq to +Nyq

;WRITE_TIFF, 'ii_mtf.tif', bytscl(II_MTF)  ;image is only from 0-1, make it 0-255
;window,/free,  xsize=N, ysize=N, title='II MTF'
;tv, bytscl(II_MTF)

;window,/free, title='slice of II MTF'
;plot, x_axis_scaled, II_MTF((N/2),*), title='II MTF',xtitle='[lp/mm]', background = 255, color=0
;WRITE_JPEG, 'ii_mtf_slice.jpg', TVRD()
print, 'done.'
;********************** END II MTF FUNCTION **********************



;***************** MAKE CCD MTF FUNCTION (SINC) ****************
print, 'Generating CCD MTF function............'
;define the extents of the x and y values
resolution  = 1                         ;steps between each value
end_value_x = N/2.0             ;if 100, goes from -100 to +100
end_value_y = N/2.0             ;if res=1 and end=100, x axis has 200 pixels.

x = findgen(num_values(end_value_x, resolution)) * resolution - end_value_x
y = findgen(num_values(end_value_y, resolution)) * resolution - end_value_y

;create the x and y value matrices
xm = x # replicate(1.0, n_elements(y))
ym = replicate(1.0, n_elements(x)) # y

info = size(xm)
img_sz = info(1)

;scl out to the pixel size that yeilds the highest lp/mm
;the other dimention will therfore be smaller..and will fall inside
IF (nyquist_x GT nyquist_y) THEN BEGIN
        scl = nyquist_x
ENDIF ELSE BEGIN
        scl= nyquist_y
ENDELSE

;multiplication factor to scale values by.  a=1 is no scaling
a = scl/(img_sz/2.0)
;a=1.0

;the sinc in freq is defined as sinc(xi/(1/b)), not sinc(xi/b)
CCD_MTF = sinc2d( (xm*a)/(1.0/delta_x), (ym*a)/(1.0/delta_y),img_sz )

;WRITE_TIFF, 'ccd MTF_nyq.tif', bytscl(CCD_MTF)
;window,/free, xsize=((end_value_x/resolution)*2), ysize=((end_value_y/resolution)*2),title='CCD MTF'
;tv, bytscl(CCD_MTF)
```

```
;window,/free, title='Slice in X'
;plot, x*a, CCD_MTF(*,(N/2.0)), xtitle='[lp/mm]', background = 255, color=0
;WRITE_JPEG, 'ccd_mtf_plot_x.jpg', TVRD()
;window,/free, title='Slice in Y'
;oplot, y*a, CCD_MTF((N/2.0),*), color=0
;WRITE_JPEG, 'ccd_mtf_plot_nyq.jpg', TVRD()
print, 'done.'
;********************** END CCD MTF FUNCTION *********************



;*********** WRITE OUT THE COMPOSITE FILTER AND PLOT *************
;Composite_MTF = II_MTF * CCD_MTF
;window,/free, xsize=N, ysize=N, title='Composite MTF'
;tv, bytscl(Composite_MTF)
;WRITE_TIFF, 'Composite_MTF.tif', bytscl(Composite_MTF)

;window,/free, title='Composite slice in X'
;plot, x*a, Composite_MTF(*,(N/2.0)), xtitle='[lp/mm]',background=255,$
;          color=0,linestyle=0,title='Composite MTF (solid line)'
;oplot, x_axis_scaled, II_MTF((N/2),*), color=0, linestyle=2;dashed
;oplot, x*a, CCD_MTF(*,(N/2.0)), color=0, linestyle=2;dashed
;WRITE_JPEG, 'CompositeSlice.jpg', TVRD()
;**************** END COMPOSITE FILTER AND PLOT ******************



;************************** COMPUTE FFT **************************
print, 'Computing FFT..........'
sz = size(ImageShot)
grid = chkbrd(sz(1), sz(2))

FFTImage = grid * FFT(ImageShot * grid)

RealPartImage = float(FFTImage)
ImagPartImage = imaginary(FFTImage)
MagImage      = abs(FFTImage)
PhaseImage    = atan(ImagPartImage, RealPartImage)

;mag_scaled = bytscl(MagImage, min=0, max=0.00000001)
;WRITE_TIFF, 'mag_of_image.tif', mag_scaled
;window,/free, xsize=N, ysize=N, title='MagImage'
;tv, mag_scaled

;window,/free, title='Slice of MagImage'
;plot, x_axis_scaled, MagImage(N/2,*), $
;          title='Slice of Magnitude of Input Image', xtitle='[lp/mm]', background = 255, color=0
;WRITE_JPEG, 'mag_plot.jpg', TVRD()
print, 'done.'
;**************************** END FFT **************************



;************** MULTIPLY MAG OF INPUT, II, and CCD ***************
print, 'Multipling filters...........'
ProductMag = MagImage * II_MTF * CCD_MTF

;ProductMagScl = bytscl(ProductMag, min=0, max=0.00000001)
;WRITE_TIFF, 'mag_result.tif', result_mag_scaled
;window,/free, xsize=N, ysize=N, title='ProductMagScl'
;tv, ProductMagScl

;window,/free, title='Slice of ProductMagScl'
;plot, x_axis_scaled, ProductMagScl(N/2,*), $
```

```
;               title='Slice of ProductMagScl', xtitle='[lp/mm]', background = 255, color=0
;WRITE_JPEG, 'mag_result_plot.jpg', TVRD()
print, 'done.'
;***************** END MULTIPLICATION OF FILTERS *****************



;******************* RECONSTRUCT AND INVERSE FFT *****************
print, 'Computing inverse FFT...........'
;make complex number based on magnitude
jj = COMPLEX(0.0,1.0)
ResultImage =  ProductMag * EXP(jj*PhaseImage)

;Compute the inverse from the Magnitude
sz = size(ResultImage)
grid = chkbrd(sz(1), sz(2))
OutputComplex= grid * FFT(ResultImage*grid, /INVERSE)

;output of IDL is complex!  so take magnitude...
OutputImage = ABS(OutputComplex)
print, 'done.'
;*********************** END RECONSTRUCT ************************




;OutputImageScaled = LinScl(OutputImage, Gain, Bias, N)
;print, 'OutputImageScaled: Min=', min(OutputImageScaled), ' Max=', max(OutputImageScaled)
;window,/free, xsize=N, ysize=N, title='OutputImageScaled'
;tv, OutputImageScaled

;WRITE_TIFF, 'OutputImageScaled.tif', OutputImageScaled



;****************** IMPLEMENT GAUSSIAN NOISE ********************
print, 'Gernerating Gaussian noise............'
;generates an image with mean=0, std=1
randval = RANDOMn(seed, N,N)

info=moment(OutputImage)
mean= info(0)

SNR = 10.0      ;let SNR = mean/std
std = mean/SNR

GausNoise  = mean + (std * randval)
FinalImage = (GausNoise + OutputImage) - mean
print, 'done.'
;******************** END GAUSSIAN NOISE ************************


Gain = 80.0E6
Bias = 0.0
OutputImageScaled = LinScl(OutputImage, Gain, Bias, N)
;print, 'OutputImageScaled: Min=', min(OutputImageScaled), ' Max=', max(OutputImageScaled)
;window,/free, xsize=N, ysize=N, title='FinalImageScaled'
;tv, FinalImageScaled

WRITE_TIFF, 'OutputImageScaled256_133.tif', OutputImageScaled


END
```

21. Appendix K

21.1 Card deck used for MODTRAN run to generate lunar scattering

```
t   2    2    2    1    0    0    0    0    0    0    0    0    1    .000
1.00
f   0f   0   330.000   1.00000   1.00000 f f f
    1    0    0    0    0    0    15.000      .000      .000      .000
.218
     0.718     0.218   180.000      .000      .000      .000    0
0.00000
    2    2   93    1
     0.000    10.000     0.000      .000     0.000      .000    90.000
.000
      0.39      0.91      0.02      0.02rm        mtaa
    0
```

The important parameters for each card deck are listed below

Card 1

t	MODTRAN band model	
2	MODEL	Mid latitude Summer
2	ITYPE	Vertical or slant path between two altitudes
2	IEMSCT	Execution in thermal plus solar/lunar radiance.
1	IMULT	Execution with multiple scattering
….		
1	SALB	Albedo of the earth

Card 2

1	IHAZE	Rural extinction, default vis = 23 km
0	ISEASN	Spring-summer
0	IVULCN	Background stratospheric profile and extinction
0	ICSTL	Used with maritime model only
0	ICLD	No clouds or rain
0	IVSA	Not used
15	VIS	Visibility
….		
0.218	GNDALT	Altitude of surface relative to sea level (km)

Card 3

0.718	H1	Initial altitude (km)

0.218	H2	Final altitude (km) (about 1700 feet)
180	ANGLE	Initial zenith angle (degrees) as measured from H1 (looking down)

Card 3A1

2	IPARM	Controls method of speciying the solar/lunar geometry on card 3A2
2	IPH	Mie-generated internal database of aerosol phase functions
93	IDAY	Day of the year used to specify the earth to sun distance. (April 3rd)
1	ISOURCE	Extraterrestrial source is the moon

Card 3A2

0	PARM1	Azimuthal angle between the observers line of sight and the observer to sun path, measured from the line of sight, positive east of north, -180 and +180
10	PARM2	The solar/lunar zenith angle at H1 (the observer)
….		
90	ANGLEM	Phase angle of the moon (50% illumination fraction)

```
****************** Ephemeris DATA for the MOON and SUN *****************
Emmett Ientilucci  9/98

----------USER DEFINED PARAMETERS:----------
Latitude           = 43.2 deg
Longitude          = -77.6 deg ( NEG puts us W of prime meridian)
Ht above sea level = 0.000038 er[ft] 800.0 feet
Temperature        = 12.8 C            55.0 F
Pressure           = 998.9 mBar       29.5 inHg
Hr behind UTC      = 4.0 (5hr behind GMT in EST, 4hr in EDT)
Current GMT Set    = 4-3-1998, 24: 0
Local Time         = 20: 0
Which is a MJD     = 35887.500000


----------MOON DATA FOR CURRENT TIME IS:---------
Moon Right Ascension, R.A.      = 1.862 rad    106.7 deg      7.11 hrs
Moon Declination, Dec           = 0.319 rad     18.3 deg
Moon azimuth, Az                = 3.443 rad   197.29 deg
Moon alt. from horz, Alt        = 1.114 rad    63.85 deg
Moon Heliocentric lng           = 105.86 deg
Moon Heliocentric lat           = -4.24 deg
Dist from moon to earth, Ea Dst  = 386618.68 km 240233.71 mi
Dist from moon to sun, Sn Dst    = 1.000111 au
< sep btwn obj & sun, Elong      = 91.8 deg?
< size of obj, Size              = 1854 arc seconds
Moon Visual magnitude, VMag      = -12
Moon phase fraction, Phs         = 51.01 percent illuminated

Moon phase angle, angle betwn
earth and sun from obj (moon)    = 1.55 rad 88.838 deg
```

```
Dist from moon to sun, r         = 1.000111
Dist from moon to earth, D_Au    = 0.002584
Dist from sun to earth, R        = 1.000026
p                                = 0.034442 Au
New Phase Angle                  = 88.026 deg
different formula, more accurate


----------SUN DATA FOR CURRENT TIME IS:----------
Sun Right Ascension, R.A.      = 0.225 rad     12.9 deg      0.86 hrs
Sun Declination, Dec           = 0.097 rad      5.5 deg
Sun azimuth, Az                = 4.922 rad   281.99 deg
Sun alt. from horz, Alt        = -0.071 rad    -4.06 deg
Sun Heliocentric lng           = 194.02 deg
Sun Heliocentric lat           = 0.00 deg
Sun Visual magnitude, VMag     = -27
```

22. Appendix L

22.1 CCD Streaking

```
;;
;; PROGRAM:        bloom
;; PUROSE:         This little program reads in a low-light-level image,
;;                 applies a user specified gain term, and then reproduces
;;                 the common blooming effects observed in saturated CCD's.
;;                 The blooming is reproduced by sorting all the amplified
;;                 (from the gain) pixel values in a given line.  The
;;                 brightest pixel value is compared to the user specified
;;                 saturation level.  If this pixel value exceeds the
;;                 saturation level, the overflow is passed to the neighboring
;;                 pixels.  The line is then resorted, and the overflow
;;                 test repeated until there are no pixels over the threshold.
;;

PRO ccd

  ;; say Hi to the nice people
  print, 'CCD gain and blooming program'
  print, 'Written by Scott D. Brown and Emmett Ientilucci'
  print, ''

  ;; Hard code some user specifed values since I don't know
  ;; how to ask for them from the user in IDL yet!
  gain = 1.7
  pixel_max = 300.0
  spread_width = 9.0

  ;; read in our low-light image
  original_image = READ_TIFF( "slant.tif" )

  ;; figure out the size of the image
  x_size = ( SIZE( original_image ))( 1 )
  y_size = ( SIZE( original_image ))( 2 )

  ;; create a window for both the original and modified images
  WINDOW, XSize=x_size*2, YSize=y_size

  ;; display the original image
  TVSCL, original_image, Order=1

  ;; convolve the image to simulate spread from the IT (temporary)
  ;; image = SMOOTH( original_image, 3, /Edge_Truncate )
  image = original_image

  ;; make a new image to store the amplified values
  amp_image = MAKE_ARRAY( x_size, y_size, Value=0, /Float )

  ;; amplify the input image by the user specified gain
  amp_image = image * gain;

  ;; drive through each line in the image and do the blooimg thing
  FOR y=0, y_size-1, 1 DO BEGIN

        ;; make a copy of the current line
        current_line = amp_image( *, y )
```

```
;; sort the pixel value in this line
sort_indexes = REVERSE( SORT( current_line ))

;; check if there is a pixel the will spill over to its neighbors
WHILE( current_line( sort_indexes( 0 )) GT pixel_max ) DO BEGIN

  ;; store the index of this full pixel
  start_x = sort_indexes( 0 )

  ;; figure out the amount of spill over to each side
  start_spill = ( current_line( start_x ) - pixel_max ) / 2.0

  ;; fix the full pixel
  current_line( start_x ) = pixel_max

  ;; seed the spill process with the starting spillover amount
  spill = start_spill

  ;; record the last overflowed pixel location
  last_x = start_x

  ;; now spread extra values in the negative direction
  FOR x=start_x-1, 0, -1 DO BEGIN

        ;; how far are we from the starting bin
        dist = last_x - x

        ;; how much spill to add to this pixel
        weight = ( spread_width - dist ) / spread_width

        ;; add the spill into this pixel
        current_line( x ) = current_line( x ) + ( weight * spill )

        ;; check if there is spill from this pixel
        IF( current_line( x ) GT pixel_max ) THEN BEGIN

          ;; how much spill is left
          spill = ( 1.0 - weight ) * spill

          ;; how much new spill
          spill = spill + current_line( x ) - pixel_max

          ;; fix up this pixel and record our last overflowed pixel
          current_line( x ) = pixel_max - 1
          last_x = x

        ENDIF ELSE BEGIN
          IF( spill LE 0.0 ) THEN BEGIN
                GOTO, DONE_NEGATIVE
          ENDIF
        ENDELSE
  ENDFOR

  ;; where we jump after finishing spilling the current max
  DONE_NEGATIVE:

  ;; re-seed the spill process with the starting spillover amount
  spill = start_spill

  ;; record the last overflowed pixel location
  last_x = start_x

  ;; now spread extra values in the positive direction
  FOR x=start_x+1, x_size-1, 1 DO BEGIN

        ;; how far are we from the starting bin
        dist = x - last_x
```

```
                    ;; how much spill to add to this pixel
                    weight = ( spread_width - dist ) / spread_width

                    ;; add the spill into this pixel
                    current_line( x ) = current_line( x ) + ( weight * spill )

                    ;; check if there is spill from this pixel
                    ;; IF( current_line( x ) GT pixel_max ) THEN BEGIN
                    IF( spill GT 0.0 ) THEN BEGIN

                       ;; how much spill is left
                       spill = ( 1.0 - weight ) * spill

                       ;; how much new spill
                       spill = spill + current_line( x ) - pixel_max

                       ;; fix up this pixel and record our last overflowed pixel
                       current_line( x ) = pixel_max - 1
                       last_x = x

                    ENDIF ELSE BEGIN
                       IF( spill LE 0.0 ) THEN BEGIN
                                GOTO, DONE_POSITIVE
                       ENDIF
                    ENDELSE
               ENDFOR

               ;; where we jump after finishing spilling the current max
               DONE_POSITIVE:

               ;; sort the pixel value in this line
               sort_indexes = REVERSE( SORT( current_line ))

             ENDWHILE

      ;; copy the line back into the image
      amp_image( *, y ) = current_line

   ENDFOR

   ;; convolve the image to simulate spread from the IT (temporary)
   final_image = BYTSCL( amp_image, Min=25, Max=255 )

   ;; display the modified image
   TVSCL, final_image, Order=1, x_size, 0

   ;; write out the modified image
   WRITE_TIFF, "new.tif", final_image
END
```

23. Appendix M

23.1 VIS/IR Fusion of DIRSIG Simulated Imagery

A fused image incorporates the unique features of the thermal and visible images in a single integrated picture. Devising techniques for combining multiple images into a single integrated picture is a problem of continuing interest in fields where the analysis of multisensor or multispectral imagery is a significant activity. Certainly no single sensor or set of bands can provide or exploit all the information inherent in a particular scene of interest. Therefore, it is the job of fusion to bring about relevant information from the various sensor types.

To demonstrate of the use of this synthetic environment for end-to-end modeling, DIRSIG was used to generate a low-light VIS and thermal IR pair [90] for use in a simplified fusion algorithm (see Figure 23-1). The modeled scene is an airfield and hangar including a fighter aircraft and support vehicle. The simulated acquisition time was 0200 hours local time under clear sky, new moon conditions. Lighting was added inside the aircraft hangar to provide a source of photons for the low-light-level camera to be modeled (left image). The IR image has the image wide spatial contrast we expect from the thermal region of the spectrum (right). Additionally, note the colder surfaces on the tops of the vehicle and aircraft that are exposed to the cold clear sky.

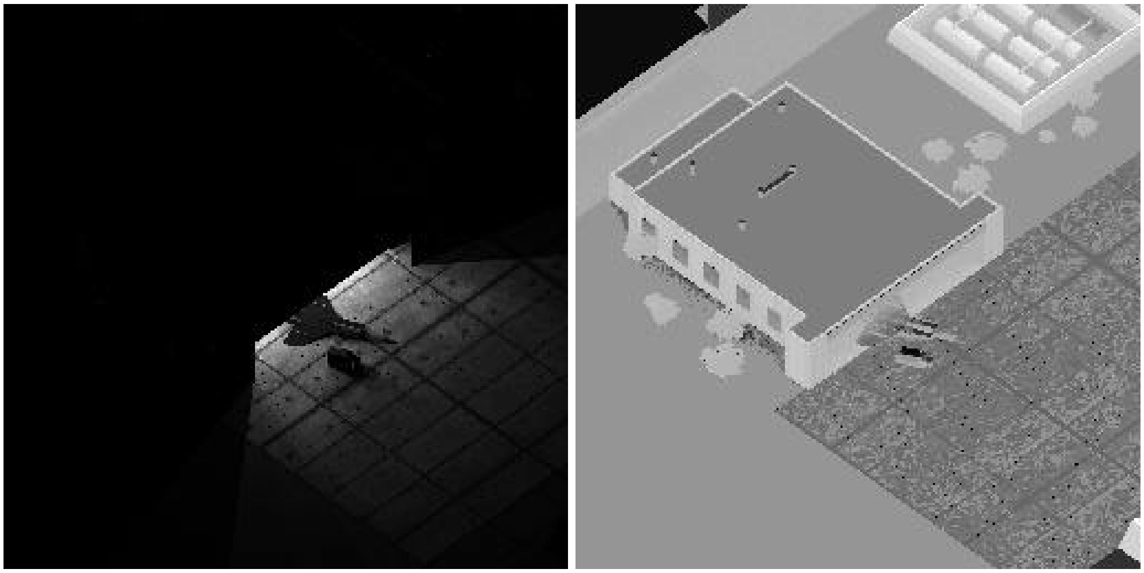

Figure 23-1 DIRSIG simulated visible (left) and thermal IR (right) radiance fields of an airfield hangar. Simulation time is 0200 hours under new moon conditions.

The visible radiance field image was processed using the preliminary characterization of the PULNiX camera and a user specified gain. The thermal IR image was also processed using noise and MTF characteristics of an Inframetrics scanning IR imager. These two images where then fused using a simple weighted addition to produce the imagery in Figure 23-2. Some blooming of the ICCD sensor can be observed along the edge of the hangar.

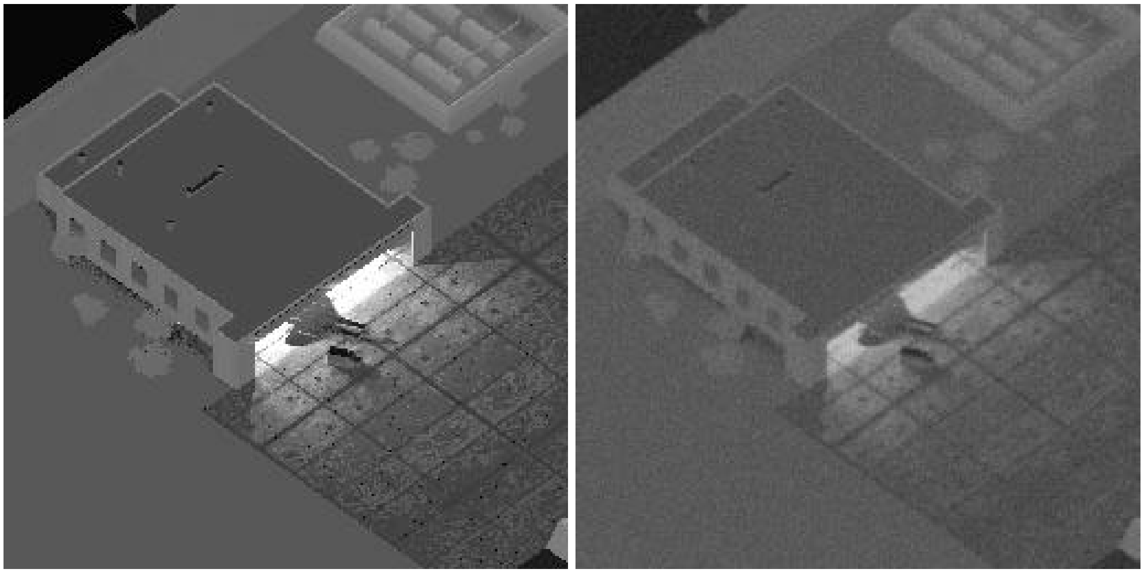

Figure 23-2 Fused product of the DIRSIG simulated images a) with out and b) with sensor effects.

23.2 Using SIG for Fusion Algorithm Development

The use of synthetic imagery for algorithm development allows the engineer to evaluate the effects of changes in acquisition parameters and conditions without the cost associated with a rigorous collection. In addition, the developer gains the availability of more accurate truth data than is conventionally available with field collect data. In regards to the development of better fusion products, the engineer can easily experiment with the use of alternate bands in the fusion process, different sensor responses (spectral shape), the possibility of multi-band fusion, new feedback and gain controls for the low-light-level camera, and approaches to compensate for the effects of blooming.

This effort has demonstrated how SIG can be used to simulate the output from fusion algorithms. Future efforts should focus on methods to compensate for extreme CCD blooming from staring at sources or viewing specular glints. For example, using information from the compliment image should be investigated as well as multi-band fusion and noise suppression techniques.

24. References

24.1 References

[1] Schott, J.R., Kuo, D., Brown, S.D., Raqueno, R.V., “Prediction of observed image spectra using synthetic image generation models,” *Proc. SPIE*, vol. 3118, p.81-93, (1997).

[2] Rankin, D.K., “Validation of DIRSIG, an infrared synthetic scene generation model,” MS Thesis, Rochester Institute of Technology, Center for Imaging Science, (1992).

[3] Webster’s New Collegiate Dictionary, G. & C. Merriam Co., Springfield, Massachusetts, p.596, (1980).

[4] Carruthers, G. R., “Electronic imaging devices in astronomy,” *Astrophysics and Space Science*, vol. 14, p.332, (1971).

[5] Coleman, C. I., Boksenberg, A., “Image intensifiers,” *Contemp. Phys.*, vol. 17, p.209, (1976).

[6] Johnson, C.B., “Photoelectronic detector technology review and update,” *Proc. SPIE*, vol. 1655, p.2-13, (1992).

[7] Csorba, Illes P., “Image intensifiers,” *Information Display*, p.16-19, Jan. (1990).

[8] Csorba, Illes P., “Image intensifiers in low light level and high speed imaging,” *SPIE Milestone Series*, vol. MS20, p.113-118, (1986).

[9] Waynant, R., Ediger, M., Electro-Optics Handbook, McGraw-Hill, New York, (1994).

[10] Kurz, E. A., “Channel electron multipliers,” *American Laboratory*, March (1979).

[11] Wiza, J. L., “Microchannel plate detectors,” *Nucl. Instrum. Methods*, vol. 162, p.587, (1979).

[12] Laprade, B.N., “Advancement in microchannel plate technology,” *Proc. SPIE*, vol. 1655, p.150-178, (1992).

[13] Timothy, J. G., Bybee, R. L., “Preliminary results with microchannel array plates employing curved microchannels to inhibit ion feedback,” *Rev. Sci. Instrum.*, vol. 48, p. 292, (1977).

[14] Timothy, J. G., “Curved-channel microchannel array plates,” *Rev Sci. Instrum.*, vol. 52, no. 8, p.1131, (1981).

[15] Laprade, B. N., “The high output technology microchannel plate,” *Proc. SPIE*, vol. 1072, p.102-110, (1989).

[16] Csorba, I.P., “Current status and performance characteristics of night vision aids,” Opto-Electronic Imaging, Chapter 3, p.34-63, (1985).

[17] Bosch, L.A., “Dynamic uses of image intensifiers,” *Proc. SPIE*, vol. 2551, p.159-172, (1995).

[18] Sturz, R.A., “Advances in low-light-level video imaging,” *Proc SPIE*, vol. 2555, p.196-206, (1995).

[19] Horch, E., “Speckle imaging in astronomy,” *International Journal of Imaging Systems and Technology*, vol. 6, p.401-417, (1995).

[20] Papaliolios, C., Mertz, L., “New two-dimensional photon camera,” *Proc. SPIE*, vol. 331, p.360-369, (1982).

[21] Lampton, M., Paresce, F Flynt, William E., “Measurement of modulation transfer function in image tubes: effects of spurious background brightness,” *Proc. SPIE*, vol. 1952, p. 276-280, 1993.., “The ranicon: A resistive anode image converter,” *Rev. Sci. Instrum*. vol. 45, p.1098-1105, (1974).

[22] Parkes, W., Evans, K.D., Mathieson, E., “High resolution position-sensitive detectors using microchannel plates,” *Nuclear Instrum.Methods*, vol. 121, p.151-159, (1974).

[23] Weiser, H., Vita, R.C., Moos, H.W., Weinstein, A., “Sensitive far UV spectrograph with a multispectral element microchannel plate detector for rockey-borne astronomy,” *Applied Optics*, vol. 1, p.3123, (1976).

[24] Opal, C.B., Feldman, P.D., Weaver, H.A., McClintock, J.A., “Two-dimensional ultraviolet imagery with a microchannel-plate/resistive-anode detector,” in “Instrumentation in Astronomy III,” *Proc. SPIE*, vol. 172, p.317, (1979).

[25] Firmani, C., et al., “High-resolution imaging with a two-dimensional resistive anode photon counter,” *Rev. Sci. Instrum*., vol. 53, no. 5, p.570, (1982).

[26] Martin, C., Jelinsky, P., Lampton, M., Malina, R.F., Anger, H.O., “Wedge-and-strip anodes for centroid finding position sensitive photon and particle detectors,” *Rev. Sci. Instrum*. vol. 52, p.1067-1074, (1981).

[27] Siegmund, O.H.W., Hailey, C.H., Stewart, R.E., Lupton, J.H., “Performance of a photon-counting microchannel plate intensifier with wedge and strip readout,” *Adv. Electronics Electron Phys*. vol. 74, p.97-105, (1988).

[28] Siegmund, O.H.W., Malina, R.F., Proceedings of American Chemical Society Symposium on Imaging Devices in Spectroscopy. (1983).

[29] Timothy, J.G., Morgan, J.S., Slater, D.C., Kasle, D.B., Bybee, R.L., Culver, H.E., “MAMA detector systems: A status report,” *Proc. SPIE* 1158, p.104-117, (1989).

[30] Timothy J.G., “Optical detectors for spectroscopy,” *Publications of the Astronomical Society of the Pacific*, vol. 95, p.810-834, (1983).

[31] Timothy, J.G., Bybee, R.L., “Proceedings of AIAA 21st Aerospace Sciences Meeting (Reno, NV), (1983).

[32] Sartot, M.A., “Characterization and modeling of microchannel plate intensified CCD SNR variations with image size,” Proc. SPIE, vol. 1655, p.74-84, (1992).

[33] Dunham, M.E., Donaghue, D.W., Schempp, W.V., Beardsley, B., “Performance factors for intensified CCD system,” *Proc. SPIE,* vol. 1655, p.66-73, (1992).

[34] Enloe, W., Sheldon, R., Reed, I., Amith, A., “An electron-bombarded CCD image intensifier with a GaAs photocathode,” Proc. SPIE, vol. 1655, p41-49, (1992).

[35] Williams G.M., Reinheimer, A.L., Johnson, C.B., Wheeler, K.D., Wodecki, N.D., Aebi, V.W., Costello, K.A., “Back-illuminated and electron-bombarded CCD low light level imaging system performance,” *Proc. SPIE,* vol. 2551, p.208-223, (1995).

[36] Coldwell, L.V., Boyle, J.J., Kennedy, O., “Low light level CCD-TV,” *Proc. 5th Int. Conf. On CCDs,* Edinb., p. 45-50, (1979).

[37] Sobieski, S., “Intensified CCDs for ultra low light level imaging,” *Proc. SPIE*, vol. 78, p.73-77, (1976).

[38] Enloe, W., Sheldon, R., Reed, L., Amith, A., “An electron-bombarded CCD image intensifier with a GaAs photocathode,” *Proc. SPIE* 1665, vol. 1655, p.41-49, (1992).

[39] Dalinenko, I.N., Malyarov, A.V., Vishnevsky, G.I., Vydrevitch, M.G, Kossov, V.G., Lazovsky, Y., “Design and fabrication technology of thinned backside-excited CCD imagers and the family of the intensified electron-bombarded CCD image tubes,” *Proc. SPIE*, vol. 2551, p.197-203, (1995).

[40] Edgecumbe, J.P., Aebi, V.W., Davis, G.A., “A GaAsP photocathode with 40% QE at 550nm,” *Proc. SPIE*, vol. 1655, p.204-209, (1992).

[41] Schreyer, H., Bohm, H.D.V., Svedevall, B., “40° image intensifier tubes in an integratied helmet system,” *Proc. SPIC,* vol. 1988, p.169-180, (1993).

[42] Heller, F., Mayer, U.M., Fickenscher, T., Schmaub, B., “Ophthalmoscope with micochannel image intensifier tube,” *Proc. SPIE*, vol. 2629, p.246-254, (1996).

[43] Hailey, H.C., Lupton, H.J., Siegmont, W.H.O. Stewart, E.R., Ziock, K.P., “An X-ray image intensifier system for precision wavelength dispersive X-ray spectroscopy,” *Rev. Sci. Instrum*., vol. 61. No. 8, p.2121-2126, (1990).

[44] Howard, N.E., “Theoretical comparison between image intensifier tubes using EBCCD and phosphor readout,” *Proc. SPIE,* vol. 2549, p.188-198, (1995).

[45] Jianxun, Z., Zuyuan, H., Qingbao, W., “Investigation of color image-intensification,” *Proc. SPIE*, vol. 2818, p.205-209, (1996).

[46] Schott, J.R., Remote Sensing: The Image Chain Approach., Oxford University Press, New York, (1997).

[47] Brown, S.D., Schott, J.R., Raqueno, R., Kraska, T., White, R., “Incorporation of bi-directional reflectance characteristics into the digital imaging and remote sensing image generation model,” *Proceedings of the Ground Target Modeling and Validation Conference,* (1997).

[48] Schott, J.R., Salvaggio, C., Brown, S.D., Rose, R.A., “Incorporation of texture in multispectral synthetic image generation tools,” *Proceedings of the SPIE Aerosense*

Conference, Targets and Backgrounds: Characterization and Representation, Vol. 2469, No. 23, (1995).

[49] DCS Corporation, “AIRSIM thermal signature prediction and analysis tool model assumptions and analytical foundations,” DCS Technical Note 9090-002-001, (1991).

[50] Schott, J.R., Mason, J.E., Salvaggio, C., Sirianni, J.D., Rose, R.A., Kulp, E.O., Rankin, D.K., “DIRISG- Digital Imaging and Remote Sensing Image Generation Model: Description, Enhancements, and Validation,” RIT/DIRS Report 92/93-51-146, July (1993).

[51] Brown, S.D., Schott, J.R., Raqueno, R., Krask, T., White, R., “Validation of the Digital Imagin and Remote Sensing Image Generation Model, DIRSIG”, Proceedings of the Ground Target Modeling and Validation Conference, (1996).

[52] Ruffner, J.W., Piccione, D., Woodward, K., “Development of a night-driving simulator concept for night vision image-intensification device training,” *Proc. SPIE*, vol. 3088, p.190-197, (1997).

[53] Anding, D.C., Szabo, A., “Real-time image visualization for sensors,” *Proc. SPIE*, vol. 2741, p.232-241, (1996).

[54] Berk, A., Bernstein, L.S., Robertson, D.C., “MODTRAN: a moderate resolution model for LOWTRAN 7,” GL-TR-89-0122, Spectral Sciences, Burlington, MA, (1989).

[55] Flynt, William E., “Measurement of modulation transfer function in image tubes: effects of spurious background brightness,” *Proc. SPIE*, vol. 1952, p.276-280, (1993).

[56] Liu, Yu; Ma, Yueqin; Jiang, Junyan; Shi, Jifang; “Comprehensive test of low-level-light image intensifiers,” *Proc. SPIE*, vol. 2899, p.550-561, (1996).

[57] Gagne, Robert M., West, Charles N., Wagner, Robert F., Quinn, P.W., “Laboratory measurements of sensitometry, MTF, veiling glare, Wiener spectrum and DQE for image intensifier tubes,” *Proc. SPIE*, vol. 1896, p.248-258, (1993).

[58] Bosch, Leon A., Boskma, Lieuwe B., “Performance of DEP super generation image intensifiers,” *Proc. SPIE*, vol. 2272, p.194-202, (1994).

[59] Lapington, Jonathan S., “Investigation of image non-linearity’s in a photon counting image tube,” *Proc. SPIE*, vol. 2209, p.549-556, (1994).

[60] Yates, George H., King, Nicholas S., Thomas, Matthew C., “Measured responsivites of Generation II and hybrid image intensifiers,” *Proc. SPIE*, vol. 2551, p.145-158, (1995).

[61] Chen, Qingyou, “Relationship between fatigue of Generation II image intensifier and input illumination,” *Proc. SPIE*, vol. 2551, p.288-292, (1995).

[62] Thomas, Matthew C., Yates, George J., Zagarino, Paul A., “Resolution and shutter profile measurements with point source inputs for a microchannel-plate image intensifier (MCPII) with a 160-ps FWHM whole-image shutter,” *Proc. SPIE*, vol. 2551, p.181-188, (1995).

[63] Sinor, Timothy W., Estrea, Joseph P., Phillips, David L., Rector, M. K., “Extended blue GaAs image intensifiers,” *Proc. SPIE*, vol. 2551, p.130-134, (1995).

[64] Estrea, Joseph P., Sinor, Timothy W., Passmore, Keith T., Rector, M. K., “Development of extended red (1.0- to 1.3-um) image intensifiers,” *Proc. SPIE*, vol. 2551, p.135-144, (1995).

[65] White, R.A., “Validation of Rochester Institute of Technology’s (RIT’s) Digital Imaging and Remote Sensing Image Generation (DIRSIG) Model-Reflective Region,” MS Thesis, Rochester Institute of Technology, Center for Imaging Science, July (1996).

[66] Kraska, T.A., “DIRSIG: Digital Imaging and Remote Sensing Image Generation Model: Infrared Airborne Validation and Input Parameter Analysis,” MS Thesis, Rochester Institute of Technology, Center for Imaging Science, April (1996).

[67] Kuo, D.S., “Synthetic Image Generation of Factory Stack and Water Cooling Tower Plumes,” Ph.D Thesis, Rochester Institute of Technology, Center for Imaging Science, August (1997).

[68] Stark, R. B., “Synthetic Image Generation Model: Application of Specular and Diffuse Reflectivity Components and Performance Evaluation in the Visible Region,” MS Thesis, Rochester Institute of Technology, Center for Imaging Science, September (1993).

[69] DCS Corporation., “AIRSIM Thermal Signature Prediction and Analysis Tool Definition and Analysis of Object Paramete Inputs., DCS Technical Note 9090-002-004, December, (1990).

[70] Weidner, V. R., Hsia, J.J., “Reflection properties of pressed polytetrafluoroethylene powder,” Journal of the Optical Society of America, vol. 71, p. 856, July (1981).

[71] Brown, S. D., DIRSIG User’s tutorial, version 2.9a, July, (1995).

[72] RCA Electro-Optics Handbook., RCA Corporation, (1974).

[73] Kingslake, R., Applied Optics and Optical Engineering, vol. 1, “Light: Its Generation and Modification,” Academic Press, New York, N.Y., (1965).

[74] Frenkel, A., Sartot, M.A., Wlodawski, M.S., “Photon-noise-limited operation of intensified CCD cameras,” Applied Optics, vol. 36, no. 22, p. 5288-97, (1997).

[75] Recent review of image intensifiers is given by C.B. Johnson and L.D. Owen in Handbook of Optics, 2^{nd} ed., M. Bass, E.W. Van Stryland, D.R Williams, and W.L. Wolfe, eds. (McGraw-Hill, New York, 1995), vol. 1, pp. 21.7-21.19.

[76] The Photonics Design and Application Handbook, Book 3, 44^{th} International Edition, Laurin Publishing Co., Inc., (1998).

[77] Johnson, C.B., private conversation, December, (1998).

[78] Williams, G.M., “A high-performance LLLTV CCD camera for nighttime polotage,” *Proc. SPIE*, vol. 1655, p.14-32, (1992).

[79] Gaskill, J.D., *Linear Systems, Fourier Transforms, and Optics*, John Wiley and Sons, New, York, (1978).

[80] Johnson, C.B., Phot. Sci Eng. 14, 413 (1970).

[81] Johnson, C.B., “MTFs: A simplified approach,” electro-optical systems design, pp 22-6, November, (1972).

[82] Castracane, J., Clow, L.P., Boskma, L.B., “high-resolution image intensifier development: preliminary results,” *Proc. SPIE*, vol. 2416, p.192-199, (1995).

[83] Tantalo, F.J., “Modeling the MTF and noise characteristics of an image chain for a synthetic image generation system,” MS Thesis, Rochester Institute of technology, (1996).

[84] Glasgow, B.B., Glaser, M.S., Whitley, R.H., “Remote imaging in the ultraviolet using intensified and nonintensified CCDs,” *Proc. SPIE*, vol. 2173, p.85-96, (1994).

[85] Moran, W.W., Ulich, B.L., Elkins, W.P., Strittmatter, R.L., DeWeert, M.J., “Intensified CCD (ICCD) dynamic range and noise performance,” *Proc. SPIE*, vol. 3173, p.430-457, (1997).

[86] Frenkel, A., Sartot, M.A., Wlodawski, M.S., “Photon-noise-limited operation of intensified CCD cameras,” Applied Optics, vol. 36, no. 22, p. 5288-97, (1997).

[87] Nutzel, G., Bosch, L., Schomaker, R., “Camera Users: Are you afraid of the dark?”, Photonics Spectra, p. 183-89, May (1999).

[88] Munechika, C.K., Warnick, J.S., Salvaggio, C., Schott, J.R., “Resolution enhancement of multispectral image data to improve classification accuracy,” *Photogrammetric Eng. And Remote Sensing*, vol. LIX, no. 1, Jan., (1993).

[89] Waxman, A.M., Savoye, E.D. Gay, D.A., Aguilar, M., Gove, A.N., Carrick, J.E., Racamato, J.P., “Electronic imaging aids for night driving: low-light CCD, uncooled thermal IR, and color-fused visible/LWIR,” *Proc. SPIE*, vol. 2902, p. 62-73, (1997).

[90] Ientilucci, E.J., Brown, S.D., Schott, J.R., Raqueno, R.V., “Multispectral simulation environment for modeling low-light-level sensor systems,” *Proc. SPIE*, vol. 3434, p. 10-19, (1998).